TECHNISCHE
UNIVERSITÄT
DARMSTADT

DENSITY-MATRIX EXPANSIONS AND NOVEL NUCLEAR ENERGY DENSITY FUNCTIONALS BASED ON CHIRAL EFFECTIVE FIELD THEORY

Vom Fachbereich Physik
der Technischen Universität Darmstadt

zur Erlangung des Grades
eines Doktors der Naturwissenschaften (Dr. rer. nat.)

genehmigte Dissertation von
Lars Zurek, M.Sc.

Referent: Prof. Achim Schwenk, Ph.D.
Korreferent: Prof. Richard John Furnstahl, Ph.D.

Darmstadt 2023
D17

Density-matrix expansions and novel nuclear energy density functionals based on chiral effective field theory

Dichtematrixentwicklungen und neue nukleare Energiedichtefunktionale basierend auf chiraler effektiver Feldtheorie

Genehmigte Dissertation von Lars Zurek, M.Sc.

Darmstadt, Technische Universität Darmstadt

Referent: Prof. Achim Schwenk, Ph.D.

Korreferent: Prof. Richard John Furnstahl, Ph.D.

Tag der Einreichung: 17.10.2023

Tag der Prüfung: 13.11.2023

Jahr der Veröffentlichung der Dissertation auf TUprints: 2023

Darmstadt 2023 – D17

Abstract

Nuclear structure is complex. A successful and widely used approach to describe atomic nuclei is nuclear density functional theory. It stands out from a range of existing methods by being applicable to all nuclei thanks to its mild computational scaling, at the same time generally reproducing properties of known nuclei accurately, and being rooted in fundamental theorems. However, for various applications higher accuracy than achieved at present and reliable uncertainty estimates are needed. In addition, extrapolations into territory without experimental data are potentially uncontrolled. How to improve the predictive power of energy density functionals is not clear though due to their largely empirical nature.

This is different for ab initio many-body approaches that employ nuclear interaction models based on chiral effective field theory, which provides by construction a recipe for improvement. While ab initio methods, which are more microscopic than density functional theory, are now able to target heavy and open-shell nuclei thanks to tremendous progress in the last decades, the treatment of both at the same time still poses a significant computational challenge. Moreover, the agreement of predictions with experimental results is at present not as good as for energy density functionals.

Therefore, a unification of ab initio approaches and nuclear energy density functionals would be welcome. The idea studied in this thesis is to extend conventional Skyrme functionals, which consist of short-range terms, with terms that describe long-range pion exchange from chiral effective field theory at the Hartree-Fock level. Hartree terms are incorporated essentially exactly and Fock terms are included by converting them to quasi-local form by employing a density-matrix expansion.

The first part of this work consists in a detailed examination of density-matrix expansions for the use in nuclear structure calculations. We investigate various choices and expansion schemes for scalar contributions. Fock energies from pion exchanges are generally well approximated by all variants considered. The use of the density-matrix expansion for chiral pion contributions is therefore supported by this investigation. Nevertheless we find different possibilities to improve over established implementations. This includes using variants that do not truncate at two derivatives in every functional term and using adjusted expansion coordinate schemes for three-nucleon interactions. For scalar-isovector energies we observe the separate treatment of neutrons and protons to be important. The results are found to apply under broad conditions, although self-consistency is not yet tested.

The second part of this work is a study focusing on the actual construction of hybrid energy density functionals consisting of chiral and phenomenological Skyrme terms. We discuss the form of the included contributions and the parameter optimization protocol and construct the GUDE family of functionals. When including pion contributions beyond next-to-leading order in the chiral expansion, we find significant improvements over a reference Skyrme functional constructed following the same protocol. In particular, nuclear masses are better reproduced. We analyze the importance of different pion contributions and identify which terms drive the observed improvements, allowing us to set up a functional with the minimal number of

chiral terms necessary. Since pions are incorporated without adding further optimization parameters to the functionals, the improvements can be attributed to the functional form of these terms. Our work therefore suggests that the considered chiral contributions constitute useful ingredients for ab initio energy density functionals.

Zusammenfassung

Dichtematrixentwicklungen und neue nukleare Energiedichtefunktionale basierend auf chiraler effektiver Feldtheorie

Kernstruktur ist komplex. Ein erfolgreicher und weit verbreiteter Ansatz zur Beschreibung von Atomkernen ist Dichtefunktionaltheorie. Sie ragt aus einer Reihe existierender Methoden heraus, da sie dank ihres geringen Rechenaufwands auf alle Kerne anwendbar ist, gleichzeitig Eigenschaften vermessener Kerne im Allgemeinen akkurat reproduziert und auf fundamentalen Theoremen beruht. Allerdings werden für verschiedene Anwendungen eine höhere Genauigkeit als derzeit erreichbar und zuverlässige Unsicherheitsabschätzungen benötigt. Darüber hinaus sind Extrapolationen in Bereiche ohne experimentelle Daten potenziell unkontrolliert. Wie die Vorhersagekraft von Energiedichtefunktionalen verbessert werden kann, ist jedoch wegen ihrer großteils empirischen Natur unklar.

Anders verhält es sich für Ab-Initio-Vielteilchenmethoden, die nukleare Wechselwirkungsmodelle verwenden, die auf chiraler effektiver Feldtheorie basieren, welche per Konstruktion ein Rezept für Verbesserungen liefert. Während Ab-Initio-Methoden, die mikroskopischer sind als Dichtefunktionaltheorie, heute dank enormer Fortschritte in den letzten Jahrzehnten auf schwere Kerne und solche mit teilweise gefüllten Schalen angewendet werden können, stellt die Beschreibung von Kernen mit beiden Eigenschaften immer noch eine signifikante Rechenherausforderung dar. Zudem ist die Übereinstimmung von Vorhersagen mit experimentellen Resultaten derzeit nicht so gut wie für Energiedichtefunktionale.

Daher wäre eine Vereinigung des Ab-Initio-Ansatzes und nuklearer Energiedichtefunktionale willkommen. Die in dieser Arbeit untersuchte Idee ist die Erweiterung konventioneller Skyrme-Funktionale, die aus kurzreichweitigen Termen bestehen, mit Termen, die den langreichweitigen Pionenaustausch aus chiraler effektiver Feldtheorie auf dem Hartree-Fock-Level beschreiben. Hartree-Terme werden im Wesentlichen exakt berücksichtigt und Fock-Terme werden durch Umwandlung in quasi-lokale Form mittels einer Dichtematrixentwicklung inkludiert.

Der erste Teil dieser Arbeit besteht in einer detaillierten Untersuchung von Dichtematrixentwicklungen für die Verwendung in Kernstrukturrechnungen. Wir untersuchen verschiedene Wahlmöglichkeiten und Entwicklungsschemata für skalare Beiträge. Pionenaustausch-Fock-Energien werden im Allgemeinen für alle betrachteten Varianten gut approximiert. Die Verwendung von Dichtematrixentwicklungen für chirale Pionenbeiträge wird daher durch diese Untersuchung gestützt. Nichtsdestoweniger finden wir verschiedene Möglichkeiten zur Verbesserung gegenüber etablierten Implementierungen. Dazu gehört das Verwenden von Varianten, die nicht bei zwei Ableitungen in jedem Funktionalterm trunkieren, und die Verwendung angepasster Koordinatenschemata für Drei-Nukleon-Wechselwirkungen. Für Skalar-Isovektor-Energien beobachten wir, dass die getrennte Behandlung von Neutronen und Protonen wichtig ist. Diese Resultate sind unter umfassenden Bedingungen gültig, auch wenn Selbstkonsistenz noch nicht getestet ist.

Der zweite Teil dieser Arbeit ist eine Studie, die sich auf die eigentliche Konstruktion hybrider Energiedichtefunktionale, die aus chiralen und phänomenologischen Skyrme-Termen

bestehen, fokussiert. Wir diskutieren die Form der enthaltenen Beiträge und das Parameteroptimierungsprotokoll und konstruieren die GUDE-Familie von Funktionalen. Wenn Pionenbeiträge jenseits der ersten nach der führenden Ordnung in der chiralen Entwicklung berücksichtigt werden, finden wir signifikante Verbesserungen gegenüber einem Referenz-Skyrme-Funktional, das nach demselben Protokoll konstruiert ist. Insbesondere Kernmassen werden besser reproduziert. Wir analysieren die Wichtigkeit der verschiedenen Pionenbeiträge und identifizieren, welche Terme die beobachteten Verbesserungen bewirken, was es uns erlaubt, ein Funktional mit der minimalen Anzahl notwendiger chiraler Terme zu bilden. Da die Pionen ohne zusätzliche Optimierungsparameter in die Funktionale eingebaut werden, können die Verbesserungen auf die funktionale Form dieser Terme zurückgeführt werden. Unsere Arbeit legt daher nahe, dass die betrachteten chiralen Beiträge nützliche Bestandteile für Ab-Initio-Energiedichtefunktionale darstellen.

Contents

1

The nuclear many-body problem

The standard model of particle physics describes our current understanding of elementary particles and their fundamental interactions. It is believed that ordinary matter, mostly consisting of electrons as well as up- and down-quarks bound into neutrons and protons, makes up about 5% of the total energy budget of today's universe [1]. Nuclear physics deals with interactions amongst neutrons and protons, collectively referred to as nucleons, and phenomena resulting therefrom. Nowadays most commonly nucleons occur in form of atomic nuclei. These are compact microscopic objects consisting of up to a few hundred nucleons bound together. See Fig. 1.1 for an overview of nuclei known experimentally (in 2012) and predicted to exist theoretically. Nuclei together with electrons constitute the building blocks of which larger objects such as atoms and molecules are composed. Also, nucleons can directly be bound into macroscopically large objects, namely into neutron stars that are kept together by the attractive gravitational force [1]. When focusing on the nuclear physics of those systems, one typically considers the idealized system of homogeneously spread out nucleons over an infinite volume, called infinite nuclear matter (INM).[1] We encounter INM again later, but this thesis mainly focuses on the description of finite nuclei.

The fundamental interaction of quarks is described by the quantum field theory called quantum chromodynamics (QCD) for the strong interaction (and quantum electrodynamics for the electromagnetic one). It can directly be used to perturbatively calculate properties of processes taking place at high energy scales such as deep inelastic scattering of a lepton on a hadron [4] or states such as heavy quarkonia [5]. Nuclei however are characterized by significantly lower energy scales. In this regime the strong coupling constant is large and prohibits converging perturbative calculations. Therefore, a different approach is needed to calculate finite nuclei. One possibility lies in solving QCD on a lattice, which acts as a non-perturbative regularization scheme [6]. However, such calculations are (computationally) very demanding and have thus so far only been applied to the lightest nuclei using unphysical quark masses [7]. One can instead make use of the fact that at low energies individual quarks are not the relevant degrees of freedom, but instead they occur confined into hadrons, the most stables ones of which are the nucleons introduced above. Therefore, a description of finite nuclei at lower resolution, namely in terms of nucleons and their interactions, is expected to be sufficient to high accuracy. Note that at even smaller energy scales, e.g., to describe vibrational excitations on top of nuclear ground states, one can switch to other effective degrees of freedom such as phonons [8].

This work deals with the intermediate energy regime characteristic for the description of nuclear ground states. We do not consider here the calculation of nuclear dynamics, i.e., reactions between different nuclei as they occur for instance in scattering experiments at

[1] See Appendix A.1 for a list of acronyms used throughout this thesis.

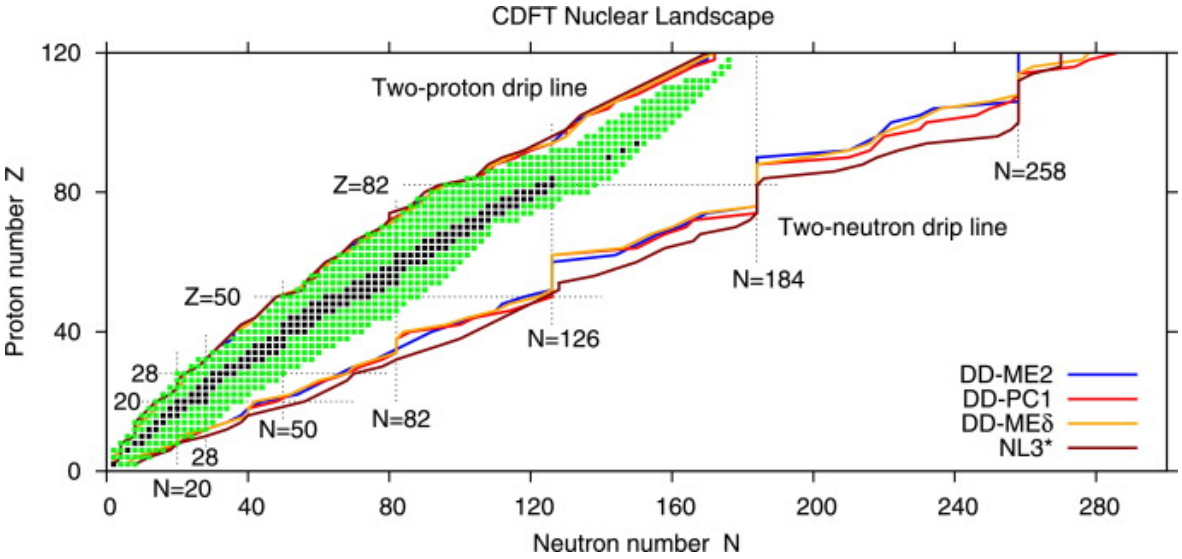

Figure 1.1: Chart of nuclides. Stable nuclei are shown in black, unstable nuclei known according to the 2012 atomic mass evaluation [2] are shown in green. The differently colored lines show the driplines as predicted with different covariant energy density functionals, which mark the limits of the existence of nuclei as bound objects. Only even-even nuclei are shown. Figure taken from Ref. [3].

particle accelerators and in nuclear fusion (e.g., see Refs. [9, 10]). Instead we deal with the nuclear structure problem where the goal is to calculate static properties of nuclei. Particular interest is on ground-state properties of nuclei such as their mass.

The situation in the nuclear structure community is at present generally as follows. For nuclei relatively close to the valley of stability, i.e. the region where nuclei are stable against radioactive decay, observables have been experimentally determined with very high precision. Thus, comparison to experiment in this regime helps clarify the validity and accuracy of a chosen theoretical approach. For very exotic nuclei, i.e. those far away from stability, experimental results are not (yet) available. Such nuclei are important for processes taking place in astrophysical sites, such as r-process nucleosynthesis [11]. These regimes can at the moment only be accessed via theoretical calculations. To give meaningful predictions theoretical uncertainty quantification is crucial, which constitutes an active field of research for the different methods that are being used to tackle the nuclear many-body problem [12–14].

A standard approach to the many-body problem consists of considering the stationary Schrödinger equation for the nucleons that form the nucleus of interest. As the nuclear interaction originates in the fundamental strong interaction only as a residual effect,[2] the derivation of a nuclear interaction potential from QCD is difficult, and the interaction between the nucleons has to be described by some potential model. The modern standard approach is chiral effective field theory (EFT), which is rooted in the symmetries of QCD, see Sec. 1.1. The solution of the Schrödinger equation, in which the potential enters, for many interacting particles is highly nontrivial. Different systematically improvable approximate methods are briefly discussed in Sec. 1.2, where we also discuss successes and challenges of these approaches,

[2]The strong interaction acts on quarks and gluons but nucleons have vanishing color charge and therefore do not feel the strong force directly. Instead, the nuclear force arises as a residual effect thereof, which can be modeled as the exchange of massive mesons between the nucleons. This is analogous to the appearance of van-der-Waals forces between electrically neutral molecules [15] and in contrast to the case of the electrostatic Coulomb potential which can be directly calculated from quantum electrodynamics, see e.g., Ref. [16].

which are generically referred to as ab initio approaches as they are based on first principles through the use of chiral EFT [17].

A different approach to the nuclear many-body problem, density functional theory (DFT), is discussed in Sec. 1.3. It can be thought of as describing the nucleus at somewhat lower resolution, where the degrees of freedom are not individual nucleons but rather the density distributions of these particles [18]. This is the numerical method used to tackle the nuclear structure problem in the present work. For DFT, the solution of the relevant equations is numerically much simpler than in ab initio approaches. Thus, with these methods one can calculate nuclei throughout the entire nuclear chart. In fact, the predicted limits of nuclear existence (called driplines) as shown with lines in Fig. 1.1 have been obtained with a version of nuclear DFT. However, the connection of energy density functionals (EDFs) to QCD is much less clear than in the case of chiral-EFT potentials. This makes a systematic improvement of nuclear energy density functionals hard, and constitutes a main reason for the interest of the nuclear theory community in the construction of EDFs from first principles, which we discuss in Sec. 1.4. This thesis can be located in that subfield of nuclear physics.

We note that several other nuclear-structure methods exist, which are often less microscopic than ab initio methods. Examples are the interacting shell model [19], halo effective field theory [20], and the microscopic-macroscopic method [21], a phenomenologically adjusted approach based on the semi-empirical mass formula. These are not considered in this thesis. An overview of the contents of the main chapters of this thesis is provided in Sec. 1.5 at the end of the present Chapter.

1.1 Chiral effective field theory

Chiral EFT is the modern approach to describe interactions between nucleons in free space. The idea of EFTs has first been formulated in pioneering work by Weinberg [22]. It originates in the observation that using suitable degrees of freedom to describe a system is crucial to obtain a computationally manageable theory. The construction principle is then roughly given as follows [15, 23, 24]: After selecting the relevant degrees of freedom, one writes down the most general Lagrangian compatible with the symmetries of the underlying theory, i.e., with the symmetries of QCD in case of the nuclear force. Then one needs to find a scheme to assess the importance of the different contributions. This is given by a power counting scheme where the different terms are associated to different powers ν in an expansion in Q/Λ_b. Here, Q is a typical small momentum scale entering the diagram of interest (the soft scale) and Λ_b is the (high) breakdown scale (hard scale) of the expansion. This is the scale around which degrees of freedom omitted in the EFT are expected to become important. In other words, an EFT describes explicitly only interactions with momenta below the hard scale (i.e., interactions over distances larger than the inverse hard scale).

The advantage of this EFT construction is that because of the power counting one can obtain an approximation to the interaction of interest by keeping only (finitely many) terms up to a certain power ν in the expansion.[3] This approximation can be refined by including terms up to larger orders. This explains why a clear separation of scales is decisive for constructing a useful EFT.

[3] Of course, this only works if the allowed values of ν are bounded from below. In chiral EFT this is given as a consequence of the spontaneous breaking of chiral symmetry in QCD [15].

Because of the power counting, one can estimate the contribution of neglected terms, which allows for an uncertainty estimate of calculations with an interaction at given order [24]. There exist simpler [24, 25] and more involved schemes [14, 26] to estimate these uncertainties and further research in this direction is ongoing. In the case of chiral EFT, this is the dominant uncertainty (e.g. compared to uncertainties from EFT parameter determination) [24].

In the case of nuclear physics at relatively low energies, nucleons constitute suitable degrees of freedom to construct an EFT since individual quarks are not resolved at these energy scales due to confinement. Using nucleons as only degrees of freedom gives rise to so-called pionless EFT (see e.g. Ref. [27]). It is valid for momenta below the pion mass m_π. Pions can be identified with the Goldstone bosons belonging to the spontaneously broken chiral symmetry of QCD [15]. Because up- and down-quarks are not fully massless, the chiral symmetry is not exact and pions have finite mass, too. Therefore, the nuclear force has finite range in contrast to the Coulomb interaction mediated by massless photons. When pions are also included as degrees of freedom in the EFT, the breakdown scale is increased to the order of the rho meson mass, $\Lambda_b \sim 0.5 - 1$ GeV[4] [24, 28]. The resulting theory is called chiral EFT. The nuclear potentials are obtained using chiral perturbation theory that describes the interaction between pions and nucleons. In the scheme first proposed by Weinberg [29, 30] the resulting interaction between nucleons is then treated fully non-perturbatively (e.g., in the Lippmann-Schwinger equation) as it describes inherently non-perturbative phenomena such as bound states [15, 23, 27].

While alternative approaches have been discussed (e.g., see Refs. [23, 27, 31]), most chiral-EFT-based studies are carried out using Weinberg power counting in which the importance of diagrams is assessed by naive dimensional analysis yielding [15, 27]

$$\nu = -4 + 2m + 2L + \sum_i \Delta_i \tag{1.1}$$

for a connected irreducible diagram with m nucleons and L loops. The sum goes over all interaction vertices in the diagram with

$$\Delta_i = d_i + \frac{n_i}{2} - 2\,, \tag{1.2}$$

where d_i denotes the number of derivatives and n_i the number of nucleon fields at a given vertex i. In this counting scheme, leading order (LO) is given by $\nu = 0$. The resulting diagrams for the first few orders of chiral interactions are shown in Fig. 1.2 and the related analytical expressions are given for instance in momentum-space representation in Ref. [32] and references therein.

One can distinguish two groups of interaction vertices in chiral EFT: contacts involving only nucleons and vertices involving pions. The latter give rise to pion exchange interactions between nucleons, which describe the long-range part of the nuclear force. Short-range contact interactions encapsulate two kinds of physics: contributions from exchange particles heavier than pions, i.e., degrees of freedom not explicitly resolved by chiral EFT [32], and terms from higher orders in the expansion which are neglected when working at a certain finite order. Note that the contacts are also necessary to renormalize the perturbatively calculated potential [23]. This is typically not carried out explicitly as the strength of the contact interactions is determined anyway by fitting to data (implicit renormalization) [33].

[4] Natural units ($\hbar = c = 1$) are used throughout this thesis.

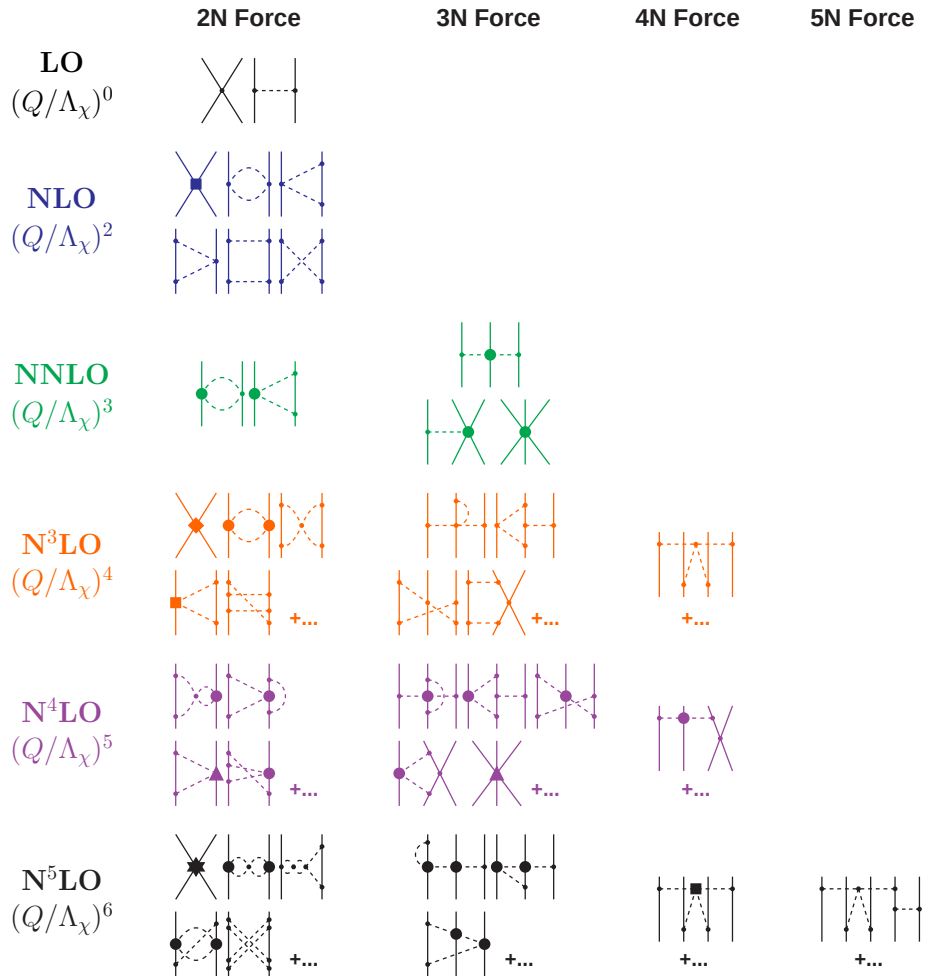

Figure 1.2: Contributions to the nuclear potential in deltaless chiral EFT. Solid lines represent nucleons and dashed lines pions. The different markers denote interaction vertices with contributions of different orders Δ_i to the power counting. Figure taken from Ref. [24].

In EFTs many-body forces arise naturally. These encapsulate the effect of successive two-body forces which are separated by a distance below the resolution scale of the EFT [34]. While according to the power counting, one would expect three-body forces in chiral EFT to first arise for $\nu = 2$, i.e., at next-to-leading order (NLO), it has been shown that these contributions cancel exactly and thus three-nucleon (3N) forces first contribute at N^{2}LO [28] as depicted in Fig. 1.2.

They can be relatively important, namely contributing about 20% to the binding energy of light nuclei [34]. Furthermore, they are necessary to obtain saturation, meaning here a minimum in the energy per particle as a function of density, close to the empirical saturation region in symmetric nuclear matter [28]. With nucleon-nucleon (NN) forces only no minimum is obtained or only at significantly too high densities [35].

In practice, many different nuclear potentials have been obtained from chiral EFT. They can differ from each other in various aspects such as the following.

1. One can distinguish two flavors of chiral EFT depending on whether delta resonances are included as explicit degrees of freedom or not. The Δ resonances are relatively low lying excitations of the nucleons; the mass difference is $m_\Delta - m_\mathrm{N} \approx 293$ MeV [15].

Figure 1.2 shows the chiral interaction diagrams for the deltaless case. In this case some potential parameters acquire unnaturally large values due to the not explicitly included Δ excitations. The chiral order-by-order convergence pattern becomes more systematic when considering deltafull interactions [36]. Then, additional terms have to be considered and 3N forces contribute already at NLO.

2. Terms are included up to different orders in the chiral expansion. At present the most accurate potentials are constructed at fifth order for NN forces[5] [37, 38] and fourth order for 3N forces [28].

3. The interactions are not unique with respect to the regularization scheme necessary when the potentials are iterated in calculations beyond the mean-field level [39]. Cutting off high momenta is consistent with the fact that the theory is valid only for momenta $Q < \Lambda_b$ [23].

4. Potentials differ in the fitting strategies used to fix the parameters, which appear in contact interactions and pion exchanges. They are referred to as low-energy constants (LECs). While one can fit to data from up-to-few-body systems only (such as NN phase shifts, e.g., see Ref. [40]), more recent works also incorporate information from heavier nuclei [41, 42] or infinite matter [43]. Newer developments include the usage of an importance-weighted ensemble of interactions instead of a single one [44].

5. The potentials can be unitarily transformed; when other operators and wavefunctions are transformed accordingly, this leaves observables unchanged. One can make use of this fact by transforming the potentials in a way that makes them more suitable for the application of many-body methods discussed in the following Section. Today, the standard tool employed to this end is called similarity renormalization group (SRG) [45].[6]

A main, unsolved issue in chiral EFT is the observation that some observables are not properly renormalized in Weinberg's prescription [24, 27]. There are several other open challenges, for instance related to regularization, power counting and LEC fitting, see Refs. [27, 38, 48] for overviews. Note also that in spite of successful applications of chiral EFT, see e.g., next Section, it is not clear if the chiral expansion actually converges [49–51].

1.2 Ab initio approaches

To describe ground states of atomic nuclei based on a nuclear interaction potential one needs to solve the A-particle Schrödinger equation, in which the potential enters. For meaningful predictions it is important that the equation is solved in a controlled fashion. Different systematically improvable many-body methods have been developed. When used together with a potential obtained from first principles such as chiral-EFT interactions, discussed in the previous Section, such methods give rise to so-called ab initio approaches.

[5] Selected sixth-order contributions are also taken into account.

[6] The SRG is employed to decouple high- and low-momentum parts of the potentials. This allows to describe low-energy physics without taking irrelevant high-momentum dynamics into account but induces many-body forces [46], which in practice are truncated at the two- or three-body level. The truncation is justified as the SRG preserves the initial chiral-EFT many-body hierarchy [47]. Truncating introduces an error. Hence, one tries to find a "sweet spot" between improved many-body convergence and sizable induced many-body forces.

While two-, three-, and four-body systems can be solved to high accuracy for example in form of Lippmann-Schwinger and Faddeev(-Yakubovsky) equations using partial wave decomposition, see e.g. Refs. [52–54], systems with more particles are more involved. Here we briefly discuss a few employed methods.

In the no-core shell model (NCSM), the many-body Schrödinger equation is set up in form of a matrix eigenvalue equation [55]. This is done by constructing the many-body space via a basis of Slater determinants built from a truncated single-particle basis, e.g., harmonic oscillator (HO) orbitals. The Schrödinger equation is solved quasi exactly in that space by large-scale matrix diagonalization. While all nucleons are treated as active degrees of freedom (unlike in other shell model approaches), the main approximation lies in the truncation of the single-particle basis. Because the matrix dimension grows exponentially in the number of single-particle orbitals and heavier nuclei require larger bases, the NCSM can currently only be employed up to about ^{16}O [55, 56]. By pre-selecting only those Slater determinants that are expected to be important, one can reach heavier nuclei like ^{40}Ca [57]. This approach is referred to as importance-truncated NCSM [58].

While NCSM and all approaches discussed in the next paragraph work in configuration space, there are also some methods that represent the wavefunction in coordinate space. They use Monte Carlo techniques to sample the quantities of interest and are therefore collectively called Quantum Monte Carlo methods. These approaches are at present limited in reach to a similar mass region as the NCSM. See Refs. [59, 60] for details on these methods.

Heavier nuclei are at present reached only by methods that do not solve the many-body problem exactly in a given many-body space. Thereby, they are able to achieve a polynomial scaling in the basis size improving over the exponential scaling of the NCSM [61]. All these methods have in common that they start out from some approximation to the ground state, in this context referred to as reference state. Typical reference states are mean-field solutions, i.e., Slater determinants with the minimal energy for the given potential, see Ch. 2 for details. On top of the reference state, corrections are included via different expansions. Since the corrections are not captured by the mean-field solution, they are referred to as correlations. Accordingly, the many-body methods are called correlation or many-body expansion methods [62, 63]. Such methods include many-body perturbation theory (MBPT), the coupled cluster (CC) method, the in-medium SRG (IMSRG), and self-consistent Green's function theory [61]. For example the CC method uses an exponential ansatz for the exact many-body wavefunction,

$$|\Psi_{\mathrm{CC}}\rangle = \mathrm{e}^{T} |\Phi_{\mathrm{ref}}\rangle \ , \tag{1.3}$$

where $|\Phi_{\mathrm{ref}}\rangle$ denotes the reference state and the cluster operator T is expanded in terms of particle-hole excitations. The standard approach in nuclear physics is to truncate the cluster operator at the two-particle-two-hole level (CC with singles and doubles). Schemes to partially consider triples exist, but taking them into account fully is currently in general too computationally expensive [64].

Ab initio calculations can generally get ground-state energies correct approximately at the 1% level [65]. Recent progress in the field of ab initio approaches includes pushing descriptions towards heavy [44, 66–68] and doubly open-shell [69–74] nuclei. While the former constitutes more of a technical challenge, the latter is achieved by employing hybrid approaches and extensions such as valence-space and multi-reference IMSRG. They allow for more efficiently describing collective (static) correlations than the correlation expansions alone can, which by construction excel at capturing dynamic correlations involving only few particles [61, 75]. See

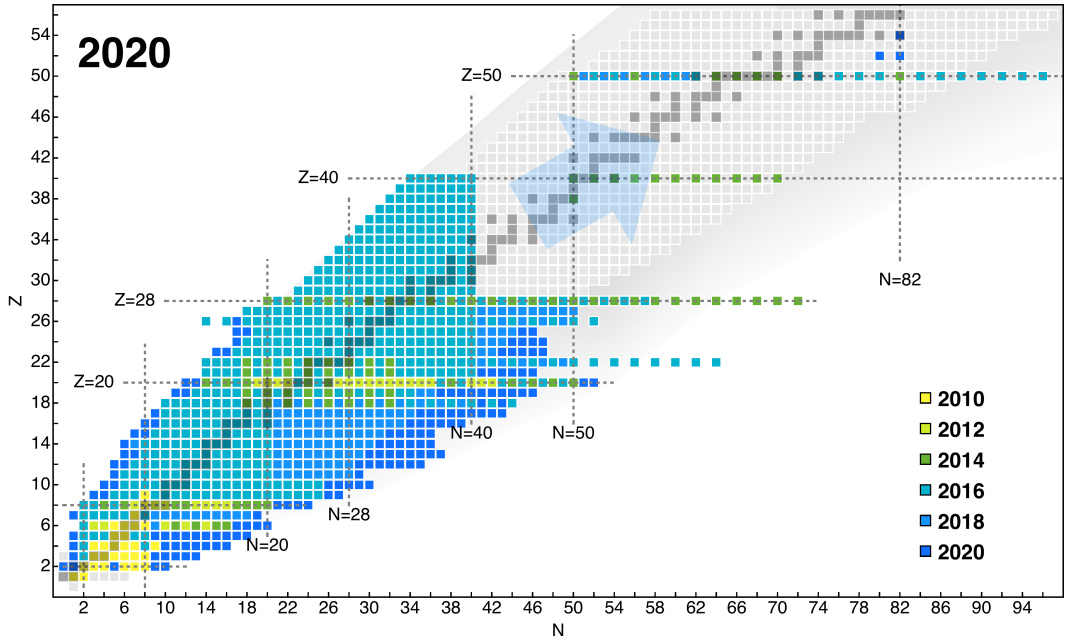

Figure 1.3: Nuclei calculated with ab initio methods up to 2020. The color coding shows up to which year the different calculations were published. This is to be compared to the reach of nuclear DFT calculations that can tackle all known nuclei and beyond. Figure taken from Ref. [61].

Fig. 1.3 for an overview of nuclei that have been calculated with ab initio methods up to 2020. In addition, higher-order, i.e., more precise, variants of existing many-body methods have been developed [64, 76, 77].

A key feature of ab initio approaches to nuclear structure is that both the used interactions obtained from chiral EFT, see Sec. 1.1, and the solution methods as discussed above are systematically improvable. These are important ingredients for a rigorous uncertainty estimate for the obtained results by assessing the size of missing higher-order contributions.

However, due to their huge numerical cost, ab initio methods are not yet ready to be employed in large-scale, high-precision calculations of nuclear ground-state observables. This is related to the fact that calculations for heavy and open-shell nuclei are particularly expensive. Even if one could overcome this computational challenge, it is unclear whether ab initio calculations are going to be able to globally compete with less microscopic methods regarding the accuracy they can achieve. At present, they generally cannot [28, 61, 64, 65]. In the next Section, we discuss a successful less microscopic method that possesses a milder scaling with particle number: density functional theory.

1.3 Nuclear density functional theory

Nuclear density functional theory[7] [83, 84] constitutes currently the most microscopic theoretical framework that can be used in global surveys of atomic nuclei thanks to its favorable computational scaling [85]. It is rooted in the seminal work by Hohenberg and Kohn proving

[7]Some authors make a distinction between nuclear density functional theory and the nuclear energy density functional method, e.g. see Refs. [78, 79]; others do not, e.g. see Refs. [80–82]. We do not make this distinction in the present document.

the existence of a universal functional of the density which, when minimized for fixed particle number, gives the ground state density and energy of a many-body system confined in an external potential [86]. While this is most commonly employed for the description of electronic systems, later works extended the existence proof to self-bound systems as constituted by atomic nuclei [87–90]. However, the form of the universal functional is unknown in either case. In practice most calculations are carried out in the Kohn-Sham formulation of DFT [91], which allows for an efficient description of the (non-interacting) kinetic energy of the system [92] and of shell effects [93] by expressing the density of interest in terms of auxiliary single-particle orbitals of an independent-particle system. In this scheme, interactions take place only via self-consistent mean fields.

Such calculations are formally similar to Hartree-Fock (HF) calculations used as a first step of ab initio approaches. The crucial difference between the two strategies lies in the employed Hamiltonian. Ab initio calculations use potentials that describe the interaction between free nucleons, e.g., as obtained from chiral EFT. Therefore, in this case the mean-field solution is only a first approximation to the true nuclear ground state that then gets refined by employing a correlation expansion method as explained in Sec. 1.2. In contrast, the functionals used in nuclear DFT are models of the interaction in the nuclear medium, meaning they are supposed to include the effect of the other nucleons in the nucleus already at the mean-field level. Therefore, no (computationally more expensive) expansion method has to be employed subsequently and the DFT solution to the nuclear many-body problem is given by the mean-field solution itself. See Ch. 2 for details on mean-field calculations.

In other words, the explicit correlation treatment integral to ab initio methods is in DFT replaced by an implicit representation of correlations encoded in the form of the EDF. In nuclear physics different empirical ansatze have been established for the form of the functional. In the non-relativistic sector, the Skyrme [94] and Gogny [95] EDFs are based on effective nucleon-nucleon interactions. Note that these effective interactions cannot be given in terms of true potentials because they contain terms with explicit density dependences. Thus, one instead uses the term pseudopotential [78, 84]. Genuine energy functionals (not derived from an underlying pseudopotential) include the Fayans [96], the SeaLL1 [97], or the BCPM [98] functionals. Different forms are also available in covariant DFT (also called relativistic DFT), see e.g., Refs. [99, 100]. See Ref. [81] for a discussion on the necessity of a relativistic approach to nuclear EDFs. Here we limit ourselves to non-relativistic functionals.

Each EDF has of order ten parameters that are optimized by fitting to experimental data, typically to ground-state properties of finite nuclei. This gives rise to different parametrizations even for a given functional form. As an example, we mention an overview of 240 Skyrme parametrizations published in Ref. [101].

Empirical EDFs have been successfully employed to describe nuclear bulk properties and some spectroscopic features throughout the known table of nuclides, except for the lightest nuclei. Examples include the UNEDF1 Skyrme parametrization [102], which describes both ground states globally and fission barriers well and reproduces ab initio results for trapped neutron drops, and the Fy(Δr) Fayans parametrization [96], which correctly predicts the non-trivial neutron number dependence of charge radii in the calcium isotopic chain, the description of which constitutes a challenge for ab initio approaches. Because of the mild scaling with mass number, EDFs can also be used to predict the location of driplines far outside the reach of present-day experiments [3, 103, 104].

These achievements are in significant parts linked to using increasingly sophisticated

parameter optimization protocols but it is widely believed that this avenue has been explored to such a degree that further improvements, necessary for instance for the description of r-process nucleosynthesis [105–110] or of single-particle energies [111], need to come from elsewhere [111–113]. The two most obvious routes are the explicit treatment of static correlations via switching from single-reference DFT, as used in this work, to a multi-reference (beyond mean-field) framework [18, 84, 95, 114, 115] and the extension of the form of the employed EDFs, which is what this thesis deals with.

In the former direction many different approaches have been worked out over the years. These include approximate projection techniques such as the Lipkin-Nogami (LN) method to restore particle number symmetry, which is broken in Hartree-Fock-Bogoliubov (HFB) theory (see Sec. 2.4), and more elaborate schemes like the generator coordinate method which treats correlations through the mixing of mean-field states [84]. In particular the latter approaches are computationally very expensive. Note that there exist different, partially unsolved, difficulties when switching to multi-reference calculations related for instance to non-integer powers of the densities in the functionals [18, 78, 116]. In the present work, we abstain from using beyond-mean-field frameworks and do not restore any broken symmetries.

Regarding extending the form of the EDFs, we note that all successful nuclear EDFs have in common that, while their forms are guided by physical considerations, there is no clear path how to improve the functionals. This is related to a missing unifying construction principle (cf. EFTs discussed in Sec. 1.1). Therefore, different empirical strategies have been pursued to extend the functionals' forms (see e.g., Refs. [117–123]). They often consist in adding similar or higher-order terms to existing EDF structures and typically involve introducing additional adjustable parameters.

Properly fitting such parameters is a non-trivial task since they cannot always be well constrained with available experimental data, see also Ch. 4. In addition, this does not address the phenomenological nature of the EDFs, which is the root cause for potentially uncontrolled extrapolations outside the fitting regions [11, 104, 113, 124, 125]. Therefore, firmly connecting nuclear EDFs to an underlying theory would be beneficial. In the following Section we discuss this in more detail.

1.4 Quest for energy density functionals from first principles

As detailed in Sec. 1.3 nuclear DFT is successful, but based on empirical EDFs. This complicates improvements of the functionals and uncertainty estimates, which makes extrapolations potentially unreliable. As discussed in Sec. 1.2, these points can be addressed in the framework of ab initio approaches. However, they are at present not able to be applied to the whole nuclear chart, unlike EDFs, due to high associated computational costs and they reproduce experimental results in general worse than EDFs. Such observations created the idea to root or inform EDFs in microscopic interaction models or build EDFs fully from first principles based on a unifying construction principle.

While different ideas to formulate an effective field theory for EDFs have been discussed [126–131], none of them has been implemented yet. Recasting EDFs as EFTs would offer guidance for more accurate functionals, as well as greater control of their uncertainties

and limits (e.g., toward the driplines), and would fill a gap in the tower of EFTs describing strong interaction phenomena [129].

Alternatively, one can remain within the overall framework of nuclear DFT while seeking guidance from microscopic ab initio theories. By employing interactions derived from chiral EFT, ab initio calculations become systematically improvable by going to higher orders in the chiral expansion. In addition, the chiral expansion provides a way to assess the model uncertainty itself while for phenomenological EDFs one only assesses the uncertainty from fitting the parameters. Different ideas for how to combine ab initio approaches and nuclear DFT exist [65, 82, 85, 97, 98, 132–143]. The approaches include determining EDF parameters [97, 136, 137, 142, 143] or even the form of some functional terms [98, 133, 134, 140] based on ab initio calculations and ideas to fully determine the form of the functional from a microscopic interaction model [85, 132, 138].

In this work, we follow a hybrid strategy first suggested in Refs. [65, 135]. It consists in adding terms arising from long-range pion exchanges as described by chiral EFT interactions at the HF level on top of a conventional Skyrme EDF structure whose parameters are subsequently refitted. The pion terms are incorporated by making use of so-called density-matrix expansions (DMEs); see Ch. 3 for details. EDFs obtained in this fashion have a much more involved density dependence than conventional Skyrme EDFs. There are two motivations for this strategy.

First, the form of the Skyrme EDF corresponds to calculating HF energies from contact interactions. Following chiral EFT, the first additional degree of freedom that appears when increasing the resolution of the description of the considered systems are pions exchanged between the nucleons. Note that while this is reminiscent of switching from pionless to chiral (i.e., pionfull) EFT in ab initio calculations, where the pions are necessary for a reasonable description of all but the lightest nuclei, this analogy is unfortunately somewhat misleading as EDFs describe interactions in the nuclear medium and are not simple free-space interactions. In addition, Skyrme EDF parameters are optimized to reproduce experimental data of finite nuclei. Thus, while one can reasonably expect adding pions explicitly to a Skyrme EDF can lead to a more accurate description of nuclear properties, it is not clear from the outset if such improvement can actually be observed.

Second, a complementary viewpoint is obtained by noticing that ab initio calculations with chiral EFT interactions often build correlations on top of an initial mean-field solution, see Sec. 1.2. In our approach, we employ the same interactions but instead of generating correlations via the many-body method, we adjust the short-range part of the interactions. This is because the dominant bulk correlations in nuclei, e.g., in expansions around HF, appear to be short-range in nature [144] and are therefore expected to be mimicable by contact interactions. On the other hand, the use of unmodified long-range interactions in a low-resolution EDF is justified by the observation that renormalization-group evolution only modifies the short-distance physics [145]. Note that this second viewpoint is similar to ideas considered in Ref. [146], where the authors attempt to capture triples excitations from coupled cluster theory by carrying out CCSD calculations using an interaction in which they adjust the strength of the three-body contact. Renormalizing also two-body contacts to mimic the effect of doubles and then performing mean-field calculations would be the next step in that framework. This has similarities to the strategy discussed here, although Skyrme contact interactions differ in several aspects from chiral-EFT contacts.

The semi-phenomenological hybrid strategy was implemented in a series of papers, Refs. [135,

140, 145, 147–149]. While encouraging improvements over EDFs without chiral terms were observed, the dependency of the results on the order of the chiral interactions showed large variability and puzzling systematics [140]: first, the inclusion of 3N forces worsened the results, and second, at leading order, which naively might be expected to have the biggest effect, no overall improvement was found. This is particularly surprising as the leading-order NN one-pion exchange constitutes the interaction with the longest range in the chiral expansion and hence is supposedly the most difficult to be correctly described by a conventional (zero-range) Skyrme pseudopotential. This thesis addresses these aspects by a careful assessment of both density-matrix expansions themselves and the construction of the hybrid EDFs; see next Sec. 1.5 for details on the scope of this work. This also addresses a key question in formalizing an EFT for EDFs: the pion as a long-range degree of freedom is missing in practice from empirical EDFs, but is it needed to reach greater accuracy for bulk properties or describing dripline physics?

1.5 Scope of this thesis

Both nuclear DFT and ab initio methods with potentials obtained from chiral EFT have been applied very successfully. However, both methods face, albeit complementary, issues. Hence, a way forward might lie in combining the two approaches in a clever way, see also the previous Sec. 1.4. A recently developed semi-phenomenological hybrid scheme to obtain nuclear EDFs was applied with promising outcomes [140] but requires further study and more careful investigation.

In the hybrid approach a simplified phase-space-averaging DME [135, 145] is used to convert Fock contributions from chiral-EFT NN and 3N pion-exchange potentials into a form suitable for a local EDF. Since the DME is applied at the HF level and the EDFs are eventually implemented at the HFB level, we discuss these mean-field methods in some detail in Ch. 2.

There could be several reasons for the partially puzzling behaviors observed for the hybrid EDFs [140], including potentially suboptimal choices for the DME. Therefore, Ch. 3 deals with density-matrix expansions. We introduce them in detail and extensively investigate different DME variants and choices, both for NN and for 3N forces. In particular, we focus on the accurate reproduction of Fock energies due to chiral pion exchanges. The results show that DMEs are generally able to approximate exact Fock energies for chiral interactions well. Nevertheless, we identify different handles for improving the accuracy of DMEs.

In Ch. 4 we carefully revisit the construction of hybrid EDFs that incorporate chiral physics via a DME. To perform these investigations we construct a new set of nuclear EDFs which we dub "Germany-USA DME EDFs" (GUDE[8] for short). We discuss the functionals' forms, the optimization of their parameters, and apply the EDFs in ground-state calculations along the entire nuclear chart. We study in detail the dependence of the results on the order of the employed chiral interaction and identify which terms are crucial to obtain improvement over EDFs without pion-exchange terms. In particular, this allows us to construct an EDF with a minimal number of chiral terms added to a Skyrme EDF obtaining significant improvement in the description of nuclear masses.

[8] *gude* [guːdə] is a common greeting in the Hessian dialect of German that is spoken in Darmstadt, among other places.

We conclude by summarizing our findings and giving an extensive outlook regarding possible future studies and developments in Ch. 5. We discuss different possibilities for constructing further improved EDFs and mention related challenges.

The contents of this thesis have partially been published in Refs. [150, 151]. In particular this pertains to the following parts of the thesis: Section 1.3 has been published in significantly shortened form as part of Ref. [151], Sec. 1.4 is partially based on both Refs. [150, 151]. Sections 3.2 to 3.4 and 3.7 are largely based on Ref. [150]. Similarly, Chapter 4 is largely based on Ref. [151].

This thesis presents the main work I have conducted during my doctoral studies. In addition, during this time I have also contributed to studies on the use of tensor factorization techniques, namely the singular value decomposition, for ab initio calculations. Results have been presented in Refs. [152, 153].

2

Basics of many-body theory

2.1 Variational principle

Nuclear many-body structure theory deals with finding solutions to the stationary Schrödinger equation, which reads in bra-ket notation

$$H\,|\Psi_i\rangle = E_i\,|\Psi_i\rangle \tag{2.1}$$

where the Hamiltonian H describes the interactions between the A nucleons in a nucleus. Here we sort the eigenstates according to their energy, i.e., $|\Psi_0\rangle$ refers to the ground state of the system. Now consider a trial many-body state $|\Psi\rangle$. Expanding it in the exact eigenstates of H, which form an orthonormal basis of the Hilbert space, gives:

$$|\Psi\rangle = \sum_i c_i\,|\Psi_i\rangle\ . \tag{2.2}$$

With this its energy expectation value is given by

$$E[\Psi] = \frac{\langle\Psi|H|\Psi\rangle}{\langle\Psi|\Psi\rangle} = \frac{\sum_i |c_i|^2 E_i}{\sum_i |c_i|^2} \geqslant \frac{\sum_i |c_i|^2 E_0}{\sum_i |c_i|^2} = E_0 \tag{2.3}$$

with the exact ground-state energy E_0. Therefore, the solution of the variational problem

$$\delta E[\Psi] = 0\,, \tag{2.4}$$

i.e., minimizing $E[\Psi]$, in some variational subspace yields an upper limit to the ground-state energy of the system. If the variational space was the whole Hilbert space, the exact ground-state energy and wavefunction would be recovered.

In practice one needs to choose a finite subset of the Hilbert space to perform the variational search. One possibility consists in minimizing over the set of fermionic product states. We discuss properties of such states, in particular with respect to the one-body density matrix (OBDM), in Sec. 2.2. One refers to such a minimization as Hartree-Fock theory, which we consider in Sec. 2.3. It is used to tackle the many-body problem in several different fields, one of them being nuclear theory. In nuclear physics pairing correlations play a particularly important role. These can be elegantly treated by an extension of HF theory which is called Hartree-Fock-Bogoliubov theory. We discuss it in Sec. 2.4. HF and HFB theory are used both as a standalone method in the context of energy density functionals, see Sec. 1.3, and as a starting point for other approaches, e.g., in the ab initio context (Sec. 1.2).

2.2 One-body density matrix and product states

Consider a normalized arbitrary state of a quantum-mechanical system, denoted by $|\Psi\rangle$. It can be associated to a OBDM $\boldsymbol{\rho}$ that can be expressed in operator form in an arbitrary single-particle basis as [154]

$$\widehat{\boldsymbol{\rho}} = \sum_{i,j} |i\rangle \, \rho_{ij} \, \langle j| \ , \tag{2.5}$$

where the matrix elements are given by

$$\rho_{ij} = \langle \Psi | a_j^\dagger a_i | \Psi \rangle \ . \tag{2.6}$$

Equation (2.6) is written in second quantization, where $a_i^\dagger$ creates a particle in state $|i\rangle$ and a_i annihilates it. With the vacuum state $|0\rangle$ this reads

$$a_i^\dagger \, |0\rangle = |i\rangle \ , \tag{2.7}$$

$$a_i \, |i\rangle = |0\rangle \ . \tag{2.8}$$

The coordinate-space representation of $\widehat{\boldsymbol{\rho}}$ is given by

$$\boldsymbol{\rho}(\mathbf{x}_1\sigma_1, \mathbf{x}_2\sigma_2) = \langle \mathbf{x}_1\sigma_1 | \widehat{\boldsymbol{\rho}} | \mathbf{x}_2\sigma_2 \rangle = \sum_{ij} \phi_i(\mathbf{x}_1\sigma_1) \rho_{ij} \phi_j^*(\mathbf{x}_2\sigma_2) \tag{2.9}$$

with normalized single-particle wavefunctions

$$\phi_i(\mathbf{x}\sigma) = \langle \mathbf{x}\sigma | i \rangle \ . \tag{2.10}$$

Here, $\mathbf{x}$ denotes the position and σ denotes potential discrete variables such as spin. The OBDM is Hermitian,

$$\rho_{ij}^* = (\langle \Psi | a_j^\dagger a_i | \Psi \rangle)^* = \langle \Psi | a_i^\dagger a_j | \Psi \rangle = \rho_{ji} \, , \tag{2.11}$$

$$\boldsymbol{\rho}(\mathbf{x}_1\sigma_1, \mathbf{x}_2\sigma_2)^* = \boldsymbol{\rho}(\mathbf{x}_2\sigma_2, \mathbf{x}_1\sigma_1) \, . \tag{2.12}$$

We can use it to write the expectation value of a one-body operator $\widehat{O}$ as [154]

$$\langle \Psi | \widehat{O} | \Psi \rangle = \mathrm{Tr}[O\boldsymbol{\rho}] \, . \tag{2.13}$$

One can also define a two-particle density matrix where [155]

$$\rho_{ijkl} = \langle \Psi | a_k^\dagger a_l^\dagger a_j a_i | \Psi \rangle \tag{2.14}$$

and, analogously, higher-body density matrices.

The simplest many-body states that one can build for a collection of A nucleons (a nucleus) are product states of single-nucleon states. As nucleons are fermions due to them possessing spin $= 1/2$, no single-particle state can be occupied by more than a single nucleon according to the Pauli principle. Therefore, a fermionic many-body wavefunction has to be antisymmetric under the exchange of two particles. Therefore, fermionic product states, here denoted by $|\Phi\rangle$,

are identified with so-called Slater determinants. In coordinate space they read

$$\Phi(\mathbf{x}_1\sigma_1,\ldots,\mathbf{x}_A\sigma_A) = \frac{1}{\sqrt{A!}}\begin{vmatrix} \phi_1(\mathbf{x}_1\sigma_1) & \ldots & \phi_A(\mathbf{x}_1\sigma_1) \\ \vdots & \ddots & \vdots \\ \phi_1(\mathbf{x}_A\sigma_A) & \ldots & \phi_A(\mathbf{x}_A\sigma_A) \end{vmatrix}. \tag{2.15}$$

In second quantization the Pauli principle is enforced via the anti-commutation relations for the fermionic annihilation and creation operators,

$$\{a_i, a_j\} = \{a_i^\dagger, a_j^\dagger\} = 0\,, \tag{2.16}$$

$$\{a_i, a_j^\dagger\} = \delta_{ij}\,. \tag{2.17}$$

Then, a Slater determinant simply reads [154]

$$|\Phi\rangle = \prod_{i=1}^{A} a_i^\dagger\,|0\rangle\ . \tag{2.18}$$

When $|\Psi\rangle$ is a Slater determinant, i.e., $|\Psi\rangle = |\Phi\rangle$, the two-body density matrix fully factorizes into products of OBDMs of the system [62]:

$$\rho_{ijkl} = \rho_{ik}\rho_{jl} - \rho_{jk}\rho_{il}\,. \tag{2.19}$$

This holds similarly for higher-body density matrices. Therefore, the OBDM contains the full information about a system described by a Slater determinant [155] and there is, up to a phase factor, a one-to-one correspondence between $\boldsymbol{\rho}$ and $|\Phi\rangle$ [154]. In mean-field approaches the wavefunction is of product form and thus the OBDM plays a particularly important role in these approaches. When switching to the basis from which the Slater determinant is constructed (e.g., HF orbitals), the OBDM is diagonal with

$$\rho_{ij} = \begin{cases} 1 & \text{if } i = j \leq A\ , \\ 0 & \text{else} \end{cases} \tag{2.20}$$

and then

$$\boldsymbol{\rho}(\mathbf{x}_1\sigma_1, \mathbf{x}_2\sigma_2) = \sum_{i=1}^{A} \phi_i(\mathbf{x}_1\sigma_1)\phi_i^*(\mathbf{x}_2\sigma_2) \tag{2.21}$$

with the sum running over occupied single-particle states and A denoting the particle number of the system.

For product states the OBDM is idempotent [154, 156, 157], i.e., it fulfills

$$\widehat{\boldsymbol{\rho}}^2 = \widehat{\boldsymbol{\rho}}\,. \tag{2.22}$$

This means it projects on the space of occupied single-particle states (so-called hole orbitals). Note that one refers to the unoccupied states as particle orbitals. In coordinate-space representation Eq. (2.22) reads

$$\boldsymbol{\rho}(\mathbf{x}_1\sigma_1, \mathbf{x}_2\sigma_2) = \sum_{\sigma_3}\int \mathrm{d}\mathbf{x}_3\, \boldsymbol{\rho}(\mathbf{x}_1\sigma_1, \mathbf{x}_3\sigma_3)\boldsymbol{\rho}(\mathbf{x}_3\sigma_3, \mathbf{x}_2\sigma_2)\,. \tag{2.23}$$

By considering only the diagonal ($\mathbf{x}_1 = \mathbf{x}_2$, $\sigma_1 = \sigma_2$) we obtain the integrated, spin-summed idempotency constraint:

$$A = \sum_{\sigma_1,\sigma_3} \int \mathrm{d}\mathbf{x}_1 \mathrm{d}\mathbf{x}_3 \, \boldsymbol{\rho}(\mathbf{x}_1\sigma_1, \mathbf{x}_3\sigma_3)\boldsymbol{\rho}(\mathbf{x}_3\sigma_3, \mathbf{x}_1\sigma_1) \,. \tag{2.24}$$

Before we continue with a discussion of Hartree-Fock theory, let us introduce a few definitions and notations we are going to use. The (local) density $\rho(\mathbf{x})$ and the kinetic density $\tau(\mathbf{x})$ can be written for a product state as

$$\rho(\mathbf{x}) = \sum_{i=1}^{A} \sum_{\sigma} |\phi_i(\mathbf{x}\sigma)|^2 \,, \tag{2.25}$$

$$\tau(\mathbf{x}) = \sum_{i=1}^{A} \sum_{\sigma} |\boldsymbol{\nabla}\phi_i(\mathbf{x}\sigma)|^2 \,. \tag{2.26}$$

While we always denote single-particle wavefunctions with an explicit spin degree of freedom in this work, one could make notation more compact by denoting wavefunctions as having two spin components. Along these lines we write the OBDM as a matrix in spin space, i.e.,

$$\boldsymbol{\rho}(\mathbf{x}_1, \mathbf{x}_2) = \begin{pmatrix} \boldsymbol{\rho}(\mathbf{x}_1 \uparrow, \mathbf{x}_2 \uparrow) & \boldsymbol{\rho}(\mathbf{x}_1 \uparrow, \mathbf{x}_2 \downarrow) \\ \boldsymbol{\rho}(\mathbf{x}_1 \downarrow, \mathbf{x}_2 \uparrow) & \boldsymbol{\rho}(\mathbf{x}_1 \downarrow, \mathbf{x}_2 \downarrow) \end{pmatrix} . \tag{2.27}$$

Additionally, we employ the short-hand notation

$$\boldsymbol{\rho}(\mathbf{x}) = \boldsymbol{\rho}(\mathbf{x}, \mathbf{x}) \tag{2.28}$$

for the local part of the OBDM.

2.3 Hartree-Fock theory

HF theory deals with solving the variational equation Eq. (2.4) in the space spanned by Slater determinants $|\Phi\rangle$. The derivation of the HF equations presented here follows Refs. [154, 158]. For an alternative derivation using an explicit representation of a transformation among Slater determinants see, e.g., Ref. [159].

We start from the idempotency condition for a one-body density matrix belonging to a product state, i.e. $\boldsymbol{\rho}^2 = \boldsymbol{\rho}$, as discussed in the previous Section. Since we wish to vary only in the space spanned by Slater determinants,

$$(\boldsymbol{\rho} + \boldsymbol{\delta\rho})^2 = \boldsymbol{\rho} + \boldsymbol{\delta\rho} \,, \tag{2.29}$$

where terms quadratic in the infinitesimal variation $\boldsymbol{\delta\rho}$ vanish. This directly gives

$$\boldsymbol{\delta\rho} = \boldsymbol{\rho}\,\boldsymbol{\delta\rho} + \boldsymbol{\delta\rho}\,\boldsymbol{\rho} \,. \tag{2.30}$$

Left-multiplying with $\boldsymbol{\rho}$ yields

$$\boldsymbol{\rho}\,\boldsymbol{\delta\rho}\,\boldsymbol{\rho} = 0 \tag{2.31}$$

and similarly one obtains

$$(1-\boldsymbol{\rho})\,\boldsymbol{\delta\rho}\,(1-\boldsymbol{\rho}) = 0\,. \tag{2.32}$$

These equations signal that to stay within the space of Slater determinants only variations in the particle-hole and hole-particle blocks of the OBDM are allowed (since $\boldsymbol{\rho}$ is a projector on the hole space).

This allows us to rewrite the differential of Eq. (2.4) as

$$0 = \delta E = \sum_{i=1}^{A}\sum_{j>A}(F_{ij}\delta\rho_{ji} + F_{ji}\delta\rho_{ij})\,, \tag{2.33}$$

where we have introduced the Fock matrix $\mathbf{F}$ with matrix elements

$$F_{ij} = \frac{\partial E}{\partial \rho_{ji}}\,. \tag{2.34}$$

Since the variations in the allowed blocks are arbitrary, Eq. (2.33) simplifies to

$$F_{ji} = F_{ij} = 0 \quad \forall\, i \leq A, j > A\,. \tag{2.35}$$

Because unitary transformations among the particles or among the holes leave the one-body density matrix and the many-body state unchanged, we can extend Eq. (2.35) to requiring the Fock matrix to be diagonal according to

$$F_{ij} = \varepsilon_i \delta_{ij}\,. \tag{2.36}$$

To find the basis that fulfills this equation, in practice we represent the Fock matrix in some single-particle basis $\{|j\rangle\}$ and solve for the transformation coefficients D_{ij} that transform this basis into the desired HF basis $\{|\phi_i\rangle = b_i^\dagger\,|0\rangle\}$ via

$$b_i^\dagger = \sum_j D_{ij} a_j^\dagger\,. \tag{2.37}$$

In this way we obtain the Hartree-Fock equations

$$\sum_k F_{jk} D_{ik} = \varepsilon_i D_{ij} \tag{2.38}$$

for the single-particle states $|\phi_i\rangle$. They have the form of a single-particle Schrödinger equation, where the Fock matrix acts as single-particle Hamiltonian and ε_i are the resulting single-particle energies. As E and therefore $\mathbf{F}$ depend on the occupied orbitals however, the HF equations are coupled and correspond to a nonlinear eigenvalue problem. Therefore in practice they are solved iteratively. Since in HF theory the whole many-body system is characterized by single particle orbitals that arise from an effective single-particle Hamiltonian that describes the interaction with all particles in the system, HF and related theories are referred to as mean-field approaches. The resulting approximation to the ground-state energy, the HF energy, is finally obtained by evaluating E using the obtained HF Slater determinant $|\Phi_{\mathrm{HF}}\rangle$:

$$E_{\mathrm{HF}} = \langle\Phi_{\mathrm{HF}}|H|\Phi_{\mathrm{HF}}\rangle\,. \tag{2.39}$$

Two-body interactions

We now consider the case where the Hamiltonian of the system H consists of a one-body part T (giving the HF kinetic energy) and a two-body interaction V. In second quantization this reads for an arbitrary single-particle basis

$$H = \sum_{ij} T_{ij} a_i^\dagger a_j + \frac{1}{4} \sum_{ijkl} \mathcal{V}_{ijkl} a_i^\dagger a_j^\dagger a_l a_k \tag{2.40}$$

with matrix elements

$$T_{ij} = \langle i|T|j\rangle \ , \tag{2.41}$$

$$V_{ijkl} = \langle ij|V|kl\rangle \ . \tag{2.42}$$

The antisymmetrized interaction matrix elements are given by

$$\mathcal{V}_{ijkl} = V_{ijkl} - V_{ijlk} \, . \tag{2.43}$$

Then,

$$\begin{aligned} E_{\mathrm{HF}} &= \sum_{ij} T_{ij} \langle \Phi_{\mathrm{HF}}|a_i^\dagger a_j|\Phi_{\mathrm{HF}}\rangle + \frac{1}{4} \sum_{ijkl} \mathcal{V}_{ijkl} \langle \Phi_{\mathrm{HF}}|a_i^\dagger a_j^\dagger a_l a_k|\Phi_{\mathrm{HF}}\rangle \\ &= \sum_{ij} T_{ij} \rho_{ji} + \frac{1}{2} \sum_{ijkl} \mathcal{V}_{ijkl} \rho_{ki} \rho_{lj} \, , \end{aligned} \tag{2.44}$$

where we made use of the antisymmetry $\mathcal{V}_{ijkl}$ and of properties of the OBDM, detailed in Sec. 2.2. With Eq. (2.34) we get

$$F_{ij} = T_{ij} + \Gamma_{ij} = T_{ij} + \sum_{kl} \mathcal{V}_{ikjl} \rho_{lk} \tag{2.45}$$

with the so-called self-consistent (or HF) field Γ [154, 160]. Plugging this into Eq. (2.36) and comparing with Eq. (2.44) in the HF basis yields that the HF energy is not just the sum of the single-particle energies,

$$E_{\mathrm{HF}} = \sum_{i=1}^{A} \varepsilon_i - \frac{1}{2} \sum_{i,j=1}^{A} \mathcal{V}_{ijij} \, . \tag{2.46}$$

Staying in the HF basis we can split the interaction contribution to E_{HF} as given by Eq. (2.44), namely

$$W_{\mathrm{HF}} = \frac{1}{2} \sum_{i,j=1}^{A} \mathcal{V}_{ijij} = W_{\mathrm{H}} + W_{\mathrm{F}} \, , \tag{2.47}$$

into the Hartree (direct) and Fock (exchange) energy, respectively given by

$$W_{\mathrm{H}} = \frac{1}{2} \sum_{i,j=1}^{A} \langle \phi_i \phi_j|V|\phi_i \phi_j\rangle \ , \tag{2.48}$$

$$W_{\mathrm{F}} = -\frac{1}{2} \sum_{i,j=1}^{A} \langle \phi_i \phi_j|V|\phi_j \phi_i\rangle \ . \tag{2.49}$$

By inserting completeness relations we can switch to coordinate space. For a translationally invariant local two-body interaction,

$$\langle \mathbf{x}_1\mathbf{x}_2|V(\boldsymbol{\sigma}_1,\boldsymbol{\sigma}_2,\boldsymbol{\tau}_1,\boldsymbol{\tau}_2)|\mathbf{x}_1',\mathbf{x}_2'\rangle = \langle \mathbf{r}|V(\boldsymbol{\sigma}_1,\boldsymbol{\sigma}_2,\boldsymbol{\tau}_1,\boldsymbol{\tau}_2)|\mathbf{r}\rangle\,\delta(\mathbf{r}-\mathbf{r}')\delta(\mathbf{R}-\mathbf{R}')\,, \tag{2.50}$$

where we introduced relative and center-of-mass coordinates

$$\mathbf{r} = \mathbf{x}_1 - \mathbf{x}_2 \quad \text{and} \quad \mathbf{R} = \frac{1}{2}(\mathbf{x}_1 + \mathbf{x}_2) \tag{2.51}$$

and their primed analogs. In Eq. (2.50) we also made the dependence of the nuclear interaction on spin and isospin explicit. With this Hartree and Fock energy read

$$W_{\mathrm{H}} = \frac{1}{2}\,\mathrm{Tr}_{12}^{\sigma\tau}\int \mathrm{d}\mathbf{R}\mathrm{d}\mathbf{r}\;\langle \mathbf{r}|V(\boldsymbol{\sigma}_1,\boldsymbol{\sigma}_2,\boldsymbol{\tau}_1,\boldsymbol{\tau}_2)|\mathbf{r}\rangle\,\boldsymbol{\rho}^{(1)}\Big(\mathbf{R}-\frac{\mathbf{r}}{2}\Big)\boldsymbol{\rho}^{(2)}\Big(\mathbf{R}+\frac{\mathbf{r}}{2}\Big)\,, \tag{2.52}$$

$$W_{\mathrm{F}} = -\frac{1}{2}\,\mathrm{Tr}_{12}^{\sigma\tau}\int \mathrm{d}\mathbf{R}\mathrm{d}\mathbf{r}\;\langle \mathbf{r}|V(\boldsymbol{\sigma}_1,\boldsymbol{\sigma}_2,\boldsymbol{\tau}_1,\boldsymbol{\tau}_2)|\mathbf{r}\rangle\,P_{12}^{\sigma\tau}\boldsymbol{\rho}^{(1)}\Big(\mathbf{R}-\frac{\mathbf{r}}{2},\mathbf{R}+\frac{\mathbf{r}}{2}\Big)\boldsymbol{\rho}^{(2)}\Big(\mathbf{R}+\frac{\mathbf{r}}{2},\mathbf{R}-\frac{\mathbf{r}}{2}\Big)\,. \tag{2.53}$$

The index 1 (2) denotes on which part of the two-body product space the OBDMs and the potential V act, i.e. 1 (2) refers to the spin and isospin space of "particle 1" ("particle 2"), $\mathrm{Tr}_{12}^{\sigma\tau}$ denotes a trace over the whole product space, and

$$P_{12}^{\sigma\tau} = P_{12}^{\sigma}P_{12}^{\tau} = \frac{1+\boldsymbol{\sigma}_1\cdot\boldsymbol{\sigma}_2}{2}\frac{1+\boldsymbol{\tau}_1\cdot\boldsymbol{\tau}_2}{2} \tag{2.54}$$

is the two-particle spin and isospin exchange operator [135].

One can split the Hartree-Fock energy arising from a three-body interaction in analogy to Eqs. (2.47), (2.52), and (2.53) into direct, single-, and double-exchange terms, see Sec. 3.5 for details.

Density-dependent pseudopotentials

Above we discussed the case of genuine two- and three-nucleon interactions. These are used in ab initio methods that deal with interaction models describing the free-space interaction between nucleons. The situation is different in nuclear DFT where interaction models describe the interaction between nucleons in the nuclear medium. To this end, interactions with an explicit density dependence (so called pseudopotentials) are typically used. These cannot be cast into the potential forms discussed above. However, we can still derive HF equations for such pseudopotentials by considering variations with respect to the orbitals instead of the OBDM.

For simplicity we assume here that the energy can be written as a spatial integral over a quasi-local energy density

$$E = \int \mathrm{d}\mathbf{R}\,\mathcal{E}(\mathbf{R})\,, \tag{2.55}$$

which depends only on the local density $\rho(\mathbf{R})$ and the kinetic density $\tau(\mathbf{R})$ like in classic applications of Kohn-Sham DFT [92]. Additional densities, as they enter in the EDFs we are going to consider in Ch. 4, can be included straightforwardly. We derive here the HF equations in coordinate space similar to the presentation in Ref. [154] but we do not restrict ourselves to a particular form of the energy density.

Slater determinants are built from A normalized single-particle orbitals ϕ_i. We impose the normalization constraint by amending Eq. (2.4) with Lagrange multipliers ε_i:

$$\delta\bar{E} = \delta\left(E - \sum_{i=1}^{A}\varepsilon_i \sum_{\sigma}\int \mathrm{d}\mathbf{R}\,|\phi_i(\mathbf{R}\sigma)|^2\right) = 0\,. \tag{2.56}$$

Let us first consider the differential of the energy only. It is given by

$$\begin{aligned}\delta E &= \sum_{i=1}^{A}\sum_{\sigma}\int \mathrm{d}\mathbf{R}\left[\frac{\delta E}{\delta\phi_i^*(\mathbf{R}\sigma)}\delta\phi_i^*(\mathbf{R}\sigma) + \frac{\delta E}{\delta\phi_i(\mathbf{R}\sigma)}\delta\phi_i(\mathbf{R}\sigma)\right] \\ &= \sum_{i=1}^{A}\sum_{\sigma}\int \mathrm{d}\mathbf{R}\left\{\left[\frac{\delta E}{\delta\rho(\mathbf{R})}\frac{\delta\rho(\mathbf{R})}{\delta\phi_i^*(\mathbf{R}\sigma)} + \frac{\delta E}{\delta\tau(\mathbf{R})}\frac{\delta\tau(\mathbf{R})}{\delta\phi_i^*(\mathbf{R}\sigma)}\right]\delta\phi_i^*(\mathbf{R}\sigma)\right. \\ &\qquad \left. + \left[\frac{\delta E}{\delta\rho(\mathbf{R})}\frac{\delta\rho(\mathbf{R})}{\delta\phi_i(\mathbf{R}\sigma)} + \frac{\delta E}{\delta\tau(\mathbf{R})}\frac{\delta\tau(\mathbf{R})}{\delta\phi_i(\mathbf{R}\sigma)}\right]\delta\phi_i(\mathbf{R}\sigma)\right\}, \end{aligned} \tag{2.57}$$

where we used the chain rule. From Eqs. (2.25) and (2.26) we get

$$\frac{\delta\rho(\mathbf{R})}{\delta\phi_i^*(\mathbf{R}\sigma)} = \phi_i(\mathbf{R}\sigma)\,, \tag{2.58}$$

$$\frac{\delta\tau(\mathbf{R})}{\delta\phi_i^*(\mathbf{R}\sigma)} = -\Delta\phi_i(\mathbf{R}\sigma)\,, \tag{2.59}$$

and the analogous equations for the conjugate orbitals. To obtain Eq. (2.59) the derivative rule for functionals that depend on derivatives was employed. Now we can write Eq. (2.56) as

$$\delta\bar{E} = \sum_{i=1}^{A}\int \mathrm{d}\mathbf{R}\left\{\left[\frac{\delta E}{\delta\rho(\mathbf{R})} - \frac{\delta E}{\delta\tau(\mathbf{R})}\Delta - \varepsilon_i\right][\phi_i(\mathbf{R}\sigma)\delta\phi_i^*(\mathbf{R}\sigma) + \phi_i^*(\mathbf{R}\sigma)\delta\phi_i(\mathbf{R}\sigma)]\right\} = 0\,. \tag{2.60}$$

By considering $\partial\bar{E}/\partial\phi_i^*(\mathbf{R}\sigma)$ we obtain from Eq. (2.60) the Hartree-Fock equations

$$\left[\frac{\delta E}{\delta\rho(\mathbf{R})} - \frac{\delta E}{\delta\tau(\mathbf{R})}\Delta\right]\phi_i(\mathbf{R}\sigma) = \varepsilon_i\phi_i(\mathbf{R}\sigma)\,. \tag{2.61}$$

2.4 Hartree-Fock-Bogoliubov theory

There are several experimental facts that suggest pairing correlations, which cannot be explained in a pure Hartree-Fock picture, play an important role in nuclei [154, 161, 162]. Among those is the odd-even staggering observed for nuclear binding energies, i.e., the fact that masses of odd nuclei are almost always larger than the average of the masses of the two adjacent even isotopes (with same neutron or proton number). This can be explained by the formation of energetically favored neutron-neutron and proton-proton pairs in nuclei. One can show that short-range attractive two-nucleon forces can be responsible for the formation of such nucleon pairs with vanishing total angular momentum [163]. Breaking up a nucleonic pair is energetically disfavored; this can be seen in spectra of even-even nuclei which start with an energy range (of about 1 MeV) that contains only few excited states. For odd nuclei this does

not hold since there one nucleon remains unpaired and can therefore be excited more easily.

Note that for nuclei with $N \approx Z$, where neutron and proton Fermi surface are close to one another, also pairing between neutrons and protons may become important [161, 164]. In this work however, we restrict ourselves to same-species pairing.

One possibility to include an explicit treatment of pairing correlations in a mean-field approach is called Hartree-Fock-Bogoliubov theory. It generalizes HF by considering medium effects not only via the self-consistent field Γ, which captures particle-hole correlations, but also via a pairing field Δ that describes particle-particle correlations. Unlike for instance in the HF+Bardeen-Cooper-Schrieffer approach, the HFB method handles the construction of the desired single-particle basis and the evaluation of their pairing correlations consistently and takes into account their interdependence [154, 165].

Like HF theory, the HFB approach is also a variational method. Here, however, the variation is performed in the space of generalized product states [154]: instead of products of single-particle states one considers products of single-quasiparticle states, where the quasiparticle operators are given by a Bogoliubov transformation,

$$\beta_j = \sum_i \left(U_{ij}^* a_i + V_{ij}^* a_i^\dagger \right), \tag{2.62}$$

$$\beta_j^\dagger = \sum_i \left(U_{ij} a_i^\dagger + V_{ij} a_i \right). \tag{2.63}$$

We require that $\beta_j, \beta_j^\dagger$ are fermionic operators. Therefore, the transformation matrix

$$\mathcal{W} = \begin{pmatrix} U & V^* \\ V & U^* \end{pmatrix} \tag{2.64}$$

has to be unitary. Then, we write the generalized product states as

$$|\Phi\rangle = \prod_i \beta_i |0\rangle \ . \tag{2.65}$$

Note that unlike for Slater determinants, the product in Eq. (2.65) is not restricted. The states defined in Eq. (2.65) are quasiparticle vacua,

$$\beta_i |\Phi\rangle = 0 \quad \forall\, i\,, \tag{2.66}$$

and can be uniquely related to the (normal) one-body density matrix $\boldsymbol{\rho}$ and the pairing tensor $\boldsymbol{\kappa}$ with matrix elements

$$\rho_{ij} = \langle \Phi | a_j^\dagger a_i | \Phi \rangle = \left(V^* V^T \right)_{ij}, \tag{2.67}$$

$$\kappa_{ij} = \langle \Phi | a_j a_i | \Phi \rangle = \left(V^* U^T \right)_{ij}. \tag{2.68}$$

One can decompose the Bogoliubov transformation into three subsequent unitary transformations: a transformation of the particle operators amongst themselves (from an initial basis represented by $\{a_i^\dagger\}$ to the canonical basis $\{b_i^\dagger\}$), a special Bogoliubov transformation that mixes creation and annihilation operators only between pairs of single-particle states (which we label with i and $-i$), and a transformation amongst the resulting quasiparticle operators. The first and third transformation do not mix creation and annihilation operators. In the

canonical basis, the product state Eq. (2.65) reads for an even particle number

$$|\Phi\rangle = \prod_{i>0}\left(u_i + v_i b_i^\dagger b_{-i}^\dagger\right)|0\rangle \tag{2.69}$$

with $u_i^2 + v_i^2 = 1$ [158, 160]. An HF state has $u_i, v_i \in \{0, 1\}$ but for an HFB state u_i and v_i can attain values in between. Thus, the representation Eq. (2.69) nicely shows that many-body states in HFB theory break particle-number symmetry.

The goal is now to find the coefficients of the Bogoliubov transformation such that the energy expectation value of the resulting product state is minimized. This is analogous to the HF case and gives rise to the HFB equations. Below, we sketch the derivation for two-body interactions following Refs. [158, 166]. The case of density-dependent forces is not discussed in this Section, it proceeds by analogously extending the HF variational principle. Instead we consider the HFB equations as they are obtained explicitly for EDFs of the GUDE form in Sec. 4.2.1.

Two-body interactions

With Eqs. (2.62), (2.63), (2.67), and (2.68) one can write the energy expectation value obtained from evaluating the Hamiltonian, Eq. (2.40), for the product state, Eq. (2.65), as

$$E[\Phi] = \sum_{ij} T_{ij}\rho_{ji} + \frac{1}{2}\sum_{ijkl}\mathcal{V}_{ijkl}\rho_{ki}\rho_{lj} - \frac{1}{4}\sum_{ijkl}\mathcal{V}_{ijkl}\kappa^*_{ji}\kappa_{kl}\,. \tag{2.70}$$

Because $|\Phi\rangle$ does not correspond to a fixed particle number, we impose the required particle number on average,[1] i.e.,

$$\mathrm{Tr}[\boldsymbol{\rho}] = A\,, \tag{2.71}$$

by amending the variational equation Eq. (2.4) with a Lagrange multiplier:

$$\delta(E - \lambda\,\mathrm{Tr}[\boldsymbol{\rho}]) = 0\,. \tag{2.72}$$

After defining the HF field as in the HF case,

$$\Gamma_{ij} = \sum_{kl}\mathcal{V}_{ikjl}\rho_{lk}\,, \tag{2.73}$$

and the pairing field as

$$\Delta_{ij} = \frac{1}{2}\sum_{kl}\mathcal{V}_{ijkl}\kappa_{kl}\,, \tag{2.74}$$

the variation of Eq. (2.70) with respect to $\boldsymbol{\rho}$ and $\boldsymbol{\kappa}$ then yields the HFB equations:

$$\begin{pmatrix} T + \Gamma - \lambda & \Delta \\ -\Delta^* & -T^* - \Gamma^* + \lambda \end{pmatrix}\begin{pmatrix} U_i \\ V_i \end{pmatrix} = \varepsilon_i \begin{pmatrix} U_i \\ V_i \end{pmatrix}. \tag{2.75}$$

In analogy to the HF case [Eq. (2.38)] Eq. (2.75) constitutes a nonlinear eigenvalue problem. The eigenvectors consist of U_i and V_i that denote columns of U and V, respectively, and the

[1] In practice one has two separate conditions for proton and neutron number.

eigenvalues are the real quasiparticle energies ε_i. One can show that for every eigenvector

$$\begin{pmatrix} U_i \\ V_i \end{pmatrix}$$

the vector

$$\begin{pmatrix} V_i^* \\ U_i^* \end{pmatrix}$$

is also an eigenvector and belongs to the eigenvalue $-\varepsilon_i$. For each such solution pair one uses only one eigenvector in setting up the quasiparticle basis $\{\beta_i^\dagger\}$ as the other eigenvector corresponds to the adjoint quasiparticle operator [154, 167].

3
Density-matrix expansions

Density-matrix expansions have been devised as a tool to translate an energy contribution from nuclear interactions into an energy density functional that depends only on (quasi-)local densities[1] [168, 169]. This translation takes places at the Hartree-Fock level.

The Fock energy depends on the full off-diagonal one-body density matrix, see Eq. (2.53), which therefore constitutes a key object for this work. In Sec. 3.1, we discuss properties of the OBDM for nuclei and infinite nuclear matter that go beyond the ones mentioned already in Sec. 2.2. The idea of the before-mentioned translation is to approximate the OBDM in terms of different local densities by applying a DME. The essential idea of DMEs is that the nonlocality that is present in the off-diagonal OBDM becomes manageable by factorizing it into universal functions. The only dependence on the system of interest is then encoded in a momentum scale that determines the fall-off of these functions and in the local densities that multiply these functions. Details on the procedure are given in Sec. 3.2.

The Hartree energy depends on local densities from the outset, see Eq. (2.52). One could however attempt to further simplify it by transforming it to a local functional (in the sense of the energy integrand depending only on one three-dimensional position variable instead of more). This can for instance be achieved by using a simple Taylor expansion for the density. In Ref. [170] it is demonstrated that this works well when considering the direct energy arising from the Gogny D1S interaction, but to achieve an accuracy of at most a few MeV this requires going at least to fourth order in the expansion. Also one may naturally expect this strategy to perform worse when considering an interaction with a larger range such as one-pion exchange arising in chiral EFT. Using a DME for the Hartree energy is also not considered useful as the fall-off of the nonlocality in the Hartree and Fock contributions behaves differently both with respect to the range and to the dependence on direction [169, 171] and can result in large errors in self-consistent calculations that treat both direct and exchange terms via the DME. In any case, the exact treatment of the Hartree contribution is in practice relatively straightforward since the direct Coulomb contribution is already treated exactly in most EDF implementations. Thus, we focus exclusively on Fock energies in this Chapter.

In Sec. 3.3 we discuss several DME variants and elaborate on different choices in the expansion of OBDMs and their squares. The latter are of particular importance for exchange energies arising from nucleon-nucleon forces. We investigate the performance of the DME variants in reproducing exact NN exchange energies in Sec. 3.4. We focus on Yukawa exchange energies as arising from one-pion exchange at leading order in chiral EFT as this constitutes the chiral interaction with the longest range and is therefore expected to be the toughest test for DMEs. A few other cases of interest, such as the Coulomb interaction including a comparison

[1] The qualifier *quasi* refers to the fact that the functional may not only depend on densities that depend on single-particle orbitals [such as $\rho_q(\mathbf{R})$], but also on densities that depend on derivatives thereof.

to results from molecular physics, are also considered. For exchange energies from 3N forces additional complications arise and more choices than in the NN sector have to be made. This is discussed in Sec. 3.5, where we consider 3N two-pion exchange at next-to-next-to-leading order (N^2LO) in the chiral expansion. After a short note on the vector part of the OBDM in Sec. 3.6, we summarize our findings in Sec. 3.7. In there, we also present lessons learned for the construction of EDFs based on realistic nuclear interactions using DMEs.

Note that all investigations in this Chapter isolate the role of the DME by performing non-self-consistent tests only. The construction of EDFs using a DME is discussed in Ch. 4.

The contents of Secs. 3.2 to 3.4 and 3.7 have largely been published as Ref. [150]. They build on the study conducted in Ref. [172], in which we investigated DMEs using HO orbitals.

3.1 Nuclear one-body density matrices

Decomposing the one-body density matrix

With the notation introduced in Eq. (2.27) the OBDM of nuclear systems is commonly split into Hermitian scalar and vector parts [145], respectively denoted by ρ and $\mathbf{s}$,

$$\boldsymbol{\rho}(\mathbf{x}_1,\mathbf{x}_2) = \frac{1}{2}[\rho(\mathbf{x}_1,\mathbf{x}_2) + \mathbf{s}(\mathbf{x}_1,\mathbf{x}_2)\cdot\boldsymbol{\sigma}] \tag{3.1}$$

with

$$\rho(\mathbf{x}_1,\mathbf{x}_2) = \mathrm{Tr}^{\sigma}[\boldsymbol{\rho}(\mathbf{x}_1,\mathbf{x}_2)]\,, \tag{3.2}$$
$$\mathbf{s}(\mathbf{x}_1,\mathbf{x}_2) = \mathrm{Tr}^{\sigma}[\boldsymbol{\rho}(\mathbf{x}_1,\mathbf{x}_2)\boldsymbol{\sigma}]\,, \tag{3.3}$$

where the traces are in spin space only and $\boldsymbol{\sigma}$ is the vector containing the spin Pauli matrices. The diagonal versions $\rho(\mathbf{x}) = \rho(\mathbf{x},\mathbf{x})$ and $\mathbf{s}(\mathbf{x}) = \mathbf{s}(\mathbf{x},\mathbf{x})$ are referred to as density and spin density, respectively [83]. They differ with respect to their behavior under time reversal [117] (here denoted by a superscript T):

$$\rho^T(\mathbf{x}) = \rho(\mathbf{x})\,, \tag{3.4}$$
$$\mathbf{s}^T(\mathbf{x}) = -\mathbf{s}(\mathbf{x})\,. \tag{3.5}$$

As a consequence, the spin density vanishes in time-reversal invariant systems (such as even-even nuclei), which are the only ones considered in this work, and the off-diagonal part of $\mathbf{s}$ also contributes very little to the total binding energy of such systems. This is demonstrated in Tab. 3.1, which contains Hartree and Fock energies in ^{208}Pb calculated with the finite-range parts of the Gogny D1S interaction. The energies are given for the different scalar/vector-isoscalar/isovector channels. The terms isoscalar and isovector refer to sums and differences of neutron and proton quantities, e.g.,

$$\rho_0(\mathbf{x}) = \rho_\mathrm{n}(\mathbf{x}) + \rho_\mathrm{p}(\mathbf{x})\,, \tag{3.6}$$
$$\rho_1(\mathbf{x}) = \rho_\mathrm{n}(\mathbf{x}) - \rho_\mathrm{p}(\mathbf{x})\,. \tag{3.7}$$

In here, we split the OBDM into separate parts for neutrons and protons. This happens in analogy to Eq. (2.27) but without block-off-diagonal parts in isospin space as we assume

Table 3.1: Hartree and Fock energies in ^{208}Pb calculated with the finite-range parts of the Gogny D1S interaction in different channels. All energies are in MeV and are taken from Ref. [170].

	ρ_0^2	ρ_1^2	$\mathbf{s}_0^2$	$\mathbf{s}_1^2$
Hartree	−12294.8	373.3	0	0
Fock	−595.0	−32.3	0.6	0.2

single-particle states do not mix neutrons and protons:

$$\boldsymbol{\rho}(\mathbf{x}_1,\mathbf{x}_2) = \begin{pmatrix} \boldsymbol{\rho}_\mathrm{n}(\mathbf{x}_1,\mathbf{x}_2) & 0 \\ 0 & \boldsymbol{\rho}_\mathrm{p}(\mathbf{x}_1,\mathbf{x}_2) \end{pmatrix}. \tag{3.8}$$

For instance, for a product state

$$\rho_q(\mathbf{x}) = \sum_{i=1}^{A_q} \sum_{\sigma} |\phi_{q,i}(\mathbf{x}\sigma)|^2 , \tag{3.9}$$

where the particle species is identified by q and A_q denotes the particle number for that species.

The isoscalar density corresponds to the total (mass) density of the system, while the isovector density describes the neutron excess, i.e. the neutron skin of the nucleus. Thus, the scalar-isoscalar contributions are by far the largest ones in finite nuclei, see Tab. 3.1. Note that the vector part of the OBDM is even small in odd nuclei because it essentially only gets contributions from the last (unpaired) nucleons. It completely vanishes (including the off-diagonal contributions) in the approximation that the single-particle wavefunctions of spin-orbit partners are identical in spin-saturated nuclei [135], i.e. those which correspond to closed main (HO) shells.

For later reference we show here how the OBDM of a nucleus containing two particle species is split similarly to Eq. (3.1),

$$\boldsymbol{\rho}(\mathbf{x}_1,\mathbf{x}_2) = \frac{1}{4}[\rho_0(\mathbf{x}_1,\mathbf{x}_2) + \rho_1(\mathbf{x}_1,\mathbf{x}_2)\tau_z + \mathbf{s}_0(\mathbf{x}_1,\mathbf{x}_2)\cdot\boldsymbol{\sigma} + \mathbf{s}_1(\mathbf{x}_1,\mathbf{x}_2)\cdot\boldsymbol{\sigma}\tau_z] , \tag{3.10}$$

where we assumed that the single-particle states do not mix neutrons and protons and τ_z is the third isospin Pauli matrix. The scalar-isoscalar, scalar-isovector, vector-isoscalar, and vector-isovector parts are obtained via traces in spin and isospin space as

$$\rho_0(\mathbf{x}_1,\mathbf{x}_2) = \mathrm{Tr}^{\sigma\tau}[\boldsymbol{\rho}(\mathbf{x}_1,\mathbf{x}_2)] , \tag{3.11}$$
$$\rho_1(\mathbf{x}_1,\mathbf{x}_2) = \mathrm{Tr}^{\sigma\tau}[\boldsymbol{\rho}(\mathbf{x}_1,\mathbf{x}_2)\tau_z] , \tag{3.12}$$
$$\mathbf{s}_0(\mathbf{x}_1,\mathbf{x}_2) = \mathrm{Tr}^{\sigma\tau}[\boldsymbol{\rho}(\mathbf{x}_1,\mathbf{x}_2)\boldsymbol{\sigma}] , \tag{3.13}$$
$$\mathbf{s}_1(\mathbf{x}_1,\mathbf{x}_2) = \mathrm{Tr}^{\sigma\tau}[\boldsymbol{\rho}(\mathbf{x}_1,\mathbf{x}_2)\boldsymbol{\sigma}\tau_z] . \tag{3.14}$$

Note that when assuming that protons and neutrons do not mix, scalar parts of the OBDM of time-reversal invariant systems are purely real and vector parts purely imaginary [173]. Then the Hermiticity of the OBDM reduces to

$$\rho_t(\mathbf{x}_1,\mathbf{x}_2) = \rho_t(\mathbf{x}_2,\mathbf{x}_1) , \tag{3.15}$$
$$\mathbf{s}_t(\mathbf{x}_1,\mathbf{x}_2) = -\mathbf{s}_t(\mathbf{x}_2,\mathbf{x}_1) . \tag{3.16}$$

Infinite nuclear matter

We end this Section by discussing unpolarized homogeneous infinite nuclear matter, for which the form of the OBDM can be calculated analytically. For this system, we can choose plane-wave states as single-particle states. In finite volume V the spatial part of their normalized wavefunctions is given by

$$\phi_{q,i}(\mathbf{x}_1) = \frac{1}{\sqrt{V}} \exp(\mathrm{i}\mathbf{k}_{q,i} \cdot \mathbf{x}_1)\,, \tag{3.17}$$

where allowed momenta $k_{q,i} \leq k_\mathrm{F}^q$ occur for two states each (spin up and down). In the limit of infinite volume the scalar part of the OBDM (the vector part vanishes by construction) is then obtained from transforming the sum over occupied states into the corresponding integral,

$$\rho_q(\mathbf{x}_1, \mathbf{x}_2) = \lim_{V\to\infty} \sum_{i\in\mathrm{occ}} \phi_{q,i}(\mathbf{x}_1)\phi^*_{q,i}(\mathbf{x}_2) = 2\int \frac{\mathrm{d}\mathbf{k}}{(2\pi)^3}\, \Theta(k_\mathrm{F}^q - k) \exp(\mathrm{i}\mathbf{k}\cdot(\mathbf{x}_1 - \mathbf{x}_2))\,. \tag{3.18}$$

By setting $\mathbf{x}_1 = \mathbf{x}_2$ we obtain the INM relation of Fermi momentum k_F^q and density:

$$k_\mathrm{F}^q = \left(3\pi^2\rho_q\right)^{1/3}. \tag{3.19}$$

Using this after evaluating Eq. (3.18) gives

$$\rho_q(\mathbf{x}_1, \mathbf{x}_2) = \frac{3j_1(k_\mathrm{F}^q r)}{k_\mathrm{F}^q r}\rho_q\,, \tag{3.20}$$

where $j_i(x)$ denotes the ith spherical Bessel function of the first kind. This expression is going to be a starting point for the construction of DMEs which we introduce in the next Section.

3.2 General introduction to density-matrix expansions

In HF theory (see Sec. 2.3) the full off-diagonal OBDM enters in the exchange contribution to the energy of the system. While exchange energies due to NN interactions can be treated exactly, that is, up to overall model space truncations, the exact treatment of 3N interactions in heavy systems poses a computational challenge. Hartree-Fock calculations with chiral Hamiltonians, which are used as a first step in ab initio approaches, handle 3N interactions in heavy nuclei by introducing an additional truncation. They take only matrix elements for certain combinations of single-particle orbitals into account [67]. For EDF calculations this is typically not done; instead we incorporate here 3N interactions by using density-matrix expansions.

The original DME, which we will refer to as NV-DME below, was introduced by Negele and Vautherin in their seminal papers, Refs. [168, 169], as a more sophisticated alternative for approximating one-body density matrices than the simple Slater approximation [174]. It allows one to approximate the nonlocal OBDM in terms of quasi-local densities by factorizing the nonlocality into universal functions. Applying it to the expression for the exchange energy facilitates its calculation, as we will see in Sec. 4.1.4 and clarifies how phenomenological zero-range Skyrme interactions are connected to the underlying nuclear forces. While several

other DME variants have been subsequently developed (see Sec. 3.3.1), a consistent extension beyond HF in MBPT is not yet available [144].

In the following we show schematically how DMEs arise as more involved approximations to the OBDM of a particle species q than truncated Taylor expansions. Here and in most of the remaining parts of this Chapter we restrict ourselves to the scalar part of the OBDM since it contributes far more to the total energy of a nucleus than the vector part, see Sec. 3.1. We switch from single-particle coordinates $\mathbf{x}_1$ and $\mathbf{x}_2$ to relative and center-of-mass coordinates defined by Eq. (2.51) and write $\rho_q(\mathbf{R};\mathbf{r})$ as a shorthand for

$$\rho_q(\mathbf{R}+\mathbf{r}/2,\mathbf{R}-\mathbf{r}/2) = \rho_q(\mathbf{x}_1,\mathbf{x}_2)\,. \tag{3.21}$$

Note that in this notation the local density is

$$\rho_q(\mathbf{R}) = \rho_q(\mathbf{R};0)\,. \tag{3.22}$$

With this notation a naive approximation for the scalar part of the OBDM, which factorizes its nonlocality, is given by a Taylor expansion about $\mathbf{R}$ truncated at order $n_{\max}$,

$$\rho_q(\mathbf{R};\mathbf{r}) \approx \sum_{n=0}^{n_{\max}} \frac{1}{n!}\Big(\frac{\mathbf{r}}{2}\cdot\boldsymbol{\nabla}_{12}\Big)^n \rho_q(\mathbf{R}_1,\mathbf{R}_2)\Big|_{\mathbf{R}_1=\mathbf{R}_2=\mathbf{R}}\,, \tag{3.23}$$

where $\boldsymbol{\nabla}_{12} = (\boldsymbol{\nabla}_1 - \boldsymbol{\nabla}_2)$ and $\boldsymbol{\nabla}_1$ ($\boldsymbol{\nabla}_2$) acts on $\mathbf{R}_1$ ($\mathbf{R}_2$). However, this approximation performs poorly at large values of r, for which the OBDM is expected to vanish. This condition can be enforced by multiplying each term of the Taylor expansion by a function $\pi_n^{n_{\max}}(kr)$ that vanishes faster than $1/r^n$ for large r (using notation similar to that in Refs. [155, 175]):

$$\rho_q(\mathbf{R};\mathbf{r}) \approx \sum_{n=0}^{n_{\max}} \frac{\pi_n^{n_{\max}}(kr)}{n!}\Big(\frac{\mathbf{r}}{2}\cdot\boldsymbol{\nabla}_{12}\Big)^n \rho_q(\mathbf{R}_1,\mathbf{R}_2)\Big|_{\mathbf{R}_1=\mathbf{R}_2=\mathbf{R}}\,. \tag{3.24}$$

Here we have introduced the momentum scale k, which determines the fall-off in the off-diagonal direction of the OBDM. If we further impose

$$\pi_n^{n_{\max}}(x) = 1 + \mathcal{O}\big(x^{n_{\max}-n+2}\big)\,, \tag{3.25}$$

the first $n_{\max}$ terms of the quasi-local approximation Eq. (3.24) match the first $n_{\max}$ terms of the Taylor series of $\rho_q(\mathbf{R};\mathbf{r})$. Specifically, the m-th term in the Taylor expansion of Eq. (3.24) is proportional to

$$\begin{aligned} &(\mathbf{r}\cdot\boldsymbol{\nabla}_{12})^m \rho_q(\mathbf{R}_1,\mathbf{R}_2) && \text{for } m \le n_{\max}\,,\\ &(rk)^{m-n}(\mathbf{r}\cdot\boldsymbol{\nabla}_{12})^n \rho_q(\mathbf{R}_1,\mathbf{R}_2) && \text{for } m > n_{\max}\,. \end{aligned}$$

The most well-known example of such approximations is the Slater approximation [174], which is often used in calculations of the Coulomb exchange energy [83]. It consists in using the INM expression for the OBDM, Eq. (3.20), also at every point in a finite nucleus. The momentum scale entering Eq. (3.20) is replaced by the local density approximation for the Fermi momentum (cf. Eq. (3.19)),

$$k_{\mathrm{F}}^q(\mathbf{R}) = \big[3\pi^2\rho_q(\mathbf{R})\big]^{1/3}\,. \tag{3.26}$$

In the following we use

$$k_\mathrm{F} = k_\mathrm{F}^q(\mathbf{R}) \tag{3.27}$$

as a short-hand notation. In the language of Eq. (3.24) the Slater approximation amounts to including only the $n = 0$ term with

$$\pi_0^0(x) = \frac{3j_1(x)}{x} \tag{3.28}$$

and $k = k_\mathrm{F}$, i.e.,

$$\rho_q(\mathbf{R};\mathbf{r}) \approx \frac{3j_1(k_\mathrm{F} r)}{k_\mathrm{F} r}\rho_q(\mathbf{R})\,. \tag{3.29}$$

By construction, the Slater approximation becomes exact in the limit of homogeneous infinite nuclear matter.

Several other approximations to the density matrix are built around the Slater approximation by adding correction terms that vanish in INM. This can be expressed nicely by regrouping certain terms in Eq. (3.24) yielding (using notation similar to Refs. [135, 145])

$$\rho_q(\mathbf{R};\mathbf{r}) \approx \sum_{n=0}^{n_\mathrm{max}} \frac{\Pi_n(kr)}{n!} r_{\alpha_1}\cdots r_{\alpha_n}\mathcal{P}_n^{\alpha_1\cdots\alpha_n}(\mathbf{R})\,. \tag{3.30}$$

Here and in the following, a summation over repeated Greek indices denoting spatial components is implied. The Π functions are normalized according to $\Pi_n(0) = 1$, and the quasi-local density combinations $\mathcal{P}_n^{\alpha_1\cdots\alpha_n}(\mathbf{R})$ are chosen such that the Taylor expansions of the exact $\rho_q(\mathbf{R};\mathbf{r})$ and of Eq. (3.30) agree up to order n_max (as before). Then all terms of Eq. (3.30) except for the zeroth vanish in nuclear matter if $\Pi_0(x) = 3j_1(x)/x$ and $k \to k_\mathrm{F}$ in that limit. Approximations with these properties are the ones we refer to as density-matrix expansions around the INM limit.

Different DME variants differ in their choices of momentum scales k and in their Π functions. As the Taylor series of Eq. (3.30) is supposed to match the exact $\rho_q(\mathbf{R};\mathbf{r})$ only up to order n_max, the higher-order terms in the Π functions can be chosen rather unrestrictedly. These choices can lead to significantly varying convergence behaviors with respect to n_max [170]. As the density combinations $\mathcal{P}_n^{\alpha_1\cdots\alpha_n}(\mathbf{R})$ are determined from a constraint on the Taylor series, they can in principle differ for different DME variants. This occurs for instance when $n_\mathrm{max} = 4$ is considered. For studies of DMEs at fourth order see e.g. Refs. [170, 176].

In general DMEs perform well at smaller r values and degrade as r increases, but even then, they are superior to straightforward truncations of the Taylor expansion of the density matrix, Eq. (3.23). Additionally, one may expect that DMEs reproduce the exact OBDM better in the interior of a typical nucleus (so for small R) than in the nuclear surface because there the resemblance to INM is worse and the omitted higher-order terms are more relevant.

The notation of Eq. (3.30) has the advantage that the Π functions do not depend on the truncation order n_max unlike the $\pi_n^{n_\mathrm{max}}$ functions used in Eq. (3.24). However, the notation is somewhat abstract. To make it a bit more explicit we give here as an example the general expression for second-order DME (i.e., a DME with $n_\mathrm{max} = 2$) used in this work:

$$\begin{aligned}\rho_q(\mathbf{R};\mathbf{r}) \approx{}& \Pi_0(kr)\rho_q(\mathbf{R}) + \mathrm{i}\Pi_1(kr) r_\alpha\, j_{q,\alpha}(\mathbf{R}) \\ &+ \frac{\Pi_2(kr)}{2} r_\alpha r_\beta \left[\frac{1}{4}\nabla_\alpha\nabla_\beta\rho_q(\mathbf{R}) - \tau_{q,\alpha\beta}(\mathbf{R}) + \frac{1}{5}\delta_{\alpha\beta}k^2\rho_q(\mathbf{R})\right],\end{aligned} \tag{3.31}$$

where the components of the current density and kinetic density tensor are given by

$$j_{q,\alpha}(\mathbf{R}) = -\frac{\mathrm{i}}{2}\nabla_{12,\alpha}\rho_q(\mathbf{R}_1,\mathbf{R}_2)\Big|_{\mathbf{R}_1=\mathbf{R}_2=\mathbf{R}}, \tag{3.32}$$

$$\tau_{q,\alpha\beta}(\mathbf{R}) = \nabla_{1,\alpha}\nabla_{2,\beta}\rho_q(\mathbf{R}_1,\mathbf{R}_2)|_{\mathbf{R}_1=\mathbf{R}_2=\mathbf{R}}\,. \tag{3.33}$$

The current density vanishes in INM because there $\rho_q(\mathbf{R}_1,\mathbf{R}_2) = \rho_q(\mathbf{R}_2,\mathbf{R}_1)$ and thus the $\boldsymbol{\nabla}_{12}$ derivative vanishes. Plugging Eq. (3.20) into Eq. (3.33) gives

$$\tau_{q,\alpha\beta}(\mathbf{R}) = \frac{1}{5}\delta_{\alpha\beta}k^2\rho_q(\mathbf{R}) \tag{3.34}$$

for INM and thus the expression in brackets in Eq. (3.31), i.e.,[2]

$$\mathcal{P}_2^{\alpha\beta}(\mathbf{R}) = \left[\frac{1}{4}\nabla_\alpha\nabla_\beta\rho_q(\mathbf{R}) - \tau_{q,\alpha\beta}(\mathbf{R}) + \frac{1}{5}\delta_{\alpha\beta}k^2\rho_q(\mathbf{R})\right] \tag{3.35}$$

vanishes as well, so that only the zeroth term of Eq. (3.31) remains as desired for the INM limit.

Finally, we note that the scalar part of the OBDM typically only has a minor dependence on the direction of the nonlocality $\mathbf{r}$ [135, 168]. Therefore, often DMEs are formulated using an angular average with respect to $\mathbf{r}$. This leads to the simpler expression

$$\rho_q(\mathbf{R};\mathbf{r}) \approx \sum_{n=0}^{n_{\max}}{}' \frac{\Pi_n(kr)}{n!(n+1)} r^n \mathcal{P}_n(\mathbf{R})\,, \tag{3.36}$$

where the prime indicates that the sum only runs over even values of n (as the angular average cancels all odd-n terms).

Continuing with our example from above we obtain for a DME of order $n_{\max} = 2$:

$$\rho_q(\mathbf{R};\mathbf{r}) \approx \Pi_0(kr)\rho_q(\mathbf{R}) + \frac{\Pi_2(kr)}{6} r^2 \left[\frac{1}{4}\Delta\rho_q(\mathbf{R}) - \tau_q(\mathbf{R}) + \frac{3}{5}k^2\rho_q(\mathbf{R})\right], \tag{3.37}$$

with the kinetic density

$$\tau_q(\mathbf{R}) = \tau_{q,\alpha\alpha}(\mathbf{R})\,. \tag{3.38}$$

3.3 Second-order density-matrix expansions

3.3.1 Considered density-matrix expansion variants

In this Section we explore different DMEs with $n_{\max} \leq 2$, which have been developed in the past. The quasi-local densities appearing in such approximations are those known from standard second-order Skyrme EDFs. Higher-order DMEs could be useful in the context of higher-order Skyrme-like EDFs [117] as they have the potential to be more accurate, see Refs. [170, 176] for related studies. Note however that this depends strongly on the DME

[2] For all DME variants considered here $\Pi_0(x) = 1 - x^2/10 + \mathcal{O}(x^4)$ and thus they all come with the same $\mathcal{P}_2^{\alpha\beta}$. If the quadratic term of the Taylor expansion of $\Pi_0(x)$ was different, $\mathcal{P}_2^{\alpha\beta}$ would be different, too (so that the approximation matches the Taylor series of the exact OBDM up to second order).

Table 3.2: DME variants investigated in this work. For each DME the order $n_{\max}$, the expansion momentum scale k, and the Π functions for the scalar parts of the OBDM are given. For the definitions of k_{F}, k_{FC}, and $G(x, Y)$ see Eqs. (3.26), (3.39), and (3.40), respectively. $J_4(x)$ is the fourth (cylindrical) Bessel function of the first kind. An asterisk ($*$) indicates that the marked Π function does not need to be specified as the corresponding term vanishes. The sixth column (INM) shows whether the specified DME reproduces the exact OBDM for nuclear matter. The seventh column ($r \to \infty$) indicates if the DME vanishes in the large-r limit. The last column (II) indicates if the DME-approximation to the OBDM obeys integrated idempotency. The symbol $\sim$ denotes DMEs which violate the constraint by less than 20 % in the investigated cases. See text for details.

DME	$n_{\max}$	k	$\Pi_0(x)$	$\Pi_2(x)$	INM	$r \to \infty$	II
Slater [174]	0	k_{F}	$\frac{3j_1(x)}{x}$	-	✓	✓	✓
PSA [135, 145]	2	k_{F}	$\frac{3j_1(x)}{x}$	$\frac{3j_1(x)}{x}$	✓		
NV [168, 169]	2	k_{F}	$\frac{3j_1(x)}{x}$	$\frac{105j_3(x)}{x^3}$	✓	✓	✓
SVCK [177]	2	k_{F}	$\frac{3j_1(x)}{x}$	$\frac{945j_4(x)}{x^4}$	✓	✓	✓
DT [170]	2	k_{F}	$\frac{3j_1(x)}{x}$	$\exp\left(-\frac{x^2}{16}\right)$	✓	✓	
CB [178, 179]	2	k_{FC}	$\frac{3j_1(x)}{x}$	$*$	✓	✓	$\sim$
BZ [179]	2	k_{FC}	$\frac{96J_4(\sqrt{2}x)}{x^4}$	$*$		✓	$\sim$
Gaussian [179, 180]	2	k_{FC}	$\exp\left(-\frac{x^2}{10}\right)$	$*$		✓	$\sim$
MG [181]	2	k_{FC}	$G(x, 21.5)$	$*$		✓	$\sim$

variant. The DMEs considered here are listed in a unifying notation with their respective references in Tab. 3.2. Although a couple of them do not use $\Pi_0(x) = 3j_1(x)/x$, hence not reproducing the correct INM limit, see Tab. 3.2, we still refer to all of them as DMEs for simplicity.

We restrict ourselves to angular-averaged DMEs as given in Eqs. (3.36) and (3.37). Hence, we only list $\Pi_0(x)$ and (where applicable) $\Pi_2(x)$ in Tab. 3.2. Lifting this restriction has the potential for better accuracy, too [170]. The DMEs considered here all use as their momentum scales either the standard local density approximation to the Fermi momentum as defined in Eq. (3.26)[3] or an alternative introduced in Ref. [178] which is given by

$$k_{\mathrm{FC}} = k_{\mathrm{FC}}^q(\mathbf{R}) = \left\{ \frac{5}{3\rho_q(\mathbf{R})} \left[\tau_q(\mathbf{R}) - \frac{1}{4}\Delta\rho_q(\mathbf{R}) \right] \right\}^{1/2} . \tag{3.39}$$

With the latter choice the second-order term in Eq. (3.37) vanishes identically and $\Pi_2(x)$ does not need to be specified. Thus, using this momentum scale can be viewed as incorporating the second-order contribution into the zeroth-order term. Additionally, it coincides with the regular

[3] See Ref. [182] for phenomenological adjustments of this momentum scale.

Fermi momentum in nuclear matter, hence not changing the corresponding limit. However, in principle, the term enclosed in square brackets in Eq. (3.39) can become negative and thus k_{FC} imaginary. This is clearly unphysical and can lead to diverging exchange energies.[4] In practice we find that k_{FC} is almost always real, which has been also found in molecular systems [184, 185]. None of the systems considered in this work produces imaginary values for k_{FC}, but for future applications one should be aware of the possibility.

We now proceed to give a few remarks regarding some of the considered DME variants at second order, for more details on the variants we refer the reader to the references listed in Tab. 3.2:

1. We employ the phase-space-averaging (PSA) density-matrix expansion in the simplified version described in Ref. [145] (also called INM-DME [135]). This is the variant that has been used in Ref. [140] to enrich a Skyrme-like EDF with density-dependent coupling functions originating from long-range parts of chiral NN+3N interactions and which we use to the same purpose in Ch. 4.

   The full PSA-DME takes the anisotropy of the local momentum distribution into account, leading to a more complicated expansion momentum scale. The authors of Refs. [135, 145] note that the anisotropy is especially pronounced in the surface of the nucleus and hence consider it only for the vector part of the OBDM which sharply peaks there.

   The envelope of the PSA-DME Π_2 function falls off like $1/r^2$ for large r, meaning that it falls off just too slow to yield a density matrix that vanishes in the large-r limit. As we will see later, this is not an issue for approximating exchange energies from finite-range forces, but it can be one in other situations.

2. The NV-DME is the "original" DME as formulated by Negele and Vautherin [168, 169], on which subsequent DME developments build. Other DME variants were developed by altering k or the Π functions utilizing the freedom coming from only the first $n_{\max}$ terms of the Taylor series of the OBDM being unambiguously determined for a DME of order $n_{\max}$. For NV-DME, the authors of Ref. [175] showed that replacing the Π functions by exponentials having the same low-order dependence on the argument leads to almost indistinguishable results when applied to exchange energies arising from the Gogny D1S interaction [186].

3. In the DT approach we use the INM limit for the model density ($\bar{\rho}_v^t$ in Ref. [170]) and set the parameter a to the same value as in Ref. [170], $a = 4/k_{\mathrm{F}}$. Note that the DT-DME, unlike the other variants, has originally been formulated without the angular averaging we use here. Then $\Pi_1(x) = \exp(-x^2/16)$ also contributes.

4. A whole class of DMEs based on the momentum scale k_{FC} was developed by Bhaduri and Zaifman in Ref. [179] (recovering also the CB- and Gaussian DMEs) by assuming different relations between the density and the kinetic density of the nucleus under consideration. Here, we refer to the particular version rated best by them as BZ-DME.

5. It has been argued that the Gaussian approximation is favored by information theory as it is based on the least biased phase-space distribution function subject to yielding the correct density and kinetic density distributions [187].

[4] Using the asymptotic behavior of Bessel functions for large arguments [183], one can show that Fock energies arising from one-pion exchange diverge when $k_{\mathrm{FC}}^2 < -m_\pi^2/4$ for CB-DME and $k_{\mathrm{FC}}^2 < -m_\pi^2/8$ for BZ-DME. For Gaussian and MG-DME all imaginary k_{FC} values lead to diverging Fock energies.

In addition to the version used here, the Gaussian approximation has been developed in a form that uses the kinetic density tensor and the density's Hessian matrix instead of their scalar counterparts in Eq. (3.39) [188], effectively amounting to using a momentum scale tensor $k_{\mathrm{FC},\alpha\beta}(\mathbf{R})$.

6. In the original construction [181], the modified Gaussian (MG) approximation uses

$$\Pi_0(x) = G(x, Y) = \left(1 - \frac{x^2}{Y}\right) \mathrm{e}^{-\left(\frac{1}{10} - \frac{1}{Y}\right)x^2} . \tag{3.40}$$

The value of the parameter $Y > 10$ then depends on the considered system and is obtained by enforcing that the approximated density matrix fulfills the integrated-idempotency constraint (as described below). This leads to the equation

$$\frac{1}{A_q} \int \mathrm{d}\mathbf{R}\, \frac{\rho_q(\mathbf{R})^2}{k_{\mathrm{FC}}^q(\mathbf{R})^3} = \frac{2}{\pi^{3/2}} \left(\frac{1}{5} - \frac{2}{Y}\right)^{3/2} \left[1 - \frac{3}{\frac{Y}{5} - 2} + \frac{15}{4\left(\frac{Y}{5} - 2\right)^2}\right]^{-1} , \tag{3.41}$$

which gets solved numerically for Y.

We observe in our calculations that the resulting values of Y do not vary much throughout the whole mass range of nuclei, thus we do not employ a specific value of Y for each nucleus. Instead, we always consider a value of $Y = 21.5$, which we obtained as an average over neutrons and protons in the nuclei considered in Sec. 4.3. The resulting energies are almost indistinguishable.[5]

7. A modification of the Gaussian approximation similar in spirit to the MG approach has been proposed in Ref. [189]. This approximation uses k_{FC} and

$$\Pi_0(x) = \sqrt{1 + ax^4}\, \exp(-x^2/10) \tag{3.42}$$

with a getting determined via the integrated-idempotency constraint. We find that the resulting values of a are very sensitive to system details. In particular, a becomes negative for INM leading to imaginary $\Pi_0(x)$ for large x. In our calculations the impact of this modification was minor, improving the results in the isovector sector but worsening them in the isoscalar case. For these reasons we do not consider this approximation here.

We now turn to a short investigation of the integrated idempotency constraint given in Eq. (2.24). After splitting the OBDM into scalar and vector parts as in Eq. (3.1) and making use of the tracelessness of Pauli matrices we obtain a condition equivalent to Eq. (2.24):

$$A_q = \frac{1}{2} \int \mathrm{d}\mathbf{x}_1 \mathrm{d}\mathbf{x}_2 [\rho_q(\mathbf{x}_1, \mathbf{x}_2)\rho_q(\mathbf{x}_2, \mathbf{x}_1) + \mathbf{s}_q(\mathbf{x}_1, \mathbf{x}_2) \cdot \mathbf{s}_q(\mathbf{x}_2, \mathbf{x}_1)] . \tag{3.43}$$

As we consider here only the scalar part of the OBDM we check this constraint for the different DMEs for the case of spin-saturated nuclei where $\mathbf{s}_q(\mathbf{R}; \mathbf{r}) \equiv 0$. Using Eq. (3.15) then reduces Eq. (3.43) to

$$A_q = \frac{1}{2} \int \mathrm{d}\mathbf{x}_1 \mathrm{d}\mathbf{x}_2\, \rho_q(\mathbf{x}_1, \mathbf{x}_2)^2 . \tag{3.44}$$

[5] For INM, Eq. (3.41) has three solutions: $Y \approx -37.1, 22.8, 47.9$.

The square of the scalar part of the OBDM (hereafter referred to as density-matrix square) is calculated according to the usual prescription [170, 185] that is neglecting terms of higher-than-second order [in agreement with the truncation order of Eq. (3.37)]:

$$\rho_q(\mathbf{R};\mathbf{r})^2 \approx \Pi_0(kr)^2\rho_q(\mathbf{R})^2 + \frac{\Pi_0(kr)\Pi_2(kr)}{3}r^2\left[\frac{1}{4}\Delta\rho_q(\mathbf{R}) - \tau_q(\mathbf{R}) + \frac{3}{5}k^2\rho_q(\mathbf{R})\right]. \tag{3.45}$$

We call this the truncated square of the density matrix. When calculating the square in this way only the Slater approximation as well as the NV- and SVCK-DMEs fulfill the integrated-idempotency constraint exactly. On the other hand, the PSA-DME violates this constraint maximally: in this case the right-hand side of Eq. (3.44) is infinite. We should also point out that the original version of the MG approximation obeys Eq. (3.44) by construction and our modification only leads to a minor deviation. The Gaussian approximation also violates the constraint only very mildly. For CB- and BZ-DME the relative deviation is smaller than 20 % in our test cases. Since DMEs constitute approximations, one may consider slight deviations from exact integrated idempotency as acceptable.

In Tab. 3.2 we summarize the integrated idempotency results, which for some of the considered DME variants were already given in Refs. [135, 185, 190], and also list which DMEs yield the correct INM and $r \to \infty$ limits. Note that while most DMEs vanish for $r \to \infty$, the type of fall-off is incorrect: it should be exponential [182, 191] but none of the Π functions fall off exponentially. We remark here that for systems where time-reversal invariance is broken, one can impose an additional constraint coming from the fact that for local interactions the HF energy is invariant under transforming the single-particle orbitals with a position-dependent phase [192, 193]. The PSA-DME fulfills this local gauge invariance constraint trivially [145]. For other DME variants one can use this constraint to fix the Π functions for odd orders, see e.g. Ref. [175]. In the present work this is of no concern since we only consider time-reversal-invariant systems.

We end this Section by noting that all of the considered DMEs can be re-expressed in an orbital-free form by assuming some relation $\tau(\rho, \boldsymbol{\nabla}\rho, \dots)$ and in a completely local form by assuming $[\tau - \frac{1}{4}\Delta\rho](\rho)$, e.g., see Ref. [189]. This could be useful for applications to other types of EDFs than Skyrme EDFs but requires further study.

3.3.2 Square of the density matrix

For time-reversal-invariant systems the current density $j_{q,\alpha}(\mathbf{R})$ vanishes as a consequence of Eq. (3.15) [194]. Thus, in these cases the conventional, truncated way of calculating the density-matrix square, Eq. (3.45), which was obtained by averaging the density matrix with respect to the orientation of $\mathbf{r}$ and then squaring it, has the feature of being identical to the expression one obtains from first squaring the density matrix [as given by Eq. (3.31)] and then performing the angular average, i.e.,

$$\langle\rho_q(\mathbf{R};\mathbf{r})\rangle^2_{\Omega_\mathbf{r}} = \langle\rho_q(\mathbf{R};\mathbf{r})^2\rangle_{\Omega_\mathbf{r}}\,. \tag{3.46}$$

Here $\langle\dots\rangle_{\Omega_\mathbf{r}}$ indicates averaging over the direction of $\mathbf{r}$. However, for certain DME variants Eq. (3.45) also possesses the undesirable characteristic of yielding a negative-valued square for some values of $\mathbf{R}$ and r.

Figure 3.1 contains an example of such behavior: We show the density-matrix square for neutrons in ^{132}Sn as a function of the nonlocality r for two values of R, 5 fm (just in the

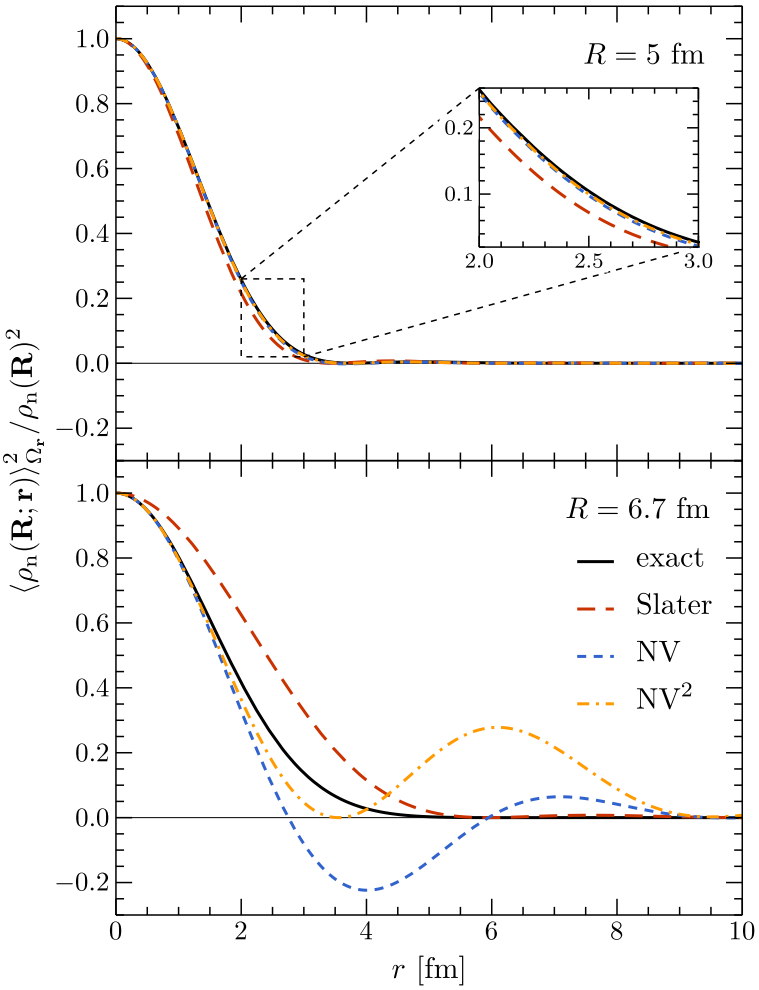

Figure 3.1: Normalized density-matrix square for two values of R in ^{132}Sn for different DMEs. The underlying orbitals are obtained from a self-consistent HF calculation with the SLy4 EDF.

surface of the nucleus, see Fig. 3.3) and 6.7 fm (quite far into the surface of the nucleus). The underlying single-particle orbitals are generated from a self-consistent HF calculation using the SLy4 EDF [195]. In addition to the exact square in solid black, Fig. 3.1 includes the Slater approximation and the NV-DME as defined in Tab. 3.2. For $R = 6.7$ fm, where the second-order correction is much larger (relative to the zeroth-order term), the NV-DME significantly underestimates the value of the square and becomes negative for 2.8 fm $\lesssim r \lesssim$ 5.9 fm.

Therefore, we additionally employ an alternative approach for squaring the density matrix. It was briefly investigated in Ref. [178] and consists in considering the full square of the angle-averaged density matrix, Eq. (3.37), (hence the approximation cannot get negative):

$$\rho_q(\mathbf{R};\mathbf{r})^2 \approx \left\{ \Pi_0(kr)\rho_q(\mathbf{R}) + \frac{\Pi_2(kr)}{6} r^2 \left[\frac{1}{4}\Delta\rho_q(\mathbf{R}) - \tau_q(\mathbf{R}) + \frac{3}{5}k^2\rho_q(\mathbf{R}) \right] \right\}^2 . \tag{3.47}$$

Whereas this equation is not in agreement with the truncation order of Eq. (3.37) and thus contains some but not all of the fourth-order terms, it effectively shifts the region where the DME approximation is poor to larger r values compared to the previously applied truncated squaring prescription. This can be seen in the lower panel of Fig. 3.1, where this approach is

labeled as NV^2. Such behavior can turn out useful when approximating expressions where the large-r behavior is damped, e.g., exchange energies from finite-range forces as considered in Sec. 4.3. In the following we refer to the same treatment of the square for PSA-, SVCK-, and DT-DMEs as PSA^2-, SVCK^2-, and DT^2-DMEs, respectively. The other investigated DME variants have no contribution from Π_2, hence Eq. (3.45) and Eq. (3.47) yield identical results in those cases.

We note that this treatment of the square makes the DMEs no longer fulfill the integrated idempotency. In addition, the statement that squaring and angular averaging commute is no longer true:

$$\langle \rho_q(\mathbf{R};\mathbf{r})\rangle^2_{\Omega_\mathbf{r}} \neq \langle \rho_q(\mathbf{R};\mathbf{r})^2\rangle_{\Omega_\mathbf{r}} \,. \tag{3.48}$$

In the particular case of the PSA-DME the truncated squaring approach yields a density-matrix square that vanishes for large r, but the PSA^2-DME does not (see also the related remark in Sec. 3.3.1). We also note that while still being constructed from the standard quasi-local Skyrme densities, the full-square DME variants lead to EDFs with more than two derivatives in some terms (as do all DMEs with the k_FC momentum scale).

In the first panel of Fig. 3.2 we show the exact isoscalar density-matrix square for the ^{132}Sn calculation considered above after averaging over all angles. The general shape is rather well reproduced by all considered DMEs. Therefore, we do not show the DME approximations themselves but instead their differences to the exact square. They are displayed in the other panels of Fig. 3.2: the zeroth-order Slater approximation in the top-right panel, DMEs using k_F with the common truncated-square approach, Eq. (3.45), in the second row, and with full squares, Eq. (3.47), in the third row, and DMEs with k_FC in the last row. The same order and grouping is used in other figures below.

The improvement when going beyond the zeroth-order Slater approximation is clearly visible for all DMEs using k_F and in particular for the CB-DME, which reproduces the exact square extremely well. While the improvement is especially pronounced for small r as can be expected from the Taylor series, NV-, SVCK-, and DT-DME (and their full-square counterparts) approximate the exact square worse at large values of r and R. This does not occur for the DMEs employing k_FC, but instead they (with the exception of CB-DME) overestimate the square at $r \approx 2.5$ fm except for R in the surface of the nucleus. This effect is particularly pronounced for the Gaussian approximation and is probably related to these DMEs not yielding the correct INM limit since this is a suitable approximation in particular in the nuclear interior where higher-order corrections are expected to be less relevant. Since in the end we want to employ DMEs to approximate Fock energies, we also need to take the interaction (and volume elements appearing in the integrals) into account. This changes the picture somewhat and is discussed in detail in Sec. 3.4.

3.3.3 Expansion coordinates

Up until now we have expanded the density matrices in the relative coordinate $\mathbf{r}$ around the center of mass $\mathbf{R}$. However, other choices are possible. It is useful to choose the expansion point to be located on the line connecting the two positions of interest, $\mathbf{x}_1$ and $\mathbf{x}_2$. Then, the nonlocality can be fully expressed in terms of only one coordinate, $\mathbf{r}$. This is not generally possible when dealing with 3N forces, see Sec. 3.5, and constitutes one of the reasons why applying a DME for such interactions is much more involved. For now we deal only with NN forces and are thus able to express the nonlocality only in terms of $\mathbf{r}$. We refer to the general

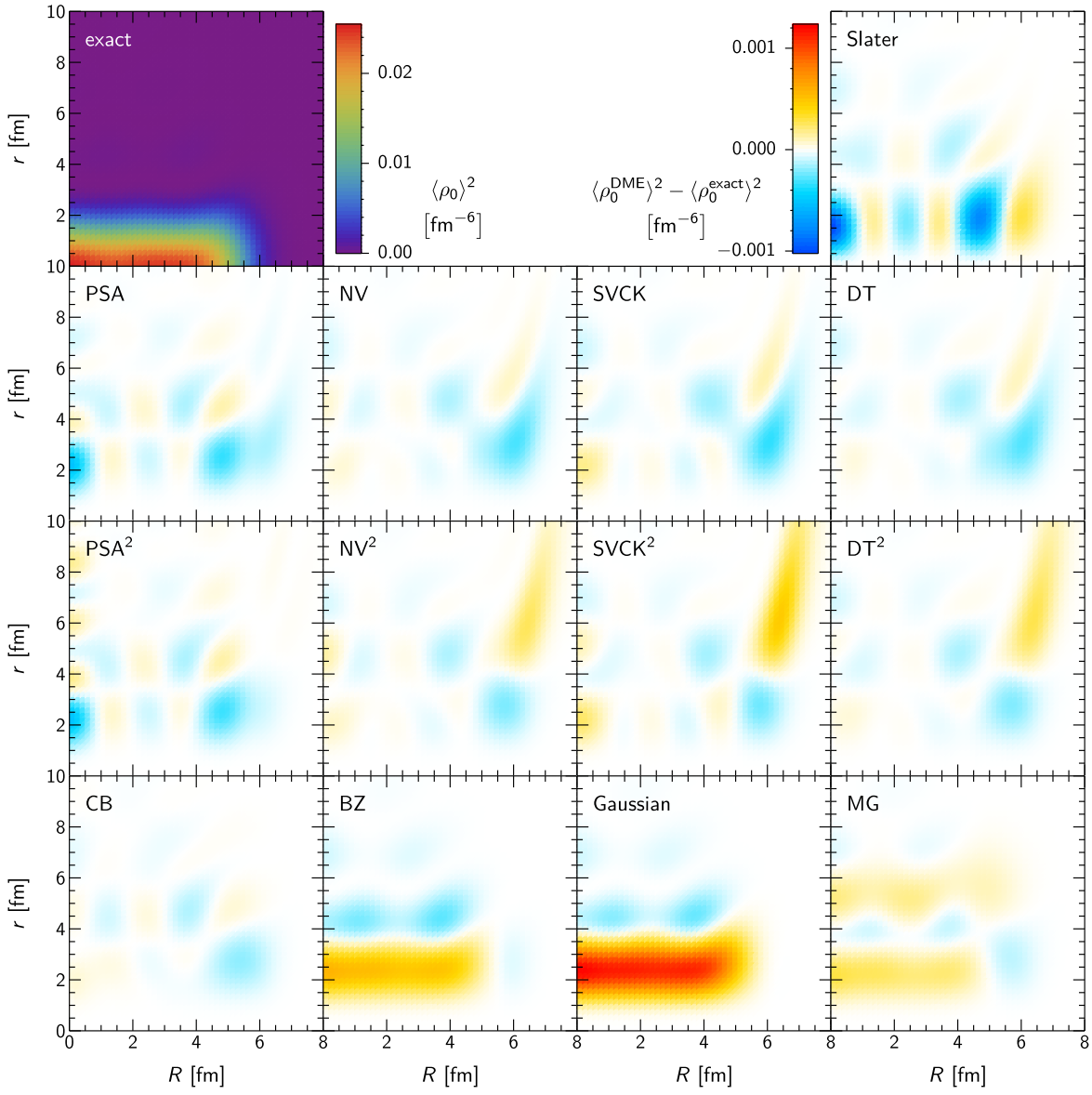

Figure 3.2: First panel: exact angle-averaged isoscalar density-matrix square in ^{132}Sn. Other panels: differences of DME approximations of this square and the exact square itself. The underlying orbitals are obtained from a self-consistent HF calculation with the SLy4 EDF.

expansion point in between $\mathbf{x}_1$ and $\mathbf{x}_2$ as

$$\mathbf{v}_a = a\mathbf{x}_1 + (1-a)\mathbf{x}_2 \tag{3.49}$$

where $a \in [0,1]$ determines the exact expansion point. For $a = 1/2$ one recovers the center of mass $\mathbf{R}$ used in the previous sections and for $a = 0$ the expansion is about the position of the second particle. For this expansion point the analogous expression to Eq. (3.31) for a DME of order $n_{\max} = 2$ reads

$$\begin{aligned}\rho_q(\mathbf{v}_a;\mathbf{r}) &= \rho_q(\mathbf{v}_a + (1-a)\mathbf{r}, \mathbf{v}_a - a\mathbf{r}) \\ &\approx \Pi_0(kr)\rho_q(\mathbf{v}_a) + \Pi_1(kr) r_\alpha \left[\left(\frac{1}{2} - a\right)\nabla_\alpha \rho(\mathbf{v}_a) + \mathrm{i} j_{q,\alpha}(\mathbf{v}_a)\right] \\ &\quad + \frac{\Pi_2(kr)}{2} r_\alpha r_\beta \left[\left(\frac{1}{2} - a + a^2\right)\nabla_\alpha \nabla_\beta \rho_q(\mathbf{v}_a) + (1-2a)\mathrm{i}\nabla_\alpha j_{q,\beta}(\mathbf{v}_a)\right. \\ &\qquad \left. - \tau_{q,\alpha\beta}(\mathbf{v}_a) + \frac{1}{5}\delta_{\alpha\beta} k^2 \rho_q(\mathbf{v}_a)\right].\end{aligned} \tag{3.50}$$

Averaging over the direction of $\mathbf{r}$ yields

$$\begin{aligned}\rho_q(\mathbf{v}_a;\mathbf{r}) \approx \Pi_0(kr)\rho_q(\mathbf{v}_a) + \frac{\Pi_2(kr)}{6} r^2 \left[\left(\frac{1}{2} - a + a^2\right)\Delta\rho_q(\mathbf{v}_a) + (1-2a)\mathrm{i}\boldsymbol{\nabla}\cdot\mathbf{j}_q(\mathbf{v}_a)\right. \\ \left. - \tau_q(\mathbf{v}_a) + \frac{3}{5}k^2\rho_q(\mathbf{v}_a)\right],\end{aligned} \tag{3.51}$$

which simplifies to Eq. (3.37) when $a = 1/2$.

For $a \neq 1/2$, angular averaging and squaring do not commute even for time-reversal-invariant systems. Both for the truncated and the full squaring prescription,

$$\langle \rho_q(\mathbf{v}_a;\mathbf{r})\rangle_{\Omega_\mathbf{r}} \langle \rho_q(\mathbf{v}_a;\mathbf{r})^*\rangle_{\Omega_\mathbf{r}} \neq \left\langle |\rho_q(\mathbf{v}_a;\mathbf{r})|^2 \right\rangle_{\Omega_\mathbf{r}}, \tag{3.52}$$

as a term proportional to $(\boldsymbol{\nabla}\rho_q)^2$ is missing on the left-hand side of Eq. (3.52).

Nevertheless, Eq. (3.51) and an accordingly adjusted momentum scale $k_\mathrm{F}^q(\mathbf{v}_a)$ were used in Ref. [185] in time-reversal-invariant molecular systems with the NV-DME, and $a = 0$ was found to lead to a much improved reproduction of the exact Coulomb exchange energies compared to the usual $a = 1/2$ choice. An optimization routine gave basically the same value ($a = 0.00638$) as the best fit for their considered systems [185]. While we are able to reproduce a similar behavior in our test systems when using the Coulomb interaction, we do not see this improvement for one-pion exchange, see Sec. 3.4.1 for details.

Moreover, it is not clear how to extend the DME variants that use k_FC to $a = 0$ because for Π_2 to not contribute one needs an adjusted momentum scale,

$$\tilde{k}_\mathrm{FC}^q(\mathbf{x}_2) = \left\{\frac{5}{3\rho_q(\mathbf{x}_2)}\left[\tau_q(\mathbf{x}_2) - \frac{1}{2}\Delta\rho_q(\mathbf{x}_2)\right]\right\}^{1/2} \tag{3.53}$$

(note the prefactor 1/2 instead of 1/4 in front of $\Delta\rho_q$). This $\tilde{k}_\mathrm{FC}^q$ is often imaginary [185], which is unphysical and can lead to diverging exchange energies. For these reasons we only consider DMEs about $\mathbf{R}$ for NN forces (except for Sec. 3.4.1 as noted).

3.4 Nucleon-nucleon force exchange energies

We now proceed to apply the different DME variants discussed in Secs. 3.3.1 and 3.3.2 to the nonlocal densities in the exchange energy arising from a local NN interaction in coordinate space. This energy is given in Eq. (2.53) and reads with the notation introduced in this Chapter:

$$W_{\mathrm{F}} = -\frac{1}{2}\,\mathrm{Tr}_{12}^{\sigma\tau}\int \mathrm{d}\mathbf{R}\mathrm{d}\mathbf{r}\,\boldsymbol{\rho}^{(1)}(\mathbf{R};-\mathbf{r})\boldsymbol{\rho}^{(2)}(\mathbf{R};\mathbf{r})\,\langle\mathbf{r}|V(\boldsymbol{\sigma}_1,\boldsymbol{\sigma}_2,\boldsymbol{\tau}_1,\boldsymbol{\tau}_2)|\mathbf{r}\rangle\,P_{12}^{\sigma\tau} \tag{3.54}$$

After breaking up the OBDMs as in Eq. (3.10) the exchange energy reads

$$\begin{aligned} W_{\mathrm{F}} = -\frac{1}{32}\,\mathrm{Tr}_{12}^{\sigma\tau}\int \mathrm{d}\mathbf{R}\,\mathrm{d}\mathbf{r}\,\Big[&\rho_0(\mathbf{R};-\mathbf{r}) + \rho_1(\mathbf{R};-\mathbf{r})\tau_z^{(1)} + \mathbf{s}_0(\mathbf{R};-\mathbf{r})\cdot\boldsymbol{\sigma}^{(1)} \\ &+ \mathbf{s}_1(\mathbf{R};-\mathbf{r})\cdot\boldsymbol{\sigma}^{(1)}\tau_z^{(1)}\Big]\Big[\rho_0(\mathbf{R};\mathbf{r}) + \rho_1(\mathbf{R};\mathbf{r})\tau_z^{(2)} + \mathbf{s}_0(\mathbf{R};\mathbf{r})\cdot\boldsymbol{\sigma}^{(2)} \\ &+ \mathbf{s}_1(\mathbf{R};\mathbf{r})\cdot\boldsymbol{\sigma}^{(2)}\tau_z^{(2)}\Big]\,\langle\mathbf{r}|V(\boldsymbol{\sigma}_1,\boldsymbol{\sigma}_2,\boldsymbol{\tau}_1,\boldsymbol{\tau}_2)|\mathbf{r}\rangle\,P_{12}^{\sigma\tau}\,. \end{aligned} \tag{3.55}$$

Depending on the spin and isospin structure of the interaction, different bilinears of the OBDM parts survive in Eq. (3.55) after carrying out the traces.

To test the different DMEs we insert these approximations into Eq. (3.55) and compare the resulting energies to the exact exchange energy. Before we can do that we need to specify both the system (which enters the OBDMs) and the interaction. Let us start with discussing the former.

We start with comparing different DMEs with the same single-particle orbitals generated from a self-consistent HF calculation employing the SLy4 parametrization of the Skyrme EDF [195] without pairing. This enables a clean comparison, but we point out that the orbitals used are not self-consistent with the EDF and DME. The HF equations are solved using the code HFBRAD [196], which works directly on a spherical coordinate-space grid. The step size is set to 0.1 fm. Reducing the step size to 0.025 fm changes the obtained total energies of the HF calculation at most in the per-mill regime. This precision is sufficient for the present application. We made sure the code and the implementation of the outputted orbitals into our DME routines work as intended by comparing against results obtained with orbitals from HOSPHE [197] and HFODD [198]. The DME implementations themselves were benchmarked against the second-order results of Ref. [170], the LO results of Ref. [149], and the one-pion-exchange Fock expressions of Refs. [199, 200]. We consider in total 11 closed-shell nuclei, ranging from light to heavy and from $N = Z$ to very asymmetric: ^{16}O, ^{24}O, ^{40}Ca, ^{48}Ca, ^{54}Ca, ^{56}Ni, ^{60}Ca, ^{80}Zr, ^{100}Sn, ^{132}Sn, and ^{208}Pb. All of these nuclei are closed-shell, hence their ground states are treated as being time-reversal invariant and Π_1 does not contribute even without the angular-average approximation. For three example nuclei the isoscalar density distributions are displayed as solid lines in Fig. 3.3. The other lines correspond to other orbital sets which we use later to check how sensitive our findings are to orbital details.

Regarding the interaction for which we investigate the Fock energies we restrict ourselves to NN forces for now because the inclusion of 3N forces involves dealing with two relative coordinates in the OBDMs (instead of one), which means that even more approximations and choices need to be considered. We consider them in Sec. 3.5.

DMEs are naturally formulated in coordinate space. Thus, using them together with

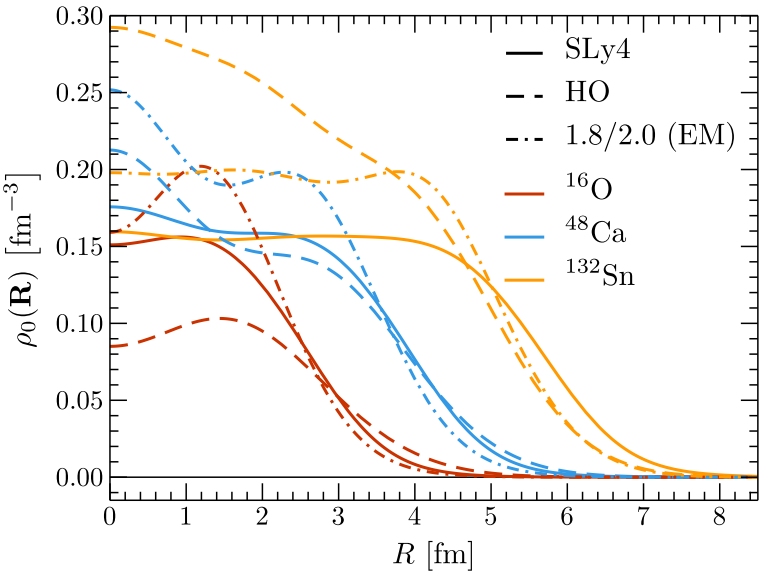

Figure 3.3: Isoscalar density distributions of selected closed-shell nuclei. Solid lines correspond to orbitals from a self-consistent HF calculation with the SLy4 EDF, dashed lines correspond to orbitals from an isotropic HO with $\hbar\omega = 10$ MeV, and dash-dotted lines correspond to orbitals obtained from a self-consistent HF calculation with the 1.8/2.0 (EM) interaction [201].

momentum-space interactions requires explicitly evaluating a Fourier transform (e.g., see Refs. [202, 203]) which hinders linking observations with the form of the Π functions. For coordinate-space interactions a Fourier transform is not necessary and the analysis is more straightforward. Therefore, we consider only interactions formulated in coordinate space.

3.4.1 Yukawa exchange energies

As DMEs are less accurate for large values of the relative distance r, a good description of the exchange energy arising from long-range interactions is particularly challenging. In chiral EFT, the interaction with the longest range is one-pion exchange, which appears already at leading order in the expansion (see Sec. 1.2), meaning that it should be particularly relevant according to the underlying power counting. Investigating one-pion exchange is also interesting because the inclusion of this term in Ref. [140] did not improve the functional's reproduction of experimental binding energies (unlike for higher order, shorter-range terms). We want to investigate here if the DME implementation might be responsible for this behavior before revisiting the functional construction itself in Ch. 4.

The one-pion exchange piece with the longest range is described by a central Yukawa interaction, which in coordinate space reads:

$$\langle \mathbf{r}|V(\boldsymbol{\sigma}_1,\boldsymbol{\sigma}_2,\boldsymbol{\tau}_1,\boldsymbol{\tau}_2)|\mathbf{r}\rangle = W_S^{\mathrm{LO}}(r)\boldsymbol{\sigma}_1\cdot\boldsymbol{\sigma}_2\boldsymbol{\tau}_1\cdot\boldsymbol{\tau}_2\,, \tag{3.56}$$

with the radial dependence

$$W_S^{\mathrm{LO}}(r) = \frac{m_\pi^3}{12\pi}\left(\frac{g_A}{2F_\pi}\right)^2\frac{\mathrm{e}^{-m_\pi r}}{m_\pi r}\,, \tag{3.57}$$

where we use $g_A = 1.29$, $F_\pi = 92.4$ MeV, and $m_\pi = 138.03$ MeV for the axial-vector coupling

constant, the pion decay constant, and the pion mass, respectively [204]. To regularize the interaction it is multiplied with a local regulator function $f(r)$,

$$W_S^{\mathrm{LO}}(r) \to W_S^{\mathrm{LO}}(r) f(r)\,. \tag{3.58}$$

While other coordinate-space regulator forms are available, e.g., see Ref. [25], we choose here [204–206]

$$f(r) = 1 - \exp\!\left(-\frac{r^4}{R_0^4}\right), \tag{3.59}$$

where the spatial cutoff R_0 specifies up to which value of r the short-distance part of the potential is smoothly cut off. We first consider $R_0 = 1.2$ fm. While regulators are not needed at the HF level, they suppress large short-distance contributions [39, 207] that would otherwise have to be absorbed into the Skyrme parameters. They can also be employed to smoothly turn on the long-distance interactions.

The tensor part of one-pion exchange has a shorter range than the central piece and its exchange energy involves only the vector part of the OBDM, so we do not consider it here. Applying a DME to the short-range piece of one-pion exchange (whether described by a smeared-out delta function or an actual one) works very well because of its short range. In a scheme where a proper delta function is used all DME variants even yield the same (exact) functional with density-independent couplings like in a Skyrme EDF.

Inserting Eq. (3.56) into Eq. (3.55) yields for the W_S^{LO} exchange energy

$$W_{\mathrm{F}} = -\frac{1}{8}\int \mathrm{d}\mathbf{R}\,\mathrm{d}\mathbf{r}\,\left[9|\rho_0(\mathbf{R};\mathbf{r})|^2 - 3|\rho_1(\mathbf{R};\mathbf{r})|^2 - 3|\mathbf{s}_0(\mathbf{R};\mathbf{r})|^2 + |\mathbf{s}_1(\mathbf{R};\mathbf{r})|^2\right] W_S^{\mathrm{LO}}(r) f(r)\,. \tag{3.60}$$

We consider the first two terms (which depend on the scalar parts of the OBDM) and refer to them as the scalar-isoscalar energy W_0,

$$W_0 = -\frac{9}{8}\int \mathrm{d}\mathbf{R}\,\mathrm{d}\mathbf{r}\,|\rho_0(\mathbf{R};\mathbf{r})|^2 W_S^{\mathrm{LO}}(r) f(r)\,, \tag{3.61}$$

and scalar-isovector energy W_1,

$$W_1 = \frac{3}{8}\int \mathrm{d}\mathbf{R}\,\mathrm{d}\mathbf{r}\,|\rho_1(\mathbf{R};\mathbf{r})|^2 W_S^{\mathrm{LO}}(r) f(r)\,. \tag{3.62}$$

The question we want to investigate now is how well do the different DME variants of Secs. 3.3.1 and 3.3.2 approximate these energies.

Scalar-isoscalar energy

We begin by considering the scalar-isoscalar Yukawa exchange-energy integrand $\mathcal{W}_0$, defined as

$$\mathcal{W}_0(R,r) = \frac{9}{8}\int \mathrm{d}\Omega_{\mathbf{R}}\,\mathrm{d}\Omega_{\mathbf{r}}\,R^2 r^2 |\rho_0(\mathbf{R};\mathbf{r})|^2 W_S^{\mathrm{LO}}(r) f(r)\,, \tag{3.63}$$

and pick ^{132}Sn as our first test case. The ^{132}Sn isoscalar (matter) density distribution is shown as the solid yellow line in Fig. 3.3. The exact integrand $\mathcal{W}_0$, displayed in the first

panel of Fig. 3.4, has the largest contributions at about $r \approx 1.5$ fm over the whole R range, which mostly reflects the nature of the regularized interaction, and peaks at $R \approx 4.7$ fm, which is close to the peak of $R^2\rho_0(\mathbf{R})^2$ at $R \approx 4.6$ fm, the expected peak position for an exactly separable OBDM. These features are rather well reproduced by the integrands that are obtained when replacing $|\rho_0(\mathbf{R};\mathbf{r})|^2$ in Eq. (3.63) by its different DME approximations. Therefore, we do not show the DME integrands themselves but instead their differences to the exact integrand. They are depicted in the other panels of Fig. 3.4.

Several trends are clearly visible from the integrand differences in Fig. 3.4: The second-order DMEs (besides the Gaussian approximation) locally reproduce the exact integrand significantly better than the zeroth-order Slater approach, highlighting the improvement due to the inclusion of higher-order terms. In particular, the region where relevant deviations first occur gets shifted from $r \approx 1$ fm in the Slater case to $r \approx 1.5$ fm for the other DMEs. In all cases the largest differences arise close to or in the surface of the nucleus. This can probably be attributed to the larger relevance of missing higher-order terms compared to the situation in the interior of the nucleus. Comparing the second and third rows of panels in Fig. 3.4 reveals that the additional term in the full-square DMEs is particularly relevant in the surface where it flips the sign of the differences for $r \gtrsim 4$ fm. Interestingly, this is not always an improvement locally but the global scalar-isoscalar energy W_0 is always closer to the exact result for the full square than for the truncated-squares approach due to (possibly fortuitous) cancellations in the former case. We provide the ratio of the DME-approximated W_0 and the exact counterpart in the top-right corner of each panel.

Regarding these global energies, all considered DME variants approximate the exact values remarkably well with SVCK^2- and MG-DMEs performing best: both yield values that deviate less than 1% from the exact result. Somewhat surprisingly, the Slater approximation follows next despite the inferior quality in local reproduction of the integrand. Again, this can be attributed to cancellations of regions of overestimation and underestimation. We also note that while the Gaussian approximation overestimates the integrand throughout the nuclear interior, yielding the worst energy reproduction, it provides an extremely good description of the integrand in the surface.

In other nuclei, the results are very similar. This can be seen from the left panel in Fig. 3.5 where we show for each DME variant the average ratio of approximated (W_0^{DME}) and exact (W_0^{exact}) scalar-isoscalar energies over the 11 test nuclei and a bar that ranges from the smallest to the largest ratio observed. Underneath each bar the values of three individual nuclei (corresponding to the density distributions shown in Fig. 3.3) are highlighted, showing that smaller ratios (typically corresponding to worse energy reproductions) almost always occur for lighter nuclei.

As before, all ratios are notably close to unity and the full-square variants of the DMEs reproduce the exact energies better than the corresponding truncated-square versions. Additionally, the spread of the ratios is smaller for the full squares. Again, the reproduction is particularly good for SVCK^2- and MG-DME and on average it is worst for the Gaussian approximation.

A detailed breakdown into the individual nuclei is given in Fig. 3.6 where the $W_0^{\mathrm{DME}}/W_0^{\mathrm{exact}}$ ratios are shown for every considered nucleus separately. The general trend towards a better reproduction of the exact scalar-isoscalar energy for heavier considered systems is clearly visible. Exceptions are BZ- and Gaussian DMEs. This can be understood from the fact that these DMEs perform poorer in the nuclear interior which grows in size and thus in

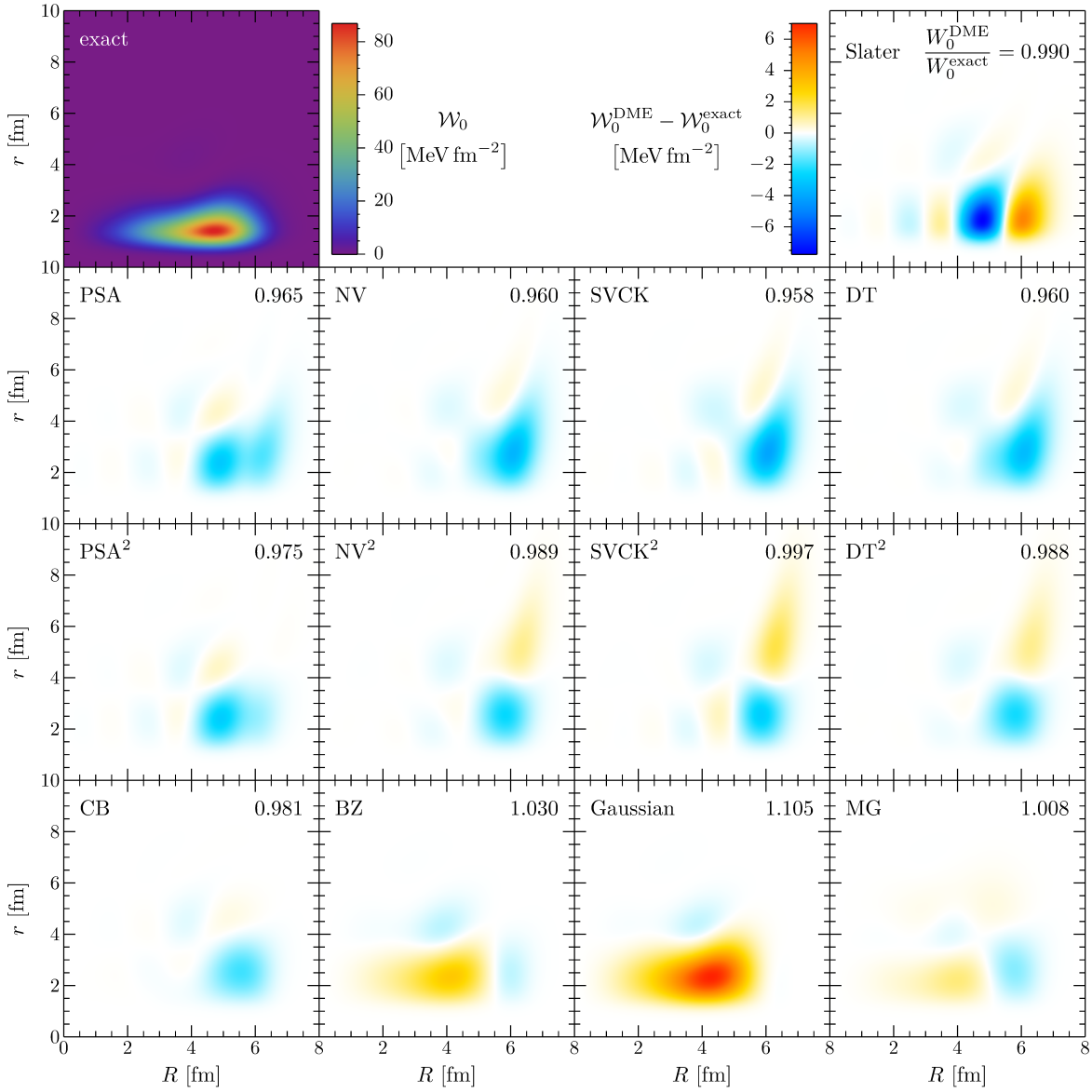

Figure 3.4: First panel: exact scalar-isoscalar exchange-energy integrand obtained for a regularized Yukawa interaction in ^{132}Sn. Other panels: differences of DME approximations of this integrand and the exact integrand itself. In every difference panel the value of the ratio of the DME-approximated energy and the exact energy is shown in the top right corner. The underlying orbitals are obtained from a self-consistent HF calculation with the SLy4 EDF. All DMEs are used with separate momentum scales for neutrons and protons.

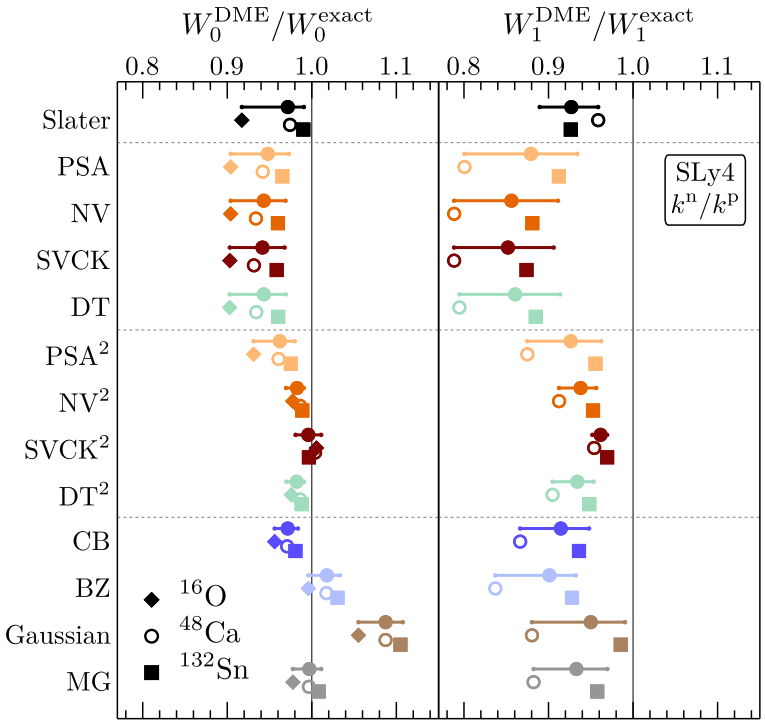

Figure 3.5: Ratios of DME-approximated and exact exchange-energy contributions for a regularized Yukawa interaction. For every DME variant the average over a set of nuclei is shown together with a bar ranging from the smallest to the largest ratio observed. Below each bar, the results for selected nuclei are given. The underlying orbitals are obtained from a self-consistent HF calculation with the SLy4 EDF. The left panel shows the results for the scalar-isoscalar contributions, where 11 closed-shell nuclei are considered (see text); the right panel shows the results for the scalar-isovector contributions (from 6 closed-shell nuclei). In both panels the DMEs are used with separate momentum scales for neutrons and protons.

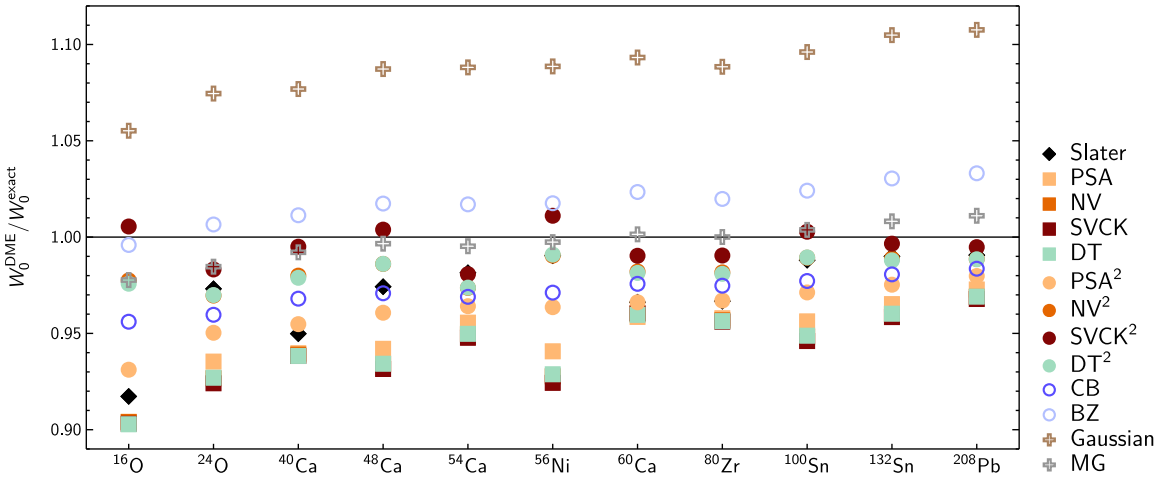

Figure 3.6: Ratios of DME-approximated and exact scalar-isoscalar exchange-energy contributions for a regularized Yukawa interaction. Results are given for 11 closed-shell nuclei where the underlying orbitals are obtained from a self-consistent HF calculation with the SLy4 EDF. DMEs are used with separate momentum scales for neutrons and protons.

significance when going to heavier nuclei. Since the other DMEs have their weaknesses mostly in the surface, they work better for larger mass numbers. Note that some DME variants (like SVCK^2) do remarkably well even for the lightest systems considered.

We find almost identical, though slightly worse, results when approximating the NV-DME Π functions with exponentials as proposed in Ref. [175]. This approximation could be useful for implementations in numerical EDF codes. For the MG-DME the results are almost indistinguishable when using the average value of the parameter $Y = 21.5$ as done here and when using specific values for each nucleus based on the integrated-idempotency constraint as described in Sec. 3.3.1.

In summary, using DMEs to approximate the scalar-isoscalar energies W_0 works remarkably well for the considered closed-shell systems and the investigated Yukawa interaction. The dependence on orbitals and interaction is investigated below. Refined improvement from few-percent accuracy for some DME variants to the 1% level can be realized by switching to full-square DMEs or other variants, in particular to SVCK^2- and MG-DME.

Scalar-isovector energy

The right panel of Fig. 3.5 contains the ratios for the scalar-isovector energies W_1 as given by Eq. (3.62). Here only the 6 asymmetric nuclei (with $N \neq Z$) in our set are considered since the isovector energies are completely negligible for the symmetric nuclei. For most DMEs the ratios $W_1^{\mathrm{DME}}/W_1^{\mathrm{exact}}$ are further away from the ideal value of unity than in the isoscalar case. This can be understood when comparing the shape of the isoscalar part of the OBDM, which is a bulk quantity, to that of the isovector part, which is basically a neutron-excess density matrix. Thus, the region contributing the most to the isovector integral is located much closer to the nuclear surface where omitted higher-order corrections are expected to be more relevant. This is also clearly visible for ^{132}Sn when comparing the scalar-isoscalar integrand $\mathcal{W}_0$ in the first panel of Fig. 3.4 with the scalar-isovector integrand $\mathcal{W}_1$, which is defined as

$$\mathcal{W}_1(R,r) = \frac{3}{8}\int \mathrm{d}\Omega_{\mathbf{R}}\,\mathrm{d}\Omega_{\mathbf{r}}\, R^2 r^2 |\rho_1(\mathbf{R};\mathbf{r})|^2 W_S^{\mathrm{LO}}(r) f(r)\,, \tag{3.64}$$

and is depicted in the first panel of Fig. 3.7. In addition, the energy contributions stem on average from a larger r value in the isovector case for all considered nuclei, which again makes an accurate description harder when using DMEs.

Nevertheless, the general trends are very similar for the isovector and the isoscalar energies. Notable exceptions are the BZ- and the Gaussian DME because their overestimations in the nuclear interior (also reflected in them not yielding the correct INM limit) matter less for the isovector part. This is also reflected in the detailed breakdown into the individual nuclei given in Fig. 3.8.

Overall, our results show that DMEs do not perform as well for scalar-isovector energies as for scalar-isoscalar energies, with typical accuracies being around 10%. For the considered asymmetric nuclei the magnitude of the scalar-isovector energies is on average only 1.3% of the scalar-isoscalar contributions. Therefore, the worse accuracy in the isovector case has no relevant effect on the total energy reproduction, though it might be important when looking at non-bulk quantities.

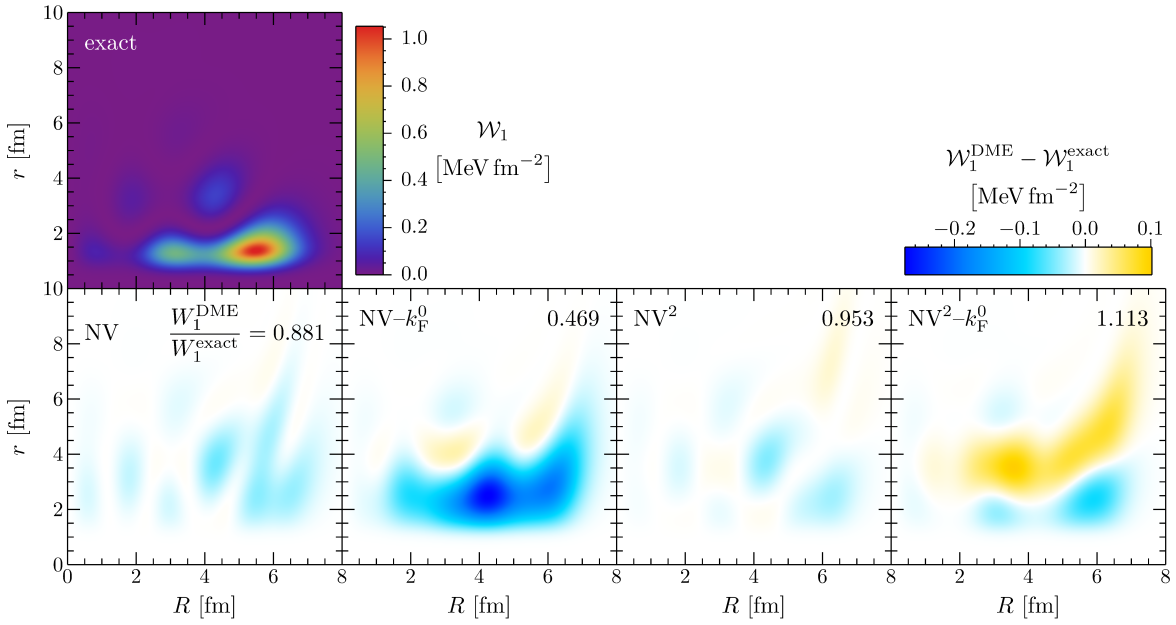

Figure 3.7: First panel: exact scalar-isovector exchange-energy integrand obtained for a regularized Yukawa interaction in ^{132}Sn. Other panels: differences of DME approximations of this integrand and the exact integrand itself. Approximations obtained with isoscalar momentum scales for both neutron and proton density matrices are labeled with "–k_{F}^0" next to the abbreviated DME name. In every difference panel the value of the ratio of the DME-approximated energy and the exact energy is shown in the top right corner. The underlying orbitals are obtained from a self-consistent HF calculation with the SLy4 EDF.

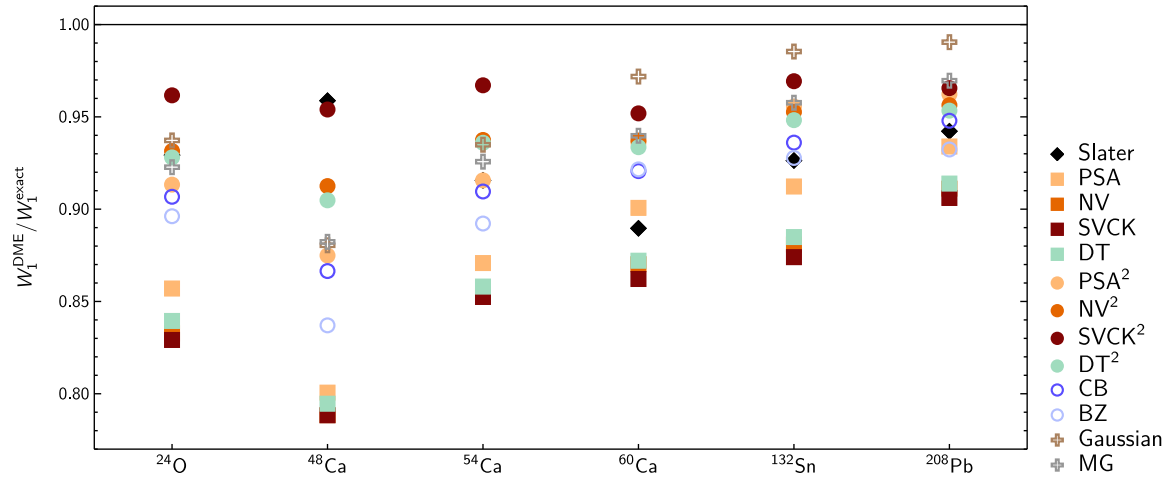

Figure 3.8: Ratios of DME-approximated and exact scalar-isovector exchange-energy contributions for a regularized Yukawa interaction. Results are given for 6 asymmetric closed-shell nuclei where the underlying orbitals are obtained from a self-consistent HF calculation with the SLy4 EDF. DMEs are used with separate momentum scales for neutrons and protons.

Isoscalar expansion momentum scale

So far, the results have been obtained by expanding neutron and proton density matrices separately as described in Sec. 3.2 and subsequently forming the isoscalar and isovector parts by the appropriate sums, Eqs. (3.6) and (3.7). However, this procedure yields EDFs where

the terms that are normally isospin invariant (such as those proportional to ρ_0^2) also contain isospin-dependent parts, though their isospin symmetry is still conserved [135]. Hence one might want to utilize another possibility that is to expand both the isoscalar and isovector parts as a whole. Then Eq. (3.37) becomes

$$\rho_t(\mathbf{R};\mathbf{r}) \approx \Pi_0(kr)\rho_t(\mathbf{R}) + \frac{\Pi_2(kr)}{6}r^2\left[\frac{1}{4}\Delta\rho_t(\mathbf{R}) - \tau_t(\mathbf{R}) + \frac{3}{5}k^2\rho_t(\mathbf{R})\right], \tag{3.65}$$

where $t = 0, 1$. Using different momentum scales for the isoscalar and isovector expansions leads to additional complications. Therefore, we follow Ref. [175] and simply use the isoscalar variants of Eqs. (3.26) and (3.39),

$$k_{\mathrm{F}}^0(\mathbf{R}) = \left[\frac{3\pi^2}{2}\rho_0(\mathbf{R})\right]^{1/3}, \tag{3.66}$$

$$k_{\mathrm{FC}}^0(\mathbf{R}) = \left\{\frac{5}{3\rho_0(\mathbf{R})}\left[\tau_0(\mathbf{R}) - \frac{1}{4}\Delta\rho_0(\mathbf{R})\right]\right\}^{1/2}, \tag{3.67}$$

for all OBDM parts. Then, this prescription is equivalent to using Eq. (3.37) but with the same momentum scale for both neutrons and protons. Because $k_{\mathrm{F(C)}}^{\mathrm{n}}(\mathbf{R}) \approx k_{\mathrm{F(C)}}^0(\mathbf{R}) \approx k_{\mathrm{F(C)}}^{\mathrm{p}}(\mathbf{R})$ one may expect the results to not be significantly different for either of the momentum scales. But in the particular case of pure isovector quantities using $k_{\mathrm{F}}^0(\mathbf{R})$ or $k_{\mathrm{FC}}^0(\mathbf{R})$ could be much worse as this effectively results in approximating the difference of neutron and proton density matrices with a momentum scale that assumes their similarity. This can also be viewed as employing a single-species procedure to approximate the neutron-skin density matrix, which almost never behaves like a single-species density matrix.

This is confirmed by the panels in the second row of Fig. 3.7, which display the differences between DME-approximated and exact scalar-isovector integrands $\mathcal{W}_1$. We show them for the NV- and NV^2-DMEs, both for separate neutron/proton momentum scales and for the isovector momentum scale k_{F}^0. The expected much larger (local) deviations in the latter case are clearly visible. This is similar for the other DMEs that are not displayed and translates also to the energy ratios $W_1^{\mathrm{DME}}/W_1^{\mathrm{exact}}$.

In the right panel of Fig. 3.9 we show these ratios, but unlike in Fig. 3.5 here the values are obtained by using the isoscalar variants of the momentum scales. The results are much worse for the isoscalar momentum scale: the average ratios range from 0.37 to 1.53 and are in all cases further away from unity than with separate momentum scales. On the other hand, the scalar-isoscalar energies are almost identical for isoscalar (Fig. 3.9) and separate momentum scales for the two species (Fig. 3.5). As explained, both observations are expected.

Whether one deems using DMEs with isoscalar momentum scales acceptable or not in light of these findings depends very much on the case at hand. The poor accuracy of the very small scalar-isovector energies effectively does not matter when one is only interested in a good description of the total energies,[6] but again this might not be true for isovector and differential quantities, such as differences along isotope chains.

[6] For some DMEs the total energy reproduction is even slightly better with the isoscalar momentum scale due to cancellations of errors between scalar-isoscalar and scalar-isovector energies.

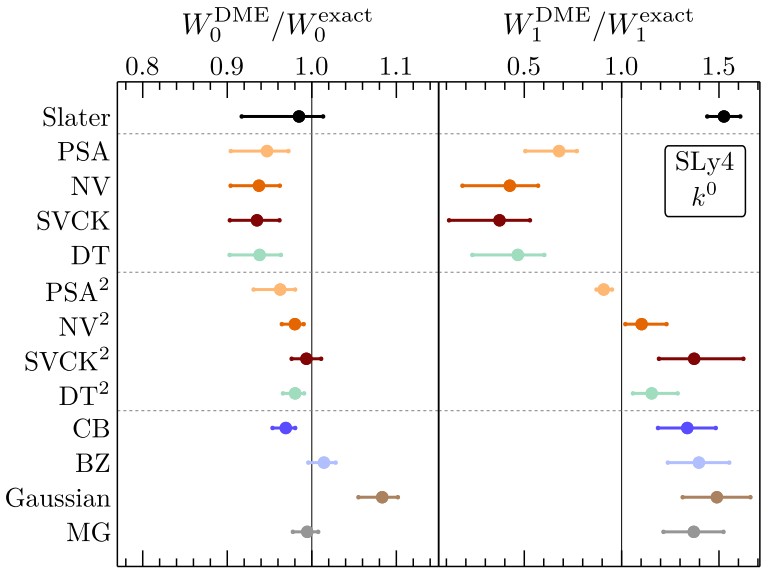

Figure 3.9: Same as Fig. 3.5 without the ratios for individual nuclei. Unlike in Fig. 3.5, here both panels show expansions with isoscalar momentum scales. Note the different axis scale of this figure when comparing to other figures.

Dependence on orbitals

Here we want to answer the question whether the results reported above depend sensitively on details of the orbitals. The orbitals used so far were obtained from self-consistent HF calculations with the SLy4 EDF. We now switch to orbitals from a simple isotropic harmonic oscillator with frequency $\hbar\omega = 10$ MeV. As can be seen in Fig. 3.3 they are quite well suited to provide a less realistic counterpart to the SLy4 orbitals. We consider the same 11 (6) nuclei as before for the scalar-isoscalar (scalar-isovector) energies.

Changing back to expansions with separate momentum scales for neutrons and protons we show the ratios $W_0^{\mathrm{DME}}/W_0^{\mathrm{exact}}$ and $W_1^{\mathrm{DME}}/W_1^{\mathrm{exact}}$ in Fig. 3.10. For both scalar-isoscalar and scalar-isovector energies the results are very similar to the SLy4 results given in Fig. 3.5. The main difference is that the spread between the smallest and the largest ratios is typically slightly smaller in the case of HO orbitals but the ranking of the DME variants according to the accuracy of their Yukawa exchange energy reproduction is very similar.

As an additional check we use orbitals obtained from spherical HF calculations based on a chiral low-momentum two- plus three-nucleon interaction [201], 1.8/2.0 (EM), which has been used widely in ab initio calculations of medium-mass nuclei. The HF orbitals are expanded in an HO basis with $\hbar\omega = 16$ MeV and $e_{\max} \leq 12$, and the three-body configurations are included up to $E_{3\max} \leq 16$. Again, we consider the same nuclei as before. For selected nuclei, the corresponding isoscalar density distributions are shown in Fig. 3.3. Figure 3.11 shows that the DME performance is very similar for these orbitals, with slightly larger spread and slightly worse energy reproduction.

Overall these investigations strongly indicate that previous findings regarding the accuracy of reproducing Yukawa exchange energies are generally true, i.e., do not sensitively depend on orbitals.

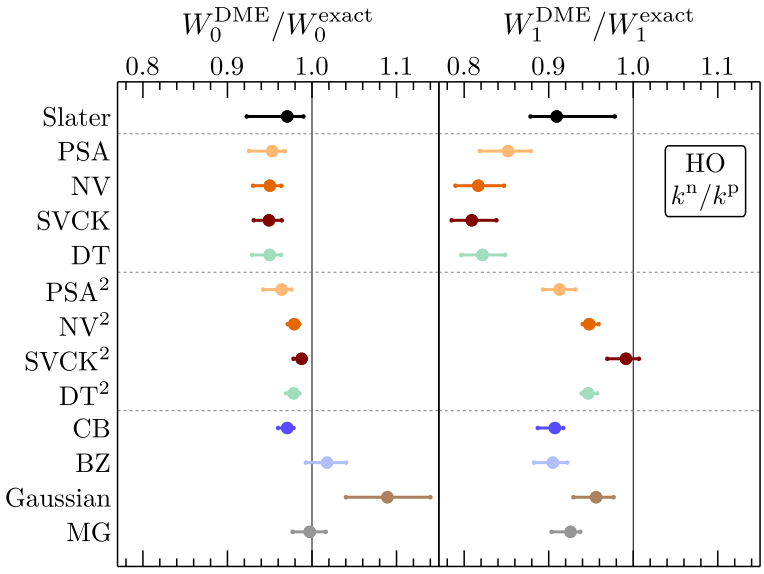

Figure 3.10: Same as Fig. 3.5 without the ratios for individual nuclei. The nuclei are given in terms of orbitals from an isotropic HO with $\hbar\omega = 10$ MeV.

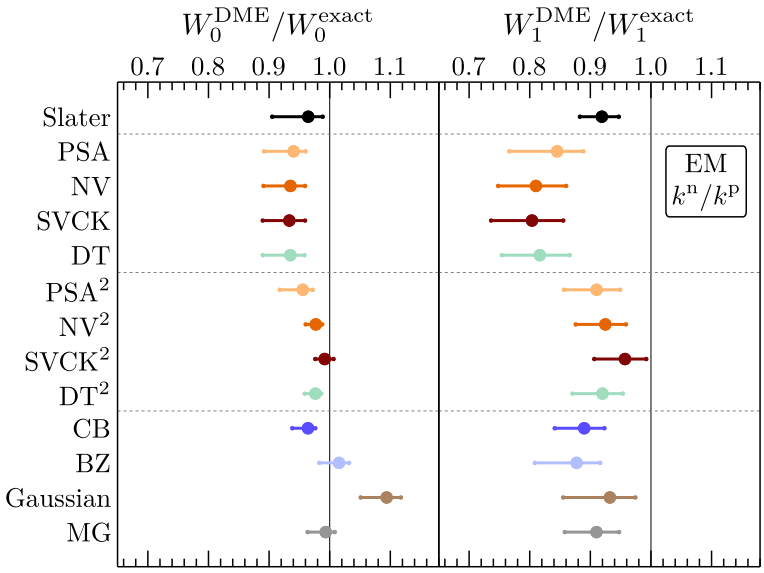

Figure 3.11: Same as Fig. 3.5 without the ratios for individual nuclei. The nuclei are given in terms of orbitals from a self-consistent HF calculation with the 1.8/2.0 (EM) interaction.

Dependence on interaction

Exchange energies from interactions with shorter ranges are expected to be better reproduced by DMEs. Our tests confirm such behavior. In particular, DMEs are exact in the limit of vanishing interaction range. But what about the opposite limit? Consider

$$W_S^{\mathrm{LO}}(m,r) = \frac{m_\pi^3}{12\pi}\left(\frac{g_A}{2F_\pi}\right)^2 \frac{\mathrm{e}^{-mr}}{m_\pi r}\,, \tag{3.68}$$

where the parameter m is the reciprocal of the interaction range. One-pion exchange is obtained for $m = m_\pi$ and the infinite-range limit (i.e., the Coulomb interaction) for $m = 0$.

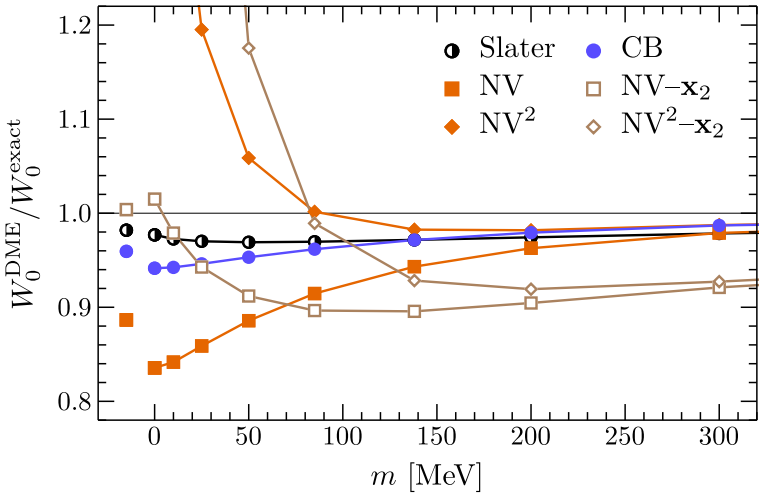

Figure 3.12: Ratio of DME-approximated and exact scalar-isosclar exchange-energy contribution for a regularized Yukawa interaction. The parameter m corresponds to the reciprocal of the interaction range. The values are averages over 11 closed-shell nuclei obtained from a self-consistent HF calculation with the SLy4 EDF. Density-matrix expansions are used with separate momentum scales for neutrons and protons and the expansions are about the two-particle center of mass $\mathbf{R}$ except for the cases marked with "–$\mathbf{x}_2$" where instead they are about the position of one particle. Extra points on the left show the result at $m = 0$ without regulators.

In Fig. 3.12 we plot the scalar-isoscalar energy ratios $W_0^{\mathrm{DME}}/W_0^{\mathrm{exact}}$ for this interaction as a function of m, where again each point is averaged over the same 11 nuclei obtained from SLy4 EDF orbitals as before. The interaction is also regularized as before [see Eqs. (3.58) and (3.59)]. The energy ratios are shown for $m = 0$, 10, 25, 50, 85, 138.03, 200, and 300 MeV. In addition, for each DME a single additional point, which corresponds to the value at $m = 0$ without regulators, i.e., to the Coulomb interaction, is drawn on the very left. Figure 3.12 contains the results for Slater-, NV-, NV^2-, and CB-DMEs. The behavior for the other second-order DMEs with k_{F} (k_{FC}) is similar to the NV/NV^2 (CB) trends.

For large interaction ranges the DME exchange-energy integrals, Eqs. (3.61) and (3.62), have to be carried out up to very high r values to obtain converged results. This is especially important for full-square DMEs because their oscillations with significant amplitudes occur for particularly large r in regions of small expansion momenta. For one-pion exchange ($m =$ 138.03 MeV) these regions are damped, but when the interaction falls off much more slowly they contribute non-negligibly. Thus, we calculate the integrals for $m \leq 25$ MeV analytically without the regulator by employing a strategy proposed in Ref. [208] and add to that the correction from the regulator, which can easily be calculated numerically due to its short range. Details on this procedure and the relevant analytical expressions are given below in Sec. 3.4.2.

As expected, the NV-DME results significantly deteriorate with increasing interaction range (i.e., decreasing m) and even more so do the NV^2-DME results. This is in agreement with results from Ref. [178]. The worse accuracy for the full-square variant is due to the unwanted large-r bump of the expansion (see Fig. 3.1 for an example) getting probed more for larger interaction ranges.

We consider here also DMEs around $\mathbf{x}_2$ as discussed in Sec. 3.3.3, which have been reported to yield good results with the Coulomb interaction in molecular systems [185]. These are labelled with an additional "–$\mathbf{x}_2$" in Fig. 3.12. While they perform worse for small

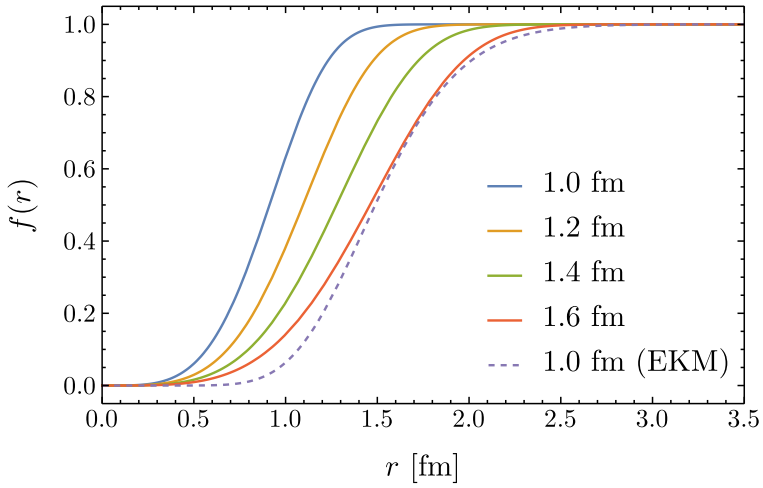

Figure 3.13: Investigated local regulators. The regulator given in Eq. (3.59) in shown for different values of the cutoff R_0 and the EKM regulator, Eq. (3.69), is shown for $R_0 = 1.0$ fm.

ranges, the NV-DME about $\mathbf{x}_2$ produces much better results for large interaction ranges than its conventional counterpart. This is despite the angle averaging being performed before squaring the density matrix. The opposite order of these two operations yields a different expression for expansions about $\mathbf{x}_2$ and should also be investigated in the future. The improved energy reproduction also holds when neglecting the regulator and agrees qualitatively with the molecular-physics result of Ref. [185] despite the different considered systems. This confirms the the low sensitivity on the considered orbitals observed above.

As elaborated on in Sec. 3.3.3, generalizing DMEs that use k_{FC} to expansions about $\mathbf{x}_2$ leads to complications and hence we give the CB-DME results only about $\mathbf{R}$. We observe that the CB-DME accuracy is significantly less range dependent than the second-order k_{F}-DMEs. The performance of the Slater approximation (which is the same for expansions about $\mathbf{R}$ and $\mathbf{x}_2$) is even less range dependent.

We also note that for PSA- and PSA^2-DME the energies are infinite in the Coulomb limit, independent of the expansion point, due to insufficient convergence of these DME variants, see also the corresponding remark in Sec. 3.3.1. Depending on the asymptotic behavior of the orbitals, the Coulomb exchange integrals can diverge for any full-square DME, see Ref. [178] for an example.

The Yukawa interaction considered in the previous subsections contains another length scale in addition to m: the regulator cutoff R_0, see Eq. (3.59). To investigate the influence of cutoff, we investigate the same local regulator as before, but now with different cutoffs $R_0 = 1.0$ fm, 1.4 fm, and 1.6 fm, and the EKM regulator [25]

$$f(r) = \left[1 - \exp\left(-\frac{r^2}{R_0^2}\right)\right]^6 \tag{3.69}$$

with cutoff $R_0 = 1.0$ fm. See Fig. 3.13 for a plot of the different regulators. Note that $R_0 = 1.0$ fm for the EKM regulator corresponds roughly to $R_0 \approx 1.6$ fm in Eq. (3.59).

In Figs. 3.14 to 3.17 we show results for the different cutoffs and regulators. The figures show that larger cutoffs correspond to a worse overall reproduction of exact exchange energies and a larger spread of the accuracies for different systems. These observations agree with

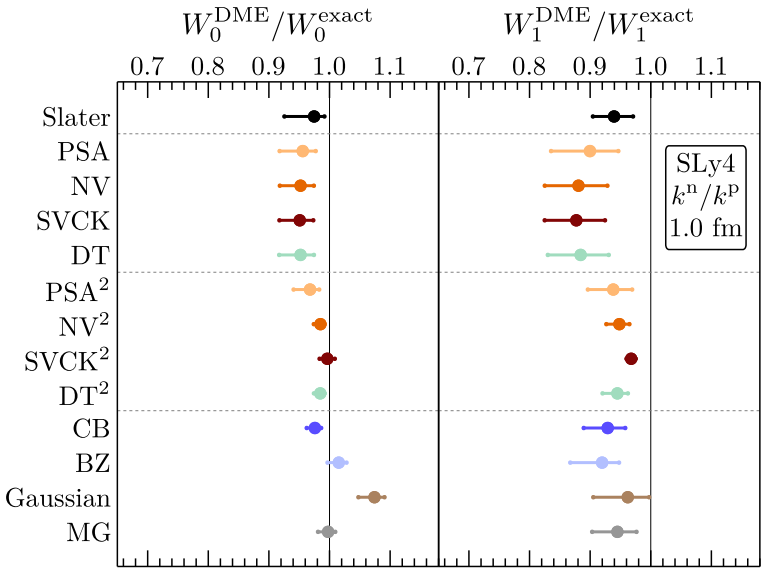

Figure 3.14: Same as Fig. 3.5 without the ratios for individual nuclei. Values are shown here for a regulator cutoff $R_0 = 1.0$ fm.

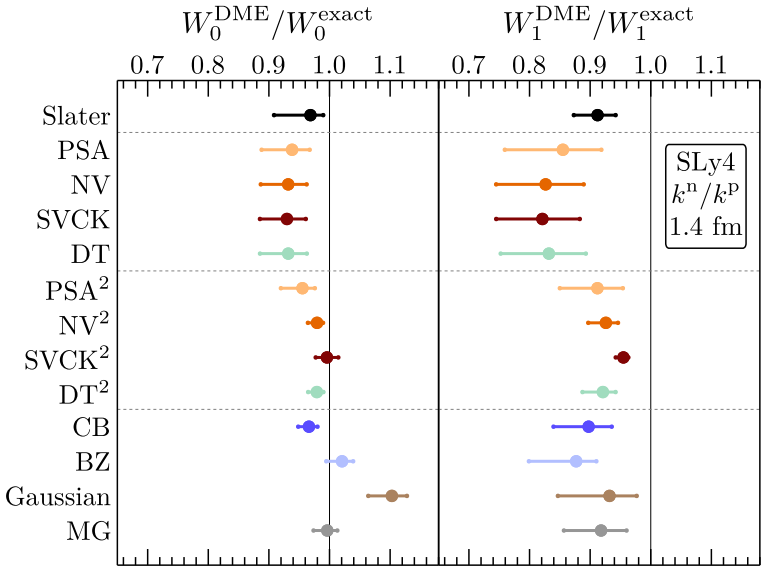

Figure 3.15: Same as Fig. 3.14 but for a cutoff $R_0 = 1.4$ fm.

expectations as the regulators cut off only short-distance parts of the interaction so that only the long-distance parts, where DMEs do not work as well, contribute to the energy.

Summing up, for not-too-long-range NN forces such as one-pion exchange, DMEs around the center of mass $\mathbf{R}$ yield the best results. This is not the case for the Coulomb interaction where for instance in the case of the NV-DME expanding about $\mathbf{x}_2$ is superior.

3.4.2 Semi-analytical energy-density-functional expressions

In the previous Section we considered the scalar-isoscalar DME exchange-energy contribution for regularized Yukawa interactions with very long ranges m^{-1}. As explained a straightforward numerical calculation of the exchange energy integrals is challenging for some DMEs due to

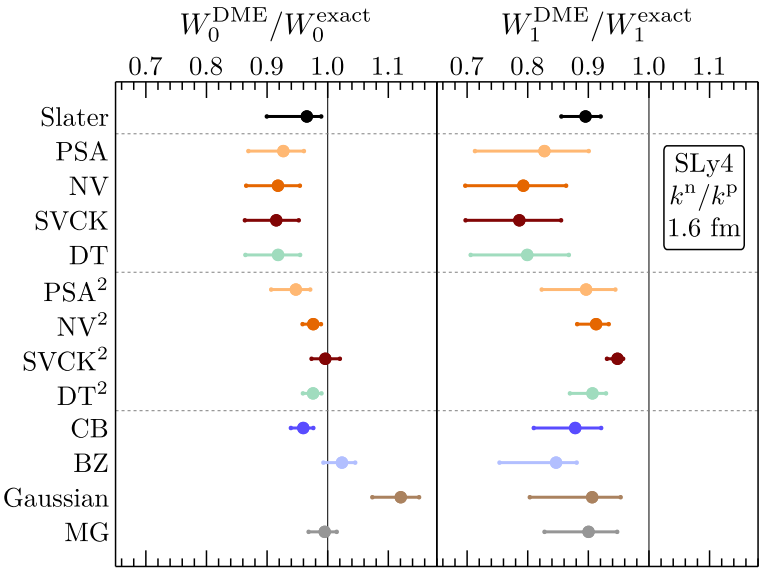

Figure 3.16: Same as Fig. 3.14 but for a cutoff $R_0 = 1.6$ fm.

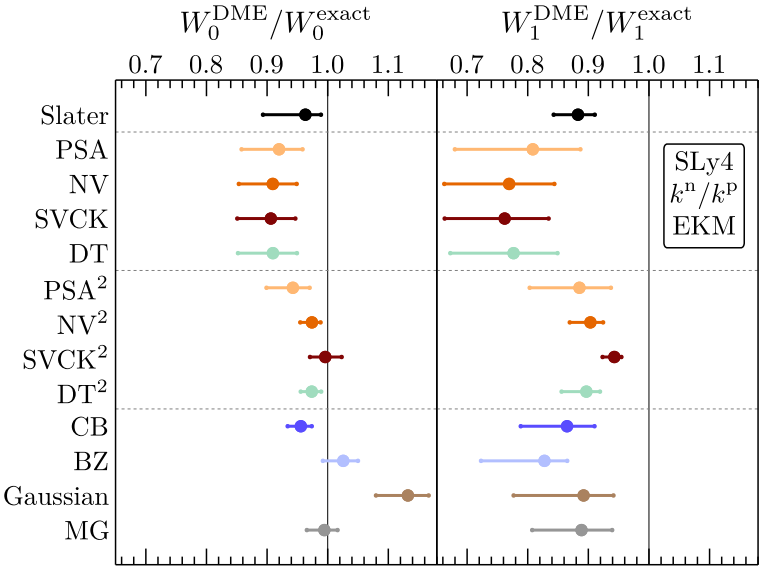

Figure 3.17: Same as Fig. 3.14 but for the EKM regulator, given in Eq. (3.69), with cutoff $R_0 = 1.0$ fm.

the oscillatory nature of the integrands. Instead we calculate the energy by splitting it into two parts,

$$W_0 = W_0^{\infty} - W_0^{\mathrm{reg}}, \tag{3.70}$$

where

$$W_0^{\infty} = -\frac{9}{8}\int \mathrm{d}\mathbf{R}\,\mathrm{d}\mathbf{r}\,|\rho_0(\mathbf{R};\mathbf{r})|^2 W_S^{\mathrm{LO}}(m,r) \tag{3.71}$$

is the exchange-energy contribution without regulators and

$$W_0^{\mathrm{reg}} = -\frac{9}{8}\int \mathrm{d}\mathbf{R}\,\mathrm{d}\mathbf{r}\,|\rho_0(\mathbf{R};\mathbf{r})|^2 W_S^{\mathrm{LO}}(m,r)[1-f(r)] \tag{3.72}$$

contains the whole regulator dependence.

The integrals in W_0^{reg} can easily be carried out numerically even for very large interaction ranges as $[1-f(r)]$ has a very short range. To tackle W_0^{∞}, which is for small m (especially for full-square DMEs) much harder to calculate numerically, we split it further according to

$$\begin{aligned} W_0^{\infty} = -\frac{9}{8}\frac{m_\pi^2}{12\pi}\left(\frac{g_A}{2F_\pi}\right)^2 \int \mathrm{d}\mathbf{R} \sum_{a,b=\mathrm{n,p}} \Big\{ & I_{00}(m,k_a,k_b)\rho_a(\mathbf{R})\rho_b(\mathbf{R}) \\ & + I_{02}(m,k_a,k_b)\rho_a(\mathbf{R})\left[\frac{1}{4}\Delta\rho_b(\mathbf{R}) - \tau_b(\mathbf{R}) + \frac{3}{5}k_b^2\rho_b(\mathbf{R})\right] \\ & + I_{22}(m,k_a,k_b)\left[\frac{1}{4}\Delta\rho_a(\mathbf{R}) - \tau_a(\mathbf{R}) + \frac{3}{5}k_a^2\rho_a(\mathbf{R})\right]\left[\frac{1}{4}\Delta\rho_b(\mathbf{R}) - \tau_b(\mathbf{R}) + \frac{3}{5}k_b^2\rho_b(\mathbf{R})\right]\Big\}, \end{aligned} \tag{3.73}$$

where k_a, k_b can be set either to the individual momentum scales for neutrons and protons or to the isoscalar momentum scale for both species and the I_{ij} functions depend on the considered DME variant. Zeroth-order DMEs have contributions only from I_{00}, second-order DMEs have additional contributions from I_{02}, and I_{22} contributes only for full-square variants.

The I_{ij} functions are calculated analytically by evaluating the integrals

$$I_{00}(m,k_a,k_b) = 4\pi \int \mathrm{d}r\, r^2 \Pi_0(k_a r)\Pi_0(k_b r)\frac{\mathrm{e}^{-mr}}{r}\,, \tag{3.74}$$

$$I_{02}(m,k_a,k_b) = \frac{4\pi}{3} \int \mathrm{d}r\, r^4 \Pi_0(k_a r)\Pi_2(k_b r)\frac{\mathrm{e}^{-mr}}{r}\,, \tag{3.75}$$

$$I_{22}(m,k_a,k_b) = \frac{4\pi}{36} \int \mathrm{d}r\, r^6 \Pi_2(k_a r)\Pi_2(k_b r)\frac{\mathrm{e}^{-mr}}{r}\,. \tag{3.76}$$

To this end we apply the method outlined in Ref. [208] and obtain after some analytical simplifications the following expressions. They are checked against their numerical counterparts for different values of m, k_a, and k_b. For the Slater approximation [or any other DME that uses $\Pi_0(x) = 3j_1(x)/x$] the I_{00} function reads

$$\begin{aligned} I_{00}(m,k_a,k_b) = \frac{3\pi}{4k_a^3k_b^3}\Big\{ & 2k_ak_b\left[3\left(k_a^2+k_b^2\right) - m^2\right] \\ & + \left[-3\left(k_a^2-k_b^2\right)^2 + 6m^2\left(k_a^2+k_b^2\right) + m^4\right] \operatorname{artanh}\left(\frac{2k_ak_b}{k_a^2+k_b^2+m^2}\right) \\ & + 8m\left[\left(k_a^3-k_b^3\right)\arctan\left(\frac{k_a-k_b}{m}\right) - \left(k_a^3+k_b^3\right)\arctan\left(\frac{k_a+k_b}{m}\right)\right]\Big\}. \end{aligned} \tag{3.77}$$

The other I_{ij} functions for NV$^{(2)}$-DME read

$$\begin{aligned} I_{02}(m,k_a,k_b) = -\frac{35\pi}{48k_a^3k_b^7}\Big\{ & 4k_ak_b\left[-22k_a^2k_b^2 + 15k_a^4 + 3k_b^4 + 6m^2\left(-13k_a^2+k_b^2\right) + 3m^4\right] \\ & - 6\Big[\left(k_a^2-k_b^2\right)^2\left(5k_a^2+k_b^2\right) + 3m^2\left(-15k_a^4 + 6k_a^2k_b^2 + k_b^4\right) + 3m^4\left(5k_a^2+k_b^2\right) \\ & + m^6\Big] \operatorname{artanh}\left(\frac{2k_ak_b}{k_a^2+k_b^2+m^2}\right) \\ & + 48mk_a^3\left[3\left(k_a^2-k_b^2\right) - 5m^2\right]\left[\arctan\left(\frac{k_a-k_b}{m}\right) - \arctan\left(\frac{k_a+k_b}{m}\right)\right]\Big\}, \end{aligned} \tag{3.78}$$

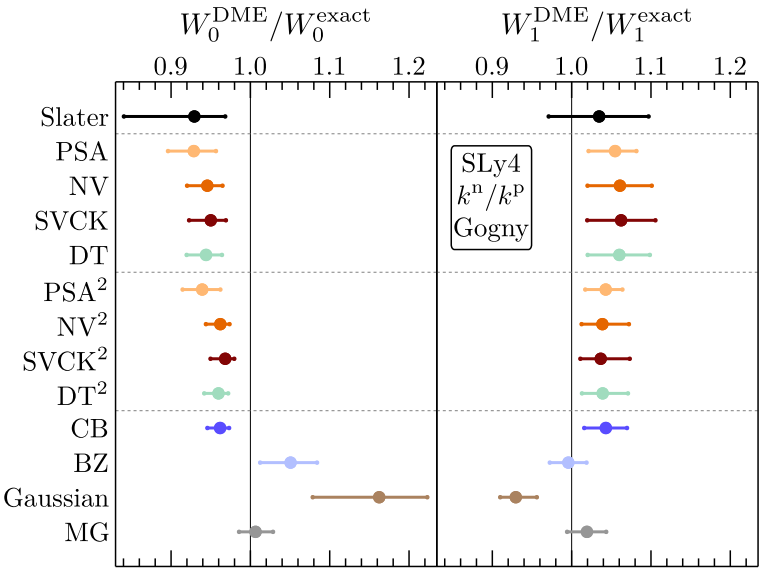

Figure 3.18: Same as Fig. 3.5 without the ratios for individual nuclei. Energies are shown for the finite-range parts of the Gogny D1S interaction.

and

$$
\begin{aligned}
I_{22}(m,k_a,k_b) = \frac{175\pi}{1536k_a^7k_b^7}\Bigg(&4k_ak_b\big\{7\big(k_a^2+k_b^2\big)\big[-22k_a^2k_b^2+15\big(k_a^4+k_b^4\big)\big] \\
&-m^2\big[134k_a^2k_b^2+141\big(k_a^4+k_b^4\big)\big]-69m^4\big(k_a^2+k_b^2\big)-15m^6\big\} \\
&+6\Big\{-7\big(k_a^2-k_b^2\big)^2\big[6k_a^2k_b^2+5\big(k_a^4+k_b^4\big)\big] \\
&+28m^2\big[5\big(k_a^6+k_b^6\big)+3\big(k_a^4k_b^2+k_a^2k_b^4\big)\big]+14m^4\big[6k_a^2k_b^2+5\big(k_a^4+k_b^4\big)\big] \\
&+28m^6\big(k_a^2+k_b^2\big)+5m^8\Big\}\operatorname{artanh}\left(\frac{2k_ak_b}{k_a^2+k_b^2+m^2}\right) \\
&+768m\left[\big(k_a^7-k_b^7\big)\arctan\left(\frac{k_a-k_b}{m}\right)-\big(k_a^7+k_b^7\big)\arctan\left(\frac{k_a+k_b}{m}\right)\right]\Bigg).
\end{aligned}
\tag{3.79}
$$

Note that for the case of a single isoscalar momentum scale, i.e., the special case $k_a = k_b$, a Mathematica package to obtain these expressions was published in Ref. [209]. For $k_a = k_b$, our equations agree with the ones outputted by that package.

3.4.3 Gogny exchange energies

As an additional test, we explore the DME performances for the finite-range parts of the Gogny D1S interaction [186], a successful phenomenological pseudopotential that was also considered in DME studies of Refs. [170, 175]. The finite-range parts are given by a sum of two Gaussians which contribute with different signs to the exchange energy. The results are shown in Fig. 3.18 for expansions with individual momentum scales for neutrons and protons and in Fig. 3.19 for expansions using isoscalar momentum scales for both species.

As for the Yukawa interaction the scalar-isovector energy reproduction is much worse when using the isoscalar momentum scale (except for the PSA^2-DME). One difference to

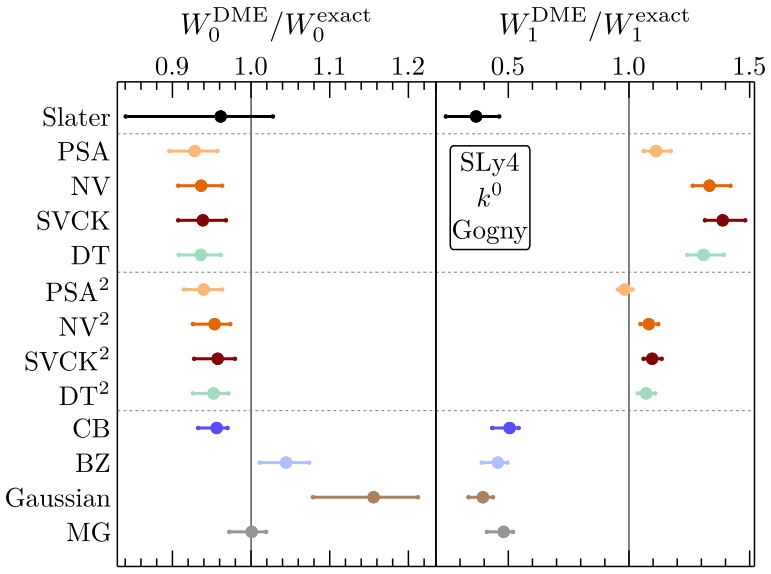

Figure 3.19: Same as Fig. 3.18 but for expansions with isoscalar momentum scales.

the Yukawa-interaction results lies in the improvement from using full squares rather than truncated squares, which is smaller here. This is because the additional term in the full square affects mainly the large-r behavior, which is not much probed by the Gaussians. In addition, the ratios obtained for the Slater approximation depend significantly more on the nucleus in the present case. This indicates that the cancellations of large local under- and overestimations as present in this approximation (see, e.g., Fig. 3.4) can be quite sensitive to system details.

We show the DME accuracies for the scalar-isosclar energy from every individual Gaussian in the D1S interaction (using individual momentum scales) in Fig. 3.20. Unsurprisingly, the energy reproduction is better for the Gaussian with the shorter range. Overall, the accuracies given in Fig. 3.20 are better than the total accuracies shown in Fig. 3.18. This is due to cancellations between the two terms. These cancellations change the ranking of the DMEs according to their accuracy in minor details when comparing to the Yukawa results shown in Fig. 3.5 but the overall conclusions of this work are still valid.

3.4.4 Combining density-matrix expansions

While in general the reproduction of exact (Yukawa) exchange energies is very good for all considered DMEs, different DMEs perform particularly well in different parts of the nucleus, see, e.g. Fig. 3.4 and related discussion. One can therefore try to combine different DMEs to achieve an even better reproduction of the exact integrands. We demonstrate this here for the CB-DME, which works particularly well in the nuclear interior, and the Gaussian approximation, which is well suited for the nuclear surface (see also Ref. [179]).

The idea is to use the ratio $\xi = k_{\mathrm{F}}/k_{\mathrm{FC}}$ to differentiate the surface from the interior. In nuclear matter $\xi = 1$, which therefore approximately holds in the center of the nucleus, while in the surface we observe $\xi < 1$. Because for both CB- and Gaussian DME only Π_0 contributes at second order, we simply interpolate between the two cases, i.e., we use Eq. (3.37) as before with $k = k_{\mathrm{FC}}$ but replace $\Pi_0(x)$ with

$$\widetilde{\Pi}_0(\xi, x) = I(\xi)\Pi_0^{\mathrm{CB}}(x) + [1 - I(\xi)]\Pi_0^{\mathrm{Gaussian}}(x)\,. \tag{3.80}$$

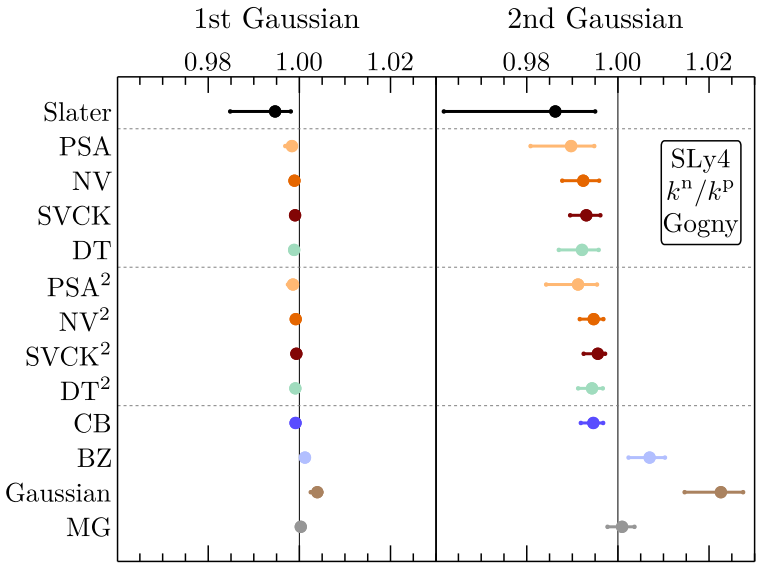

Figure 3.20: Same as Fig. 3.18 but only scalar-isoscalar energy ratios $W_0^{\mathrm{DME}}/W_0^{\mathrm{exact}}$ are shown. The left panel shows results when only taking the Gaussian with the shorter range into account, the right panel show results for the Gaussian with the longer range only.

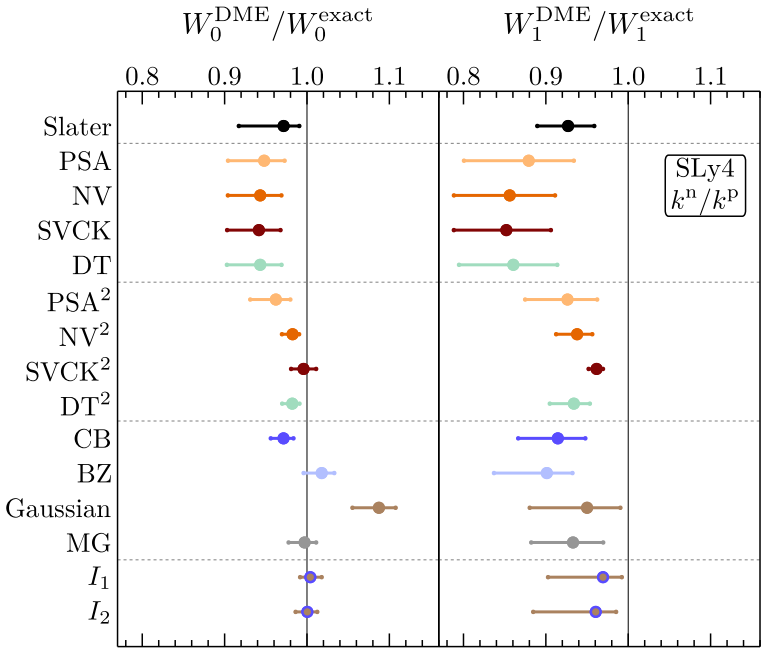

Figure 3.21: Same as Fig. 3.5 without the ratios for individual nuclei. In addition, results are shown for two different combinations of CB- and Gaussian DME. See text for details.

$I(\xi)$ labels the interpolating function that fulfills $I(0) \approx 0$ and $I(1) = 1$. $\widetilde{\Pi}_0(\xi, x)$ reduces to $\Pi_0^{\mathrm{CB}}(x)$ for INM and hence describes the OBDM of INM correctly. We show in Fig. 3.21 that an almost perfect scalar-isoscalar energy reproduction (with very small variation between different nuclei) can be achieved for instance with the following choices:

$$I_1(\xi) = \exp\left(-\left(\xi^{-20} - 1\right)^2\right), \tag{3.81}$$

$$I_2(\xi) = \frac{2}{3}[1+\exp(-25(\xi-1))]^{-1} + \frac{2}{3}\exp\left(-625(\xi-1)^2\right). \tag{3.82}$$

Also the scalar-isovector energy is on average better reproduced with this approach than with any considered DME.

3.5 Three-nucleon force exchange energies

As detailed in Sec. 1.2, three-nucleon forces first enter at N^{2}LO in deltaless chiral EFT. They can be separated into contact interaction, one-pion exchange, and two-pion exchange. We concentrate ourselves on the latter since these are the only terms included in the EDFs of Ref. [140] and Ch. 4. Also the other terms are of shorter range and include less off-diagonal OBDMs that need to be expanded. Hence, we expect them to be less of a challenge for DMEs. Note that in deltafull chiral EFT there are additional three-body terms already at NLO. They have the same structure as N^{2}LO two-pion exchange (with the exception that the $V_{C,1}$ part, see Sec. 3.5.2, does not contribute).

One can split the N^{2}LO two-pion exchange into three parts: a short-range piece (SR; that is proportional to two delta functions), an intermediate-range piece (IR; one delta function and one function with finite range), and a long-range piece (LR; two finite-range functions). We only consider IR and LR parts in the following as DMEs work very well for SR interactions.

As interactions are symmetric under the exchange of particles we can write the three-body potential V schematically as

$$V = V^{(1)} + V^{(2)} + V^{(3)}, \tag{3.83}$$

where $V^{(i)}$ is symmetric under exchange of j and k ($i \neq j \neq k \neq i$). With two-particle exchange operators P_{ij} one can then express the whole interaction in terms of one component [202],

$$V = V^{(1)} + P_{23}P_{13}V^{(1)}P_{13}P_{23} + P_{23}P_{12}V^{(1)}P_{12}P_{23}. \tag{3.84}$$

The HF energy arising from a 3N force is in analogy to the NN case [Eqs. (2.47) to (2.49)] given by

$$W_{\mathrm{HF}}^{(3\mathrm{N})} = \frac{1}{6}\sum_{i,j,k=1}^{A} \langle\phi_i\phi_j\phi_k|V\mathcal{A}_{123}|\phi_i\phi_j\phi_k\rangle \tag{3.85}$$

with the three-body antisymmetrizer

$$\mathcal{A}_{123} = (1 + P_{13}P_{12} + P_{23}P_{12})(1 - P_{12}). \tag{3.86}$$

With Eq. (3.84) one obtains after some algebraic manipulations [202]

$$W_{\mathrm{HF}}^{(3\mathrm{N})} = \frac{1}{2}\sum_{i,j,k=1}^{A} \langle\phi_i\phi_j\phi_k|V^{(1)}(1 - 2P_{12} - P_{23} + 2P_{23}P_{12})|\phi_i\phi_j\phi_k\rangle\ . \tag{3.87}$$

We split this into direct and exchange energies, given by

$$W_{\mathrm{H}}^{(3\mathrm{N})} = \frac{1}{2}\sum_{i,j,k=1}^{A} \langle\phi_i\phi_j\phi_k|V^{(1)}|\phi_i\phi_j\phi_k\rangle\ , \tag{3.88}$$

$$W_{\mathrm{F}}^{(3\mathrm{N})} = W_{\mathrm{SE}}^{(3\mathrm{N})} + W_{\mathrm{DE}}^{(3\mathrm{N})} \,, \tag{3.89}$$

respectively. Single-exchange (SE) and double-exchange (DE) energies are given by

$$W_{\mathrm{SE}}^{(3\mathrm{N})} = -\frac{1}{2} \sum_{i,j,k=1}^{A} \langle \phi_i \phi_j \phi_k | V^{(1)} (2P_{12} + P_{23}) | \phi_i \phi_j \phi_k \rangle \,, \tag{3.90}$$

$$W_{\mathrm{DE}}^{(3\mathrm{N})} = \sum_{i,j,k=1}^{A} \langle \phi_i \phi_j \phi_k | V^{(1)} P_{23} P_{12} | \phi_i \phi_j \phi_k \rangle \,. \tag{3.91}$$

For a translationally invariant local interaction the energies read in coordinate space

$$W_{\mathrm{H}}^{(3\mathrm{N})} = \frac{1}{2} \mathrm{Tr}_{123}^{\sigma\tau} \int \mathrm{d}\mathbf{x}_1 \mathrm{d}\mathbf{x}_2 \mathrm{d}\mathbf{x}_3 \, V^{(1)}(\mathbf{r}_{12}, \mathbf{r}_{13}) \boldsymbol{\rho}^{(1)}(\mathbf{x}_1) \boldsymbol{\rho}^{(2)}(\mathbf{x}_2) \boldsymbol{\rho}^{(3)}(\mathbf{x}_3) \,, \tag{3.92}$$

$$\begin{aligned} W_{\mathrm{SE}}^{(3\mathrm{N})} = &- \mathrm{Tr}_{123}^{\sigma\tau} \int \mathrm{d}\mathbf{x}_1 \mathrm{d}\mathbf{x}_2 \mathrm{d}\mathbf{x}_3 \, V^{(1)}(\mathbf{r}_{12}, \mathbf{r}_{13}) P_{12}^{\sigma\tau} \boldsymbol{\rho}^{(1)}(\mathbf{x}_2, \mathbf{x}_1) \boldsymbol{\rho}^{(2)}(\mathbf{x}_1, \mathbf{x}_2) \boldsymbol{\rho}^{(3)}(\mathbf{x}_3) \\ &- \frac{1}{2} \mathrm{Tr}_{123}^{\sigma\tau} \int \mathrm{d}\mathbf{x}_1 \mathrm{d}\mathbf{x}_2 \mathrm{d}\mathbf{x}_3 \, V^{(1)}(\mathbf{r}_{12}, \mathbf{r}_{13}) P_{23}^{\sigma\tau} \boldsymbol{\rho}^{(1)}(\mathbf{x}_1) \boldsymbol{\rho}^{(2)}(\mathbf{x}_3, \mathbf{x}_2) \boldsymbol{\rho}^{(3)}(\mathbf{x}_2, \mathbf{x}_3) \,, \end{aligned} \tag{3.93}$$

$$W_{\mathrm{DE}}^{(3\mathrm{N})} = \mathrm{Tr}_{123}^{\sigma\tau} \int \mathrm{d}\mathbf{x}_1 \mathrm{d}\mathbf{x}_2 \mathrm{d}\mathbf{x}_3 \, V^{(1)}(\mathbf{r}_{12}, \mathbf{r}_{13}) P_{23}^{\sigma\tau} P_{12}^{\sigma\tau} \boldsymbol{\rho}^{(1)}(\mathbf{x}_3, \mathbf{x}_1) \boldsymbol{\rho}^{(2)}(\mathbf{x}_1, \mathbf{x}_2) \boldsymbol{\rho}^{(3)}(\mathbf{x}_2, \mathbf{x}_3) \,, \tag{3.94}$$

where we suppressed the spin-isospin dependence of the interaction

$$V^{(1)}(\mathbf{r}_{12}, \mathbf{r}_{13}) = \langle \mathbf{r}_{12}, \mathbf{r}_{13} | V^{(1)}(\boldsymbol{\sigma}_1, \boldsymbol{\sigma}_2, \boldsymbol{\sigma}_3, \boldsymbol{\tau}_1, \boldsymbol{\tau}_2, \boldsymbol{\tau}_3) | \mathbf{r}_{12}, \mathbf{r}_{13} \rangle \tag{3.95}$$

as a shorthand notation and

$$\mathbf{r}_{ij} = \mathbf{x}_i - \mathbf{x}_j \,. \tag{3.96}$$

3.5.1 Density-matrix expansions for three-nucleon forces

To investigate the DME performance only single- and double-exchange energies are of interest since the direct energy does not depend on the full off-diagonal OBDM. The goal of this Section is not to conduct a complete study of DMEs applied to 3N forces, but instead to focus on the challenges and choices that come into play due to the more involved Eqs. (3.93) and (3.94) compared to their NN counterpart Eq. (3.54).

This means that as before, we will only consider terms that depend solely on the scalar parts of the OBDMs after splitting them as in Eq. (3.10). This is because the vector parts of the OBDMs typically contribute very little to the total energy, see also Sec. 3.1. We restrict ourselves to approximations where terms of higher than second order (to be understood as before but now with respect to the product of three density matrices) are neglected, i.e., we use here only approximations with truncated cubes. For the most part, we are going to look only at purely isoscalar contributions. As noted before considering expansions with an isoscalar momentum scale is a reasonable ansatz for these cases, which we make use of here since it shortens the resulting equations. In addition, we will consider only PSA-DME.

In other words, the focus of this Section is on the impact of expansion coordinate choices. In Secs. 3.3.3 and 3.4.1 we discussed possible choices for the point around which one expands the OBDMs in the NN case. As the 3N energies depend on two relative coordinates, one can not only pick different expansion points here but also different expansion variables and schemes. To illustrate the variety of possible options we briefly list choices made in the literature.

The authors of Ref. [202] consider the use of Jacobi coordinates, i.e., $\mathbf{R}_{123}, \mathbf{r}_i, \mathbf{r}_{jk}$ (with $i \neq j \neq k \neq i$), where

$$\mathbf{r}_i = \mathbf{x}_i - \mathbf{R}_{jk} \tag{3.97}$$

with the corresponding two- and three-body center-of-mass coordinates being defined as

$$\mathbf{R}_{jk} = \frac{\mathbf{x}_j + \mathbf{x}_k}{2} = \mathbf{R}_{123} - \frac{\mathbf{r}_i}{3}\,, \tag{3.98}$$

$$\mathbf{R}_{123} = \frac{\mathbf{x}_1 + \mathbf{x}_2 + \mathbf{x}_3}{3}\,. \tag{3.99}$$

For instance in the case of the second contribution to the single-exchange energy, Eq. (3.93), they expand in $\mathbf{r}_{23}$ about $\mathbf{R}_{23}$ and subsequently employ a modified DME to expand the result in $\mathbf{r}_1$ about $\mathbf{R}_{123}$. For double exchange, Eq. (3.94), they consider two alternative approaches, namely using the same set of Jacobi coordinates for the expansion of every OBDM and using a different set of Jacobi coordinates for every OBDM, which requires re-expressing them in terms of a single coordinate set after performing the expansions. Note that because no pair of density matrices in the double-exchange energy is evaluated at the same positions, the employed angle averaging introduces an additional approximation even when expanding about the average of the two arguments of a density matrix. In other words, one does not profit from Eq. (3.46) unlike in the NN case.

In Ref. [149] different approaches are used for different terms with the general idea to minimize the number of performed expansions. This involves in some cases using an angle-averaged DME about $\mathbf{x}_i$ for expanding $\rho_t(\mathbf{x}_i, \mathbf{x}_j)$ and in other cases a combined DME and Taylor expansion, as detailed below, in $\mathbf{r}_{ij}$ and $\mathbf{r}_k$ about $\mathbf{x}_k$.

All coordinate and expansion choices we discuss now can be seen as extensions of the discussion in Sec. 3.3.3. There, we considered expanding $\rho_q(\mathbf{x}_1, \mathbf{x}_2)$ in $\mathbf{r}_{12}$ about a generalized expansion point $\mathbf{v}_a$. When applying an analogous strategy to other OBDMs appearing in the same integrand, we need to express the local densities evaluated at the different expansion points in terms of local densities at a joint point. Otherwise we would not end up with a local energy density functional.

Therefore, we consider the following procedure: First apply a second-order DME in $\mathbf{r}_{ij}$ about

$$\mathbf{v}_a^{ij} = a\mathbf{x}_i + (1-a)\mathbf{x}_j\,. \tag{3.100}$$

to $\rho_q(\mathbf{x}_i, \mathbf{x}_j) = \rho_q(\mathbf{v}_a^{ij} + (1-a)\mathbf{r}_{ij}, \mathbf{v}_a^{ij} - a\mathbf{r}_{ij})$. This yields

$$\begin{aligned}\rho_q(\mathbf{x}_i, \mathbf{x}_j) \approx\ & \Pi_0(kr_{ij})\rho_q(\mathbf{v}_a^{ij}) + \Pi_1(kr_{ij})r_{ij,\alpha}\left[\left(\frac{1}{2} - a\right)\nabla_\alpha\rho_q(\mathbf{v}_a^{ij}) + \mathrm{i}j_{q,\alpha}(\mathbf{v}_a^{ij})\right] \\ & + \frac{\Pi_2(kr_{ij})}{2}r_{ij,\alpha}r_{ij,\beta}\left[\left(\frac{1}{2} - a + a^2\right)\nabla_\alpha\nabla_\beta\rho_q(\mathbf{v}_a^{ij}) + (1-2a)\mathrm{i}\nabla_\alpha j_{q,\beta}(\mathbf{v}_a^{ij})\right. \\ & \left. - \tau_{q,\alpha\beta}(\mathbf{v}_a^{ij}) + \frac{1}{5}\delta_{\alpha\beta}k^2\rho_q(\mathbf{v}_a^{ij})\right]\,.\end{aligned} \tag{3.101}$$

as given in Eq. (3.50). Then perform a Taylor expansion of the local densities in Eq. (3.101) in

$$\mathbf{N}_a^{ij} = \mathbf{v}_a^{ij} - \mathbf{E} \tag{3.102}$$

about the joint expansion point $\mathbf{E}$, which remains unspecified at this point. We truncate the

Taylor series such that we keep only up to quadratic terms in $\{\mathbf{r}_{ij}, \mathbf{N}_a^{ij}\} \otimes \{k, \boldsymbol{\nabla}\}$ (except for the dependence hidden in the Π functions). For instance, for the first term

$$\rho_q(\mathbf{v}_a^{ij}) \approx \rho_q(\mathbf{E}) + \mathbf{N}_a^{ij} \cdot \boldsymbol{\nabla}\rho_q(\mathbf{E}) + \frac{1}{2}\left(\mathbf{N}_a^{ij} \cdot \boldsymbol{\nabla}\right)^2 \rho_q(\mathbf{E})\,. \tag{3.103}$$

The results of Ref. [170] indicate that this is a good approximation, in particular compared to the DME accuracy. Other approaches are possible, e.g. the use of a modified DME as mentioned above [202].

Overall, the procedure followed here gives for time-reversal-invariant systems (where $\mathbf{j}_q \equiv 0$)

$$\begin{aligned}\rho_q(\mathbf{x}_i, \mathbf{x}_j) \approx \Pi_0(kr_{ij})&\left[\rho_q(\mathbf{E}) + \mathbf{N}_a^{ij} \cdot \boldsymbol{\nabla}\rho_q(\mathbf{E}) + \frac{1}{2}\left(\mathbf{N}_a^{ij} \cdot \boldsymbol{\nabla}\right)^2 \rho_q(\mathbf{E})\right] \\ &+ \Pi_1(kr_{ij}) r_{ij,\alpha}\left(\frac{1}{2} - a\right)\left[\nabla_\alpha \rho_q(\mathbf{E}) + \mathbf{N}_a^{ij} \cdot \boldsymbol{\nabla}\nabla_\alpha \rho_q(\mathbf{E})\right] \\ &+ \frac{\Pi_2(kr_{ij})}{2} r_{ij,\alpha} r_{ij,\beta}\left[\left(\frac{1}{2} - a + a^2\right)\nabla_\alpha \nabla_\beta \rho_q(\mathbf{E}) - \tau_{q,\alpha\beta}(\mathbf{E}) + \frac{1}{5}\delta_{\alpha\beta} k^2 \rho_q(\mathbf{E})\right].\end{aligned} \tag{3.104}$$

The DME momentum scale k would need to be evaluated at the DME expansion point $\mathbf{v}_a^{ij}$ to be consistent to before. Instead we use

$$k = k(\mathbf{E}) \approx k(\mathbf{v}_a^{ij}) \tag{3.105}$$

because derivative correction terms would be of order three or higher when plugged into Eq. (3.104).

To simplify the result one can perform an average with respect to the solid angle of $\mathbf{r}_{ij}$ justified by the typically minor dependence of the scalar part of the OBDM on it [135, 168]. Then,

$$\begin{aligned}\rho_q(\mathbf{x}_i, \mathbf{x}_j) \approx \Pi_0(kr_{ij})&\left[\rho_q(\mathbf{E}) + \mathbf{N}_a^{ij} \cdot \boldsymbol{\nabla}\rho_q(\mathbf{E}) + \frac{1}{2}\left(\mathbf{N}_a^{ij} \cdot \boldsymbol{\nabla}\right)^2 \rho_q(\mathbf{E})\right] \\ &+ \frac{\Pi_2(kr_{ij})}{6} r_{ij}^2\left[\left(\frac{1}{2} - a + a^2\right)\Delta\rho_q(\mathbf{E}) - \tau_q(\mathbf{E}) + \frac{3}{5}k^2\rho_q(\mathbf{E})\right]\end{aligned} \tag{3.106}$$

in agreement with the result from Ref. [149].

3.5.2 Two-pion exchange

Three-nucleon two-pion exchange at N^{2}LO V_C can be split according to its LEC structure:

$$V_C = V_{C,1} + V_{C,3} + V_{C,4}\,. \tag{3.107}$$

The individual parts read [210]

$$V_{C,1}^{(1)}(\mathbf{r}_{12}, \mathbf{r}_{13}) = A_1 \boldsymbol{\tau}_2 \cdot \boldsymbol{\tau}_3\, \boldsymbol{\sigma}_2 \cdot \hat{\mathbf{r}}_{12}\, \boldsymbol{\sigma}_3 \cdot \hat{\mathbf{r}}_{13} Z(r_{12}) Z(r_{13})\,, \tag{3.108}$$

$$V_{C,3}^{(1)}(\mathbf{r}_{12}, \mathbf{r}_{13}) = A_3 2\boldsymbol{\tau}_2 \cdot \boldsymbol{\tau}_3 \{Q_{12}(\mathbf{r}_{12}), Q_{13}(\mathbf{r}_{13})\}\,, \tag{3.109}$$

$$V_{C,4}^{(1)}(\mathbf{r}_{12}, \mathbf{r}_{13}) = A_4 2\mathrm{i}\boldsymbol{\tau}_1 \cdot (\boldsymbol{\tau}_2 \times \boldsymbol{\tau}_3)[Q_{12}(\mathbf{r}_{12}), Q_{13}(\mathbf{r}_{13})]\,, \tag{3.110}$$

where the newly introduced functions are

$$Z(r) = \frac{m_\pi r}{3}[1 - T(r)]Y(r)\,, \tag{3.111}$$

$$Q_{ij}(\mathbf{r}) = [S_{ij}(\mathbf{r})T(r) + \boldsymbol{\sigma}_i \cdot \boldsymbol{\sigma}_j]Y(r) - \boldsymbol{\sigma}_i \cdot \boldsymbol{\sigma}_j \Delta(\mathbf{r})\,, \tag{3.112}$$

$$S_{ij}(\mathbf{r}) = 3\boldsymbol{\sigma}_i \cdot \hat{\mathbf{r}}\, \boldsymbol{\sigma}_j \cdot \hat{\mathbf{r}} - \boldsymbol{\sigma}_i \cdot \boldsymbol{\sigma}_j\,, \tag{3.113}$$

$$Y(r) = \frac{\mathrm{e}^{-m_\pi r}}{m_\pi r}\,, \tag{3.114}$$

$$T(r) = 1 + \frac{3}{m_\pi r} + \frac{3}{(m_\pi r)^2}\,, \tag{3.115}$$

$$\Delta(\mathbf{r}) = \frac{4\pi}{m_\pi^3}\delta(\mathbf{r})\,. \tag{3.116}$$

The constants are given by

$$A_1 = \frac{g_A^2 m_\pi^6 c_1}{16\pi^2 F_\pi^4}, \qquad A_3 = \frac{g_A^2 m_\pi^6 c_3}{1152\pi^2 F_\pi^4}, \qquad A_4 = -\frac{g_A^2 m_\pi^6 c_4}{2304\pi^2 F_\pi^4}\,. \tag{3.117}$$

The two-pion exchange expressions agree with Ref. [149]. Note the last line in eq. (21) of Ref. [140] should have a + instead of a − to agree with these expressions.

Here, we use $g_A = 1.27, m_\pi = 138$ MeV, $F_\pi = 92.4$ MeV, $c_1 = -0.57$ GeV^{-1}, $c_3 = -3.87$ GeV^{-1}, and $c_4 = 2.89$ GeV^{-1} [149, 211]. To regularize the interactions, we multiply all Yukawa functions $Y(r)$ with a local regulator function $f(r)$,

$$Y(r) \to Y(r)f(r)\,. \tag{3.118}$$

We choose here

$$f(r) = \left[1 - \exp\left(-\frac{r^2}{R_0^2}\right)\right]^6\,, \tag{3.119}$$

where the spatial cutoff is set to $R_0 = 1.0$ fm [25, 140]. We use a three-dimensional delta distribution for $\delta(\mathbf{r})$, which simplifies some of the equations, see below. This is in agreement with the choice of Refs. [140, 149]. Other schemes use a smeared-out delta function, see e.g., Ref. [212].

As a consequence of the spin-isospin structure given in Eqs. (3.108) to (3.110) both the direct and the first contribution to the single-exchange energy vanish after carrying out the traces. We introduce

$$\cos\theta_{12,13} = \hat{\mathbf{r}}_{12} \cdot \hat{\mathbf{r}}_{13}\,, \tag{3.120}$$

$$\delta_{abc} = \delta_{t,a}\delta_{t',b}\delta_{t'',c} \tag{3.121}$$

and carry out the traces in Eqs. (3.93) and (3.94). The resulting contributions that depend only on scalar parts of the OBDM read (see also Ref. [149])

$$W_{\mathrm{SE}}^{C,1} = -\frac{1}{8}A_{C,1}\int \mathrm{d}\mathbf{x}_1\mathrm{d}\mathbf{x}_2\mathrm{d}\mathbf{x}_3 \sum_{t,t',t''} \rho_t(\mathbf{x}_1)\rho_{t'}(\mathbf{x}_3,\mathbf{x}_2)\rho_{t''}(\mathbf{x}_2,\mathbf{x}_3)(3\delta_{000} - \delta_{011})$$
$$\times\, Z(r_{12})Z(r_{13})\cos\theta_{12,13}\,, \tag{3.122}$$

$$W_{\mathrm{DE}}^{C,1} = \frac{1}{16} A_{C,1} \int \mathrm{d}\mathbf{x}_1 \mathrm{d}\mathbf{x}_2 \mathrm{d}\mathbf{x}_3 \sum_{t,t',t''} \rho_t(\mathbf{x}_3,\mathbf{x}_1)\rho_{t'}(\mathbf{x}_1,\mathbf{x}_2)\rho_{t''}(\mathbf{x}_2,\mathbf{x}_3)$$
$$\times (3\delta_{000} + 3\delta_{110} - \delta_{101} - \delta_{011}) Z(r_{12}) Z(r_{13}) \cos\theta_{12,13}\,, \tag{3.123}$$

$$W_{\mathrm{SE}}^{C,3} = -\frac{3}{2} A_{C,3} \int \mathrm{d}\mathbf{x}_1 \mathrm{d}\mathbf{x}_2 \mathrm{d}\mathbf{x}_3 \sum_{t,t',t''} \rho_t(\mathbf{x}_1)\rho_{t'}(\mathbf{x}_3,\mathbf{x}_2)\rho_{t''}(\mathbf{x}_2,\mathbf{x}_3)(3\delta_{000} - \delta_{011})$$
$$\times \big[T(r_{12})Y(r_{12})T(r_{13})Y(r_{13})\big(3\cos^2\theta_{12,13} - 1\big) + Y(r_{12})Y(r_{13}) - Y(r_{12})\Delta(\mathbf{r}_{13})$$
$$-\Delta(\mathbf{r}_{12})Y(r_{13}) + \Delta(\mathbf{r}_{12})\Delta(\mathbf{r}_{13})\big]\,, \tag{3.124}$$

$$W_{\mathrm{DE}}^{C,3} = \frac{3}{4} A_{C,3} \int \mathrm{d}\mathbf{x}_1 \mathrm{d}\mathbf{x}_2 \mathrm{d}\mathbf{x}_3 \sum_{t,t',t''} \rho_t(\mathbf{x}_3,\mathbf{x}_1)\rho_{t'}(\mathbf{x}_1,\mathbf{x}_2)\rho_{t''}(\mathbf{x}_2,\mathbf{x}_3)(3\delta_{000} + 3\delta_{110} - \delta_{101} - \delta_{011})$$
$$\times \big[T(r_{12})Y(r_{12})T(r_{13})Y(r_{13})\big(3\cos^2\theta_{12,13} - 1\big) + Y(r_{12})Y(r_{13}) - Y(r_{12})\Delta(\mathbf{r}_{13})$$
$$-\Delta(\mathbf{r}_{12})Y(r_{13}) + \Delta(\mathbf{r}_{12})\Delta(\mathbf{r}_{13})\big]\,, \tag{3.125}$$

$$W_{\mathrm{SE}}^{C,4} = 0\,, \tag{3.126}$$

$$W_{\mathrm{DE}}^{C,4} = 3A_{C,4} \int \mathrm{d}\mathbf{x}_1 \mathrm{d}\mathbf{x}_2 \mathrm{d}\mathbf{x}_3 \sum_{t,t',t''} \rho_t(\mathbf{x}_3,\mathbf{x}_1)\rho_{t'}(\mathbf{x}_1,\mathbf{x}_2)\rho_{t''}(\mathbf{x}_2,\mathbf{x}_3)(3\delta_{000} - \delta_{110} - \delta_{101} - \delta_{011})$$
$$\times \left[\frac{1}{2}T(r_{12})Y(r_{12})T(r_{13})Y(r_{13})\big(1 - 3\cos^2\theta_{12,13}\big) + Y(r_{12})Y(r_{13}) - Y(r_{12})\Delta(\mathbf{r}_{13})\right.$$
$$\left.-\Delta(\mathbf{r}_{12})Y(r_{13}) + \Delta(\mathbf{r}_{12})\Delta(\mathbf{r}_{13})\right]. \tag{3.127}$$

We split these energies further according to their isospin and interaction structures:

$$W_{\mathrm{SE},tt't''}^{\mathrm{LR}} = W_{\mathrm{SE},tt't''}^{ZZ} + W_{\mathrm{SE},tt't''}^{TYTY} + W_{\mathrm{SE},tt't''}^{YY}\,, \tag{3.128}$$
$$W_{\mathrm{DE},tt't''}^{\mathrm{LR}} = W_{\mathrm{DE},tt't''}^{ZZ} + W_{\mathrm{DE},tt't''}^{TYTY} + W_{\mathrm{DE},tt't''}^{YY}\,, \tag{3.129}$$
$$W_{\mathrm{F},tt't''}^{\mathrm{IR}} = W_{\mathrm{SE},tt't''}^{Y\Delta} + W_{\mathrm{DE},tt't''}^{Y\Delta}\,. \tag{3.130}$$

These are single-exchange energies from long-range terms, double-exchange energies from long-range terms, and energies from intermediate-range terms. In the latter case we do not distinguish between single and double exchange as their structure is identical when actual delta distributions are used. The indices $tt't''$ refer to the isospin structure.

Two examples of the terms on the right-hand side of Eqs. (3.128) to (3.130) read

$$W_{\mathrm{SE},000}^{ZZ} = -\frac{3}{8} A_{C,1} \int \mathrm{d}\mathbf{x}_1 \mathrm{d}\mathbf{x}_2 \mathrm{d}\mathbf{x}_3\, \rho_0(\mathbf{x}_1)\rho_0(\mathbf{x}_3,\mathbf{x}_2)\rho_0(\mathbf{x}_2,\mathbf{x}_3) Z(r_{12}) Z(r_{13}) \cos\theta_{12,13}\,, \tag{3.131}$$

$$W_{\mathrm{DE},110}^{Y\Delta} = \left(-\frac{9}{4} A_{C,3} + 3A_{C,4}\right) \int \mathrm{d}\mathbf{x}_1 \mathrm{d}\mathbf{x}_2 \mathrm{d}\mathbf{x}_3\, \rho_1(\mathbf{x}_3,\mathbf{x}_1)\rho_1(\mathbf{x}_1,\mathbf{x}_2)\rho_0(\mathbf{x}_2,\mathbf{x}_3)$$
$$\times \left[Y(r_{12})\Delta(\mathbf{r}_{13}) + \Delta(\mathbf{r}_{12})Y(r_{13})\right], \tag{3.132}$$

where the latter contains contributions from both $W_{\mathrm{DE}}^{C,3}$ and $W_{\mathrm{DE}}^{C,4}$. Other cases are named in analogy.

We consider different approximation schemes for the three groups given by Eqs. (3.128) to (3.130). In all cases, we keep only terms up to second order and local densities are evaluated either at $\mathbf{x}_1$ or $\mathbf{R}_{123}$, but other choices are of course possible. In detail the considered expansion schemes are:

1. for LR SE:
   (a) DME of $\rho_t(\mathbf{x}_2,\mathbf{x}_3)$ in $\mathbf{r}_{23}$ about $\mathbf{R}_{23}$, local densities Taylor expanded about $\mathbf{x}_1$
   (b) DME of $\rho_t(\mathbf{x}_2,\mathbf{x}_3)$ in $\mathbf{r}_{23}$ about $\mathbf{R}_{23}$, local densities Taylor expanded about $\mathbf{R}_{123}$
2. for LR DE:
   (a) angle-averaged DME of $\rho_t(\mathbf{x}_2,\mathbf{x}_3)$ in $\mathbf{r}_{23}$ about $\mathbf{R}_{23}$, of $\rho_t(\mathbf{x}_1,\mathbf{x}_2)$ and $\rho_t(\mathbf{x}_1,\mathbf{x}_3)$ about $\mathbf{x}_1$, local densities Taylor expanded about $\mathbf{x}_1$
   (b) non-angle-averaged DME of $\rho_t(\mathbf{x}_2,\mathbf{x}_3)$ in $\mathbf{r}_{23}$ about $\mathbf{R}_{23}$, of $\rho_t(\mathbf{x}_1,\mathbf{x}_2)$ and $\rho_t(\mathbf{x}_1,\mathbf{x}_3)$ about $\mathbf{x}_1$, local densities Taylor expanded about $\mathbf{x}_1$
   (c) DME of $\rho_t(\mathbf{x}_i,\mathbf{x}_j)$ in $\mathbf{r}_{ij}$ about $\mathbf{R}_{ij}$, local densities Taylor expanded about $\mathbf{x}_1$
   (d) DME of $\rho_t(\mathbf{x}_i,\mathbf{x}_j)$ in $\mathbf{r}_{ij}$ about $\mathbf{R}_{ij}$, local densities Taylor expanded about $\mathbf{R}_{123}$
3. for IR:
   (a) angle-averaged DME of $\rho_t(\mathbf{x}_1,\mathbf{x}_i)$ in $\mathbf{r}_{1i}$ about $\mathbf{x}_1$ [for the term proportional to $\Delta(\mathbf{r}_{1j})$ with $1\neq i\neq j$]
   (b) non-angle-averaged DME of $\rho_t(\mathbf{x}_1,\mathbf{x}_i)$ in $\mathbf{r}_{1i}$ about $\mathbf{x}_1$ [for the term proportional to $\Delta(\mathbf{r}_{1j})$ with $1\neq i\neq j$]
   (c) DME of $\rho_t(\mathbf{x}_1,\mathbf{x}_i)$ in $\mathbf{r}_{1i}$ about $\mathbf{R}_{1i}$ [for the term proportional to $\Delta(\mathbf{r}_{1j})$ with $1\neq i\neq j$], local densities Taylor expanded about $\mathbf{x}_1$
   (d) DME of $\rho_t(\mathbf{x}_1,\mathbf{x}_i)$ in $\mathbf{r}_{1i}$ about $\mathbf{R}_{1i}$ [for the term proportional to $\Delta(\mathbf{r}_{1j})$ with $1\neq i\neq j$], local densities Taylor expanded about $\mathbf{R}_{123}$.

The list above contains schemes that are not marked as either angle-averaged nor non-angle-averaged. This is because for such schemes the two options, i.e., Eqs. (3.104) and (3.106), yield the same result. Cases labelled (a) are the ones used in Ref. [140]. The resulting analytic expressions for these cases are provided in Ref. [149].

As an example case we show for Eq. (3.131) how we proceed in calculating the energy according to prescription 1.(a): Using Eq. (3.104) with $a=1/2$, $\mathbf{N}^{23}_{1/2}=-\mathbf{r}_1$, and $\mathbf{E}=\mathbf{x}_1$ yields

$$\begin{aligned}
W^{ZZ}_{\mathrm{SE},000} \approx& -\frac{3}{8}A_{C,1}\int \mathrm{d}\mathbf{x}_1\mathrm{d}\mathbf{r}_{12}\mathrm{d}\mathbf{r}_{13}\, Z(r_{12})Z(r_{13})\cos\theta_{12,13}\,\rho_0(\mathbf{x}_1)\\
&\times\left\{\Pi_0(kr_{23})\left[\rho_0(\mathbf{x}_1)-\mathbf{r}_1\cdot\boldsymbol{\nabla}\rho_0(\mathbf{x}_1)+\frac{1}{2}(\mathbf{r}_1\cdot\boldsymbol{\nabla})^2\rho_0(\mathbf{x}_1)\right]\right.\\
&\left.+\frac{\Pi_2(kr_{23})}{2}r_{23,\alpha}r_{23,\beta}\left[\frac{1}{4}\nabla_\alpha\nabla_\beta\rho_0(\mathbf{x}_1)-\tau_{0,\alpha\beta}(\mathbf{x}_1)+\frac{1}{5}\delta_{\alpha\beta}k^2\rho_0(\mathbf{x}_1)\right]\right\}^2\\
\approx& -3\pi^2A_{C,1}\int \mathrm{d}\mathbf{x}_1\mathrm{d}r_{12}\mathrm{d}r_{13}\mathrm{d}\cos\theta_{12,13}\, r_{12}^2r_{13}^2\, Z(r_{12})Z(r_{13})\cos\theta_{12,13}\,\rho_0(\mathbf{x}_1)\\
&\times\left[\Pi_0(kr_{23})^2\left(\rho_0(\mathbf{x}_1)^2+\frac{1}{3}r_1^2\Big\{\rho_0(\mathbf{x}_1)\Delta\rho_0(\mathbf{x}_1)+[\boldsymbol{\nabla}\rho_0(\mathbf{x}_1)]^2\Big\}\right)\right.\\
&\left.+\frac{\Pi_0(kr_{23})\Pi_2(kr_{23})}{6}r_{23}^2\,\rho_0(\mathbf{x}_1)\left[\frac{1}{4}\Delta\rho_0(\mathbf{x}_1)-\tau_0(\mathbf{x}_1)+\frac{3}{5}k^2\rho_0(\mathbf{x}_1)\right]\right].
\end{aligned}\tag{3.133}$$

In the second step we truncated all terms at second order. The coordinates in the integrand are related to each other via

$$4r_1^2 = r_{12}^2 + r_{13}^2 + 2r_{12}r_{13}\cos\theta_{12,13}\,, \tag{3.134}$$
$$r_{23}^2 = r_{12}^2 + r_{13}^2 - 2r_{12}r_{13}\cos\theta_{12,13}\,. \tag{3.135}$$

Expressions can get quite involved. One such example is scheme 2.(b) which gives

$$\begin{aligned} W_{\mathrm{DE},101}^{TYTY} \approx\, & 6\pi^2(A_{C,3} - 2A_{C,4}) \int \mathrm{d}\mathbf{x}_1 \mathrm{d}r_{12}\mathrm{d}r_{13}\mathrm{d}\cos\theta_{12,13}\, r_{12}^2 r_{13}^2 \\ & \times \Bigg[\widetilde{\Pi}_{000}\rho_0\rho_1\left(\rho_1 + \frac{1}{6}r_1^2\Delta\rho_1\right) + \frac{\widetilde{\Pi}_{100}}{6}\mathbf{r}_1\cdot\mathbf{r}_{12}\rho_1(\boldsymbol{\nabla}\rho_0\cdot\boldsymbol{\nabla}\rho_1) \\ & + \frac{\widetilde{\Pi}_{010}}{6}\mathbf{r}_1\cdot\mathbf{r}_{13}\rho_0(\boldsymbol{\nabla}\rho_1)^2 + \frac{\widetilde{\Pi}_{110}}{12}\mathbf{r}_{12}\cdot\mathbf{r}_{13}\rho_1(\boldsymbol{\nabla}\rho_0\cdot\boldsymbol{\nabla}\rho_1) \\ & + \frac{\widetilde{\Pi}_{200}}{6}r_{12}^2\rho_1^2\left(\frac{1}{2}\Delta\rho_0 - \tau_0 + \frac{3}{5}k^2\rho_0\right) + \frac{\widetilde{\Pi}_{020}}{6}r_{13}^2\rho_0\rho_1\left(\frac{1}{2}\Delta\rho_1 - \tau_1 + \frac{3}{5}k^2\rho_1\right) \\ & + \frac{\widetilde{\Pi}_{002}}{6}r_{23}^2\rho_0\rho_1\left(\frac{1}{4}\Delta\rho_1 - \tau_1 + \frac{3}{5}k^2\rho_1\right)\Bigg] \\ & \times T(r_{12})Y(r_{12})T(r_{13})Y(r_{13})\left(1 - 3\cos^2\theta_{12,13}\right), \end{aligned} \tag{3.136}$$

where we suppressed the dependence of the local densities on $\mathbf{x}_1$ and used the definition [149]

$$\widetilde{\Pi}_{ijl} = \Pi_i(kr_{12})\Pi_j(kr_{13})\Pi_l(kr_{23})\,. \tag{3.137}$$

The coordinate scalar products can be expressed in terms of the integration variables by using

$$\mathbf{r}_1 = \frac{\mathbf{r}_{12} + \mathbf{r}_{13}}{2}\,, \tag{3.138}$$
$$\mathbf{r}_{23} = \mathbf{r}_{13} - \mathbf{r}_{12}\,. \tag{3.139}$$

Note that Eq. (3.136) contains Π_1 functions. For PSA-DME [145],

$$\Pi_1(x) = \frac{3j_1(x)}{x}\,. \tag{3.140}$$

For many other DME variants the Π_1 function had never been defined. When $\Pi_0(x) = \Pi_1(x) = \Pi_2(x)$, as fulfilled by PSA-DME, prescription 2.(b) equals 2.(c) and 3.(b) equals 3.(c).

3.5.3 Intermediate-range and long-range exchange energies

To test the approximation schemes explained in Sec. 3.5.2, we need to select which systems to consider. Here we pick ^{16}O, ^{48}Ca, ^{132}Sn, and ^{208}Pb. As before we use single-particle orbitals generated from a self-consistent HF calculation employing the SLy4 parametrization of the Skyrme EDF [195] without pairing. The orbitals are obtained with the code HOSPHE which solves the HF equations by expanding single-particle orbitals in a spherical HO basis [197]. We set the basis size to 16 HO shells, which yields sufficiently realistic orbitals for the given application. The basis frequency is set according to $\hbar\omega = 1.2 \times 41A^{-1/3}$ MeV [197].

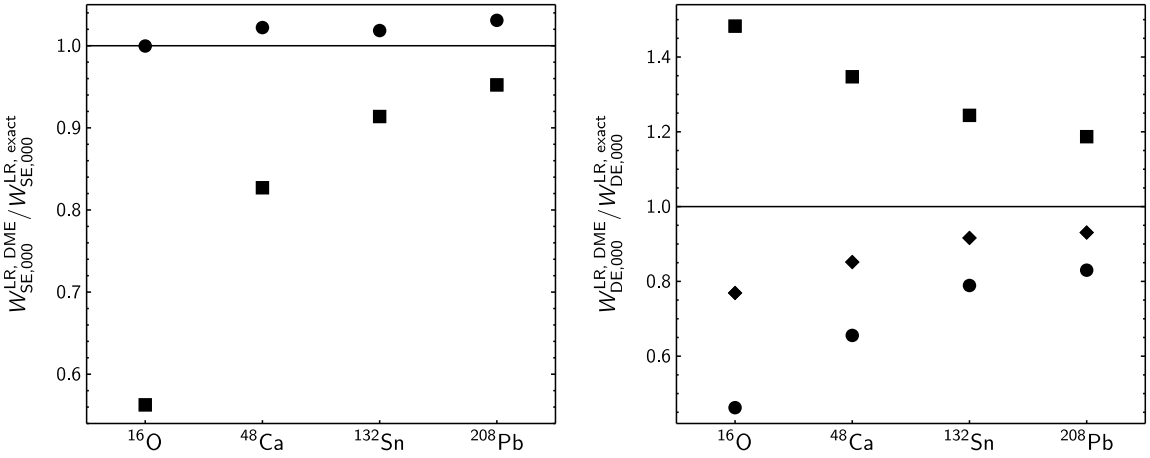

Figure 3.22: Ratios of DME-approximated and exact scalar-isoscalar exchange-energy contributions for the long-range parts of a two-pion-exchange three-nucleon interaction. Results are given for 4 closed-shell nuclei where the underlying orbitals are obtained from a self-consistent HF calculation with the SLy4 EDF. The left panel shows single-exchange energies, the right panel double-exchange energies. Values are shown with circles (●) for schemes (a), with squares (■) for schemes (b), and with diamonds (◆) for scheme 2.(d). All values are obtained with the PSA-DME with an isoscalar momentum scale. For PSA-DME, schemes 2.(b) and 2.(c) are identical.

For the long-range terms, we show ratios of DME-approximated and exact exchange energies in Fig. 3.22. As stated before, we consider here only scalar-isoscalar energies. For both SE (left panel) and DE (right panel), the better performance of the DMEs for heavier systems is clearly visible and in agreement with expectations. In the SE case the energy reproduction is very good for scheme 1.(a) for all considered nuclei, while scheme 1.(b) significantly underestimates the true value, in particular for ^{16}O it misses about half of the energy.

For DE, there is no scheme which works very well for all nuclei, but the hierarchy of approximation schemes is the same throughout all considered nuclei. In particular, case 2.(d) performs best. This is plausible when comparing to case 2.(c), which differs from 2.(d) only in the Taylor part of the expansion. Cubic terms are the leading terms that are neglected in the Taylor series. For 2.(c) the distances, over which the Taylor series are carried out, are r_1, $r_{12}/2$, and $r_{13}/2$. For 2.(d) these are $r_1/3$, $r_2/3$, and $r_3/3$. By using

$$\mathbf{r}_1 = -\mathbf{r}_2 - \mathbf{r}_3\,, \tag{3.141}$$

$$\mathbf{r}_{1i} = -\frac{2}{3}\mathbf{r}_i - \frac{1}{3}\mathbf{r}_j \tag{3.142}$$

for $1 \neq i \neq j \neq 1$, one can express the cubic sums of these distances in the same set of coordinates, namely in r_2, r_3, and

$$\cos\theta_{2,3} = \hat{\mathbf{r}}_2 \cdot \hat{\mathbf{r}}_3\,. \tag{3.143}$$

The cubic sum for the distances corresponding to 2.(c) is larger than the cubic sum for 2.(d) for $\cos\theta_{2,3} = 1$ and $\cos\theta_{2,3} = 0$. For $\cos\theta_{2,3} = -1$ the 2.(c) cubic sum is larger than the 2.(d) sum for $r_2 \lesssim 2r_3/3$ and $r_2 \gtrsim 3r_3/2$. In other words, the phase space for which scheme 2.(c) corresponds to Taylor expansions over smaller cubic distances than scheme 2.(d) is small. Thus, it is plausible that 2.(d) performs better.

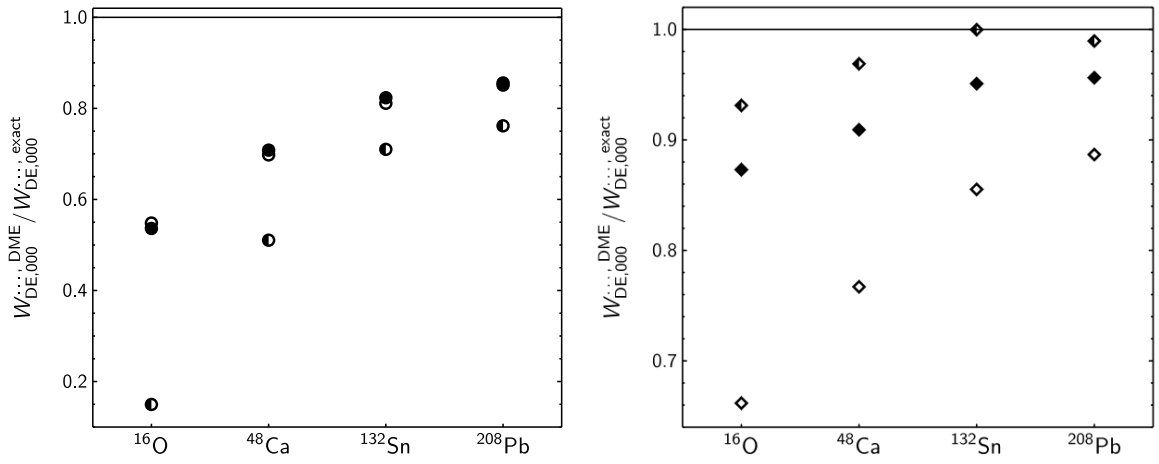

Figure 3.23: Ratios of DME-approximated and exact scalar-isoscalar double-exchange-energy contributions for different long-range parts of a two-pion-exchange three-nucleon interaction. Results are given for 4 closed-shell nuclei where the underlying orbitals are obtained from a self-consistent HF calculation with the SLy4 EDF. The left panel shows energies obtained with scheme 2.(a), the right panel energies obtained with 2.(d). Values are shown with filled symbols (●, ◆) for the ZZ interaction part, with half-filled ones (◐, ⬖) for $TYTY$, and with empty ones (○, ◇) for YY. All values are obtained with the PSA-DME with an isoscalar momentum scale.

Note that setting up a similar argument for LR SE is not straightforward because there both local and non-local densities are Taylor expanded and it is not obvious if these expansions are of equal importance. The observation that 1.(a) does much better than 1.(b) suggests that schemes in which local densities are expanded as little as possible are preferable for LR SE.

When splitting up the LR SE energies further into the different interaction parts as in Eq. (3.128), scheme 1.(a) is consistently better than 1.(b) for all parts. Interestingly, for double exchange the scheme quality depends on the considered interaction part, which have different radial and angular dependences, see Eqs. (3.123), (3.125), and (3.127). This is shown in Fig. 3.23, of which the left panel shows how well the DE energy for the different interaction parts is reproduced with scheme 2.(a), the right panel shows the same for 2.(d). In the former case, the exact energy due to $TYTY$ is most poorly reproduced, while in the latter case this term works best. For 2.(b) (not shown), $TYTY$ energies are reproduced better than ZZ, but worse than YY. These observations demonstrate that the quality of expansion schemes found here might not directly carry over to three-body forces of other form or even only forces of the same form with different LECs.

We now switch to the intermediate-range terms. For these, the ratios of DME-approximated and exact exchange energies are shown in Fig. 3.24. Scheme 3.(b) performs clearly better than the other ones and does well even for ^{16}O. As for LR SE, the best scheme does not involve an expansion of the local density. This also applies to 3.(a), but the angle average in its DME leads to the observed energy underestimation.

We now consider the total scalar-isoscalar Fock energy from intermediate- and long-range force parts combined. In Fig. 3.25 we show the ratios between DME-approximated and exact exchange energies for three different expansion scheme combinations. These are:

- the "Navarro Pérez" combination: This is used in the EDFs of Ref. [140] with the expressions obtained in Ref. [149]. It consists of schemes 1.(a), 2.(a), and 3.(a).

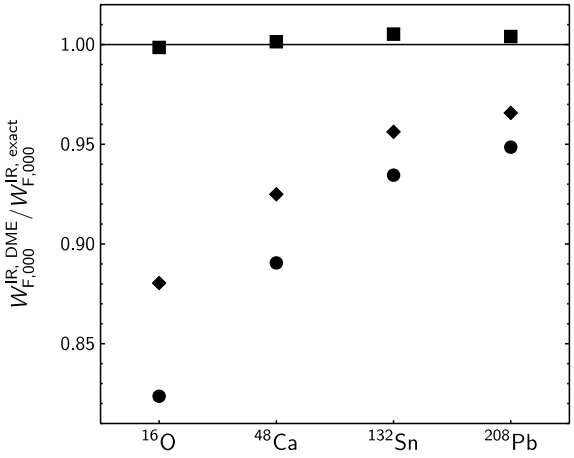

Figure 3.24: Ratios of DME-approximated and exact scalar-isoscalar exchange-energy contributions for the intermediate-range parts of a two-pion-exchange three-nucleon interaction. Results are given for 4 closed-shell nuclei where the underlying orbitals are obtained from a self-consistent HF calculation with the SLy4 EDF. Values are shown with circles (●) for scheme 3.(a), with squares (■) for scheme 3.(b), and with diamonds (◆) for scheme 3.(d). All values are obtained with the PSA-DME with an isoscalar momentum scale. For PSA-DME, schemes 3.(b) and 3.(c) are identical.

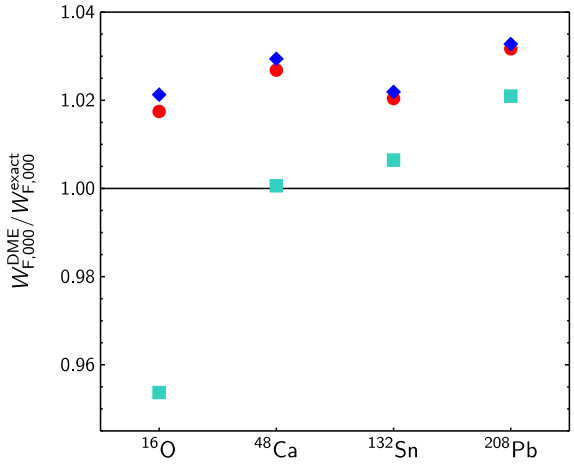

Figure 3.25: Ratios of DME-approximated and exact scalar-isoscalar exchange-energy contributions for the combination intermediate-range and long-range parts of a two-pion-exchange three-nucleon interaction. Results are given for 4 closed-shell nuclei where the underlying orbitals are obtained from a self-consistent HF calculation with the SLy4 EDF. Values are shown with red circles (●) for the "Navarro Pérez" scheme combination, with turquoise squares (■) for the "consistent" combination, and with blue diamonds (◆) for the "best scheme per term" combination. All values are obtained with the PSA-DME with an isoscalar momentum scale.

- the "consistent" combination, which consists of the schemes where OBDMs are expanded about their midpoints and all local densities are expanded about $\mathbf{x}_1$. These are schemes 1.(a), 2.(c), and 3.(c). Remember that for PSA-DME 2.(c) equals 2.(b) and 3.(c) equals 3.(b).

- the "best scheme per term" combination. For this the individually best schemes as obtained above are used, namely 1.(a), 2.(d), and 3.(b).

For all schemes the deviations to the exact scalar-isoscalar energies are at most at the few-percent level. Except for the light ^{16}O nucleus, the "consistent" combination performs best. Both other combinations overestimate the exact energies always by about 2 to 3 %. Somewhat surprisingly, the "best scheme per term" combination performs least well (except in ^{16}O). This is because the errors for the different terms add up in an unfavorable fashion as LR DE is attractive, while LR SE and IR exchange are repulsive. On the other hand, errors turn out to cancel almost fully for the "consistent" scheme in ^{48}Ca and ^{132}Sn. Note that the LR SE contribution is typically about an order of magnitude larger than the other two.

As in the NN case using an isoscalar momentum scale for approximating scalar-isovector energies does not work as well as for scalar-isoscalar energies. For instance, for scheme 1.(a) in ^{132}Sn the ratio $W^{\text{LR, DME}}_{\text{SE,011}}/W^{\text{LR, exact}}_{\text{SE,011}} \approx 0.89$, while $W^{\text{LR, DME}}_{\text{SE,000}}/W^{\text{LR, exact}}_{\text{SE,000}} \approx 1.02$. However, similar to the NN case, scalar-isovector contributions are in size about two orders of magnitude smaller than the scalar-isoscalar contributions, so that the less accurate reproduction of the energies involving isovector OBDM parts does not have a significant effect. This holds at least for bulk properties such as total energies but might be different when looking at non-bulk quantities.

3.6 Note on expansions of vector parts of one-body density matrices

Up to now we discussed only density-matrix expansions for the scalar part of the OBDM. Existing DME variants for the vector part include the NV- [168, 169], PSA- [135, 145], and DT-DME [170]. While the relative quality of the reproduction of the exact energies when applying these DMEs is worse for vector than for scalar energies, the vector part normally contributes only very little to the total energy as alluded to in Sec. 3.1. Thus, overall, the absolute error induced by using a DME for the scalar parts is typically much larger than the error induced from the vector ones. This is explicitly demonstrated for instance in Ref. [170]. This also explains why there has been much less focus on developing approximations for the vector part of the OBDM than for the scalar part.

For the same reason, we do not investigate DMEs for the vector parts of OBDMs in this work. We just note here that because the vector part of the OBDM is not a bulk quantity unlike the scalar part, different aspects may be considered when constructing an approximation. For instance, the anisotropy of the local momentum distribution becomes important. A variant of the PSA-DME has been developed which takes this explicitly into account [135, 171]. Note that even the simplified PSA-DME performs better at second order for the vector OBDM parts than NV- and DT-DME [170].

3.7 Summary and guidance for ab initio energy density functionals

Density-matrix expansions allow to approximate off-diagonal OBDMs in terms of (quasi-)local densities by factorizing the nonlocality into universal functions. Therefore, they can be used

to convert exchange energies from (realistic) nuclear interactions into a form corresponding to a local EDF. In this Chapter, we have carried out a detailed re-examination of DMEs and compared several zeroth- and second-order DMEs for scalar parts of OBDMs, focusing on the accurate non-self-consistent reproduction of exact exchange energies in closed-shell nuclei.

In general, all considered DMEs approximate the investigated NN exchange energies very well and different DME choices generally lead to tolerable variations. Of those DMEs that do not lead to more than two derivatives in any EDF term (like conventional Skyrme EDFs) we find best energy reproduction for the Slater approximation, although locally it approximates the energy integrands worse than second-order DMEs. When allowing for EDF terms with more than two derivatives, but still using only the standard Skyrme densities, one can also employ the full-square DMEs. These perform better than their truncated-square counterparts and the ones that use k_{FC} as their momentum scale. Overall we find best results for the SVCK^2- and MG-DMEs, although the latter yields the wrong INM limit. If necessary, one can obtain even better results by deviating from the DME approach in a narrow sense and combining different DME variants as exemplified in Sec. 3.4.4.

Regarding a good reproduction of scalar-isovector energies we find that it is crucial to treat neutrons and protons separately in DMEs. Using a single isoscalar momentum scale can lead to results wrong by more than 50%, though the effect on the total exchange energy is very small due to the small absolute size of isovector contributions.

For 3N forces even more choices have to be made regarding the DME than in the NN sector. Again, overall, the different schemes approximate the investigated exchange energies well. Except for light systems we find that the "consistent" expansion scheme performs best, although partially benefiting from cancellation of errors.

The findings of this Chapter are robust in the sense that they hold along the entire nuclear mass range, are confirmed also for less realistic orbital shapes, and are valid for different regulators and interaction ranges (except for very-long-range interactions, see Sec. 3.4.1). All these results are based on non-self-consistent tests and should therefore be regarded as provisional. For instance, it is at this stage unclear how local errors in the reproduction of exchange-energy integrands (e.g., see Slater approximation in Fig. 3.4) influence the results of the self-consistency loop in an EDF calculation of nuclei. Hence, one of next steps is to implement the findings of this work into EDFs like the ones discussed in the next Chapter.

However, our findings indicate that DMEs work very well for nuclear NN and 3N interactions with respect to approximating (bulk) exchange energies with high accuracy. Hence, we believe the present findings suggest the EDF improvement coming from an enhanced DME treatment will be minor, especially considering that the Skyrme couplings get refitted after incorporating the DME in the approach discussed in this thesis. Therefore, in the construction of the EDFs detailed in Ch. 4, we stick to the DME choices made in previous work, Ref. [140].

If fine (local) details matter or very high accuracy is needed, several refinement possibilities exist as shown here. In general, EDF practitioners can test the performance of the DME variant of their choice by switching to one of the other variants discussed here. If the results are quantitatively very similar, this suggests that further EDF improvements need to come from elsewhere, and not from DME improvements. Such self-consistent tests of different DME variants are not carried out in the present work. In addition, we did not test DMEs for vector parts of the OBDM and did not consider DME terms with an odd number of derivatives that are relevant in not-time-reversal-invariant systems. These topics are left for future investigations.

4

Semi-phenomenological hybrid energy density functionals

One approach to combining ab initio approaches to nuclear structure and DFT is given by a semi-phenomenological hybrid strategy for building EDFs. This strategy has led to promising results [140] but requires further investigation. We discussed the general idea of this approach and the motivation behind it in Sec. 1.4. In one sentence the idea can be summarized as extending a traditional Skyrme EDF structure by long-range pion-exchange terms derived from chiral EFT at the HF level.

The chiral Fock contributions are included in terms of a DME. Our results obtained in Ch. 3 put the DME applicability for long-range pion contributions on a solid footing, showing that different DME choices generally lead to tolerable variations. Therefore, we stick here to the choices made in Ref. [140] regarding the DME implementation. This is despite isovector contributions and some 3N terms not being well reproduced. However, these are small and therefore are not expected to be of concern at the present accuracy levels.

In this Chapter we turn our attention to the construction and optimization of functionals according to the hybrid strategy. We do this by generating the GUDE family of functionals, which includes several improvements and corrections compared to the earlier work of Ref. [140]. We begin by discussing the structure of the EDFs including the chiral contributions in Sec. 4.1. Nuclear properties are determined from the functionals by solving the corresponding HFB equations. The numerical setup is discussed in Sec. 4.2, where we also elaborate on the parameter optimization that is crucial to obtain a quantitatively successful EDF. We discuss which parameters are optimized, the used experimental data set, and the optimization algorithm. The results of the optimizations are presented in Sec. 4.3. We give the obtained GUDE parametrizations and investigate their performance by comparing against experimental data for even-even nuclei. In particular, we construct a GUDE variant which reproduces the main improvements found in this work by adding only a minimal number of terms arising from pion exchanges. Section 4.4 contains a detailed analysis of the order-by-order behavior of the functionals in the GUDE family. It turns out that the relevance of terms in our approach does not agree with naive expectations based on the power counting employed in chiral EFT. We investigate the reasons for this behavior. We end by summarizing our findings in Sec. 4.5.

Note that the contents of this Chapter have in large parts been published as Ref. [151].

4.1 Form of the energy density functionals

The EDFs we construct in this work can be split into six parts according to

$$E = E_{\mathrm{H}}^{\chi} + E_{\mathrm{F}}^{\chi} + E_{\mathrm{Skyrme}} + E_{\mathrm{pair}} + E_{\mathrm{Coulomb}} + E_{\mathrm{kin}} \,. \tag{4.1}$$

The conventional part of the EDFs consists of the latter four terms, which we discuss in Sec. 4.1.1.

In Sec. 4.3 we construct a conventional functional, below labelled as "no chiral", that contains only these four terms and serves as a reference functional for comparing the performance of the other EDFs that we construct following the same optimization protocol. These additionally contain the first two terms in Eq. (4.1), E_{H}^{χ} and E_{F}^{χ}, which represent the Hartree and Fock energy from pion exchanges, respectively. The expressions for the pion exchanges which enter the definitions of E_{H}^{χ} and E_{F}^{χ} are taken directly from interactions derived from chiral EFT at different orders, see Sec. 4.1.2. Because the low-energy constants of the pion exchanges are determined from few-body data [211] and are not adjusted in the present work, the additional inclusion of these terms does not lead to an increase in the number of adjustable functional parameters. See Secs. 4.1.3 and 4.1.4 for details regarding the pion Hartree and Fock terms.

While the structure of the functionals constructed here agrees with the one from Ref. [140], we introduce several changes and improve various aspects in the construction and optimization of the functionals compared to that work. These changes, stated in detail in the following Sections, are mostly driven by the idea to enable a cleaner comparison of the functionals constructed at (different) chiral orders.

4.1.1 Conventional parts

Here we discuss the parts of the GUDE structure that corresponds to a conventional Skyrme EDF. The Skyrme part itself reads

$$E_{\mathrm{Skyrme}} = \sum_{t=0,1} \int \mathrm{d}\mathbf{R} \left[C_t^{\rho\rho}(\rho_0)\rho_t^2 + C_t^{\rho\tau}\rho_t\tau_t + C_t^{\rho\Delta\rho}\rho_t\Delta\rho_t + C_t^{\rho\nabla J}\rho_t\boldsymbol{\nabla}\cdot\mathbf{J}_t + C_t^{JJ}J_{t,ab}J_{t,ab} \right] , \tag{4.2}$$

where

$$C_t^{\rho\rho}(\rho_0) = C_{t0}^{\rho\rho} + C_{tD}^{\rho\rho}\rho_0^{\gamma} \,. \tag{4.3}$$

Summations over spacial indices a, b are implied. The coupling constants $C_{t0}^{\rho\rho}$, $C_{tD}^{\rho\rho}$, $C_t^{\rho\tau}$, $C_t^{\rho\Delta\rho}$, $C_t^{\rho\nabla J}$, C_t^{JJ} and the exponent γ constitute parameters that are adjusted to data as described in Sec. 4.2.3. In Eq. (4.2), we have suppressed the dependence on the position $\mathbf{R}$ of the (quasi-)local densities. They read [83, 213]

$$\rho_t(\mathbf{R}) = \rho_t(\mathbf{R},\mathbf{R}) \,, \tag{4.4}$$

$$\tau_t(\mathbf{R}) = \boldsymbol{\nabla}\cdot\boldsymbol{\nabla}'\rho_t(\mathbf{R},\mathbf{R}')\big|_{\mathbf{R}'=\mathbf{R}} \,, \tag{4.5}$$

$$J_{t,ab}(\mathbf{R}) = -\frac{\mathrm{i}}{2}\big(\nabla_a - \nabla'_a\big)s_{t,b}(\mathbf{R},\mathbf{R}')\Big|_{\mathbf{R}'=\mathbf{R}} \tag{4.6}$$

$$\mathbf{J}_t(\mathbf{R}) = \varepsilon_{abc} J_{t,ab}(\mathbf{R}) \mathbf{e}_c \,, \tag{4.7}$$

where $\mathbf{e}_c$ is the unit vector in the Cartesian direction c and the different OBDM parts (ρ_t, $\mathbf{s}_t$) were introduced in Eqs. (3.11) to (3.14). The (quasi-)local densities are referred to as density ρ, kinetic density τ, spin-current tensor $\underline{\underline{J}}$, and spin-orbit current (or vector spin current) $\mathbf{J}$.

Since we only apply our EDFs for calculations of even-even nuclei, which are assumed to be time-reversal invariant, time-odd densities are not taken into account in the construction. The Skyrme structure given in Eq. (4.2) agrees with the one used in Ref. [112, 140]. It is generalized compared to EDFs that are truly derived from an underlying Skyrme interaction. One can convert it into notation used for those EDFs by applying the formulas given e.g. in Refs. [83, 173] to convert the couplings C_t^{uv} into t_i, x_i, W_0 parameters. Note that the tensor part of E_{Skyrme} corresponds to the case of a Skyrme force with only central and no tensor parts, cf. Ref. [213].

Within the HFB framework, the pairing contribution to our EDFs is given in the mixed-pairing prescription [214] as

$$E_{\text{pair}} = \frac{1}{4} \sum_{q=\text{n,p}} \int \mathrm{d}\mathbf{R}\, V_0^q \left[1 - \frac{1}{2} \frac{\rho_0(\mathbf{R})}{\rho_s} \right] \tilde{\rho}_q^2(\mathbf{R}) \,, \tag{4.8}$$

where $\rho_s = 0.16$ fm^{-3} is chosen as the empirical saturation density, which is approached in the center of heavy nuclei, so that pairing is somewhat weakened in the center [83, 214]. The pairing densities $\tilde{\rho}_q(\mathbf{R})$ are related to the pairing tensor via [173]

$$\tilde{\rho}_q(\mathbf{R}) = -2 \sum_\sigma \sigma \kappa_q(\mathbf{R}\sigma, \mathbf{R} - \sigma) \,. \tag{4.9}$$

The pairing tensor can be written as [173]

$$\kappa_q(\mathbf{R}\sigma, \mathbf{R}'\sigma') = \langle \Phi | a_{q,\mathbf{R}',\sigma'} a_{q,\mathbf{R},\sigma} | \Phi \rangle \ , \tag{4.10}$$

cf. Eq. (2.68).

The neutron and proton pairing strengths V_0^{n} and V_0^{p} are adjusted to data as described in Sec. 4.2.3. Because of the zero range of the underlying effective pairing force, a cutoff of $E_{\text{cut}} = 60$ MeV to truncate the quasiparticle space is employed. This cutoff was missing in the implementation of Ref. [140]. Thus, in that work the quasiparticle space was truncated implicitly only, via the finite size of the employed basis.

The Coulomb energy is obtained here as in Refs. [102, 112, 140, 215]: the Hartree term is calculated exactly using the Gaussian substitution method [216, 217] and the exchange term is calculated with the Slater approximation [174]; see Ref. [218] for an assessment of the accuracy of these methods. Overall, the Coulomb contribution reads [196]

$$E_{\text{Coulomb}} = -\frac{3e^2}{4} \int \mathrm{d}\mathbf{R} \left(\frac{3}{\pi} \right)^{1/3} \rho_p(\mathbf{R})^{4/3} + \frac{e^2}{2} \int \mathrm{d}\mathbf{R} \mathrm{d}\mathbf{R}' \, \frac{\rho_p(\mathbf{R}) \rho_p(\mathbf{R}')}{|\mathbf{R} - \mathbf{R}'|} \,. \tag{4.11}$$

We use $e^2 = 1.439978408596513$.

The kinetic energy is given by

$$E_{\text{kin}} = \int \mathrm{d}\mathbf{R} \, \frac{\hbar^2}{2m} \tau_0(\mathbf{R}) \,, \tag{4.12}$$

with $\hbar^2/(2m) = 20.73553$ MeV fm^2.

4.1.2 Chiral interactions

For the construction of the EDFs we consider pion exchanges at different orders in the chiral expansion up to N^{2}LO both with and without the explicit inclusion of intermediate Δ isobars as well as with and without 3N forces. Chiral EFT interactions contain pion exchanges and contact interactions. We take only the finite-range parts of the pion exchanges explicitly into account.[1] Expressions for the corresponding interaction terms in coordinate space are given in Refs. [140, 149]. The low-energy constants that appear are taken from the determination of Ref. [211] (columns "Q^2, no Δ" and "Q^2, fit 1" of Table 1 therein). Note that we use $g_A = 1.27$ and $h_A = 3g_A/\sqrt{2}$ as chosen in Ref. [211]. The previous implementation [140] used the Fock coefficient functions derived in Ref. [149] for which the slightly inconsistent combination of $g_A = 1.29$ with low-energy constants from Ref. [211] had been considered. The finite-range interactions are regularized by multiplying them with the local regulator function

$$f(r) = \left[1 - \exp\left(-\frac{r^2}{R_c^2}\right)\right]^n , \tag{4.13}$$

where we choose $R_c = 1.0$ fm and $n = 6$ (cf. [25]). Investigating the choice of the regularization scheme is left for future work.

Contact interactions as well as correlations involving pions beyond the HF level are assumed to be effectively captured by the EDFs by adjusting the parameters of E_{Skyrme} and E_{pair} to data from finite nuclei.

4.1.3 Chiral long-range Hartree terms

The Hartree terms from the pion exchanges are included essentially exactly by evaluating the corresponding integrals. Since we consider only even-even nuclei, the spin density vanishes due to time-reversal symmetry so that only the central part of the NN interactions contribute and Eq. (2.52) reduces to

$$E_{\text{H}}^{\chi} = \frac{1}{2}\sum_{t=0,1}\int \mathrm{d}\mathbf{R}\mathrm{d}\mathbf{r}\, V_t(r)\rho_t\left(\mathbf{R}+\frac{\mathbf{r}}{2}\right)\rho_t\left(\mathbf{R}-\frac{\mathbf{r}}{2}\right). \tag{4.14}$$

To make use of the capability of `HFBTHO`, which uses many analytic properties of Gaussian matrix elements in an HO basis [219], to solve the HFB equations for potentials given by sums of Gaussians [220], we approximate the central chiral potentials as

$$V_0(r) = V_C(r) \to \tilde{V}_C(r) = \sum_{i=1}^{N}\left(W_i - \frac{H_i}{2}\right)\mathrm{e}^{-r^2/\mu_i^2}, \tag{4.15}$$

$$V_1(r) = W_C(r) \to \tilde{W}_C(r) = -\sum_{i=1}^{N}\frac{H_i}{2}\mathrm{e}^{-r^2/\mu_i^2}. \tag{4.16}$$

A similar idea was implemented in Ref. [221]. Together with $B_i = M_i = 0$ (which do not contribute here due to time-reversal invariance of the considered systems) Eqs. (4.15) and (4.16)

[1] For the 3N forces, we do not include one-pion-exchange terms, which consist of both a pion exchange and a contact interaction. This is in agreement with the choice of Refs. [140, 149].

correspond to a Gogny-like interaction,

$$V_G = \sum_{i=1}^{N} (W_i + B_i P_\sigma - H_i P_\tau - M_i P_\sigma P_\tau) \mathrm{e}^{-r^2/\mu_i^2} \,. \tag{4.17}$$

Note that in Eqs. (4.15) to (4.17) we correct several mistakes compared to Eqs. (30) to (33) of Ref. [140]. The wrong equations in Ref. [140] led to an incorrect implementation of the Hartree terms in the functionals constructed therein. This is because the chiral potentials were approximated by Gaussians according to the equations of Ref. [140] but the implementation into the functionals follwed the correct equations of Ref. [220].

To reproduce the behavior of the regulator [Eq. (4.13)] at the origin, the conditions

$$H_N = -\sum_{i=1}^{N-1} H_i \,, \qquad\qquad W_N = -\sum_{i=1}^{N-1} W_i \tag{4.18}$$

are imposed. The remaining free parameters W_i, H_i, μ_i are obtained by a fitting routine.

As in Ref. [140], $N = 5$ Gaussians are used here as a compromise between accuracy of the approximation and computational requirements for evaluating and storing the resulting integrals [222]. The Gaussians used in Ref. [140] were obtained by simultaneously fitting all 13 parameters for the isoscalar V_C and isovector W_C potentials. Here, we fit first only the 9 parameters for the isoscalar potential V_C since it contributes significantly more to the energy of finite nuclei than its isovector counterpart. We keep the resulting Gaussian widths μ_i fixed for the subsequent fitting of the remaining 4 parameters of the isovector potential W_C. We obtain the parameters of the Gaussians by χ^2 minimizations where the loss functions are given by

$$\chi^2 = \sum_r \Big\{ r^2 \Big[\tilde{V}_t(r) - V_t(r) \Big] \Big\}^2 \,, \tag{4.19}$$

which are evaluated on an evenly spaced grid from $r = 0$ to 8 fm with step width 0.125 fm. We include the r^2 prefactor in the definition of the χ^2 to account for the increased importance of larger r due to the presence of the volume element in the Hartree energy, Eq. (4.14). This factor had not been included in the determination of the Gaussian parameters in Refs. [140, 222]. We provide the Gaussian parameters obtained in the new fit in Tab. A.1 in the Appendix.

In Figs. 4.1 and 4.2 we plot $r^2[V_t(r) - \tilde{V}_t(r)]$ including contributions up to including N^{2}LO in the chiral expansion (without explicitly resolved Δ excitations). The new fitting strategy improves the fit of V_C without a significant degradation in fitting W_C. When evaluating the Hartree energy expectation value in ^{208}Pb the difference between the value obtained with the exact and the approximated potential at N^{2}LO is about 5 MeV (on a total Hartree energy of about 4000 MeV) with the Gaussian parameters obtained in this work. This is a significant improvement over the difference of 37 MeV obtained with the Gaussian parameters of Refs. [140, 222]. Similar improvements are obtained for the fits of the potentials at other chiral orders. For these comparisons the underlying single-particle orbitals were generated from a self-consistent HF calculation with the SLy4 EDF [195] using the code `HOSPHE` [197].

Note that it is not clear if and how the observed improvements translate into improvements of the constructed EDFs. This is because the Skyrme parameters are fitted to data after adding the terms originating in the chiral potentials and this fitting can (partly) compensate the errors from the non-perfect Gaussian approximations. For the same reason it is also hard to

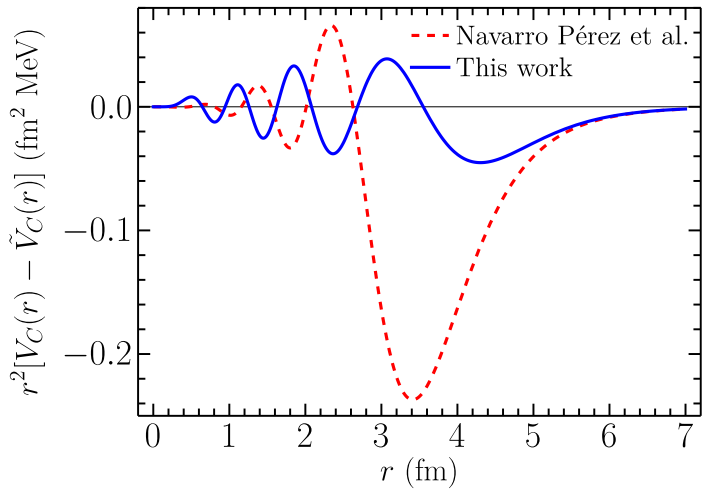

Figure 4.1: r^2-weighted difference between isoscalar central potential at N^{2}LO in the chiral expansion and its approximations by sums of five Gaussians according to Eq. (4.15). Both the approximation of Refs. [140, 222] and the one obtained here are shown.

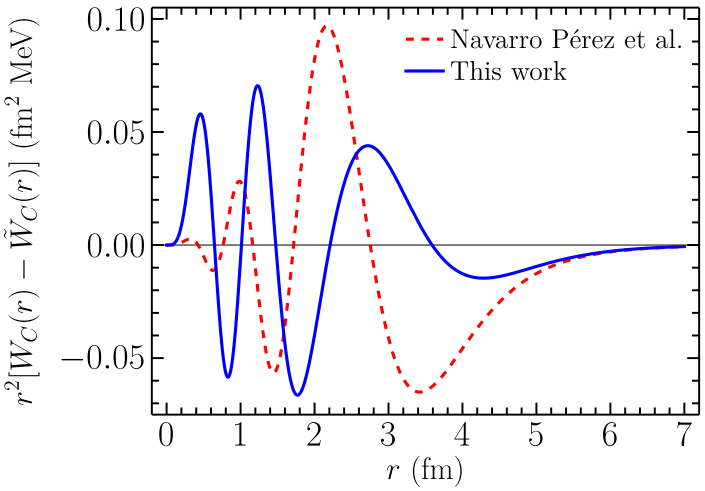

Figure 4.2: Same as Fig. 4.1 but for the isovector potential.

gauge a priori the impact of other changes we introduced compared to Ref. [140].

For later reference we introduce a notation for contributions arising when performing a Taylor expansion of one density entering Eq. (4.14) in the relative coordinate $\mathbf{r}$ about the argument of the other density. We write

$$E_{\mathrm{H}}^{\chi} = \sum_{t=0,1} \int \mathrm{d}\mathbf{R} \sum_{n=0}^{\infty} T_t^{\rho\Delta^n\rho} \rho_t(\mathbf{R}) \Delta^n \rho_t(\mathbf{R}) \tag{4.20}$$

with

$$T_t^{\rho\Delta^n\rho} = 2\pi \int \mathrm{d}r\, r^2 V_t(r) \frac{r^{2n}}{(2n+1)!}\,. \tag{4.21}$$

Finally, we recall that there are no Hartree contributions from the long-range parts of 3N forces at the orders we consider.

4.1.4 Chiral long-range Fock terms

The GUDE functionals include pion-exchange Fock contributions in a quasi-local form which is achieved by using a DME. One starts from the expression for the Fock energy, which is for local NN forces given in Eq. (2.53). As studied in Ch. 3, a DME allows to approximately rewrite the OBDM as a sum of terms in which the non-locality is factored out. After applying the DME and carrying out the traces and the integral in the non-locality $\mathbf{r}$ one obtains a quasi-local approximation for the Fock energy, which leaves only one integral to be carried out numerically. For the NN forces used here it reads [149]

$$E^{\chi}_{\mathrm{F,NN}} = \sum_{t=0,1} \int \mathrm{d}\mathbf{R} \Big\{ g_t^{\rho\rho}(\rho_0)\rho_t^2 + g_t^{\rho\tau}(\rho_0)\rho_t\tau_t + g_t^{\rho\Delta\rho}(\rho_0)\rho_t\Delta\rho_t + g_t^{JJ,2}(\rho_0)J_{t,ab}J_{t,ab} + g_t^{JJ,1}(\rho_0)[J_{t,aa}J_{t,bb} + J_{t,ab}J_{t,ba}] \Big\} . \tag{4.22}$$

As before we consider only terms that contribute in time-reversal invariant systems. Note that while Ref. [149] uses separate functions $g_t^{JJ,1}$ and $g_t^{JJ,3}$ multiplying $J_{t,aa}J_{t,bb}$ and $J_{t,ab}J_{t,ba}$, respectively, these turn out to be identical [135]. This is in agreement with the situation obtained for the Skyrme tensor force, cf. Ref. [223]. Note also that $J_{t,aa} \equiv 0$ when axial symmetry is conserved [166], which is the case for all calculations performed in this work. Equation (4.22) looks very similar to the Skyrme part of the functional, Eq. (4.2). However, in Eq. (4.22) the prefactors of the density bilinears (the g coefficient functions g_t^{uv}) are not constants (whose values are determined by fitting to data) but functions of the isoscalar density ρ_0 and are fixed once one picks a chiral interaction model and a DME variant.

From a computational point of view, using a DME does not provide a significant benefit when considering only chiral NN interactions,[2] but it is a suitable strategy to make the addition of 3N interactions feasible. For those interactions the equation for the Fock contributions is determined analogously to the NN case by starting from Eqs. (3.93) and (3.94) and reads [149]

$$\begin{aligned} E^{\chi}_{\mathrm{F,3N}} = \int \mathrm{d}\mathbf{R} \Big\{ & g^{\rho_0^3}(\rho_0)\rho_0^3 + g^{\rho_0^2\tau_0}(\rho_0)\rho_0^2\tau_0 + g^{\rho_0^2\Delta\rho_0}(\rho_0)\rho_0^2\Delta\rho_0 + g^{\rho_0(\nabla\rho_0)^2}(\rho_0)\rho_0\boldsymbol{\nabla}\rho_0\cdot\boldsymbol{\nabla}\rho_0 \\ & + g^{\rho_0\rho_1^2}(\rho_0)\rho_0\rho_1^2 + g^{\rho_1^2\tau_0}(\rho_0)\rho_1^2\tau_0 + g^{\rho_1^2\Delta\rho_0}(\rho_0)\rho_1^2\Delta\rho_0 + g^{\rho_0\rho_1\tau_1}(\rho_0)\rho_0\rho_1\tau_1 \\ & + g^{\rho_0\rho_1\Delta\rho_1}(\rho_0)\rho_0\rho_1\Delta\rho_1 + g^{\rho_0(\nabla\rho_1)^2}(\rho_0)\rho_0\boldsymbol{\nabla}\rho_1\cdot\boldsymbol{\nabla}\rho_1 \\ & + \rho_0\epsilon_{cab}\left[g^{\rho_0\nabla\rho_0 J_0}(\rho_0)\nabla_c\rho_0 J_{0,ab} + g^{\rho_0\nabla\rho_1 J_1}(\rho_0)\nabla_c\rho_1 J_{1,ab}\right] \\ & + \rho_1\epsilon_{cab}\left[g^{\rho_1\nabla\rho_1 J_0}(\rho_0)\nabla_c\rho_1 J_{0,ab} + g^{\rho_1\nabla\rho_0 J_1}(\rho_0)\nabla_c\rho_0 J_{1,ab}\right] \\ & + \rho_0\left[g^{\rho_0 J_0^2,1}(\rho_0)J_{0,aa}J_{0,bb} + g^{\rho_0 J_0^2,2}(\rho_0)J_{0,ab}J_{0,ab} + g^{\rho_0 J_0^2,3}(\rho_0)J_{0,ab}J_{0,ba}\right] \\ & + \rho_0\left[g^{\rho_0 J_1^2,1}(\rho_0)J_{1,aa}J_{1,bb} + g^{\rho_0 J_1^2,2}(\rho_0)J_{1,ab}J_{1,ab} + g^{\rho_0 J_1^2,3}(\rho_0)J_{1,ab}J_{1,ba}\right] \\ & + \rho_1\left[g^{\rho_1 J_0 J_1,1}(\rho_0)J_{1,aa}J_{0,bb} + g^{\rho_1 J_0 J_1,2}(\rho_0)J_{1,ab}J_{0,ab} + g^{\rho_1 J_0 J_1,3}(\rho_0)J_{1,ab}J_{0,ba}\right] \Big\} . \end{aligned} \tag{4.23}$$

In the actual HFB calculations with `HFBTHO` the g coefficients are approximated with

[2] This is because the NN Fock terms could also be incorporated essentially exactly in the same fashion as the Hartree terms. This is common practice for Gogny EDFs.

interpolation functions of the form

$$g_t^{uv}(\rho_0) \to \tilde{g}_t^{uv}(\rho_0) = \tilde{g}_t^{uv}(0) + \sum_{i=1}^{N} a_i \arctan(b_i \rho_0^{c_i})^i \,, \tag{4.24}$$

$$g^{uvw}(\rho_0) \to \tilde{g}^{uvw}(\rho_0) = \tilde{g}^{uvw}(0) + \sum_{i=1}^{N} a_i \arctan(b_i \rho_0^{c_i})^i \,, \tag{4.25}$$

where $N = 3$ and the coefficients $\tilde{g}_t^{uv(w)}(0), a_i, b_i, c_i$ are fitted separately for each g coefficient. For details on the interpolation see Ref. [140]. Note that Eq. (47) therein contains an error which is corrected in Eqs. (4.24) and (4.25) above.

In this work we stick to the choice of Refs. [140, 149] and use the (simplified) PSA-DME [135, 145] and the "Navarro Pérez" expansion scheme as discussed in Sec. 3.5 for the 3N forces. The DME is applied to the isoscalar and isovector parts of the one-body density matrix using an isoscalar momentum scale, which works well for the former, but not for the latter. However, the isovector Fock contributions are small and again we expect the Skyrme parameter fitting to partly compensate the errors. We leave the investigation of the impact of making different choices for the DME, discussed in Ch. 3, in the EDF construction for future work.

Note that some of the 3N Fock terms used in Ref. [140] were incorrect; these have been corrected in the present work. We provide the resulting interpolation parameters entering Eqs. (4.24) and (4.25) in Tabs. A.2 and A.3 and introduce the notation

$$w_t^{uv}(\rho_0) = C_t^{uv}(\rho_0) + \tilde{g}_t^{uv}(\rho_0) \tag{4.26}$$

for the combination of Skyrme coefficient and NN g coefficient function of the same kind. In addition, we use

$$W_t^{uv}(\rho_0) = C_t^{uv}(\rho_0) + T_t^{uv} + \tilde{g}_t^{uv}(\rho_0) + \tilde{g}^{\rho_0 u_t v_t}(\rho_0)\rho_0 \tag{4.27}$$

for the combination of Skyrme coefficient, Taylor-expanded Hartree contribution, as well as NN and 3N g coefficient functions of the same kind.

4.2 Numerical methods

4.2.1 Hartree-Fock-Bogoliubov calculations

We obtain nuclear ground states based on the EDFs described in the previous subsections by performing HFB calculations. By varying the EDF, Eq. (4.2), with respect to the single-particle orbitals in analogy to the derivation of the HF equations for density-dependent forces discussed in Sec. 2.3, one obtains the HFB equations for the GUDE functionals. They read [cf. Eq. (2.75)]

$$\begin{pmatrix} h & \tilde{h} \\ \tilde{h} & -h \end{pmatrix} \begin{pmatrix} U_i \\ V_i \end{pmatrix} = \begin{pmatrix} \varepsilon + \lambda & 0 \\ 0 & \varepsilon - \lambda \end{pmatrix} \begin{pmatrix} U_i \\ V_i \end{pmatrix} , \tag{4.28}$$

where we introduced the fields h and $\tilde{h}$. Here and below we suppress the dependence of the orbitals, densities, and fields on position $\mathbf{R}$ and spin for brevity. The pairing field is obtained

from the variation with respect to $\tilde{\rho}_q$ as

$$\tilde{h}_q = \frac{1}{2}V_0^q\left(1-\frac{1}{2}\frac{\rho_0}{\rho_s}\right)\tilde{\rho}_q\,, \tag{4.29}$$

where q depends on whether the field acts on the neutron or proton state. The field h, which belongs to the particle-hole part of the EDF, can be expressed in agreement with standard notation for Skyrme HFB equations [166, 167, 196] in terms of the effective mass field M, the HF field U,[3] the spin-orbit field B, and (for protons) the Coulomb field V_c:

$$h_q = -\boldsymbol{\nabla}M_q\boldsymbol{\nabla} + U_q + \frac{1}{2\mathrm{i}}(\boldsymbol{\nabla}_a\sigma_b B_{q,ab} + B_{q,ab}\boldsymbol{\nabla}_a\sigma_b) + \delta_{qp}V_c\,, \tag{4.30}$$

where Einstein summation convention is employed for the spacial indices.

We obtain M_q from varying the EDF with respect to τ_q:

$$M_q = \frac{\hbar^2}{2m} + \sum_{t=0,1}\left[S_{tq}w_t^{\rho\tau}(\rho_0)\rho_t + g^{\rho_t^2\tau_0}(\rho_0)\rho_t^2\right] + S_{1q}g^{\rho_0\rho_1\tau_1}(\rho_0)\rho_0\rho_1\,. \tag{4.31}$$

To keep the equations relatively compact we introduce the sign factor

$$S_{tq} = \frac{\partial\tau_t}{\partial\tau_q} = \begin{cases} -1 & \text{when } t=1 \text{ and } q=\mathrm{p}\ , \\ 1 & \text{else}\ , \end{cases} \tag{4.32}$$

which holds analogously for other kinds of densities.

From varying with respect to ρ_q we get

$$\begin{aligned} U_q = \sum_{t=0,1}\Big[& S_{tq}2w_t^{\rho\rho}(\rho_0)\rho_t + w_t^{\rho\rho}(\rho_0)'\rho_t^2 + S_{tq}w_t^{\rho\tau}(\rho_0)\tau_t + g_t^{\rho\tau}(\rho_0)'\rho_t\tau_t + S_{tq}2w_t^{\rho\Delta\rho}(\rho_0)\Delta\rho_t \\ & + g_t^{\rho\Delta\rho}(\rho_0)'\rho_t\Delta\rho_t + g_t^{\rho\Delta\rho}(\rho_0)'\rho_t\Delta\rho_0 + g_t^{\rho\Delta\rho}(\rho_0)''\rho_t(\boldsymbol{\nabla}\rho_0)^2 + S_{tq}C_t^{\rho\nabla J}\boldsymbol{\nabla}\cdot\mathbf{J}_t \\ & + g_t^{JJ,2}(\rho_0)'J_{t,ab}J_{t,ab} + g_t^{JJ,1}(\rho_0)'J_{t,ab}J_{t,ba} + S_{tq}\int \mathrm{d}\mathbf{R}'\,V_t(|\mathbf{R}-\mathbf{R}'|)\rho_t(\mathbf{R}')\Big] \\ & - \frac{1}{8}V_0^q\frac{1}{\rho_s}\tilde{\rho}_q^2 + \frac{\delta E^{\chi}_{\mathrm{F,3N}}}{\delta\rho_q}\,, \end{aligned} \tag{4.33}$$

where primes denote derivatives with respect to ρ_0. We abstain from explicitly stating the very lengthy result for $\delta E^{\chi}_{\mathrm{F,3N}}/\delta\rho_q$ that can be obtained similarly by applying functional derivative rules and do not show terms depending on $J_{t,aa}$, which vanish for axial symmetry [166].

Variation with respect to $J_{q,ab}$ gives rise to

$$\begin{aligned} B_{q,ab} = \sum_{t=0,1} S_{tq}\Big\{ & 2C_t^{JJ}J_{t,ab} + 2g_t^{JJ,2}(\rho_0)J_{t,ab} + 2g_t^{JJ,1}(\rho_0)J_{t,ba} + C_t^{\rho\nabla J}\rho_t \\ & + \rho_0\epsilon_{iab}g^{\rho_0\nabla\rho_t J_t}(\rho_0)\nabla_i\rho_t + \rho_1\epsilon_{iab}g^{\rho_1\nabla\rho_{1-t}J_t}(\rho_0)\nabla_i\rho_{1-t} \\ & + \rho_0 2\Big[g^{\rho_0 J_t^2,2}(\rho_0)J_{t,ab} + g^{\rho_0 J_t^2,3}(\rho_0)J_{t,ba}\Big] \\ & + \rho_1\Big[g^{\rho_1 J_0 J_1,2}(\rho_0)J_{1-t,ab} + g^{\rho_1 J_0 J_1,3}(\rho_0)J_{1-t,ba}\Big]\Big\}\,. \end{aligned} \tag{4.34}$$

[3] The HF field U (or U_q) is not to be confused with the upper component of the HFB orbital U_i.

Lastly, the Coulomb field reads

$$V_c = -e^2\left(\frac{3}{\pi}\right)^{1/3}\rho_p^{1/3} + e^2\int \mathrm{d}\mathbf{R}'\,\frac{\rho_p(\mathbf{R}')}{|\mathbf{R}-\mathbf{R}'|}\,. \tag{4.35}$$

For vanishing chiral contributions the fields given above agree with the usual results for a Skyrme interaction as given in Ref. [166] after identifying the representation of the Skyrme EDF in terms of couplings C_t^{uv} with the traditional notation using t_i, x_i, W_0 parameters. The conversion formulas are given e.g. in Refs. [83, 173, 224].

The HFB equations [Eq. (4.28)] are solved with the DFT code `HFBTHO` which expands the single-particle wavefunctions in a harmonic-oscillator basis in cylindrical coordinates [166, 217, 218, 220]. For calculations of ground states bases without axial deformation are used. In all cases the basis consists of 20 HO shells and the spherical frequency ω_0 of the HO basis is set according to the empirical formula $\omega_0 = 1.2 \times 41/A^{1/3}$ MeV [217] unless noted otherwise. The HFB equations are then solved by iteratively diagonalizing the HFB Hamiltonian in configuration space, while evaluation of the potentials and densities is performed in coordinate space [166]. The iterative procedure is carried out until either self-consistency is reached (determined in terms of the norm of the difference of the HFB matrix of subsequent steps being smaller than ε) or a certain number of steps have been carried out and the result is flagged as unconverged, see later for details. HFB solutions are obtained using the kick-off mode of `HFBTHO` in which an axial quadrupole deformation constraint is applied during at most the first 10 HFB iteration steps to guide the solution towards the desired local minimum, then the constraint is lifted [217, 220].

4.2.2 Note on symmetry projection

The axially symmetric HFB calculations carried out here break particle-number symmetry (see discussion in Sec. 2.4), rotational symmetry, and translational symmetry. In this work, we abstain from restoring any symmetries. Doing this exactly requires the use of computationally expensive frameworks.

Translational symmetry is commonly approximately restored by subtracting a center-of-mass correction (proportional to $1/A$) to the kinetic energy [83]. This works well for nuclei in the medium-mass regime and beyond. However, this approximate correction has several issues, see e.g., Refs. [102, 225]. In particular it causes conceptual problems for calculations of nuclear fission, where a nucleus splits into fragments, as it is not additive in particle number. Hence, the center-of-mass correction was dropped in the construction of the functionals of Refs. [102, 112, 140] and we also do not take it into account.

In Ref. [140], particle number projection was approximated with a variant of the Lipkin-Nogami prescription derived for a seniority-pairing interaction with an adjusted effective strength [226]. In Ref. [227] it was shown that this scheme compared well against the numerically expensive variation-after-projection scheme in well-deformed nuclei, but not near closed shells; see also Ref. [228]. In addition to the lack of consistency between the actual pairing interaction and the one used for the LN scheme, the LN scheme is not variational. For these reasons, we drop this prescription and work at the HFB level only. Note that the UNEDF1-HFB parameterization of the Skyrme EDF was also performed without the seniority-based LN scheme of its parent UNEDF1 and its performance was only slightly worse [79].

Rotational symmetry is also not restored here. It is known to add up to a few MeV of

correlation energy, in particular for very deformed states [78]. Such statements are made for a given EDF parametrization though. The missing restorations can therefore be expected to be partially compensated by the EDF parameter optimization that we discuss below.

Future development of this work's EDFs should nevertheless involve revisiting restoration of the broken symmetries. This is a topic of ongoing research due to the computational complexity of projection techniques and different issues thereof as mentioned above. See Ref. [18] for an overview.

4.2.3 Optimization of Skyrme and pairing parameters

E_{Skyrme} and E_{pair} contain in total 15 parameters C_t^{uv}, γ, and V_0^q which need to be determined from fitting to data. Note that E_{H}^{χ} and E_{F}^{χ} are free of adjustable parameters. Thus, the number of optimization parameters is the same for functionals constructed here with and without chiral terms. The volume parameters $C_{t0}^{\rho\rho}, C_{tD}^{\rho\rho}, C_t^{\rho\tau}$, and γ can be related to properties of infinite nuclear matter. Expressing the exponent γ in terms of INM parameters at saturation gives

$$\begin{aligned}\gamma =&\left\{-(K-K_{\text{fr}})-9\left(E-E_{\text{sat,fr}}+\frac{P_{\text{fr}}}{\rho_c}\right)+\frac{\hbar^2}{2m}\left[4\left(M_{\text{s}}^{*-1}-M_{\text{s,fr}}^{*-1}\right)-3\right]C\rho_c^{2/3}+A_\gamma(u_c)\right\}\\ &\Big/\left\{9\left(E-E_{\text{sat,fr}}+\frac{P_{\text{fr}}}{\rho_c}\right)+\frac{3\hbar^2}{2m}\left[2\left(M_{\text{s}}^{*-1}-M_{\text{s,fr}}^{*-1}\right)-3\right]C\rho_c^{2/3}+B_\gamma(u_c)\right\},\end{aligned} \tag{4.36}$$

where quantities indexed "fr" represent the contributions from the finite-range Hartree terms to the INM parameters (see Ref. [229]). P denotes the pressure of symmetric matter at saturation density, $C = 3/5 \cdot (3\pi^2/2)^{2/3}$, and $u_c = (3\pi^2\rho_c/2)^{1/3}/m_\pi$. The expressions for $A_\gamma(u_c)$ and $B_\gamma(u_c)$ are given in Appendix C of Ref. [148]. The equations for the other volume parameters can easily be obtained from the ones given in Ref. [148] by adding the respective contributions from the finite-range Hartree terms [229].

Proceeding in this way we express the volume parameters via saturation density ρ_c, saturation energy E, incompressibility of symmetric nuclear matter K, isoscalar effective mass M_{s}^*, symmetry energy at saturation density a_{sym}, its slope L_{sym}, and isovector effective mass M_{v}^*. As in previous works [102, 112, 140, 215] we do not optimize the isovector effective mass, which is known to be poorly constrained by typical data sets [215], but instead keep it fixed at its SLy4 value, $M_{\text{v}}^{*-1} = 1.249$. This leaves 14 parameters to be optimized.

Using INM properties at saturation density as optimization parameters instead of EDF volume parameters allows us to impose physically motivated constraints on these parameters and is expected to allow the GUDE functionals to also describe infinite matter reasonably well.[4] The bounds that we impose are not allowed to be violated in our optimization procedure. We take the same bounds as in Refs. [102, 112, 140, 215] except for K and L_{sym}. For the incompressibility K we extend the allowed range to [180, 260] MeV based on the analysis of Ref. [230] using different forces from chiral EFT, which obtained a range of [182, 262] MeV, and a study assessing the nuclear matter properties of Skyrme EDFs, which used [200, 260] MeV based on different experimental and empirical results [101]. For the slope parameter L_{sym}

[4] In finite nuclei, densities typically reach up to saturation density. Using constraints at much higher densities could be problematic because of the restricted density dependence of Skyrme EDFs, which might then lead to a significant deterioration of the description of finite nuclei. Note that the analysis of Ref. [101] seems to be in agreement with these considerations. The authors find that multiple Skyrme parametrizations do not pass a constraint employing information beyond twice saturation density despite them passing all other considered tests.

Table 4.1: Parameters optimized in this work and their bound constraints.

$\mathbf{x}$	lower bound	upper bound
ρ_c (fm^{-3})	0.15	0.17
E (MeV)	−16.2	−15.8
K (MeV)	180	260
M_{s}^{*-1}	0.9	1.5
a_{sym} (MeV)	28	36
L_{sym} (MeV)	30	80
$C_0^{\rho\Delta\rho}$	$-\infty$	∞
$C_1^{\rho\Delta\rho}$	$-\infty$	∞
$C_0^{\rho\nabla J}$	$-\infty$	∞
$C_0^{\rho\nabla J}$	$-\infty$	∞
C_0^{JJ}	$-\infty$	∞
C_1^{JJ}	$-\infty$	∞
V_0^{n}	$-\infty$	∞
V_0^{p}	$-\infty$	∞

Table 4.2: Characteristics of the components of the loss function. n_i is the number of data points for each data type i and w_i is the inverse weight. For the latter, all units are MeV except R_{p} which is in fm.

i	E_{sph}	E_{def}	Δ_{n}	Δ_{p}	R_{p}	E^*
n_i	29	47	7	6	28	4
w_i	1.95	0.227	0.0457	0.0703	0.0177	0.85

we use [30, 80] MeV based on the overlapping region of different experimental and theoretical constraints, see Refs. [231, 232]. Collectively we denote our set of optimization parameters as $\mathbf{x}$. The parameters and their ranges are summarized in Tab. 4.1.

They are determined by minimizing a loss function, which is given by a weighted sum of squared errors:

$$\chi^2(\mathbf{x}) = \sum_{i=1}^{D_T} \sum_{j=1}^{n_i} \left(\frac{s_{i,j}(\mathbf{x}) - d_{i,j}}{w_i} \right)^2 , \tag{4.37}$$

where $s_{i,j}(\mathbf{x})$ are the EDF predictions and $d_{i,j}$ the data. D_T is the number of different data types. In this work we consider ground-state energies of spherical (E_{sph}) and deformed (E_{def}) nuclei, neutron (Δ_{n}) and proton (Δ_{p}) odd-even staggerings, proton point radii (R_{p}), and fission isomer excitation energies (E^*), therefore $D_T = 6$. For every data type i we employ a different inverse weight w_i that represents the expected errors in describing the different observables [79, 233]. Rather than the somewhat arbitrary values set in Ref. [140], we choose for the weights the estimates determined from the Bayesian calibration of the UNEDF1 functional [234]; see Tab. 4.2 for the numerical values. This choice is justified by the fact that the data types contained in our fit data set are the same as for UNEDF1. In addition, the form of the functionals (at least for our reference EDF without contributions from chiral EFT) as well as the employed optimization protocol are similar. Thus, we consider those posterior estimates as good proxies also for the functionals considered here.

Table 4.2 also contains a brief overview of the experimental data $d_{i,j}$ considered as part of

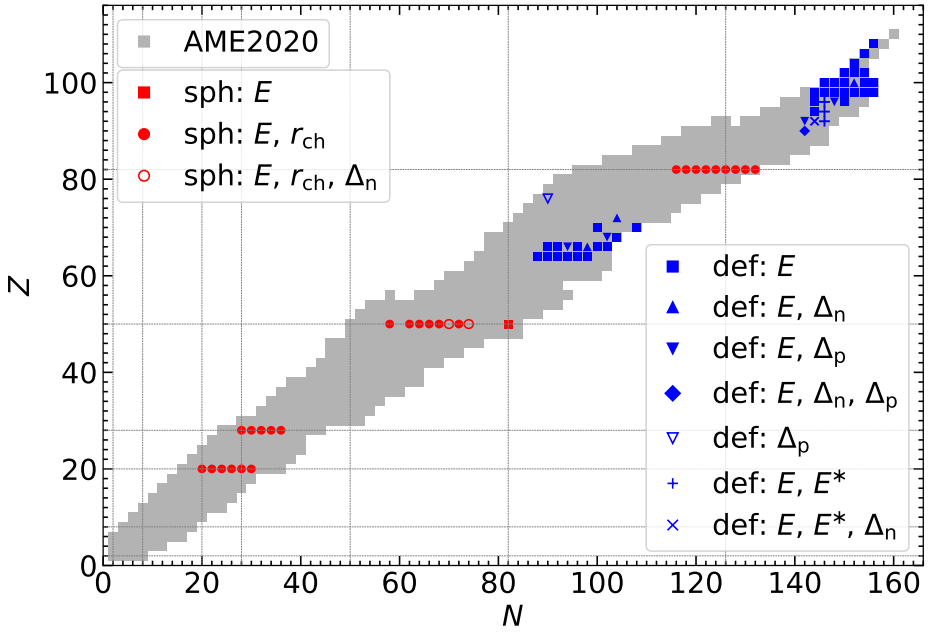

Figure 4.3: Experimental data used for optimization of EDF parameters. All even-even nuclei of which the ground-states binding energies are given in the 2020 atomic mass evaluation [235] (excluding evaluated masses) are depicted in gray. Nuclei included in the fit protocol are shown with different red and blue symbols depending on the considered data types.

the χ^2 and Fig. 4.3 shows in detail which data types are considered for which nuclei[5] and the used values are given in Tabs. A.4 to A.9. The experimental data is similar to the data used in Refs. [112, 140]. However, we exclude single-particle level splittings from the data set. These were introduced in Ref. [112] together with removing the restriction of $C_0^{JJ} = C_1^{JJ} = 0$ for the tensor part of UNEDF1 in an attempt to improve the description of nuclear shell structure. The reported standard deviations for the tensor coefficients were quite large and the observed improvement of the shell structure relatively small. Because the blocking calculations carried out to determine the single-particle structure are numerically expensive, we therefore decide to remove the the single-particle level splittings from the data set. With those exceptions, we consider the same data types for the same nuclei as in Refs. [112, 140]. The sources for the experimental data are listed in the following.

We determine nuclear ground-state energies E_{sph} and E_{def} (here collectively referred to as E) according to

$$E = -(E_{\mathrm{ato}} - E_{\mathrm{el}}) \tag{4.38}$$

from atomic binding energies E_{ato} collected in the 2020 atomic mass evaluation (AME) [235]. For the electronic binding energies we assume [235]

$$E_{\mathrm{el}} = \left(14.4381 Z^{2.39} + 1.55468 \times 10^{-6} Z^{5.35}\right) \mathrm{eV}\,. \tag{4.39}$$

Neutron odd-even staggerings are determined for a nucleus with Z protons and N neutrons

[5] In the data set ^{62}Ni and ^{64}Ni are assumed to be spherical. However, the global ground-state calculations discussed in Sec. 4.3.3 show that for the GUDE functionals their ground states are deformed. The differences in energy between the spherical and the deformed solutions are not large (at most about 0.4 MeV). Regardless, in the future the classification of these nuclei in the optimization data set should be adjusted.

from the experimental ground-state energies according to [112]

$$\Delta_{\mathrm{n}}(Z,N) = \frac{1}{2}\left[\Delta_{\mathrm{n}}^{(3)}(Z,N-1) + \Delta_{\mathrm{n}}^{(3)}(Z,N+1)\right] \tag{4.40}$$

with the three-point mass indicator [228]

$$\Delta_{\mathrm{n}}^{(3)}(Z,N) = \frac{1}{2}[2E(Z,N) - E(Z,N-1) - E(Z,N+1)]\,. \tag{4.41}$$

Proton odd-even staggerings are determined analogously.

We use data for charge radii r_{ch} from Ref. [236]. For ^{56}Ni, which had not been measured yet, we take the value determined in Ref. [237]. The charge radii are converted into proton point radii according to [140]

$$R_{\mathrm{p}}^2 = r_{\mathrm{ch}}^2 - r_{\mathrm{p}}^2 - \frac{N}{Z} r_{\mathrm{n}}^2\,, \tag{4.42}$$

where we use the 2018 Committee on Data of the International Science Council recommended value for the proton charge radius $r_{\mathrm{p}} = 0.8414$ fm [238] and the 2022 Particle Data Group average for the neutron charge radius square $r_{\mathrm{n}}^2 = -0.1155$ fm^2 [239].

For the fission isomer energies we use as before the values collected in Ref. [240].

The EDF predictions $s_{i,j}(\mathbf{x})$ are obtained for given values of the parameters $\mathbf{x}$ at every optimization step by solving HFB equations with the setup explained in Sec. 4.2.1. The value of the quadrupole moment used to initialize the kick-off mode is computed by assuming a ground-state deformation of $\beta_2 = 0.3$ for deformed nuclei and a fission isomer deformation of $\beta_2 = 0.6$. See Ref. [234] for a detailed analysis on the role of the quadrupole values concluding that sensitivity to the precise values is quite low. In total, 81 HFB calculations are performed at every optimization step: 77 for the ground states of the nuclei in the data set, for which no axial basis deformation is used, and 4 for the fission isomers, which are calculated with an axial basis deformation parameter of $\beta = 0.4$. The calculations are initialized from the solution of the Schrödinger equation for a Woods–Saxon potential whose deformation is chosen in agreement with the basis deformation. If an HFB calculation does not converge after 500 iteration steps, it is aborted and flagged as unconverged.

We use the average neutron (proton) HFB pairing gap as EDF prediction for neutron (proton) odd-even staggering. While this is an approximation [241], actually determining odd-even mass differences would require calculating ground states of odd nuclei for which additional EDF terms enter due to broken time-reversal invariance and the determination of odd ground states via blocking calculations is much more involved than calculating ground states of even-even nuclei [242].

To find the parameter set $\mathbf{x}$ for which $\chi^2(\mathbf{x})$ is minimized within the bound constraints discussed above we employ the derivative-free optimization algorithm `POUNDERS` [243, 244]. It solves the nonlinear least squares problem by constructing a quadratic model for each term in the χ^2. The resulting quadratic model for the χ^2 is assumed to be valid only within a certain trust region. Minimizing the model in this region yields a solution candidate point. Then new quadratic models are constructed around this point and the trust region is updated. In this way an iterative optimization procedure is obtained, see Ref. [244] for details on the algorithm. `POUNDERS` needs significantly fewer iteration steps to converge to a minimum than a conventional Nelder-Mead optimization routine [215, 243].

At every iteration step, the trust region is essentially a hypersphere around the current

candidate point (in a space where the different optimization parameters are scaled as described in Ref. [243]). The hypersphere's radius shrinks when getting closer to the minimum. Sometimes `POUNDERS` shrinks this radius too quickly despite the current candidate point not being sufficiently close to the optimum yet. In such scenarios restarting `POUNDERS` from the current candidate point helps to accelerate the convergence and allows it to possibly jump to another valley in the parameter landscape. Therefore, we restart the optimization every 150 iteration steps and in doing so set the trust region radius back to its initial value of $\Delta_0 = 0.1$.

We use the parameter sets obtained at different orders in the chiral expansion in Ref. [140] as starting points for the optimization of the corresponding GUDE functionals constructed here. For the reference "no chiral" functional we start the optimization from the UNEDF2 parameters [112]. For a few EDFs we carry out the optimizations more than once employing also other Skyrme parametrizations as starting points (namely SLy4 [195], SkM* [245], and NRAPR [246]).[6] We find that if those optimization runs converge, they converge to the same solutions as the other optimizations. This gives us confidence that the parametrizations we obtain constitute global optima (within the employed bound constraints).

Because we carry out these optimizations with a reduced HFB accuracy ($\varepsilon = 10^{-4}$) to save on runtime, we perform a final optimization of every EDF for at most 100 optimization iteration steps with the HFB convergence criterion set to $\varepsilon = 10^{-5}$. This is the same value we also use in Sec. 4.3 to predict observables with the EDFs. We start this final optimization from the best solution candidate found until then and use $\Delta_0 = 0.05$. Only parameter sets that yield no unconverged calculations are eligible as final parametrizations.

4.3 Results

4.3.1 Obtained parametrizations

The parameter values obtained from the optimizations described in Sec. 4.2.3 are given in Tab. 4.3. Parameters that ended up at their bounds are underlined. We provide the EDF parameters with larger precision in Tabs. A.10 and A.11, both in their explicit representation and equivalently in terms of INM properties. We refer to the Skyrme-type GUDE functional without any chiral terms as "no chiral". The other GUDE EDFs are labelled according to up to which order chiral terms are included and whether they include interaction terms with explicitly resolved intermediate Δ excitations and 3N forces. We categorize the EDFs according to their properties discussed in the next paragraphs: we refer to the "no chiral" functional as class 0, to the LO and NLO functionals collectively as class 1, and to the remaining functionals as class 2. This latter class contains also a functional labelled "min. chiral". It is constructed with the idea of adding as few terms as possible to the "no chiral" version while still obtaining an EDF that behaves like a member of class 2. Details of the construction of this functional are discussed in Sec. 4.3.2. In Tab. 4.3, the different classes are indicated by vertical lines. The "reduced $R_{c,3N}$" functional, which is also included in this Table, is discussed in Sec. 4.4.

[6] Because the original SLy4 parametrization does not use the mixed pairing prescription employed here, the pairing strengths are adjusted for the SLy4 starting point: we start these optimizations with $V_0^{\mathrm{n}} = V_0^{\mathrm{p}} = -258.2$ MeV fm^3. Also, the SLy4 EDF does not contain tensor terms; thus we set $C_0^{JJ} = C_1^{JJ} = 0$. The NRAPR EDF does not include pairing at all. For the corresponding starting point we pick $V_0^{\mathrm{n}} = V_0^{\mathrm{p}} = -280$ MeV fm^3 similar to the choice made in Ref. [243]. The same choice is made for SkM*.

Table 4.3: Parameters of the different GUDE variants obtained in this work. Values that are underlined correspond to cases where the minimum was attained at a parameter bound. ρ_c is given in fm^{-3}, E, K, a_{sym}, and L_{sym} are in MeV, the surface coefficients $C_t^{\rho\Delta\rho}$, $C_t^{\rho\nabla J}$ and C_t^{JJ} are in MeV fm^5, and the pairing strengths V_0^{q} are in MeV fm^3. The last row gives the value of the loss function (4.37) at the minimum.

	class 0	class 1		class 2							
	no chiral	LO	NLO	N^{2}LO	N^{2}LO+3N	NLOΔ	NLOΔ+3N	N^{2}LOΔ	N^{2}LOΔ+3N	min. chiral	reduced $R_{c,3\mathrm{N}}$
ρ_c	0.15463	0.15430	0.15423	0.15779	0.15749	0.15571	0.15615	0.15606	0.15681	0.15832	0.15905
E	$\underline{-15.8}$	$\underline{-15.8}$	$\underline{-15.8}$	$\underline{-15.8}$	$\underline{-15.8}$	$\underline{-15.8}$	$\underline{-15.8}$	$\underline{-15.8}$	$\underline{-15.8}$	-15.830	-15.817
K	$\underline{260}$	$\underline{260}$	$\underline{260}$	222.2	215.2	240.8	230.9	236.0	222.4	223.6	215.6
M_{s}^{*-1}	0.9788	0.9579	0.9641	0.9048	0.9027	$\underline{0.9}$	$\underline{0.9}$	$\underline{0.9}$	0.9057	0.9173	0.9622
a_{sym}	29.95	30.98	30.99	28.07	28.45	28.43	28.63	28.37	28.60	28.58	28.82
L_{sym}	41.4	59.6	58.9	34.1	$\underline{30}$	$\underline{30}$	$\underline{30}$	$\underline{30}$	$\underline{30}$	$\underline{30}$	$\underline{30}$
$C_0^{\rho\Delta\rho}$	-41.4	-37.5	-38.4	24.5	9.4	18.5	8.2	27.0	10.9	22.5	-10.1
$C_1^{\rho\Delta\rho}$	-6.4	-25.0	-15.1	-83.2	-21.6	-12.9	-3.4	-17.3	-5.6	-38.8	-31.8
$C_0^{\rho\nabla J}$	-62.3	-72.9	-74.2	-82.6	-88.3	-65.5	-77.7	-65.3	-86.3	-61.4	-128.5
$C_1^{\rho\nabla J}$	11.0	18.1	15.5	-39.3	18.6	17.5	23.5	14.9	19.7	3.4	27.6
C_0^{JJ}	-43.4	-75.1	-75.8	-53.4	-78.1	-100.4	-97.4	-103.3	-83.7	-38.8	-70.1
C_1^{JJ}	-30.1	-15.0	-12.3	12.3	1.3	-10.2	-8.0	-11.0	-2.6	-4.2	28.5
V_0^{n}	-218.4	-219.9	-220.9	-207.2	-209.1	-205.8	-207.2	-206.5	-209.1	-206.5	-222.5
V_0^{p}	-259.9	-263.0	-263.2	-246.4	-255.5	-251.9	-253.7	-252.5	-255.3	-249.4	-267.4
γ	0.467	0.546	0.541	0.358	0.320	0.432	0.385	0.418	0.352	0.363	-0.225
χ^2	122.4	144.9	145.5	89.3	88.7	86.2	89.1	86.5	90.7	87.4	90.4

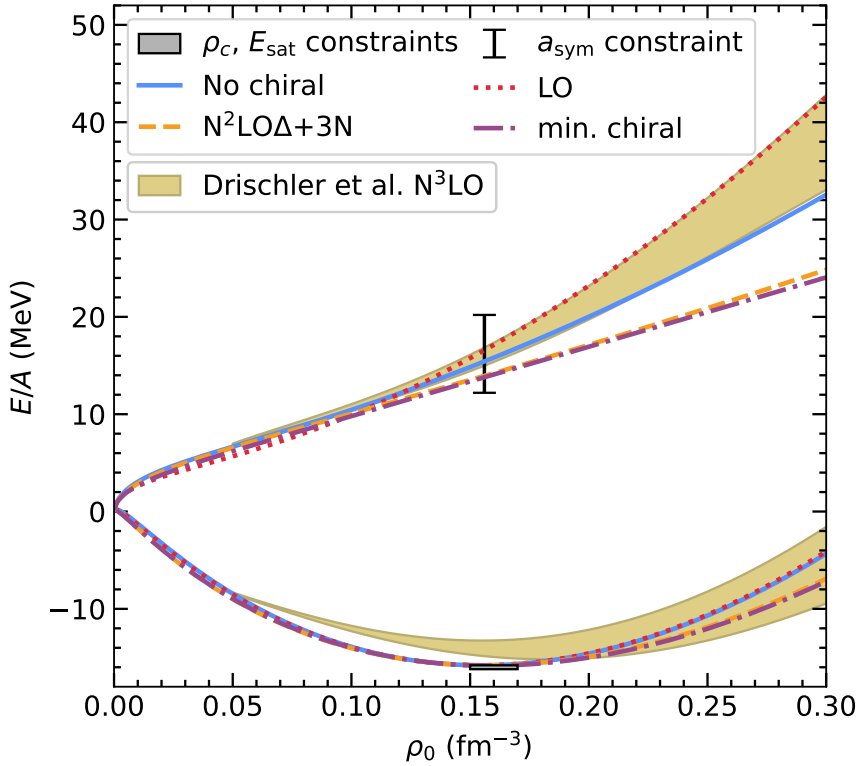

Figure 4.4: Energy per particle in infinite nuclear matter for selected GUDE functionals constructed in this work. For each EDF, both pure neutron matter and symmetric nuclear matter energies are shown. The bound constraints on saturation density, saturation energy, and symmetry energy employed in the optimization of the EDFs are also depicted. For comparison, we show the 1σ uncertainty bands from a calculation employing a chiral Hamiltonian by Drischler et al. for $\rho_0 \geqslant 0.05$ fm^{-3} [231].

We start with a discussion of the INM parameters of the different GUDE variants. The saturation energy E ends up at its upper bound[7] for almost all optimized functionals. This also holds for the value of the incompressibility K for classes 0 and 1. For class 2 the incompressibility acquires lower values inside the allowed parameter range. All other considered nuclear matter parameters also indicate a qualitative difference between classes 0 and 1 on the one hand and class 2 on the other hand: the variation of the INM parameters within these groups is much smaller than the difference between them. The main parameter difference between class 0 and class 1 lies in an increased value of the slope parameter L_{sym} for the chiral functionals. When going to the class 2 functionals L_{sym} gets significantly reduced and ends up at its lower bound for most of the EDFs, with a correspondingly lower a_{sym} parameter. These reductions follow approximately the known empirical correlations, see, e.g., Ref. [232]. Note that for some of the EDFs the inverse isoscalar effective mass M_{s}^{*-1} attains its lower bound, too. While $M_{\mathrm{s}}^{*-1} = 0.9$ is relatively low compared to typical values [101], this value was also obtained for UNEDF0 [215].

In Fig. 4.4 we show the energy per particle for pure neutron matter and symmetric nuclear matter for four functionals constructed in this work, one each from class 0 and 1 and two from

[7]Note that for the N^{2}LO+3N (obtained value of E: -15.801) and N^{2}LOΔ (-15.8001) EDFs the value of E did not quite end up at the bound when the optimizations finished. Given that these values are very close to the bounds we expect that letting `POUNDERS` run longer would lead to parameter sets where these parameters are right at the bound.

class 2. The differences between the EDFs are very small up to about saturation density. This is not surprising since this region is probed by finite nuclei and hence strongly constrained by the fit to experimental data. The differences between the different classes become much more pronounced for $\rho_0 \gtrsim \rho_c$, in particular for neutron matter. This region is not probed by finite nuclei, which is also why the deviation from the additionally given ab initio result observed for class 2 in this density regime for neutron matter is not surprising. The plotted uncertainty bands have been obtained by Drischler et al. [231] based on the MBPT calculations from Ref. [43] with a chiral NN+3N Hamiltonian at next-to-next-to-next-to-leading order with momentum cutoff 500 MeV [247] and 3N forces fit to saturation. The difference of the EDFs to the ab initio results that is visible for symmetric matter is a consequence of the saturation energy bounds employed in this work, which are not obeyed by the ab initio results. Note that the curves for the two class 2 representatives, the N^{2}LOΔ+3N and the "min. chiral" variant, are very close to each other even for $\rho_0 > \rho_c$. This holds analogously for other EDFs from the same class.

Overall, and in particular within the classes as defined above, the description of INM at saturation density and below shows a large consistency between the different functionals. This may be considered surprising given that the chiral contributions are quite different in size depending on the chiral order. However, it indicates that the optimization of the Skyrme and pairing coefficients to data can to a large degree wash out the effect of the additional terms. We return to this issue in Sec. 4.4.

In Tab. 4.3 we also provide the value of the γ exponent for the different EDFs. Compared to the "no chiral" variant it is larger for class 1, but smaller for class 2, indicating that the density-dependent terms absorb different physics for the two classes. Along the same lines we note that at every order γ is smaller by about 0.05 for functionals including chiral 3N contributions.

For all GUDE variants the generally observed hierarchy of pairing strengths $|V_0^{\mathrm{p}}| > |V_0^{\mathrm{n}}|$ [228, 248] holds. The somewhat weaker strengths obtained for the class 2 EDFs when comparing to the other classes is in agreement with the lower M_{s}^{*-1} values for class 2 [83].

Note that a direct comparison of the surface parameters of the different GUDE variants makes little sense because the chiral contributions to the corresponding terms depend on the functional and are not included in the C_t^{uv} values given in Tab. 4.3.

Based on starting optimization runs of the same GUDE variant from different initial points [12] we find that the parameters of the isovector part of the EDF[8] are relatively ill-constrained with our optimization protocol. This is in agreement with observations made in other nuclear EDF optimizations [112, 113, 215, 229, 249]. To better determine the isovector parameters the optimization data set has to be augmented; see also Ch. 5. Also the C_0^{JJ} parameter seems poorly constrained. To quantify these statements a rigorous statistical analysis should be carried out in future work.

The last row of Tab. 4.3 contains the value of the loss function χ^2 at the optimum. For the "no chiral" EDF it is around 120. Adding the chiral terms at LO (and NLO) according to the construction described in Sec. 4.1 worsens the χ^2 at the minimum: it attains values around 145. This stems from a slightly worse description of ground-state and fission isomer energies.

However, the additional inclusion of chiral terms at N^{2}LO or of the Δ contributions at NLO

[8] We use established, but imprecise terminology here referring to terms depending on isovector densities as the isovector part of the EDF although the corresponding energy density is an isoscalar.

Table 4.4: Exact scalar Hartree energies and differences of scalar Hartree energies calculated with Taylor expansions of the densities up to a given order [cf. Eq. (4.20)] and the corresponding exact energies (all in MeV). The densities are generated from calculations with the SLy4 EDF. Results are given for the chiral pion exchanges considered here at N^{2}LO and for the finite-range parts of the Gogny D1S functional [186].

Interaction	Nucleus	Exact energy	Differences at order 0	2	4
Chiral N^{2}LO	^{48}Ca	−759	−118	22	−9
	^{208}Pb	−3937	−290	40	−15
Gogny D1S	^{48}Ca	−9827	−433	27	−4
	^{208}Pb	−47695	−1028	49	−7

reduces the χ^2 at the minimum to about 90. In particular experimental energies of spherical nuclei in the fitting set are better described by the class 2 functionals. The root-mean-square deviation (RMSD) for those is 2.5 MeV for the "no chiral" EDF, but only 1.6 MeV for the class 2 GUDE variants. The other data types in the χ^2 are typically either slightly improved or are equally well described when comparing to the "no chiral" functional.

We note that the N^{2}LO EDF constitutes a slight deviation to these general trends (which can also been seen from some of the parameter values listed in Tab. 4.3): it describes the radii in the χ^2 worse than all other EDFs but proton odd-even staggerings are much improved.

4.3.2 Investigation of improved functionals and construction of "min. chiral" functional

As discussed in the previous section and further in Sec. 4.3.3 we observe an improvement over the "no chiral" functional when going to EDFs that include chiral terms entering at N^{2}LO (or NLO when including interactions with explicit Δ excitations). It turns out that only a small subset of the terms that contribute at these orders is actually necessary to achieve the improvement.

First, the inclusion of chiral isovector contributions is not required. This is hardly surprising given that the Skyrme part of the EDFs contains 6 parameters contributing solely to the isovector part which is to be compared to 7 parameters for the isoscalar terms, but the isoscalar energy contributions are at least an order of magnitude larger than the isovector ones [170]. The similar amount of parameters for the two EDF parts suggests one may expect a similar relative precision for the corresponding energy contributions. The resulting absolute deviations would then be much bigger for isoscalar energies. Thus, one can expect omitting chiral isovector contributions does not significantly impact the description of bulk properties of finite nuclei (after refitting the EDF parameters). Of course this is amplified by the inadequacy of the optimization data set to accurately fix the EDF isovector parameters.

Performing an optimization of an EDF as described by Eq. (4.1) but taking into account from the chiral side only Fock contributions up to N^{2}LO yields a class-1-like functional which suggests that the switch to class 2 is due to the Hartree terms. Indeed N^{2}LO (NLO with Δs) is the first order which for even-even systems has isoscalar pion-exchange Hartree contributions. These are by far the largest chiral contributions to the energy. In Tab. 4.4 we show the expectation values of the exact Hartree energy from pion-exchange contributions up to N^{2}LO in the chiral expansion. They are obtained with densities generated from calculations

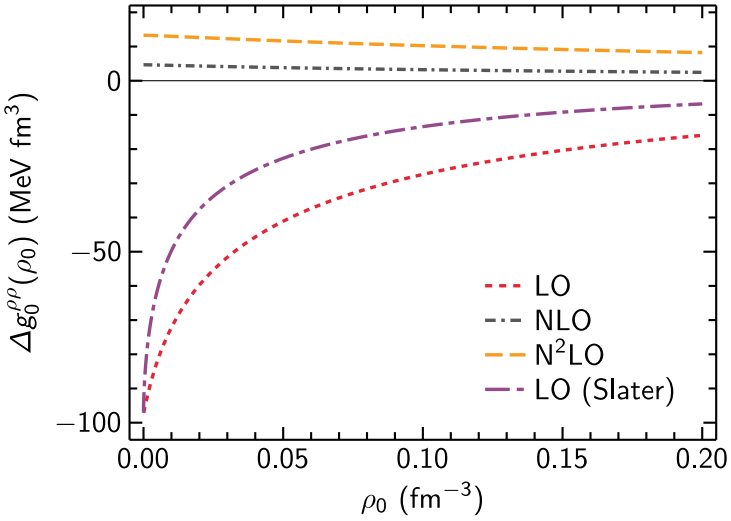

Figure 4.5: Contributions to $g_0^{\rho\rho}$ arising at different chiral orders. We show contributions at LO, NLO, and N^{2}LO calculated from the interaction specified in Sec. 4.1.2 using the PSA-DME. In addition, we show the LO contribution when using the Slater approximation instead of the PSA-DME.

performed with the code HOSPHE [197] employing the SLy4 EDF [195]. Additionally, we provide the difference to these exact values for energies that we obtain when Taylor expanding one density entering the Hartree energy, see Eq. (4.20). For comparison we also provide the analogous numbers obtained with the finite-range parts of the Gogny EDF in the D1S parametrization, see Ref. [170] for a more extensive study.

One can see that the energies obtained with the Taylor series converge relatively slowly towards the exact values. In particular when going to second order in the Taylor expansion the approximated value is still off by about 40 MeV in ^{208}Pb. The second-order expression for the energy has a Skyrme-like structure (density bilinears consisting of up to second-order densities multiplied with constant prefactors). Therefore, one may expect that a Skyrme EDF cannot fully account for the chiral Hartree contributions at N^{2}LO if they are left out (as is the case for classes 0 and 1). It is thus conceivable that class 2 GUDE variants behave differently from classes 0 and 1.[9]

Carrying out the optimization of an EDF where in the chiral part only the isoscalar Hartree contributions entering at N^{2}LO are included leads to a functional with $\chi^2 \approx 112$ at the minimum, which is clearly larger than the values observed for class 2. For this EDF the pairing strengths take a non-physical value $V_0^q \approx 40$ MeV fm^3. These observations suggest another term is additionally needed to reproduce the class 2 behavior.

In Fig. 4.5 we show the contributions to the $g_0^{\rho\rho}$ coefficient arising at different chiral orders, but the following discussion applies also similarly to other g coefficients. The total $g_0^{\rho\rho}$ coefficient at a given order is the sum of all depicted contributions $\Delta g_0^{\rho\rho}$ up to that order. The LO contribution shows a strong density dependence with its value at $\rho_0 = 0$ being about 5 times as large as the value at $\rho_0 = \rho_c$. The contributions at NLO and N^{2}LO are much smaller and their density dependence is much weaker, which is why their effects can be easily captured by simply adjusting Skyrme coefficients. In principle even the strongly density-dependent LO

[9] Note that the argument put forward above is not a direct proof because the fitting of the EDF parameters may shuffle around contributions among more terms than the ones technically entering the Taylor-expanded energy.

coefficient could be quite well mimicked by a Skyrme EDF due the presence of the $C_{tD}^{\rho\rho}\rho_0^\gamma$ term but since this term has to capture several different types of unresolved physics [116], one may expect that adding the LO $g_0^{\rho\rho}$ contribution explicitly still has a relevant effect. Optimizing an EDF with both isoscalar chiral long-range Hartree contributions at N^{2}LO and Fock contributions at LO yields a functional belonging to class 2 as desired.

We showed in Sec. 3.4 that Fock energies from a Yukawa interaction can be well approximated by using the Slater approximation instead of the more involved PSA-DME applied for the GUDE functionals so far. However this comes at the price of a worse local reproduction of the Yukawa Fock energy density essentially everywhere in the nucleus. Using the Slater approximation instead of the PSA-DME reduces the amount of non-vanishing isoscalar NN g coefficient functions from five to one. We show the non-zero $g_0^{\rho\rho}$ coefficient at LO in Fig. 4.5. We find that the resulting EDFs differ by similar amounts as other functionals in class 2 differ from each other. Therefore it seems safe to use the simpler Slater approximation in the present EDF construction, at least for bulk properties.[10]

We refer to the EDF constructed according to Eq. (4.1) including for E_{H}^{χ} only the isoscalar NN pion-exchange Hartree contribution entering at N^{2}LO and as E_{F}^{χ} the isoscalar NN pion-exchange Fock contribution at LO (described by the Slater approximation) as the "min. chiral" GUDE variant. The parameters obtained when optimizing this functional are given in Tab. 4.3 and with higher precision in Appendix A.2, where we also provide the parameters used in the interpolations for the chiral Hartree and Fock contributions according to Eqs. (4.15) and (4.24). The INM parameters and the χ^2 value at the optimum are in the ranges of the other class 2 functionals (see Tab. 4.3) indicating that the "min. chiral" variant indeed also belongs to this class. This explicitly demonstrates that the two identified terms are enough to achieve the improvement over classes 0 and 1.

4.3.3 Global comparison to experiment

We now investigate the performance of the different functional variants in the GUDE family obtained in Sec. 4.3.1 by calculating the ground states of even-even nuclei included in the 2020 AME [235]. We include all 663 nuclei with actual measured masses, leaving out those for which only evaluated masses are available. Every nucleus is calculated five times with `HFBTHO` in kick-off mode setting the initial deformation constraint to $\beta = -0.2, -0.1, 0, 0.1, 0.2$ respectively. This is done so that oblate deformed, spherical, and prolate deformed solutions are considered as possible ground states for every nucleus. The HFB calculations are carried out until they are converged (typically within at most about 100 HFB iteration steps) or until the amount of unconverged calculations for a given functional does not get further reduced for at least 800 HFB steps. For most GUDE variants only about a handful of the 3315 calculations end up unconverged at the end of this procedure. The N^{2}LO EDF is the only exception from this rule: even after more than 3000 HFB steps 111 calculations are still unconverged. Note however that only 4 of those constitute the calculation with lowest binding energy for the corresponding nucleus and for every nucleus at least one calculation is converging.

For every nucleus, we pick among the converged calculations the one with the lowest energy as a first ground-state candidate and apply on it two filters to exclude unphysical solutions. Whenever a filter is triggered, the calculation with the next-lowest energy for the

[10] When leaving out the regulator for the Fock contribution, the resulting coefficient can be evaluated analytically, see Sec. 3.4.2. Then one also obtains a class 2 EDF, which is an option if one does not want to use the g coefficient interpolation.

Table 4.5: Deviations of ground-state energies, two-neutron and two-proton separation energies (all in MeV), and charge radii (in fm) calculated with the different GUDE variants and the corresponding experimental values. For every observable root-mean-square deviations and mean deviations are provided. The values are calculated from all even-even nuclei with $Z \geqslant 8$ included in the experimental data sets, see text for details on those.

		no chiral	LO	NLO	N^{2}LO	N^{2}LO+3N	NLOΔ
RMSD	E	2.11	2.09	2.13	1.56	1.41	1.47
	S_{2n}	0.86	0.85	0.89	0.74	0.73	0.73
	S_{2p}	0.74	0.74	0.77	0.61	0.61	0.60
	r_{ch}	0.024	0.024	0.025	0.024	0.023	0.022
Mean dev.	E	0.630	0.532	0.560	0.324	0.302	0.369
	S_{2n}	0.089	0.093	0.094	−0.060	−0.015	0.001
	S_{2p}	−0.027	−0.036	−0.044	0.153	0.082	0.064
	r_{ch}	−0.0092	−0.0093	−0.0090	−0.0017	0.0003	−0.0018

		NLOΔ+3N	N^{2}LOΔ	N^{2}LOΔ+3N	min. chiral	reduced $R_{c,3N}$
RMSD	E	1.50	1.42	1.53	1.45	1.43
	S_{2n}	0.75	0.73	0.77	0.75	0.76
	S_{2p}	0.62	0.59	0.64	0.63	0.67
	r_{ch}	0.022	0.023	0.023	0.022	0.022
Mean dev.	E	0.393	0.296	0.387	0.293	0.205
	S_{2n}	0.010	−0.006	−0.003	−0.015	−0.029
	S_{2p}	0.053	0.073	0.069	0.081	0.096
	r_{ch}	−0.0025	−0.0006	−0.0014	−0.0010	0.0014

same nucleus is considered instead. First we do not consider solutions with $E/A < -11$ MeV. This filter turns out to be triggered only a few times by calculations with EDFs that include interactions with explicit Δ isobars in the chiral terms. Second we apply a filter to remove solutions with unphysically large deformations. This is done by applying the 1.5 interquartile range rule, which is a simple measure to detect outliers of a distribution [250], on the values of the deformation parameter β_2 of all remaining ground state candidates. The β_2 parameter is much less mass-number dependent than the axial quadrupole moment of the nucleus Q_{20} and is related to it according to

$$\beta_2 = \sqrt{\frac{\pi}{5}} Q_{20} / \left(A R_m^2\right) \tag{4.43}$$

with the root-mean-square matter point radius R_m. The deformation filter is in practice triggered at most for two nuclei per EDF.[11]

We compare the resulting ground-state energies against the values extracted from the 2020 AME (taking into account an electronic binding energy correction as mentioned before). Table 4.5 contains the corresponding root-mean square and mean deviations obtained for nuclei with $Z \geqslant 8$. We also give the deviations of the two-neutron (S_{2n}) and two-proton (S_{2p})

[11] Interestingly, one nucleus where the deformation filter is triggered for all EDFs with chiral terms is the unbound ^{8}Be, for which a superdeformed state is energetically favored by the calculations. This is in agreement with the usual picture of this resonance as a two-α molecule [251]. However of course the predicted energies are quite far away from the experimental result similar to the situation in other very light nuclei.

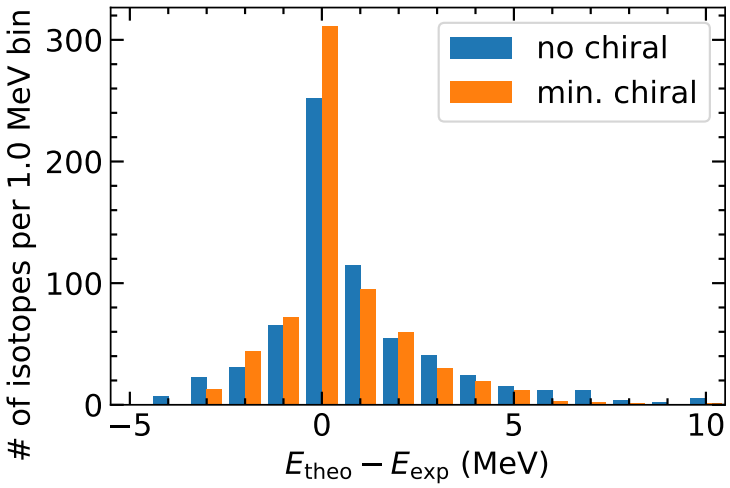

Figure 4.6: Distributions of ground-state energy differences between calculated and experimental results. They are shown for the "no chiral" and "min. chiral" GUDE functionals in bins with a width of 1 MeV each. Note that the last bin contains also values with an energy difference larger than 10.5 MeV.

separation energies obtained from the same data set, and of the charge radii from Ref. [236]. GUDE variants of the same class behave very similar for all these quantities with the only exception being somewhat larger mean deviations observed for separation energies for the N^{2}LO functional compared to other class 2 EDFs.

While classes 0 and 1 perform similarly, an improvement is observed for all observables when going to class 2. In particular, the ground-state energy RMSD is significantly reduced by roughly 30% from 2.1 MeV for classes 0 and 1 to about 1.5 MeV for the various class 2 EDFs. The mean deviation $\langle E_{\mathrm{theo}} - E_{\mathrm{exp}} \rangle$ is almost halved down to 0.3 MeV, indicating that the energies are less biased towards underbinding for class 2. This can also be seen in Fig. 4.6,[12] which shows the histogram of the quantity $E_{\mathrm{theo}} - E_{\mathrm{exp}}$. Calculations which produce extremely underbound nuclei (those at the very right of the distribution) occur much less often for the class 2 "min. chiral" functional than for the reference "no chiral" EDF. Such cases correspond mostly to very light nuclei. For the class 2 variants almost half of all nuclei are described with a mass error of less than 0.5 MeV. Note that while the binding energies included in the χ^2 are described better by class 0 than by class 1, the performance on all even-even nuclei binding energies is very similar for these two classes.

In the upper row of Fig. 4.7 we show ground-state energy residuals for four GUDE variants.[13] One can clearly see that the class 2 EDFs describe energies around the $N = 82$ and $N = 126$ shell closures much better than the classes 0 and 1 variants. We note that due to the parameter optimization involved in the construction of every functional it is not clear if the additional chiral terms entering the class 2 functionals are actually directly improving the description of (near-)closed-shell nuclei or if they instead improve the open shells and indirectly allow the parameter optimization to yield a better reproduction of closed shells. In addition, the observed underbinding for light nuclei is reduced for the class 2 variants.

[12] Note that this and following figures contain also nuclei with $Z < 8$, unlike the values provided in Tab. 4.5.

[13] The outlier that can be seen at $N = 146$ in the case of N^{2}LOΔ+3N is ^{234}Ra. For that functional the prolate solution has an energy relatively close to experiment and all the other nuclei of the radium chain are prolate in the calculations, too. But for ^{234}Ra the prolate solution is not (quite) converged and thus the oblate solution is assumed as the ground state, but its energy is higher by about 5 MeV.

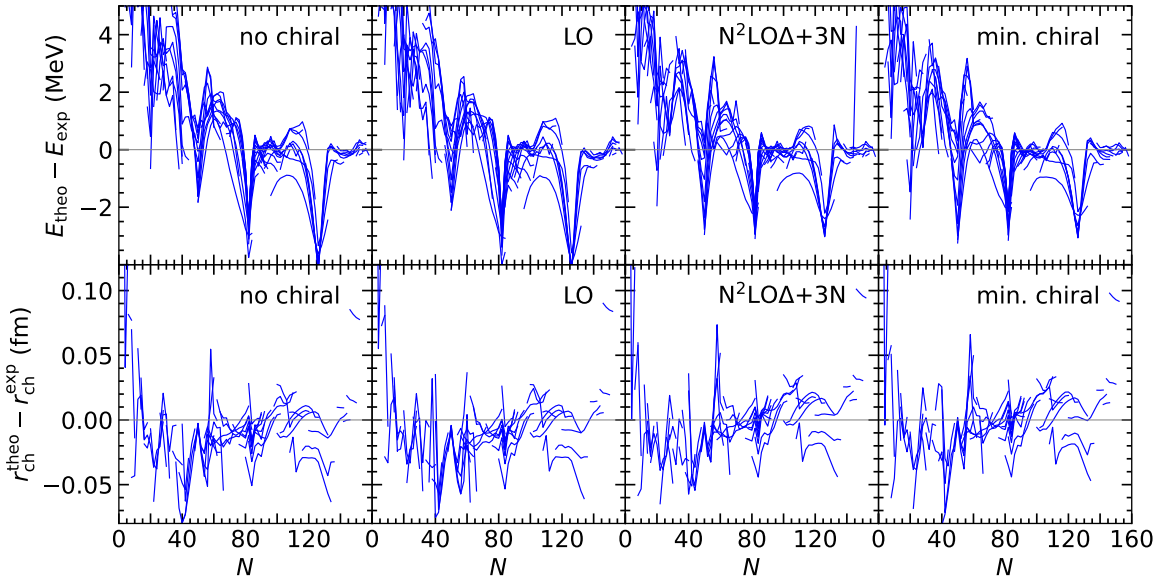

Figure 4.7: Differences of ground-state energies (upper panels) and charge radii (lower panels) for even-even nuclei between values obtained with selected GUDE variants and experiment.

For both two-neutron and two-proton separation energies class 2 EDFs give a small improvement over classes 0 and 1: the RMSD values are reduced by about 12%. In addition, the bias on S_{2n} values is almost completely gone while it is increased for S_{2p}. We depict two-neutron separation energies for the "no chiral" and "min. chiral" functionals in Fig. 4.8. This shows that their description is improved for some light nuclei and around the $N = 82$, 126 (and $N = 40$ sub-) shell closures. Not very surprisingly this agrees mostly with the regions where ground-state energies are improved.

The strength of a few shell closures is overpredicted by all GUDE variants. This can be seen in form of sudden color changes in Fig. 4.8 and leads to the spikes visible for ground-state energies in Fig. 4.7. In Fig. 4.9 we present two-neutron separation energies along the thorium isotopic chain, where such behavior is clearly visible at $N = 126$ (i.e., $A = 216$). The predictions at and around the shell closure are significantly improved for class 2 functionals, but large deviations with experiment still persist. Note that the underprediction of two-neutron separation energies for nuclei just above the shell closure also occurs for other EDFs, for instance when performing calculations with UNEDF2 [112] with even larger magnitude. Further away from the shell closure, measured values are in excellent agreement with theoretical predictions for all GUDE variants. Note that ^{232}Th is part of the optimization data set.

The description of charge radii is least affected by the additional chiral terms added in class 2. This can also be seen in the lower row of panels of Fig. 4.7. Charge radii are only slightly better described for $N \approx 40$ to 100 and their mean deviation is slightly closer to zero for class 2.

4.3.4 Shell structure and deformation properties

To investigate the quality of the GUDE family with respect to nuclear shell structure we compute single-particle levels using blocking calculations; see Refs. [102, 242] for details on the procedure. While other strategies to extract single-particle energies exist, using block-

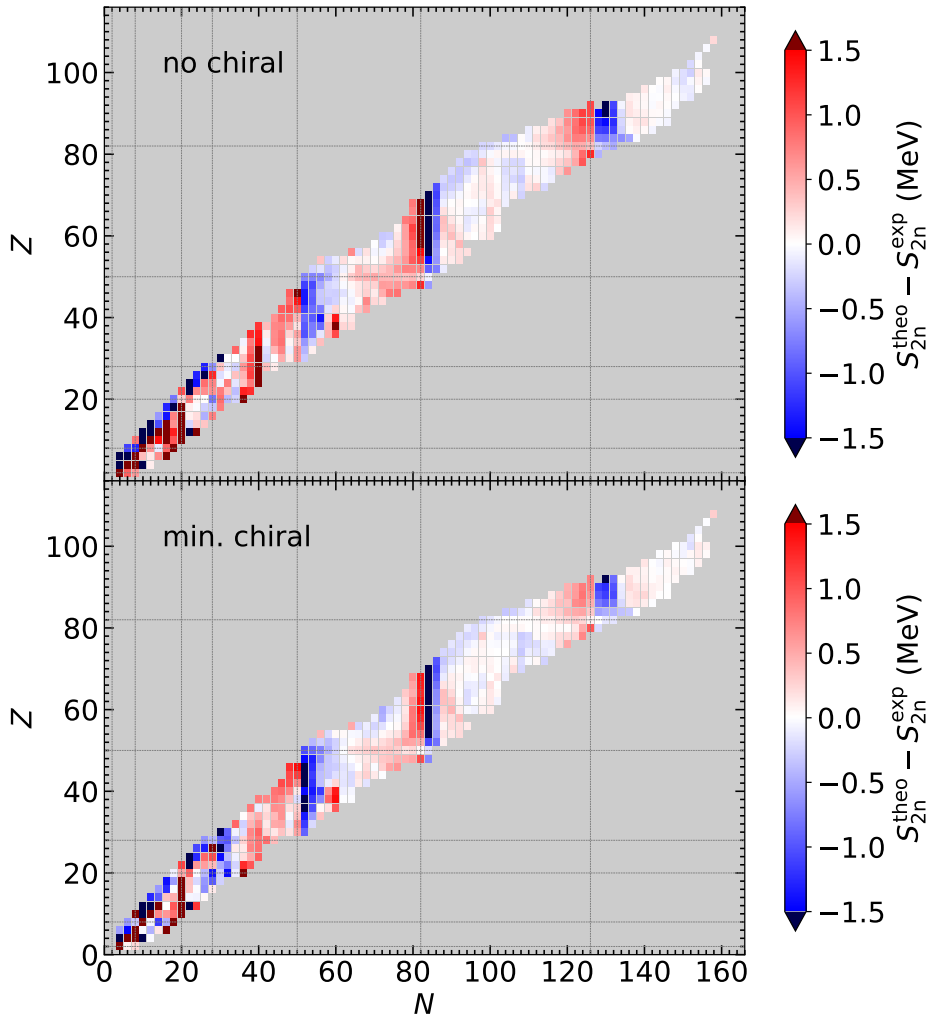

Figure 4.8: Differences of two-neutron separation energies between calculated and experimental results for even-even nuclei. They are shown for the "no chiral" and "min. chiral" GUDE variants.

ing calculations at the HFB level is both logically consistent with the construction of the functionals at the HFB level and helps with reducing systematic errors when comparing with experiment [102]. Calculations use the same setting for the HO basis as before namely with 20 full, spherical shells. In this context one should be reminded that single-particle energies are not observables but extracted in a model-dependent way from experiment [252, 253]. Here we compare to the values given in Ref. [254]. Furthermore, it is well known that the single-particle shell structure depends strongly on beyond mean-field effects such as particle-vibration couplings [255–258]. As a consequence, blocking calculations should not be expected to perfectly match "experimental" single-particle data in closed shell nuclei. They are simply meant as a validation check to guarantee that basic features of the nuclear shell structure are properly reproduced.

As an illustrative example, we show in Fig. 4.10 the obtained neutron single-particle spectra of ^{208}Pb for selected GUDE EDFs representative of the different classes. One can make the following general observations. First, the single-particle levels turn out to be largely insensitive to the GUDE variant. In particular, no significant difference of the shell structure is visible when comparing class 2 EDFs with classes 0 and 1. Second, the obtained shell gaps in ^{208}Pb

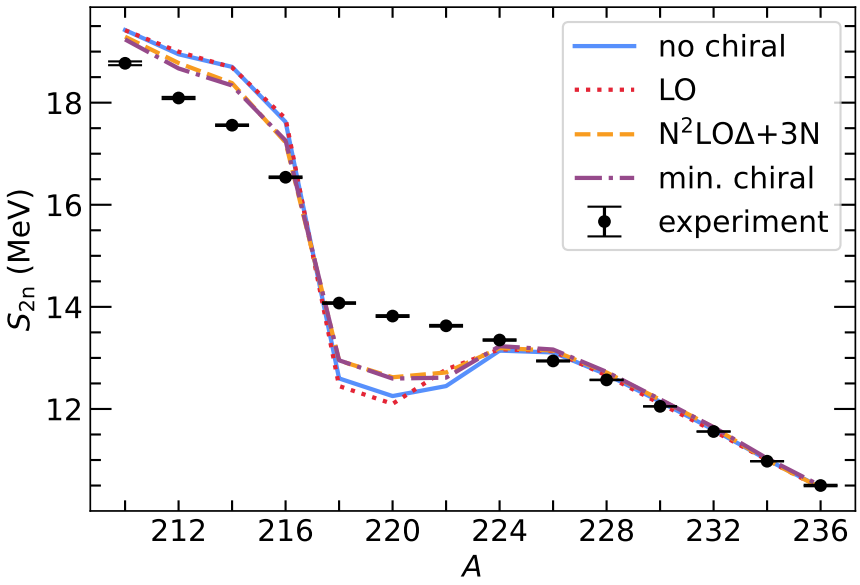

Figure 4.9: Two-neutron separation energies for the thorium isotopic chain.

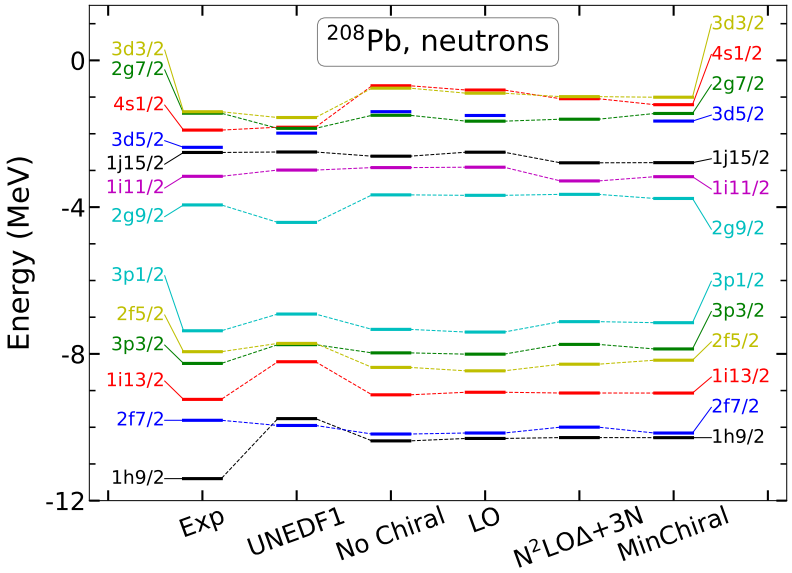

Figure 4.10: Single-particle spectrum for neutrons in ^{208}Pb for a selection of GUDE functionals. Figure taken from Ref. [151].

are in good agreement with the ones extracted from experiment and a little better reproduced than for the UNEDF1 functional. Third, the level ordering of the occupied neutron orbitals is also in slightly better agreement with experiment. These qualitative conclusions apply to other doubly closed shell nuclei and suggest a decent reproduction of the shell structure by the GUDE functionals.

Next, we test deformation properties of the EDFs on the standard fission benchmark case of ^{240}Pu. The HFB calculations are carried out in a deformed HO basis with 30 shells included and with the HO frequency and basis deformation optimized for that nucleus; see Ref. [259] for details. A constraint on the octupole moment is imposed during the first 10 iterations to

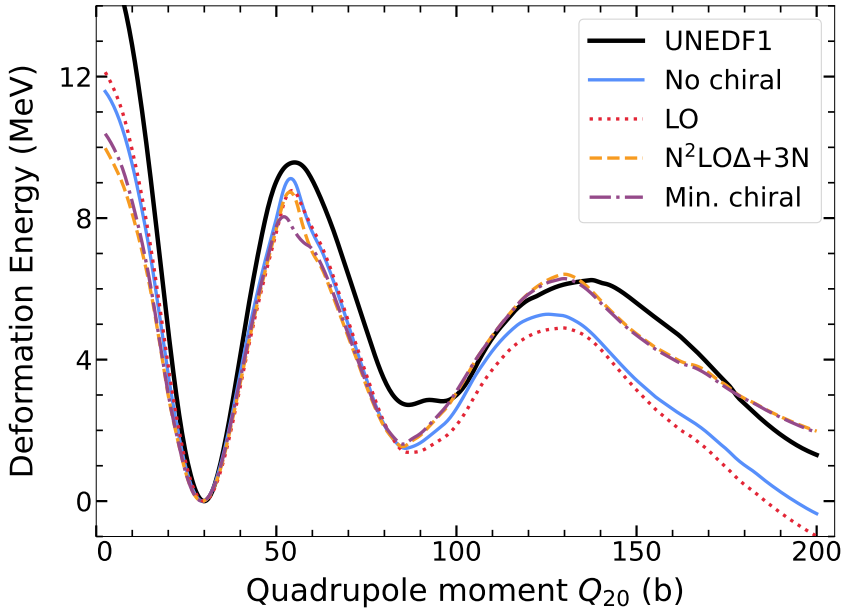

Figure 4.11: Deformation energy of ^{240}Pu as a function of the axial quadrupole moment. Calculations assume axial symmetry. Figure taken from Ref. [151].

ensure the fission goes through the most likely pathway. Calculations assume axial symmetry.

In Fig. 4.11 we show the deformation energy, i.e., the energy difference between the configuration with given deformation and the ground state, as a function of the quadrupole moment for selected GUDE functionals as well as for UNEDF1 for comparison. Including triaxiality typically reduces the height of the first fission barrier by about 2 MeV [216, 259], see also the difference of the UNEDF1 curves in Ref. [102] and Ref. [140]. Note that Ref. [102] in addition to performing triaxial calculations also allows for reflection asymmetry, but this has no relevant effect on the first barrier [259]. Hence, the overall agreement with values extracted from experiment [260] is in fact very good for all considered GUDE variants.[14] The energy of the fission isomer E^* is predicted too low by about 1 MeV compared to the value used in the optimization set (2.8 MeV) [240]. Seeing that the results for UNEDF1, UNEDF2, and the DME EDFs of Ref. [140] agree very well with this experimental value, this is probably a consequence of the reduced weight of fission isomer energies in the present optimization protocol. Note that a newer experimental estimate for the fission isomer energy of 2.25 MeV [261] is closer to the GUDE values.

For values of Q_{20} larger than the value at the fission isomer state a clear difference between results obtained for classes 0 and 1 and class 2 emerge as already observed for other quantities in this paper. We may speculate that such differences are the result of a competition between bulk and shell effects. Table 4.3 and Fig. 4.12 show that the symmetry energy $a_{\rm sym}$ and the surface coupling function $W_{\rm surf}$ (defined below), respectively, differ substantially for the classes 0 and 1 and class 2 parametrizations. For classes 0 and 1, the value of the symmetry energy is $a_{\rm sym} \approx 30$ MeV while it is $a_{\rm sym} \approx 28.5$ MeV for class 2 EDFs. The surface coupling function, which contains the full contribution to the isoscalar surface energy (Skyrme plus chiral terms),

[14] This holds in particular when keeping in mind that the experimental uncertainty for the fission barrier (which is not an observable) is usually estimated to be of the order of 1 MeV [259].

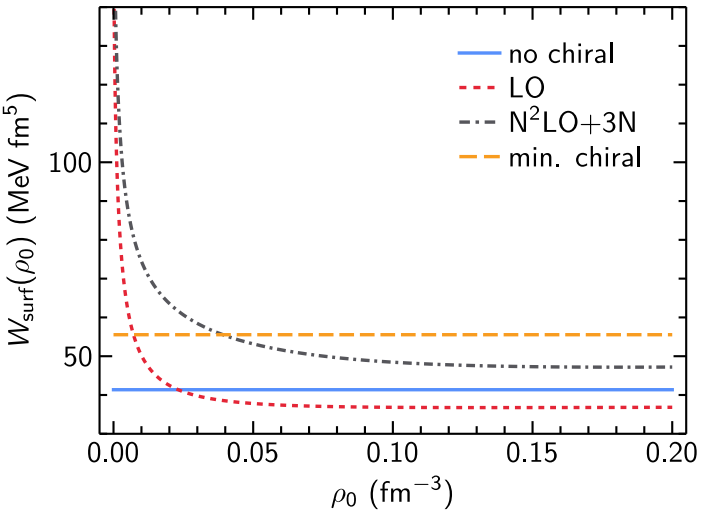

Figure 4.12: $W_{\rm surf}$ for different GUDE variants.

is given by

$$W_{\rm surf}(\rho_0) = W_0^{(\nabla\rho)^2}(\rho_0) + W_{0,\int}^{\rho\Delta\rho}(\rho_0)\,, \tag{4.44}$$

where

$$W_{0,\int}^{\rho\Delta\rho}(\rho_0) = -W_0^{\rho\Delta\rho}(\rho_0) - \frac{\partial W_0^{\rho\Delta\rho}(\rho_0)}{\partial\rho_0}\rho_0 \tag{4.45}$$

arises from integrating by parts:

$$\int \mathrm{d}\mathbf{R}\, W_0^{\rho\Delta\rho}(\rho_0)\rho_0\Delta\rho_0 = \int \mathrm{d}\mathbf{R}\, W_{0,\int}^{\rho\Delta\rho}(\rho_0)\boldsymbol{\nabla}\rho_0\cdot\boldsymbol{\nabla}\rho_0\,. \tag{4.46}$$

$W_{\rm surf}$ is for intermediate densities much stronger for class 2 functionals than for classes 0 and 1. Together, $a_{\rm sym}$ and $W_{\rm surf}$ will impact the surface and surface-symmetry contributions to the bulk energy, which are known to be key drivers of deformation properties [262, 263]. At the same time, Fig. 4.10 also shows a small but visible difference in the neutron shell structure between class 2 and the other GUDE variants functionals, with the $N = 126$ shell gap being a little smaller for class 2. Such differences will be amplified as deformation increases and this could play a role in the deformation energy.

4.4 Analysis of chiral contributions

In this section we analyze why the only significant effects we obtain from including chiral interactions explicitly into the GUDE functionals occur for the switch from class 1 to class 2, i.e., at N^{2}LO (NLO when including Δ isobars explicitly) in the chiral expansion.

As stated in Sec. 4.3, only little change over the reference "no chiral" EDF is seen when going to LO in the present construction, see especially Tab. 4.5. This is not surprising since one-pion exchange is known to largely average out for bulk properties [148, 264] because at this order pions enter at the mean-field level only through Fock contributions, which are small. For non-bulk quantities such as behaviors along isotopic chains, small differences between the "no chiral" and LO EDFs are visible, see for instance the oxygen chain shown in Fig. 4.13.

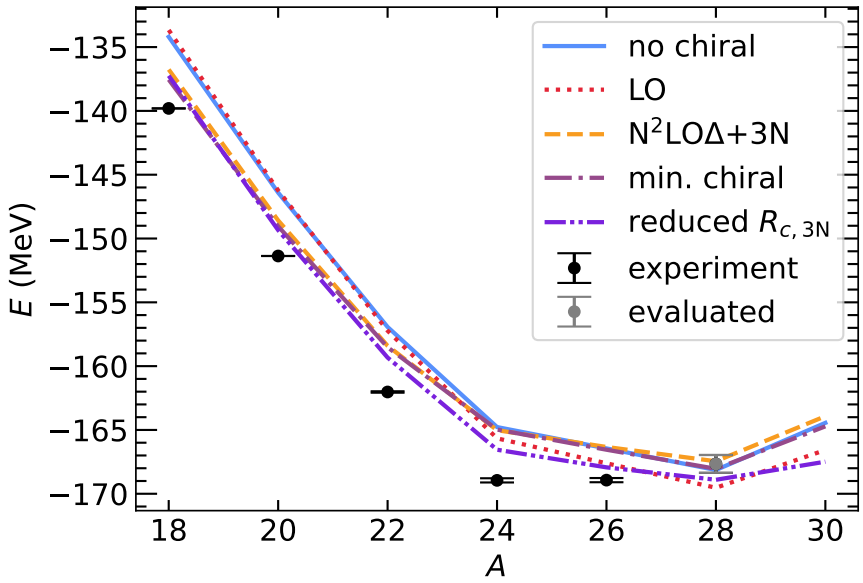

Figure 4.13: Ground-state energies of oxygen isotopes for selected GUDE variants. We also show experimental and evaluated results as provided in Ref. [235].

At NLO pions enter at the HF level only through Fock and isovector Hartree contributions. Since these are very small and can be captured well by Skyrme terms due to the weak density dependence of the resulting g coefficients, see, e.g., Fig. 4.5, the almost identical performance of the LO and NLO functionals is to be expected.

When going to N^{2}LO a significant improvement, in particular for the global description of ground-state energies, is achieved. The detailed analysis of Sec. 4.3.2 indicates that the interplay of two contributions is responsible for this. The attractive pion Hartree contribution at N^{2}LO is large and apparently cannot be completely mimicked by Skyrme terms only. Its addition together with LO Fock terms leads to the improvement.

While the incompressibility is at its upper bound for classes 0 and 1, it is much smaller for the N^{2}LO EDF (and the other class 2 ones), see Tab. 4.3. This is probably a consequence of the strongly attractive central isoscalar two-pion exchange entering at N^{2}LO in the chiral expansion; see for example Ref. [35], where the second derivative of the energy per particle at $\rho_0 \approx 0.16$ is strongly reduced at N^{2}LO in calculations employing only chiral NN forces.

This observation raises the question whether the additional chiral terms in class 2 lead to a better description of experiment by themselves or whether the improvement is realized indirectly by moving the unbounded optimum "closer" to the bound constraint region and thereby reducing the achievable χ^2 values within this region. To address this issue one could perform an unconstrained optimization for the different GUDE functionals. Preliminary unconstrained optimizations suggest that the latter mechanism is the dominant one because the difference of the obtained χ^2 values largely (but not fully) seems to vanish for the unbounded optima. Note however that these conclusions are preliminary, since for some of the EDFs competing minima seem to occur during the unbounded optimizations and sometimes the unconstrained optima seem to correspond to situations where some INM parameters attain values far away from physically expected regions (e.g., $L_{\mathrm{sym}} \approx 5$ MeV). We leave the resolution of these issues for future work.

Similar improvement as for the N^{2}LO EDF is observed for the NLOΔ EDF. This reflects

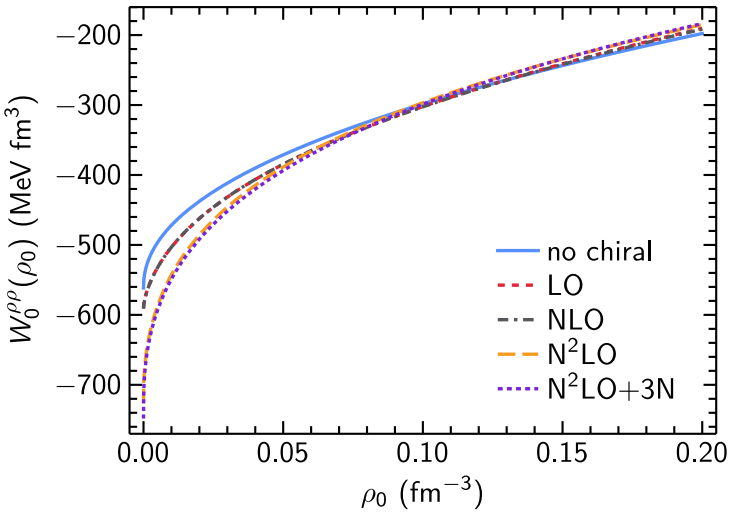

Figure 4.14: $W_0^{\rho\rho}$ for different GUDE variants.

that in Δ-full chiral EFT the dominant two-pion-exchange contribution is promoted from N^{2}LO to NLO [211]. At N^{2}LOΔ some additional attraction is brought in. For the interactions used here the additional contributions (which in Δ-less chiral EFT partly would only occur at even higher orders [265]) are similar in size as the difference between the chiral contributions at N^{2}LO and NLOΔ. The GUDE functionals are generally not sensitive to such differences on a qualitative level; see Tab. 4.5.

All statements made above dealt with chiral NN interactions only. The inclusion of 3N forces does not seem to have a significant effect on the description of nuclei and INM at any considered order; see Sec. 4.3.[15] In ab initio calculations, 3N forces are important for a quantitative reproduction of nuclei, are key for shell structure and for the limits of bound nuclei [34, 266]. For instance, for the oxygen isotopes, the additional repulsion from 3N forces moves the location of the predicted neutron drip line in agreement with experiment [70, 267–270]. In Fig. 4.13 we show the ground-state energies of oxygen isotopes as predicted by a few GUDE functionals. Comparing the N^{2}LOΔ+3N results with the other EDFs shows that including 3N forces does not move the location of the neutron drip line for the EDFs. Similar conclusions hold for the other GUDE variants with 3N forces. In agreement with other EDF calculations [104], all EDFs constructed in this work predict ^{28}O to be the heaviest oxygen isotope stable against emitting two neutrons while experimentally it is ^{24}O.

The crucial difference between the negligible role of 3N forces observed here and their relevant effects in ab initio calculations lies in the fact that the EDFs constructed here yield good saturation properties also without the presence of chiral 3N forces – see Tab. 4.3 and Fig. 4.4 – while they are absolutely necessary to achieve reasonable saturation in calculations of INM employing chiral interactions [201, 271]. In such ab initio calculations, the role of 3N forces is already visible at the HF level, so one could have expected an impact also here. The fact that this is not the case suggests the fitted EDF terms can compensate missing 3N pion exchanges in the density regime relevant for finite nuclei (at least their volume contributions).

For the terms which depend only on ρ_0 this is illustrated in Fig. 4.14, which shows $W_0^{\rho\rho}$ for different GUDE functionals. The curves for N^{2}LO with and without 3N forces are basically on

[15] A slight exception is given at N^{2}LO. However, the N^{2}LO functional seems to be somewhat of an outlier while N^{2}LO+3N behaves like other class 2 EDFs.

top of each other signalling that for the EDF without 3N pion exchanges the Skyrme part of the EDF mostly takes over the role of the 3N terms (see also the different γ values in Tab. 4.3). This observation correlates well with the original reason to introduce a density-dependent coefficient into nuclear EDFs, namely to replace a genuine 3N interaction [272].

The observation that fitting the EDF parameters can almost fully compensate missing 3N pion exchanges is in apparent contradiction with the wrong drip line position observed for the oxygen chain. In other words the question is why the GUDE family predicts the wrong drip line location even though the functionals either explicitly contain or are essentially able to effectively encapsulate chiral 3N physics. One simple explanation is the lack of sufficiently neutron-rich nuclei in the experimental data set used in the optimization meaning that the optimization might simply "not know" of the importance of the 3N pion exchanges for these regions of the nuclear chart. Since chiral 3N contributions grow with increasing neutron number [266, 267, 273], the description of nuclei closer to stability might not be significantly altered but drip lines might be much improved when optimizing an EDF with chiral 3N contributions using an experimental data set containing more asymmetric nuclei. While in many cases experimental information on very neutron-rich isotopes is not yet available, this is expected to change with next-generation radioactive isotope beam facilities such as FRIB [11] or FAIR [274]. Another reason is the importance of beyond mean-field effects that are known to significantly impact the nuclear structure in light nuclei [275, 276].

The choice of the regulator used for the chiral interactions may also matter. Typical non-local regulators for the 3N force yield more repulsion in pure neutron matter than local ones [207]. The GUDE functionals use local regulators, see Sec. 4.1.2. In neutron matter one can mimic the effect of the non-local regulators by employing local ones with small coordinate-space cutoffs [207]. Thus, we construct a series of EDFs following the GUDE protocol at N^{2}LO+3N but with reduced cutoffs for the 3N terms until we reach $R_{c,3\mathrm{N}} = 0.3$ fm (which corresponds roughly to 0.5 fm for the regulator used in Ref. [207]). The cutoff for the NN contributions is kept unchanged at 1.0 fm. The resulting functional is labeled "reduced $R_{c,3\mathrm{N}}$". It is very similar to class 2 functionals in terms of χ^2, most INM parameters, and global behavior. See Tabs. 4.3 and 4.5 for detailed values.[16] As shown in Fig. 4.13 the "reduced $R_{c,3\mathrm{N}}$" functional locally behaves somewhat different from the class 2 variants, but it does also not predict the correct dripline location. This is linked to its low value of $\gamma \approx -0.22$,[17] which indicates that the fit largely compensates the additional repulsion brought in via the 3N forces. Again, an adjusted optimization data set might lead to larger effects from the different 3N contributions.

As alluded to above, the existence of strict bounds that we impose on some EDF parameters during their optimization somewhat complicates the analysis of the effect of different chiral contributions. Some conclusions drawn in the present section might thus not hold in other optimization settings.

[16] The obtained M_s^{*-1}, pairing strengths, and some surface parameters differ from typical class 2 values. In fact, the significantly different parameter landscape is the reason why it was necessary to reduce the 3N cutoff over several steps in the construction of the "reduced $R_{c,3\mathrm{N}}$" functional. Note that couple of very light nuclei do not converge for this functional.

[17] This value is significantly lower than usual values for Skyrme EDFs, which typically have $\gamma \approx 1/6$ to $1/3$ [83]. Note that this is not concerning though as the contributions from the chiral forces are not accounted for in the GUDE γ values.

4.5 Summary

In this Chapter we constructed semi-phenomenological EDFs, dubbed GUDE, consisting of pion exchanges taken from chiral EFT at different orders and a phenomenological Skyrme part. The long-range pion-exchange interactions are included at the Hartree-Fock level (using a DME for the Fock contributions) without adjustment and thereby do not change the number of free EDF parameters. The GUDE functionals with chiral terms perform significantly better than a reference Skryme functional without chiral terms constructed within the same protocol, especially in terms of accurately describing ground-state energies while at the same time giving physically plausible properties for INM. In particular, the description of light nuclei and nuclei around shell closures is improved. Due to the parameter optimization carried out for every EDF it is however not clear if the inclusion of pion exchanges is directly responsible for this or if a more complicated indirect mechanism is at play. In any case the improvements can be traced back to the combination of two terms: Fock contributions from one-pion exchange at leading order in the chiral expansion and Hartree contributions from two-pion exchange at $\mathrm{N^2LO}$. This is demonstrated with the "min. chiral" variant of the GUDE EDFs which contains only those two terms in addition to the phenomenological part and achieves similar improvements as observed for the other class 2 GUDE functionals, which contain additional terms stemming from pion exchanges.

Conversely, adding only pion-exchange terms at LO or NLO does not give any improvement. While it might seem like a contradiction to the chiral EFT power counting – according to which the importance of additional terms is reduced with every higher order included – it may simply result from the fact that we include pion exchanges only at the HF level, i.e., beyond-mean field effects from pions are not explicitly included and the structure of the contact interactions present in the EDFs does not change with increasing order unlike in chiral EFT. Along similar lines, including long-range 3N forces does not yield significant improvement because the optimization procedure of the (density-dependent) contact terms in the traditional part of our EDFs allows to approximately capture their effects.

The order-by-order systematics of the GUDE functionals shows much less variability and surprising behavior compared to what was observed in Ref. [140], where functionals had been constructed following the same strategy as used here. In particular, we consider it promising that the inclusion of chiral long-range 3N forces does not lead to a worsening of the EDFs, unlike before. We attribute this to the different improvements, bugfixes, and other changes established in the present work. The analysis carried out in Sec. 4.4 mostly explains the obtained order-by-order behavior. In some regards further insight is still needed. For instance, the detailed mechanism how the improvement is realized at $\mathrm{N^2LO}$ (and why some LO terms are additionally needed which on their own do not provide improvement) is still unclear. We believe that insight might be gained from performing optimizations without imposing bound constraints on INM properties.

Going beyond NLO in the present construction does not only improve the description of finite nuclei, it also considerably changes properties of INM as shown in Tab. 4.3. The incompressibility K is significantly reduced and isovector parameters also change strongly. The decrease of the slope parameter L_{sym} is particularly strong, with it typically ending up at our optimization protocol's lower bound of 30 MeV.

However, in current EDFs isovector terms are generally poorly constrained [113, 277];

the present work is no exception. This is not of significant consequence when comparing to bulk properties of experimentally accessible nuclei as done here, but limits the predictive power for applications to extreme neutron-rich conditions in astrophysics. Examples are mass calculations for r-process nucleosynthesis [109, 125] and neutron-star [278–280] calculations. This is because the size of isovector contributions grows significantly when going to very neutron-rich systems. We discuss possible measures against these problems as part of the next Ch. 5, with which we conclude this thesis.

5
Conclusions and outlook

Nuclear density functional theory is a well established method to describe properties of atomic nuclei. In its standard formulation (Kohn-Sham DFT [91]) it corresponds to a mean-field calculation based on an energy density functional that is adjusted to nuclear data, see also Ch. 2. Thanks to its favorable computational scaling, it can be applied to nuclei throughout the entire nuclear chart. EDFs have been successfully applied for global predictions of nuclear masses, but also to describe properties of individual nuclei. Among those are cases where other approaches have not been able to conform with the experimentally determined values.

However, a clear strategy how to further improve EDFs is not known. This might be remedied by constructing EDFs truly from first principles. Different strategies have been proposed to this end [126–131], but none of them has yet been successfully carried out. The present work follows a related strategy [65, 135, 140, 145, 147–149]. It consists in amending a conventional empirical Skyrme EDF with HF long-range terms arising in the exchange of pions between nucleons as described by chiral EFT, which provides a systematic framework for the construction of nuclear potentials based on the symmetries of the underlying fundamental theory, namely QCD. This strategy was discussed in detail in Sec. 1.4.

We mention here only that the chiral Fock terms are included in quasi-local form by means of a density-matrix expansion. In Ch. 3 we carried out an extensive investigation of DMEs finding that exact exchange energies from pion exchanges are generally well approximated by all DME variants considered. We identify different possibilities to obtain even better approximations. This entails an improved treatment of scalar-isovector parts of OBDMs and the use of adjusted expansion schemes for 3N interactions. A more detailed summary of the DME investigation was given in Sec. 3.7. For the construction of semi-phenomenological hybrid EDFs according to the strategy outlined above we stick to the DME choices made in Ref. [140], which we expect to be adequate for the present application.

The construction of those functionals, here referred to as the GUDE family, was carried out in Ch. 4. We find that the global reproduction of ground-state energies of atomic nuclei is significantly improved once pions are included at N^2LO (or at NLO when also explicitly including Δ isobars) in the chiral expansion. In particular, we find that the joint inclusion of isoscalar one-pion-exchange Fock terms at LO (by means of the Slater approximation) and isoscalar Hartree terms arising from two-pion exchange at N^2LO are responsible for the observed improvement. This is exemplified by the good performance of the "min. chiral" functional which contains no other chiral terms. These statements are based on a comparison to a reference functional without any chiral terms that is constructed according to the same protocol. The parameter optimization is set up such that properties of INM are restricted to physically plausible values. Therefore, our results do not necessarily suggest that the inclusion of pion exchanges improves the description of nuclear masses per se. Instead, they show

that it is the simultaneous description of finite nuclei and infinite matter that profits from considering pions as explicit degrees of freedom. See Sec. 4.5 for a more detailed summary of the investigation of the GUDE functionals.

Here we abstain from repeating the points discussed in detail in that Sections. Instead we discuss open question and issues and consider different possible directions of future work. This includes different ideas on how to build less empirical, improved functionals starting from the ones presented in this thesis.

Contributions from chiral effective field theory

While we find that the reproduction of ground-state energies is strongly improved when adding pions according to the present strategy, other investigated observables of finite nuclei, namely charge radii, shell structure, and deformation properties, show a much smaller or no significant improvement. Developing a better understanding of this would be advantageous to make further progress in developing the applied hybrid approach.

We have also left the study of the dependence of the EDFs on the chiral interactions including their regulators for future work. In addition, ab initio calculations that employ coordinate-space versions of chiral interactions use smeared-out delta functions instead of true delta distributions to describe regularized contact interactions [204–206]. This corresponds to the assumption of working at a finite resolution scale. The GUDE family is based on Skyrme EDFs, which correspond to (partially density-dependent) in-medium contact interactions. It could be of interest to replace these zero-range contacts with smeared out ones to better connect to regularized finite-range terms.

Also, it would be of interest to investigate if adding pion-exchange terms, in particular those included in the "min. chiral" variant, to functionals of other type, gives similar improvement as observed here. This is difficult to analyse a priori since it is not always clear what kind of physics is already described by existing functional structures such as the finite-range Gaussians that are used in Gogny EDFs.

For similar reasons it is also hard to phenomenologically address an important question in formalizing an EFT for EDFs, namely if pions constitute a degree of freedom that has to be explicitly included. The present study shows that including pions that are exchanged between nucleons can yield more accurate EDFs, but at the moment it is not clear how an eventual EFT for EDFs will be formulated. It is conceivable that it will use the densities themselves (instead of individual nucleons) as degrees of freedom [85, 129] which renders the meaning of pion exchange in such a framework unclear.

A similar problem arised in this work: the inclusion of chiral 3N pion exchanges did not yield EDFs that behave significantly differently from EDFs where only chiral NN forces are present. The investigation carried out in Sec. 4.4 suggests that the other terms in the GUDE functionals can partially compensate missing 3N forces. This is in agreement with the original reason to introduce density-dependent contacts into Skyrme EDFs [272].

The missing effects from including 3N interactions could also be related to choices made in the DME used to include the 3N forces. In Sec. 3.5 we investigated it in some detail in non-self-consistent tests. An extension to self-consistent tests might thus be useful. In addition, one should further study the application of DMEs to 3N interactions. This could be in terms of considering other DME variants than the PSA-DME or by not truncating the density-matrix cubes that occur to second-order terms only. For NN interactions, we carried out such investigations in Ch. 3 and found that the reproduction of exact Fock energies

can indeed be improved (albeit starting from a level that seems satisfactory for the present applications). In particular, we found that isovector energies can be strongly improved over the implementation used in Ref. [140] and in Ch. 4 by expanding neutron and proton OBDMs separately with individual momentum scales instead of jointly.

In this work, we included as chiral 3N contributions only the ones stemming from intermediate-range and long-range two-pion exchange. The inclusion of 3N one-pion exchange, which is of intermediate range, should also be considered [149]. Moreover, different regularization schemes should be explored. In ab initio calculations the inclusion of 3N forces is crucial to correctly predict the location of the neutron drip line in the oxygen chain, see the related discussion in Sec. 4.4. In the present work, adding chiral 3N terms does not help. In fact, the behaviour of the EDFs in INM suggests that the GUDE variants without chiral 3N contributions behave as if they contain the 3N physics anyway due to the presence of the density-dependent Skyrme contact. However, this statement does not necessarily apply to surface terms. Therefore, a 3N-interaction effect might be visible if the optimization data set is amended by experimental information on sufficiently neutron-rich nuclei close to the dripline as the 3N terms might help to describe this data. The Skyrme coefficient adjustment could then improve the description of other regions of the nuclear chart.

Here we discussed including contributions into EDFs from chiral EFT only at the HF level. How to do that at higher orders in MBPT is at present unclear, although different strategies are being discussed, see e.g., Refs. [65, 85, 129]. This would constitute a major step towards a true ab initio EDF.

Optimization data set

All GUDE variants underbind nuclei on average as shown by their positive mean deviations for ground-state energies. This seems to be because the EDFs over-predict the strength of shell closures. As the χ^2 optimization tries to balance all errors out, it leads to (single-)closed-shell nuclei typically being significantly overbound and nuclei further away from shell closures being underbound. This might be remedied by increasing the amount of data from open-shell nuclei in the fit or by adjusting the data weights in the optimization. One could also extend the optimization data by explicitly including separation energies. This could help with their description and would therefore have significant impact on nucleosynthesis yields from r-process calculations [106, 108, 110].

The use of differential quantities as fit observables was also found to be useful in a study of Fayans functionals: the authors of Ref. [96] find that charge radius staggering is more sensitive to pairing (at least for the Fayans form of the pairing contributions) than energy staggering, which is used in this thesis.

Adding ground-state data for very neutron-rich nuclei, which is expected to become available in the not-too-distant future, should allow to better constrain isovector terms of the EDFs. These are at present poorly constrained, but are relevant in particular for applications to astrophysics. In addition, including experimental data on neutron skins or dipole polarizabilities [277, 281–283] in the data set, possibly combined with fitting to ab initio results for neutron drops [207, 284–286], is expected to reduce the uncertainties of the isovector terms. See Refs. [102, 112, 286, 287] for examples of EDF calculations of neutron drops. Surface properties can also be targeted by matching to ab initio calculations of perturbed nuclear matter, see Ref. [288].

Other parts of the functionals

It might also be advisable to simply reduce the number of free isovector parameters in the functionals. This would allow for speeding up the parameter optimization as the dimension of the parameter space, in which the minimum has to be found, would be reduced. The speed-up could be utilized to more easily investigate the effect of individual changes to the EDF construction as presented in this Chapter by reoptimizing the EDF parameters after every incorporated change. In the GUDE functionals there are 6 purely isoscalar parameters and 5 purely isovector ones (the exponent γ contributes to both sectors and the pairing strengths also have mixed contributions). However, isoscalar energies are typically about an order of magnitude larger than isovector ones (as can for instance be seen from the Bethe-Weizsäcker mass formula [97]). Following the sensible assumption that the number of parameters is positively correlated with the achievable accuracy, this suggests that one should be able to reduce the number of isovector parameters without significant loss in accuracy for total energies. Note that if the number of free parameters is changed, the Bayesian information criterion could be applied like in Ref. [289] to determine if changes in RMSDs reflect more than just the changed number of parameters. Studies that investigate natural sizes of Skyrme parameters [290, 291] could also be of interest in this context.

The Coulomb contributions to the EDFs are free of adjustable parameters. However, this does not mean it could not be improved. The GUDE functionals treat the Coulomb Fock energy in the Slater approximation. As shown in Sec. 3.4.1, using the NV-DME instead is more accurate (when expanding about the position of one particle). Another possibility lies in calculating the Coulomb contributions (Hartree and Fock) essentially exactly by approximating the Coulomb potential as a sum of Gaussians [218], similar to how the chiral Hartree terms are treated already. Due to the infinite range of the Coulomb interaction, a relatively large number of Gaussians is needed though for an accurate representation. Reference [218] uses nine Gaussians.

Corrections to the Coulomb interaction could also be taken into account. These include a correction arising from the finite site of nucleons [292], from vacuum polarization [292], and the relativistic Breit correction due to finite light speed [293]. As shown in the cited references, the size of these electromagnetic contributions in ^{208}Pb is about 7 MeV, 4 MeV, and 2 MeV, respectively. While the EDF parameter fitting partially compensates this, certain observables like mirror nuclei mass differences might be particularly sensitive to such corrections.

The arc-like behavior of charge radii in the calcium isotopic chain is correctly predicted by functionals that use Fayans pairing and fit to differential charge radii [96]. Skyrme EDFs and ab initio calculations do not describe this behavior correctly [96, 294, 295]. This indicates that the pairing part of the GUDE functionals should be improved. However, little is known about the particle-particle component of the nuclear effective interaction [296]. See Refs. [134, 297] for studies on pairing from chiral NN and 3N interactions. To prevent issues with self-pairing [298] that become problematic in the calculation of odd nuclei, the particle-particle part of the EDF should be based on the same interaction as the particle-hole part. This would require larger adjustments of the EDF structure. Note that self-pairing occurs also for conventional functional parametrizations.

A related topic are self-interaction issues [298], by which the GUDE family may also be plagued. For the chiral contributions this is because Fock contributions are included via a DME but the Hartree contributions are included quasi-exactly by approximating the chiral potentials as sums of Gaussians. However, this could be remedied by also treating the Fock

terms (at the same chiral order) quasi-exactly, which does not lead to significant computational overhead. In this work, we used the DME because this simplifies the inclusion of 3N forces in EDF frameworks. However, their inclusion did not lead to significant improvement and they could thus be left out at the present stage (like in the N^{2}LO GUDE version), see related discussion above.

Correlations beyond mean-field approaches

Our work shows that the explicit inclusion of long-range pion-exchange interactions from chiral EFT at the HF level into a Skyrme EDF improves the description of finite nuclei. This suggests that such terms will be relevant when generating an EDF completely from first principles. It might be necessary to account for effects of different types of correlations explicitly to create such an EDF.

Collective correlations may be expected to be captured by going beyond the mean-field description. However, different instabilities and pathologies occur when EDFs not derived from actual Hamiltonians are used in those frameworks [115]. Therefore, functionals of the GUDE form could not directly be used. Among other things, one would need to remove the terms that correspond to a density-dependent pseudopotential or at least replace them by a density dependence only in terms of integer powers, see Refs. [299, 300]. Note that it might be possible to "back-translate" a density-dependent pseudopotential into an actual one by reverse engineering the potential by means of reversely applying the Slater approximation or similar. Another possibility lies in replacing the density-dependent terms by a 3N interaction. This is carried out by using a phenomenological form fitted to data with promising results in Ref. [301]. It would therefore be of interest if using the ab initio 3N pion exchanges as done in this thesis allows to successfully leave out the density-dependent terms (possibly in conjunction with introducing a true 3N contact interaction). This would also give further insight in necessary physical content for the construction of successful nuclear EDFs. Another density dependence that is currently present in the GUDE functionals stems from using the DME for the chiral Fock contributions. Incorporating the pion exchanges quasi-exactly also in the Fock part, see discussion above, would address possible related issues. Note that some beyond-mean-field effects can also be captured by different approximate schemes while staying at the single-reference level; see Sec. 4.2.2 for a related discussion.

Including effects from short-distance correlations from resummed ladder diagrams as described by Brueckner-Hartree-Fock theory should be simpler then switching to a beyond-mean-field approach: in Ref. [144] density-dependent Skyrme terms generated from a counterterm expansion capturing such correlations were computed. A next step towards ab initio EDFs could therefore be the inclusion of such terms.

Uncertainty quantification and emulators

For practical applications, correlated uncertainties (or better, distributions) for the EDF parameters should be determined. They could be estimated using Bayesian inference, see Refs. [113, 234, 302] for example applications to EDFs. This would allow to carry through the uncertainty estimates when applying functionals of the GUDE family in other calculations. Such a Bayesian scheme could also be extended to incorporate expectations for INM parameters via prior distributions in the optimization instead of imposing them as hard parameter bounds as done here. Note that the authors of Refs. [101] conclude that information from infinite

matter should not just be used at saturation density but instead at different densities (within the validity of the EDF approach).

Determining posterior parameter distributions requires a lot of EDF evaluations. Therefore, using techniques to cheaply emulate the calculations are necessary [113, 234, 302]. Having such emulators available would also be very beneficial to investigate other EDF adjustments as discussed in this Chapter, as this would allow to reoptimize the EDF parameters often and so the effect of individual EDF changes could be more easily analyzed. Basis extrapolation techniques might also help; see Refs. [122, 303] for EDF applications and Refs. [304, 305] for a machine learning approach used with NCSM calculations. Employing them would also address the fact that the present calculations are not fully converged with respect to basis size in some heavy nuclei. The quality of the obtained results in heavy nuclei is good anyway. This is likely related to the fact that heavy nuclei are also present in the optimization data set and hence the fit "knows" about the finite basis size. Nevertheless, actually converged calculations would be preferable, in particular in view of EDFs fully determined from first principles.

Finally...

While the path to ab initio EDFs still lies mostly in the dark, the work presented in this thesis tried – and hopefully did – to shed some light on it. Especially the significant improvement found when adding chiral pion exchange terms to Skyrme EDFs is promising and suggests pion exchanges could be relevant ingredients for a desired ab initio EDFs. Many exciting avenues are still to be explored.

A
Appendix

A.1 List of acronyms

Here we give an overview of acronyms used in this thesis. Most acronyms that label variants of density-matrix expansions (see Tab. 3.2) or energy density functionals are not listed here.

3N	three-nucleon
AME	atomic mass evaluation
CC	coupled cluster
DE	double exchange
DFT	density functional theory
DME	density-matrix expansion
EDF	energy density functional
EFT	effective field theory
GUDE	Germany-USA DME EDF
HF	Hartree-Fock
HFB	Hartree-Fock-Bogoliubov
HO	harmonic oscillator
IMSRG	in-medium similarity renormalization group
INM	infinite nuclear matter
IR	intermediate-range
LEC	low-energy constant
LN	Lipkin-Nogami
LO	leading order
LR	long-range
MBPT	many-body perturbation theory
NCSM	no-core shell model
NLO	next-to-leading order
N^2LO	next-to-next-to-leading order
NN	nucleon-nucleon
OBDM	one-body density matrix
PSA	phase-space-averaging
QCD	quantum chromodynamics
RMSD	root-mean-square deviation
SE	single exchange
SR	short-range
SRG	similarity renormalization group

A.2 Detailed values for obtained functionals

Here we provide the interpolation coefficients and experimental data used for the construction of the different GUDE functionals as explained in Secs. 4.1, 4.2, and 4.3.2. We give the coefficients used for approximating the long-range NN potentials by sums of Gaussians in the implementation of the Hartree energy (see Sec. 4.1.3 for details) in Tab. A.1 and the coefficients used for approximating the g coefficient functions entering the NN and 3N long-range Fock contributions (see Sec. 4.1.4 for details) in Tabs. A.2 and A.3. The data that enters the χ^2 [Eq. (4.37)] is given in Tabs. A.4 to A.9.

In addition, we provide in Tabs. A.10 and A.11 the parameters obtained from the EDF optimizations with larger precision than in Tab. 4.3.

Table A.1: Coefficients used for approximating the central NN potentials up to different chiral orders by sums of Gaussians according to Eqs. (4.15) and (4.16). These approximations are used when determining Hartree energies from long-range NN forces. At LO there is no Hartree contribution from central long-range NN forces. Values marked with $*$ are determined from the other coefficients following Eq. (4.18). μ_i are given in fm; W_i and H_i are in MeV.

Order	Parameter	$i=1$	$i=2$	$i=3$	$i=4$	$i=5$
NLO	μ_i	1.861	1.123	0.592	0.547	0.523
	W_i	0.321	5.889	−135.515	297.855	$*$
	H_i	0.643	11.777	−271.031	595.710	$*$
N^{2}LO	μ_i	1.668	1.028	0.557	0.519	0.494
	W_i	−2.568	−67.480	1311.972	−2370.681	$*$
	H_i	1.577	13.128	−529.648	1110.926	$*$
NLOΔ	μ_i	1.628	1.011	0.556	0.514	0.485
	W_i	−2.092	−58.508	915.404	−1548.760	$*$
	H_i	2.223	28.540	−616.435	1140.924	$*$
N^{2}LOΔ	μ_i	1.525	0.976	0.581	0.507	0.455
	W_i	−3.420	−85.755	559.105	−748.259	$*$
	H_i	2.747	37.365	−270.799	379.888	$*$
min. chiral	μ_i	1.668	1.028	0.557	0.519	0.494
	W_i	−3.356	−74.044	1576.796	−2926.144	$*$
	H_i	0	0	0	0	0

Table A.2: Coefficients used for approximating the NN g coefficient functions at different chiral orders according to Eq. (4.24). These approximations are used when determining Fock energies from long-range NN forces. $\tilde{g}_t^{uv}(0)$ and a_i are given in MeV fm^3 for the $g_t^{\rho\rho}$ coefficients and in MeV fm^5 for the other coefficients; b_i are in fm^{3c_i}; c_i are unitless.

Order	Coeff.	$\tilde{g}_t^{uv}(0)$	a_1	b_1	c_1	a_2	b_2	c_2	a_3	b_3	c_3
LO	$g_0^{\rho\rho}$	−97.079	−26.334	1.160	0.787	−15.463	12.061	0.517	50.452	7.710	0.394
	$g_1^{\rho\rho}$	32.360	8.778	1.160	0.787	5.154	12.061	0.517	−16.817	7.710	0.394
	$g_0^{\rho\Delta\rho}$	−135.329	13.408	6.818	0.547	108.740	8.090	0.337	−39.506	6.365	0.381
	$g_1^{\rho\Delta\rho}$	45.110	−4.469	6.818	0.547	−36.247	8.090	0.337	13.169	6.365	0.381
	$g_0^{\rho\tau}$	541.314	−53.632	6.818	0.547	−434.961	8.090	0.337	158.022	6.365	0.381
	$g_1^{\rho\tau}$	−180.438	17.877	6.818	0.547	144.987	8.090	0.337	−52.674	6.365	0.381
	$g_0^{JJ,2}$	511.615	−61.254	5.481	0.551	−365.930	7.883	0.337	128.583	5.205	0.363
	$g_1^{JJ,2}$	−170.538	20.418	5.481	0.551	121.977	7.883	0.337	−42.861	5.205	0.363
	$g_0^{JJ,1}$	−496.761	2.713	2.182	1.967	424.360	7.577	0.339	−169.369	3.874	0.265
	$g_1^{JJ,1}$	165.587	−0.904	2.182	1.967	−141.453	7.577	0.339	56.456	3.874	0.265
NLO	$g_0^{\rho\rho}$	−92.414	−28.350	1.209	0.756	−12.945	13.391	0.533	47.833	7.893	0.397
	$g_1^{\rho\rho}$	18.113	14.799	1.660	0.727	−8.892	6.832	0.490	−5.112	11.436	0.425
	$g_0^{\rho\Delta\rho}$	−133.746	51.826	0.091	0.354	139.152	7.637	0.341	−57.752	5.942	0.339
	$g_1^{\rho\Delta\rho}$	41.059	−10.248	0.791	0.431	−48.978	8.068	0.348	25.518	5.437	0.314
	$g_0^{\rho\tau}$	534.984	−335.837	0.056	0.354	−556.291	7.637	0.341	230.744	5.942	0.339
	$g_1^{\rho\tau}$	−164.235	40.915	0.790	0.431	195.724	8.065	0.348	−101.894	5.436	0.314
	$g_0^{JJ,2}$	529.575	−57.846	4.922	0.542	−380.591	7.819	0.338	134.029	4.915	0.348
	$g_1^{JJ,2}$	−175.125	19.073	5.028	0.543	126.067	7.825	0.338	−44.277	4.973	0.351
	$g_0^{JJ,1}$	−493.051	4.138	1.560	1.692	424.222	7.574	0.339	−171.182	3.873	0.266
	$g_1^{JJ,1}$	169.297	−0.277	7.971	3.165	−141.668	7.594	0.339	55.358	3.818	0.260
N^{2}LO	$g_0^{\rho\rho}$	−79.108	−3.432	44.960	0.819	−22.040	1.814	0.593	36.334	7.990	0.396
	$g_1^{\rho\rho}$	70.310	−19.631	2.125	0.758	11.298	8.128	0.466	−21.219	6.918	0.381
	$g_0^{\rho\Delta\rho}$	−130.284	18.461	0.474	0.386	139.063	7.723	0.342	−60.934	5.783	0.334
	$g_1^{\rho\Delta\rho}$	53.187	−10.110	2.497	0.489	−48.841	8.091	0.348	22.537	5.748	0.319

Table A.2: Continued

Order	Coeff.	$\tilde{g}_t^{uv}(0)$	a_1	b_1	c_1	a_2	b_2	c_2	a_3	b_3	c_3
N^{2}LO	$g_0^{\rho\tau}$	521.136	−73.855	0.474	0.386	−556.197	7.723	0.342	243.692	5.783	0.334
	$g_1^{\rho\tau}$	−212.747	40.422	2.498	0.489	195.244	8.090	0.348	−90.060	5.746	0.319
	$g_0^{JJ,2}$	572.310	−60.009	3.625	0.521	−424.700	7.787	0.341	159.184	4.504	0.308
	$g_1^{JJ,2}$	−136.240	39.531	0.709	0.640	157.807	7.873	0.341	−96.846	3.709	0.264
	$g_0^{JJ,1}$	−484.386	8.572	1.058	1.346	422.202	7.566	0.339	−176.112	3.791	0.265
	$g_1^{JJ,1}$	166.408	−0.678	3.083	2.248	−141.061	7.578	0.339	56.249	3.806	0.263
NLOΔ	$g_0^{\rho\rho}$	−60.147	−3.167	50.494	0.829	−31.522	1.937	0.590	35.523	8.131	0.398
	$g_1^{\rho\rho}$	52.379	−7.073	2.459	0.812	6.943	10.194	0.493	−17.755	7.515	0.390
	$g_0^{\rho\Delta\rho}$	−126.451	30.275	0.721	0.413	158.521	8.292	0.352	−82.741	5.721	0.309
	$g_1^{\rho\Delta\rho}$	48.934	−5.369	2.358	0.474	−45.249	7.777	0.342	18.820	5.854	0.337
	$g_0^{\rho\tau}$	505.803	−121.101	0.721	0.413	−634.086	8.292	0.352	330.963	5.721	0.309
	$g_1^{\rho\tau}$	−195.738	21.469	2.359	0.474	180.903	7.778	0.342	−75.215	5.853	0.337
	$g_0^{JJ,2}$	574.645	−59.569	3.413	0.516	−432.712	7.802	0.341	164.158	4.531	0.304
	$g_1^{JJ,2}$	−143.022	30.181	0.693	0.684	159.723	7.876	0.341	−91.222	3.835	0.265
	$g_0^{JJ,1}$	−486.530	7.308	1.134	1.414	422.779	7.568	0.339	−174.819	3.815	0.265
	$g_1^{JJ,1}$	168.823	−0.321	6.352	2.944	−141.672	7.592	0.339	55.365	3.845	0.261
N^{2}LOΔ	$g_0^{\rho\rho}$	−68.314	−3.596	44.454	0.820	−29.168	1.822	0.606	36.973	7.927	0.396
	$g_1^{\rho\rho}$	62.107	−16.764	1.967	0.746	7.379	9.002	0.464	−16.983	7.496	0.386
	$g_0^{\rho\Delta\rho}$	−129.479	29.112	0.670	0.402	164.128	8.498	0.354	−84.813	5.917	0.307
	$g_1^{\rho\Delta\rho}$	50.622	−8.624	2.324	0.486	−46.907	7.900	0.345	21.081	5.761	0.328
	$g_0^{\rho\tau}$	517.916	−116.447	0.670	0.402	−656.514	8.498	0.354	339.251	5.917	0.307
	$g_1^{\rho\tau}$	−202.490	34.477	2.325	0.486	187.512	7.900	0.345	−84.238	5.760	0.328
	$g_0^{JJ,2}$	580.393	−64.418	3.070	0.514	−444.277	7.854	0.342	173.647	4.549	0.296
	$g_1^{JJ,2}$	−138.925	24.449	0.809	0.812	158.223	7.856	0.341	−92.646	3.698	0.263
	$g_0^{JJ,1}$	−481.221	10.313	0.990	1.276	421.391	7.563	0.339	−178.018	3.758	0.265

Table A.2: Continued

Order	Coeff.	$\tilde{g}_t^{uv}(0)$	a_1	b_1	c_1	a_2	b_2	c_2	a_3	b_3	c_3
N^{2}LOΔ	$g_1^{JJ,1}$	168.009	−0.420	4.647	2.641	−141.531	7.587	0.339	55.577	3.849	0.262
min. chiral	$g_0^{\rho\rho}$	−97.070	−18.405	8.936	0.664	−193.220	−1.755	0.343	188.980	2.680	0.232
	other	0	0	0	0	0	0	0	0	0	0

Table A.3: Coefficients used for approximating the 3N g coefficient functions at different chiral orders according to Eq. (4.25). These approximations are used when determining Fock energies from long-range 3N forces. $\tilde{g}^{uvw}(0)$ and a_i are given in MeV fm^6 for the $g^{\rho_0^3}$ and $g^{\rho_0\rho_1^2}$ coefficients and in MeV fm^8 for the other coefficients; b_i are in fm^{3c_i}; c_i are unitless.

Order	Coeff.	$\tilde{g}^{uvw}(0)$	a_1	b_1	c_1	a_2	b_2	c_2	a_3	b_3	c_3
N^{2}LO	$g^{\rho_0^3}$	71.577	−433.605	2.311	0.694	349.194	5.746	0.436	−52.185	10.952	0.368
	$g^{\rho_0\rho_1^2}$	−71.571	126.250	3.021	0.806	−63.991	8.820	0.504	6.055	18.810	0.418
	$g^{\rho_0^2\tau_0}$	425.441	928.610	3.461	0.544	2750.361	6.273	0.381	−2267.742	9.377	0.381
	$g^{\rho_0\rho_1\tau_1}$	−15.529	183.567	1.298	0.667	−784.702	4.396	0.343	391.108	11.307	0.397
	$g^{\rho_1^2\tau_0}$	−141.822	−76.279	55.391	0.723	127.158	22.884	0.539	−13.319	5.727	0.650
	$g^{\rho_0^2\Delta\rho_0}$	88.874	964.634	1.079	0.512	1202.961	10.231	0.409	−1351.031	4.764	0.297
	$g^{\rho_0\rho_1\Delta\rho_1}$	−59.288	−663.804	12.319	0.467	825.625	2.870	0.229	−179.127	1.941	0.383
	$g^{\rho_1^2\Delta\rho_0}$	−29.634	−44.125	1.730	0.545	−27.748	8.737	0.345	43.810	8.489	0.425
	$g^{\rho_0(\nabla\rho_0)^2}$	649.397	182.875	9.969	0.667	−1279.198	5.309	0.418	609.158	5.180	0.318
	$g^{\rho_0(\nabla\rho_1)^2}$	−216.466	−60.958	9.969	0.667	426.399	5.309	0.418	−203.053	5.180	0.318
	$g^{\rho_0\nabla\rho_0 J_0}$	−603.235	−712.600	1.860	0.517	−327.224	11.989	0.351	679.538	8.413	0.406
	$g^{\rho_0\nabla\rho_1 J_1}$	201.078	237.533	1.860	0.517	109.075	11.989	0.351	−226.513	8.413	0.406
	$g^{\rho_1\nabla\rho_1 J_0}$	−67.032	11.504	0.653	0.419	73.676	7.219	0.343	−34.420	5.246	0.329
	$g^{\rho_1\nabla\rho_0 J_1}$	201.090	238.673	2.093	0.465	−18.630	5.287	0.235	−142.782	8.132	0.381
	$g^{\rho_0 J_0^2,2}$	33.020	507.691	3.827	0.536	1745.313	6.629	0.389	−1350.934	9.247	0.379
	$g^{\rho_0 J_1^2,2}$	−279.115	−312.085	2.840	0.527	−56.249	18.819	0.364	238.968	12.743	0.433
	$g^{\rho_1 J_0 J_1,2}$	−22.033	123.137	1.161	0.476	209.397	10.975	0.405	−185.858	6.970	0.329

Table A.3: Continued

Order	Coeff.	$\tilde{g}_t^{uv}(0)$	a_1	b_1	c_1	a_2	b_2	c_2	a_3	b_3	c_3
	$g^{\rho_0 J_0^2,3}$	−37.902	−343.268	3.998	0.533	−1256.184	6.583	0.385	964.445	9.350	0.380
N^{2}LO	$g^{\rho_0 J_1^2,3}$	280.762	86.793	3.354	0.637	317.869	4.639	0.356	−308.210	9.858	0.389
	$g^{\rho_1 J_0 J_1,3}$	25.281	−91.743	1.380	0.503	−174.413	6.907	0.348	143.686	6.789	0.380
	$g^{\rho_0^3}$	0.007	−322.680	2.172	0.683	316.975	5.495	0.438	−59.455	11.311	0.378
	$g^{\rho_0 \rho_1^2}$	−0.000	101.874	2.498	0.756	−95.436	6.475	0.478	15.788	14.671	0.404
	$g^{\rho_0^2 \tau_0}$	−0.040	918.350	3.279	0.517	3751.450	6.373	0.367	−2776.249	9.227	0.380
	$g^{\rho_0 \rho_1 \tau_1}$	0.015	−321.517	3.572	0.521	−1307.531	6.394	0.376	973.370	9.139	0.379
	$g^{\rho_1^2 \tau_0}$	0.004	−108.914	2.486	0.531	−111.653	10.799	0.342	116.832	10.203	0.417
	$g^{\rho_0^2 \Delta\rho_0}$	0.005	−70.109	4.621	0.829	−354.301	6.258	0.497	252.976	13.304	0.408
	$g^{\rho_0 \rho_1 \Delta\rho_1}$	−0.002	28.850	4.905	0.820	129.308	6.764	0.506	−94.459	13.466	0.409
	$g^{\rho_1^2 \Delta\rho_0}$	0.001	−10.383	1.551	0.616	28.059	6.383	0.467	−13.799	12.830	0.403
	$g^{\rho_0 (\nabla\rho_0)^2}$	318.846	−93.264	4.285	0.727	−165.288	7.951	0.534	57.096	15.274	0.416
NLOΔ	$g^{\rho_0 (\nabla\rho_1)^2}$	−106.282	31.088	4.285	0.727	55.096	7.951	0.534	−19.032	15.274	0.416
	$g^{\rho_0 \nabla\rho_0 J_0}$	0.025	−500.981	1.845	0.514	−571.774	9.958	0.343	583.941	7.985	0.400
	$g^{\rho_0 \nabla\rho_1 J_1}$	−0.008	166.994	1.845	0.514	190.591	9.958	0.343	−194.647	7.985	0.400
	$g^{\rho_1 \nabla\rho_1 J_0}$	0.000	−13.703	2.103	0.533	−12.500	9.933	0.343	13.811	8.539	0.410
	$g^{\rho_1 \nabla\rho_0 J_1}$	−0.003	95.921	2.103	0.533	87.501	9.933	0.343	−96.678	8.539	0.410
	$g^{\rho_0 J_0^2,2}$	−0.026	467.014	3.602	0.515	2082.300	6.426	0.371	−1526.085	9.318	0.380
	$g^{\rho_0 J_1^2,2}$	0.012	−227.443	2.689	0.523	−230.933	11.732	0.343	241.043	11.396	0.423
	$g^{\rho_1 J_0 J_1,2}$	0.003	−65.944	2.938	0.512	−270.738	6.152	0.368	200.944	8.660	0.379
	$g^{\rho_0 J_0^2,3}$	0.018	−299.281	3.589	0.509	−1514.810	6.415	0.364	1088.085	9.486	0.382
	$g^{\rho_0 J_1^2,3}$	−0.009	156.495	2.512	0.518	172.827	11.489	0.342	−175.201	10.877	0.418
	$g^{\rho_1 J_0 J_1,3}$	−0.002	41.267	3.073	0.510	198.776	6.072	0.362	−143.560	8.891	0.381
	$g^{\rho_0^3}$	70.077	−395.595	2.322	0.695	313.109	5.773	0.436	−45.574	10.866	0.366
N^{2}LOΔ	$g^{\rho_0 \rho_1^2}$	−70.072	113.853	3.070	0.812	−51.613	9.558	0.517	3.263	25.361	0.445
	$g^{\rho_0^2 \tau_0}$	429.181	801.787	3.495	0.550	2288.313	6.242	0.383	−1920.582	9.411	0.382

Table A.3: Continued

Order	Coeff.	$\tilde{g}_t^{uv}(0)$	a_1	b_1	c_1	a_2	b_2	c_2	a_3	b_3	c_3
	$g^{\rho_0\rho_1\tau_1}$	−18.010	217.447	1.250	0.598	−651.293	4.096	0.339	298.263	11.897	0.401
	$g^{\rho_1^2\tau_0}$	−143.061	−71.039	2.950	0.598	145.015	9.809	0.428	−26.299	8.817	0.295
	$g^{\rho_0^2\Delta\rho_0}$	87.013	886.884	1.081	0.509	1121.859	10.098	0.406	−1247.766	4.839	0.300
	$g^{\rho_0\rho_1\Delta\rho_1}$	−58.051	−647.843	11.833	0.459	838.141	2.764	0.225	−195.285	1.934	0.367
	$g^{\rho_1^2\Delta\rho_0}$	−29.013	−42.023	1.741	0.543	−25.026	9.192	0.344	41.024	8.627	0.426
	$g^{\rho_0(\nabla\rho_0)^2}$	611.446	163.102	9.986	0.666	−1160.804	5.290	0.417	549.506	5.089	0.315
	$g^{\rho_0(\nabla\rho_1)^2}$	−203.814	−121.795	14.685	0.499	520.353	1.925	0.252	−198.801	1.892	0.333
	$g^{\rho_0\nabla\rho_0 J_0}$	−603.238	−652.638	1.861	0.517	−262.942	−12.392	0.352	612.345	8.457	0.407
$N^2LO\Delta$	$g^{\rho_0\nabla\rho_1 J_1}$	201.079	−217.546	−1.861	0.517	87.647	12.392	0.352	−204.115	8.457	0.407
	$g^{\rho_1\nabla\rho_1 J_0}$	−67.031	9.312	0.740	0.421	73.211	7.221	0.341	−33.214	5.482	0.339
	$g^{\rho_1\nabla\rho_0 J_1}$	201.080	265.394	2.036	0.446	−64.429	3.501	0.235	−128.399	8.051	0.377
	$g^{\rho_0 J_0^2,2}$	36.543	447.602	3.860	0.540	1480.040	6.671	0.392	−1156.794	9.261	0.379
	$g^{\rho_0 J_1^2,2}$	−280.288	−285.965	2.853	0.527	−34.692	22.217	0.374	214.712	12.878	0.433
	$g^{\rho_1 J_0 J_1,2}$	−24.381	122.600	1.187	0.469	223.887	11.111	0.404	−193.483	7.355	0.333
	$g^{\rho_0 J_0^2,3}$	−41.322	−303.153	4.047	0.537	−1057.730	6.627	0.389	821.965	9.368	0.380
	$g^{\rho_0 J_1^2,3}$	281.894	128.853	3.170	0.575	−268.420	11.629	0.443	46.671	9.522	0.295
	$g^{\rho_1 J_0 J_1,3}$	27.558	−87.482	1.405	0.512	−169.185	7.097	0.345	138.337	6.856	0.380

Table A.4: Ground-state energies of deformed nuclei used in GUDE optimization data set. See main text for details on the data source.

Number	Z	N	E_{def} (MeV)
1	108	156	−1925.60791
2	106	154	−1907.95996
3	104	152	−1889.61975
4	102	154	−1897.63623
5	102	152	−1884.59338
6	102	150	−1870.30261
7	100	156	−1901.58997
8	100	154	−1890.02966
9	100	152	−1877.97302
10	100	150	−1864.57471
11	100	148	−1850.60657
12	100	146	−1836.17053
13	98	156	−1891.20447
14	98	154	−1880.36853
15	98	152	−1869.09021
16	98	150	−1856.88000
17	98	148	−1843.88513
18	98	146	−1830.35461
19	98	144	−1816.30310
20	96	150	−1846.97034
21	96	148	−1834.99280
22	96	146	−1822.49829
23	96	144	−1809.43518
24	94	146	−1812.64392
25	94	144	−1800.46362
26	92	146	−1800.92725
27	92	144	−1789.64783
28	92	142	−1777.80481
29	90	142	−1765.96716
30	72	104	−1418.38916
31	70	108	−1431.22510
32	70	100	−1377.74121
33	68	104	−1391.19385
34	68	102	−1378.67602
35	66	102	−1362.57422
36	66	100	−1350.45764
37	66	98	−1337.69824
38	66	96	−1323.76904
39	66	94	−1309.11780
40	66	92	−1293.70984
41	66	90	−1277.68945
42	64	98	−1321.45752
43	64	96	−1308.97620
44	64	94	−1295.58166
45	64	92	−1281.28418
46	64	90	−1266.31262
47	64	88	−1251.17102

Table A.5: Ground-state energies of spherical nuclei used in GUDE optimization data set. See main text for details on the data source.

Number	Z	N	E_{sph} (MeV)
48	82	132	−1662.72424
49	82	130	−1653.94751
50	82	128	−1644.98450
51	82	126	−1635.86194
52	82	124	−1621.75610
53	82	122	−1606.93787
54	82	120	−1591.62598
55	82	118	−1575.79370
56	82	116	−1559.46765
57	50	82	−1102.67541
58	50	74	−1049.78967
59	50	72	−1035.35547
60	50	70	−1020.37073
61	50	68	−1004.78314
62	50	66	−988.51361
63	50	64	−971.40478
64	50	62	−953.35748
65	50	58	−914.48700
66	28	36	−561.71606
67	28	34	−545.22082
68	28	32	−526.80499
69	28	30	−506.41803
70	28	28	−483.95416
71	20	30	−427.48959
72	20	28	−415.98260
73	20	26	−398.75470
74	20	24	−380.94119
75	20	22	−361.87714
76	20	20	−342.03360

Table A.6: Proton point radii used in GUDE optimization data set. See main text for details on the data source.

Number	Z	N	R_p (fm)	Number	Z	N	R_p (fm)
77	82	132	5.51054	91	50	64	4.54874
78	82	130	5.49202	92	50	62	4.53293
79	82	128	5.47280	93	50	58	4.49713
80	82	126	5.45277	94	28	36	3.78398
81	82	124	5.44142	95	28	34	3.76525
82	82	122	5.43117	96	28	32	3.73549
83	82	120	5.42102	97	28	30	3.69753
84	82	118	5.41127	98	28	28	3.64216
85	82	116	5.40223	99	20	30	3.43994
86	50	74	4.61569	100	20	28	3.39764
87	50	72	4.60496	101	20	26	3.41457
88	50	70	4.59281	102	20	24	3.43602
89	50	68	4.57954	103	20	22	3.42430
90	50	66	4.56455	104	20	20	3.39135

Table A.7: Neutron odd-even staggerings used in GUDE optimization data set. See main text for details on the data source.

Number	Z	N	Δ_n (MeV)	Number	Z	N	Δ_n (MeV)
105	100	152	0.50015	109	66	98	0.67862
106	90	142	0.68158	110	50	74	1.25031
107	92	144	0.56900	111	50	70	1.31630
108	72	104	0.67688				

Table A.8: Proton odd-even staggerings used in GUDE optimization data set. See main text for details on the data source.

Number	Z	N	Δ_p (MeV)	Number	Z	N	Δ_p (MeV)
112	96	148	0.56650	115	76	90	1.16116
113	92	142	0.60651	116	68	102	0.50403
114	90	142	0.73727	117	66	94	0.72778

Table A.9: Fission isomer excitation energies used in GUDE optimization data set. See main text for details on the data source.

Number	Z	N	E^* (MeV)	Number	Z	N	E^* (MeV)
118	92	144	2.7500	120	94	146	2.800
119	92	146	2.5576	121	96	146	1.900

Table A.10: Parameters of five GUDE variants obtained in this work. Values are given with larger precision than in Tab. 4.3. The first block contains infinite nuclear matter properties, the second block contains volume parameters, the third block contains surface and pairing parameters. ρ_c is given in fm^{-3}; E, K, a_{sym}, and L_{sym} are in MeV; M_{s}^{*-1} and γ are unitless; $C_{t0}^{\rho\rho}$ and V_0^q are in MeV fm^3; $C_{tD}^{\rho\rho}$ are in MeV fm$^{3+3\gamma}$; $C_t^{\rho\tau}$, $C_t^{\rho\Delta\rho}$, $C_t^{\rho\nabla J}$, and C_t^{JJ} are in MeV fm^5.

	no chiral	LO	NLO	N^{2}LO	N^{2}LO+3N
ρ_c	0.154627	0.154303	0.154226	0.157794	0.157487
E	−15.800000	−15.800000	−15.800000	−15.800000	−15.800617
K	260.000000	260.000000	260.000000	222.156593	215.169356
M_{s}^{*-1}	0.978840	0.957868	0.964136	0.904830	0.902703
a_{sym}	29.947210	30.978217	30.986839	28.074821	28.451480
L_{sym}	41.403904	59.557448	58.929019	34.060157	30.000000
γ	0.467263	0.546481	0.540882	0.357776	0.319539
$C_{00}^{\rho\rho}$	−561.5747594	−493.058565	−498.957047	−478.951236	−501.232886
$C_{10}^{\rho\rho}$	256.474663	175.5386526	204.9642334	235.1914767	261.8034818
$C_{0D}^{\rho\rho}$	771.7501242	768.0645082	766.3179039	833.5514478	764.6499675
$C_{1D}^{\rho\rho}$	−181.0432405	33.9369989	24.91377541	−121.3307494	−130.2450028
$C_0^{\rho\tau}$	−2.837616483	−16.19027949	−14.20939783	−18.20934566	−9.398965365
$C_1^{\rho\tau}$	−36.34101224	−35.72605432	−38.58578858	−31.95034503	−37.2770355
$C_0^{\rho\Delta\rho}$	−41.360849	−37.545052	−38.371795	24.465063	9.378165
$C_1^{\rho\Delta\rho}$	−6.374070	−25.027970	−15.125440	−83.185726	−21.558434
$C_0^{\rho\nabla J}$	−62.313931	−72.932104	−74.231821	−82.640190	−88.285325
$C_1^{\rho\nabla J}$	10.977633	18.125119	15.511063	−39.280488	18.589884
C_0^{JJ}	−43.423512	−75.136767	−75.772409	−53.445835	−78.114179
C_1^{JJ}	−30.103491	−15.011692	−12.348909	12.327645	1.315540
V_0^{n}	−218.419432	−219.915977	−220.892183	−207.226762	−209.130669
V_0^{p}	−259.856128	−263.026416	−263.198016	−246.409462	−255.482939

Table A.11: Parameters of the remaining five GUDE variants obtained in this work. Values are given with larger precision than in Tab. 4.3. The first block contains infinite nuclear matter properties, the second block contains volume parameters, the third block contains surface and pairing parameters. ρ_c is given in fm^{-3}; E, K, a_{sym}, and L_{sym} are in MeV; M_{s}^{*-1} and γ are unitless; $C_{t0}^{\rho\rho}$ and V_0^q are in MeV fm^3; $C_{tD}^{\rho\rho}$ are in MeV fm$^{(3+3\gamma)}$; $C_t^{\rho\tau}$, $C_t^{\rho\Delta\rho}$, $C_t^{\rho\nabla J}$, and C_t^{JJ} are in MeV fm^5.

	NLOΔ	NLOΔ+3N	N^{2}LOΔ	N^{2}LOΔ+3N	min. chiral
ρ_c	0.155710	0.156150	0.156059	0.156813	0.158321
E	−15.800000	−15.800000	−15.800103	−15.800000	−15.830489
K	240.808221	230.949151	236.005642	222.416912	223.630207
M_{s}^{*-1}	0.900000	0.900000	0.900000	0.905720	0.917315
a_{sym}	28.428459	28.626512	28.369537	28.602820	28.577424
L_{sym}	30.000000	30.000000	30.000000	30.000000	30.000000
γ	0.431779	0.384940	0.418363	0.352279	0.362663
$C_{00}^{\rho\rho}$	−440.938936	−469.857840	−414.369856	−458.396247	−448.578043
$C_{10}^{\rho\rho}$	284.2839153	288.3043756	279.5242635	285.9589989	286.4499084
$C_{0D}^{\rho\rho}$	809.5512233	767.9004022	811.1521308	748.3282038	779.7312893
$C_{1D}^{\rho\rho}$	−173.2073388	−151.3897111	−170.0986457	−140.0288978	−194.6211393
$C_0^{\rho\tau}$	−14.09619566	−9.524118645	−15.9958227	−6.596697455	−10.8373869
$C_1^{\rho\tau}$	−37.74910965	−39.96450129	−34.99292774	−38.73238976	−43.55936377
$C_0^{\rho\Delta\rho}$	18.539204	8.200442	26.968500	10.902157	22.529940
$C_1^{\rho\Delta\rho}$	−12.897887	−3.446181	−17.334941	−5.618126	−38.778743
$C_0^{\rho\nabla J}$	−65.546615	−77.680867	−65.286022	−86.266268	−61.387891
$C_1^{\rho\nabla J}$	17.547827	23.477143	14.859272	19.740384	3.420560
C_0^{JJ}	−100.354612	−97.434124	−103.341411	−83.747600	−38.769379
C_1^{JJ}	−10.200099	−8.006188	−10.985856	−2.583113	−4.165623
V_0^{n}	−205.784648	−207.169326	−206.505020	−209.097262	−206.524796
V_0^{p}	−251.862481	−253.725925	−252.490376	−255.283726	−249.407466

Bibliography

[1] A. Fraknoi, D. Morrison, and S. Wolff, *Astronomy 2e* (OpenStax, Houston, 2022) (cit. on p. 1).

[2] M. Wang, G. Audi, A. H. Wapstra, F. G. Kondev, M. MacCormick, X. Xu, and B. Pfeiffer, "The AME2012 atomic mass evaluation", Chin. Phys. C **36**, 1603 (2012) (cit. on p. 2).

[3] A. V. Afanasjev, S. E. Abgemava, D. Ray, and P. Ring, "Nuclear landscape in covariant density functional theory", Phys. Lett. B **726**, 680 (2013), arXiv:1309.3289 [nucl-th] (cit. on pp. 2, 9).

[4] G. Sterman, J. Smith, J. C. Collins, J. Whitmore, R. Brock, J. Huston, J. Pumplin, W.-K. Tung, H. Weerts, C.-P. Yuan, et al., "Handbook of perturbative QCD", Rev. Mod. Phys. **67**, 157 (1995) (cit. on p. 1).

[5] Y. Sumino, "A Modern View of Perturbative QCD and Application to Heavy Quarkonium Systems", 2014, arXiv:1407.5353 [hep-ph] (cit. on p. 1).

[6] R. Gupta, "Introduction to Lattice QCD", 1998, arXiv:hep-lat/9807028 [hep-lat] (cit. on p. 1).

[7] W. Detmold, "Nuclear Physics from Lattice QCD", in *Lattice QCD for Nuclear Physics*, edited by H.-W. Lin and H. B. Meyer (Springer, Cham, 2014), pp. 153–194 (cit. on p. 1).

[8] E. A. Coello Pérez and T. Papenbrock, "Effective field theory for nuclear vibrations with quantified uncertainties", Phys. Rev. C **92**, 064309 (2015), arXiv:1510.02401 [nucl-th] (cit. on p. 1).

[9] P. Navrátil, S. Quaglioni, G. Hupin, C. Romero-Redondo, and A. Calci, "Unified ab initio approaches to nuclear structure and reactions", Phys. Scripta **91**, 053002 (2016), arXiv:1601.03765 [nucl-th] (cit. on p. 2).

[10] G. Hupin, S. Quaglioni, and P. Navrátil, "Ab initio predictions for polarized deuterium-tritium thermonuclear fusion", Nature Commun. **10**, 351 (2019), arXiv:1803.11378 [nucl-th] (cit. on p. 2).

[11] M. R. Mumpower, R. Surman, G. C. McLaughlin, and A. Aprahamian, "The impact of individual nuclear properties on r-process nucleosynthesis", Prog. Part. Nucl. Phys. **86**, 86 (2016), arXiv:1508.07352 [nucl-th], Corrigendum: Prog. Part. Nucl. Phys. **87**, 116 (2016) (cit. on pp. 2, 10, 105).

[12] N. Schunck, J. D. McDonnell, D. Higdon, J. Sarich, and S. M. Wild, "Uncertainty Quantification and Propagation in Nuclear Density Functional Theory", Eur. Phys. J. A **51**, 169 (2015), arXiv:1503.05894 [nucl-th] (cit. on pp. 2, 92).

[13] S. Yoshida, N. Shimizu, T. Togashi, and T. Otsuka, "Uncertainty quantification in the nuclear shell model", Phys. Rev. C **98**, 061301 (2018), arXiv:1810.03263 [nucl-th] (cit. on p. 2).

[14] J. A. Melendez, R. J. Furnstahl, D. R. Phillips, M. T. Pratola, and S. Wesolowski, "Quantifying Correlated Truncation Errors in Effective Field Theory", Phys. Rev. C **100**, 044001 (2019), arXiv:1904.10581 [nucl-th] (cit. on pp. 2, 4).

[15] E. Epelbaum, H.-W. Hammer, and U.-G. Meißner, "Modern Theory of Nuclear Forces", Rev. Mod. Phys. **81**, 1773 (2009), arXiv:0811.1338 [nucl-th] (cit. on pp. 2–5).

[16] M. E. Peskin and D. Y. Schroeder, *An Introduction To Quantum Field Theory* (CRC Press, Boca Raton, 1995) (cit. on p. 2).

[17] A. Ekström, C. Forssén, G. Hagen, G. R. Jansen, W. Jiang, and T. Papenbrock, "What is ab initio in nuclear theory?", Front. Phys. **11**, 1129094 (2023), arXiv:2212.11064 [nucl-th] (cit. on p. 3).

[18] J. A. Sheikh, J. Dobaczewski, P. Ring, L. M. Robledo, and C. Yannouleas, "Symmetry restoration in mean-field approaches", J. Phys. G **48**, 123001 (2021), arXiv:1901.06992 [nucl-th] (cit. on pp. 3, 10, 85).

[19] E. Caurier, G. Martinez-Pinedo, F. Nowacki, A. Poves, and A. P. Zuker, "The Shell model as unified view of nuclear structure", Rev. Mod. Phys. **77**, 427 (2005), eprint: nucl-th/0402046 (cit. on p. 3).

[20] H.-W. Hammer, C. Ji, and D. R. Phillips, "Effective field theory description of halo nuclei", J. Phys. G **44**, 103002 (2017), arXiv:1702.08605 [nucl-th] (cit. on p. 3).

[21] P. Möller and J. R. Nix, "Nuclear masses from a unified macroscopic-microscopic model", Atom. Data Nucl. Data Tabl. **39**, 213 (1988) (cit. on p. 3).

[22] S. Weinberg, "Phenomenological Lagrangians", Physica A **96**, 327 (1979) (cit. on p. 3).

[23] R. Machleidt and D. R. Entem, "Chiral effective field theory and nuclear forces", Phys. Rep. **503**, 1 (2011), arXiv:1105.2919 [nucl-th] (cit. on pp. 3, 4, 6).

[24] R. Machleidt and F. Sammarruca, "Can chiral EFT give us satisfaction?", Eur. Phys. J. A **56**, 95 (2020), arXiv:2001.05615 [nucl-th] (cit. on pp. 3–6).

[25] E. Epelbaum, H. Krebs, and U.-G. Meißner, "Improved chiral nucleon-nucleon potential up to next-to-next-to-next-to-leading order", Eur. Phys. J. A **51**, 53 (2015), arXiv:1412.0142 [nucl-th] (cit. on pp. 4, 44, 54, 65, 78).

[26] R. J. Furnstahl, N. Klco, D. R. Phillips, and S. Wesolowski, "Quantifying truncation errors in effective field theory", Phys. Rev. C **92**, 024005 (2015), arXiv:1506.01343 [nucl-th] (cit. on p. 4).

[27] H.-W. Hammer, S. König, and U. van Kolck, "Nuclear effective field theory: status and perspectives", Rev. Mod. Phys. **92**, 025004 (2020), arXiv:1906.12122 [nucl-th] (cit. on pp. 4, 6).

[28] K. Hebeler, "Three-nucleon forces: Implementation and applications to atomic nuclei and dense matter", Phys. Rept. **890**, 1 (2021), arXiv:2002.09548 [nucl-th] (cit. on pp. 4–6, 8).

[29] S. Weinberg, "Nuclear forces from chiral Lagrangians", Phys. Lett. B **251**, 288 (1990) (cit. on p. 4).

[30] S. Weinberg, "Effective chiral Lagrangians for nucleon-pion interactions and nuclear forces", Nucl. Phys. B **363**, 3 (1991) (cit. on p. 4).

[31] O. Thim, E. May, A. Ekström, and C. Forssén, "Bayesian Analysis of χEFT at Leading Order in a Modified Weinberg Power Counting", 2023, arXiv:2302.12624 [nucl-th] (cit. on p. 4).

[32] R. Machleidt, "Chiral Symmetry and the Nucleon-Nucleon Interaction", Symmetry **8**, 26 (2016) (cit. on p. 4).

[33] A. M. Gasparyan and E. Epelbaum, "Nucleon-nucleon interaction in chiral effective field theory with a finite cutoff: Explicit perturbative renormalization at next-to-leading order", Phys. Rev. C **105**, 024001 (2022), arXiv:2110.15302 [nucl-th] (cit. on p. 4).

[34] H.-W. Hammer, A. Nogga, and A. Schwenk, "Three-body forces: From cold atoms to nuclei", Rev. Mod. Phys. **85**, 197 (2013), arXiv:1210.4273 [nucl-th] (cit. on pp. 5, 104).

[35] J. Hu, Y. Zhang, E. Epelbaum, U.-G. Meißner, and J. Meng, "Nuclear matter properties with nucleon-nucleon forces up to fifth order in the chiral expansion", Phys. Rev. C **96**, 034307 (2017), arXiv:1612.05433 [nucl-th] (cit. on pp. 5, 103).

[36] A. Ekström, G. Hagen, T. D. Morris, T. Papenbrock, and P. D. Schwartz, "Δ isobars and nuclear saturation", Phys. Rev. C **97**, 024332 (2018), arXiv:1707.09028 [nucl-th] (cit. on p. 6).

[37] D. Rodriguez Entem, R. Machleidt, and Y. Nosyk, "Nucleon-Nucleon Scattering Up to N^{5}LO in Chiral Effective Field Theory", Front. in Phys. **8**, 57 (2020) (cit. on p. 6).

[38] E. Epelbaum, H. Krebs, and P. Reinert, "High-precision nuclear forces from chiral EFT: State-of-the-art, challenges and outlook", Front. in Phys. **8**, 98 (2020), arXiv:1911.11875 [nucl-th] (cit. on p. 6).

[39] A. Dyhdalo, R. J. Furnstahl, K. Hebeler, and I. Tews, "Regulator Artifacts in Uniform Matter for Chiral Interactions", Phys. Rev. C **94**, 034001 (2016), arXiv:1602.08038 [nucl-th] (cit. on pp. 6, 44).

[40] D. R. Entem and R. Machleidt, "Accurate charge-dependent nucleon-nucleon potential at fourth order of chiral perturbation theory", Phys. Rev. C **68**, 041001(R) (2003), arXiv:nucl-th/0304018 (cit. on p. 6).

[41] A. Ekström, G. R. Jansen, K. A. Wendt, G. Hagen, T. Papenbrock, B. D. Carlsson, C. Forssén, M. Hjorth-Jensen, P. Navrátil, and W. Nazarewicz, "Accurate nuclear radii and binding energies from a chiral interaction", Phys. Rev. C **91**, 051301(R) (2015), arXiv:1502.04682 [nucl-th] (cit. on p. 6).

[42] T. Hüther, K. Vobig, K. Hebeler, R. Machleidt, and R. Roth, "Family of Chiral Two- plus Three-Nucleon Interactions for Accurate Nuclear Structure Studies", Phys. Lett. B **808**, 135651 (2020), arXiv:1911.04955 [nucl-th] (cit. on p. 6).

[43] C. Drischler, K. Hebeler, and A. Schwenk, "Chiral interactions up to next-to-next-to-next-to-leading order and nuclear saturation", Phys. Rev. Lett. **122**, 042501 (2019), arXiv:1710.08220 [nucl-th] (cit. on pp. 6, 92).

[44] B. Hu, W. Jiang, T. Miyagi, Z. Sun, A. Ekström, C. Forssén, G. Hagen, J. D. Holt, T. Papenbrock, S. R. Stroberg, and I. Vernon, "Ab initio predictions link the neutron skin of ^{208}Pb to nuclear forces", Nature Phys. **18**, 1196 (2022), arXiv:2112.01125 [nucl-th] (cit. on pp. 6, 7).

[45] S. K. Bogner, R. J. Furnstahl, and R. J. Perry, "Similarity Renormalization Group for Nucleon-Nucleon Interactions", Phys. Rev. C **75**, 061001(R) (2007), arXiv:nucl-th/0611045 (cit. on p. 6).

[46] S. K. Bogner, R. J. Furnstahl, R. J. Perry, and A. Schwenk, "Are low-energy nuclear observables sensitive to high-energy phase shifts?", Phys. Lett. B **649**, 488 (2007), arXiv:nucl-th/0701013 (cit. on p. 6).

[47] E. D. Jurgenson, P. Navratil, and R. J. Furnstahl, "Evolving Nuclear Many-Body Forces with the Similarity Renormalization Group", Phys. Rev. C **83**, 034301 (2011), arXiv:1011.4085 [nucl-th] (cit. on p. 6).

[48] I. Tews, Z. Davoudi, A. Ekström, J. D. Holt, K. Becker, R. Briceño, D. J. Dean, W. Detmold, C. Drischler, T. Duguet, et al., "Nuclear Forces for Precision Nuclear Physics: A Collection of Perspectives", Few Body Syst. **63**, 67 (2022), arXiv:2202.01105 [nucl-th] (cit. on p. 6).

[49] D. R. Entem and R. Machleidt, "Chiral 2π exchange at fourth order and peripheral NN scattering", Phys. Rev. C **66**, 014002 (2002), arXiv:nucl-th/0202039 (cit. on p. 6).

[50] E. Epelbaum, H. Krebs, and U.-G. Meißner, "Precision Nucleon-Nucleon Potential at Fifth Order in the Chiral Expansion", Phys. Rev. Lett. **115**, 122301 (2015), arXiv:1412.4623 [nucl-th] (cit. on p. 6).

[51] R. Machleidt and F. Sammarruca, "Chiral EFT based nuclear forces: Achievements and challenges", Phys. Scripta **91**, 083007 (2016), arXiv:1608.05978 [nucl-th] (cit. on p. 6).

[52] E. Epelbaum, W. Glöckle, and U.-G. Meißner, "Improving the convergence of the chiral expansion for nuclear forces II: Low phases and the deuteron", Eur. Phys. J. A **19**, 401 (2004), arXiv:nucl-th/0308010 (cit. on p. 7).

[53] E. Epelbaum, "Few-nucleon forces and systems in chiral effective field theory", Prog. Part. Nucl. Phys. **57**, 654 (2006), arXiv:nucl-th/0509032 (cit. on p. 7).

[54] S. Binder, A. Calci, E. Epelbaum, R. J. Furnstahl, J. Golak, K. Hebeler, H. Kamada, H. Krebs, J. Langhammer, S. Liebig, et al. (LENPIC Collaboration), "Few-nucleon systems with state-of-the-art chiral nucleon-nucleon forces", Phys. Rev. C **93**, 044002 (2016), arXiv:1505.07218 [nucl-th] (cit. on p. 7).

[55] B. R. Barrett, P. Navrátil, and J. P. Vary, "Ab initio no core shell model", Prog. Part. Nucl. Phys. **69**, 131 (2013) (cit. on p. 7).

[56] J. M. Yao, A. Belley, R. Wirth, T. Miyagi, C. G. Payne, S. R. Stroberg, H. Hergert, and J. D. Holt, "*Ab initio* benchmarks of neutrinoless double-β decay in light nuclei with a chiral Hamiltonian", Phys. Rev. C **103**, 014315 (2021), arXiv:2010.08609 [nucl-th] (cit. on p. 7).

[57] R. Roth, S. Binder, K. Vobig, A. Calci, J. Langhammer, and P. Navrátil, "Medium-Mass Nuclei with Normal-Ordered Chiral NN+3N Interactions", Phys. Rev. Lett. **109**, 052501 (2012), arXiv:1112.0287 [nucl-th] (cit. on p. 7).

[58] R. Roth, "Importance Truncation for Large-Scale Configuration Interaction Approaches", Phys. Rev. C **79**, 064324 (2009), arXiv:0903.4605 [nucl-th] (cit. on p. 7).

[59] J. Carlson, S. Gandolfi, F. Pederiva, S. C. Pieper, R. Schiavilla, K. E. Schmidt, and R. B. Wiringa, "Quantum Monte Carlo methods for nuclear physics", Rev. Mod. Phys. **87**, 1067 (2015) (cit. on p. 7).

[60] J. E. Lynn, I. Tews, S. Gandolfi, and A. Lovato, "Quantum Monte Carlo Methods in Nuclear Physics: Recent Advances", Ann. Rev. Nucl. Part. Sci. **69**, 279 (2019), arXiv:1901.04868 [nucl-th] (cit. on p. 7).

[61] H. Hergert, "A Guided Tour of *ab initio* Nuclear Many-Body Theory", Front. in Phys. **8**, 379 (2020), arXiv:2008.05061 [nucl-th] (cit. on pp. 7, 8).

[62] J. Hoppe, A. Tichai, M. Heinz, K. Hebeler, and A. Schwenk, "Natural orbitals for many-body expansion methods", Phys. Rev. C **103**, 014321 (2021), arXiv:2009.04701 [nucl-th] (cit. on pp. 7, 17).

[63] A. Tichai, P. Demol, and T. Duguet, "Towards heavy-mass ab initio nuclear structure: Open-shell Ca, Ni and Sn isotopes from Bogoliubov coupled-cluster theory", 2023, arXiv:2307.15619 [nucl-th] (cit. on p. 7).

[64] G. Hagen, T. Papenbrock, M. Hjorth-Jensen, and D. J. Dean, "Coupled-cluster computations of atomic nuclei", Rep. Prog. Phys. **77**, 096302 (2014), arXiv:1312.7872 [nucl-th] (cit. on pp. 7, 8).

[65] J. E. Drut, R. J. Furnstahl, and L. Platter, "Toward ab initio density functional theory for nuclei", Prog. Part. Nucl. Phys. **64**, 120 (2010), arXiv:0906.1463 [nucl-th] (cit. on pp. 7, 8, 11, 109, 111).

[66] P. Arthuis, C. Barbieri, M. Vorabbi, and P. Finelli, "*Ab Initio* Computation of Charge Densities for Sn and Xe Isotopes", Phys. Rev. Lett. **125**, 182501 (2020), arXiv:2002.02214 [nucl-th] (cit. on p. 7).

[67] T. Miyagi, S. R. Stroberg, P. Navrátil, K. Hebeler, and J. D. Holt, "Converged ab initio calculations of heavy nuclei", Phys. Rev. C **105**, 014302 (2022), arXiv:2104.04688 [nucl-th] (cit. on pp. 7, 30).

[68] K. Hebeler, V. Durant, J. Hoppe, M. Heinz, A. Schwenk, J. Simonis, and A. Tichai, "Normal ordering of three-nucleon interactions for ab initio calculations of heavy nuclei", Phys. Rev. C **107**, 024310 (2023), arXiv:2211.16262 [nucl-th] (cit. on p. 7).

[69] E. Gebrerufael, K. Vobig, H. Hergert, and R. Roth, "Ab Initio Description of Open-Shell Nuclei: Merging No-Core Shell Model and In-Medium Similarity Renormalization Group", Phys. Rev. Lett. **118**, 152503 (2017), arXiv:1610.05254 [nucl-th] (cit. on p. 7).

[70] S. R. Stroberg, A. Calci, H. Hergert, J. D. Holt, S. K. Bogner, R. Roth, and A. Schwenk, "Nucleus-dependent valence-space approach to nuclear structure", Phys. Rev. Lett. **118**, 032502 (2017), arXiv:1607.03229 [nucl-th] (cit. on pp. 7, 104).

[71] T. Miyagi, S. Stroberg, J. Holt, and N. Shimizu, "Ab initio multishell valence-space Hamiltonians and the island of inversion", Phys. Rev. C **102**, 034320 (2020), arXiv:2004.12969 [nucl-th] (cit. on p. 7).

[72] S. R. Stroberg, J. D. Holt, A. Schwenk, and J. Simonis, "*Ab Initio* Limits of Atomic Nuclei", Phys. Rev. Lett. **126**, 022501 (2021), arXiv:1905.10475 [nucl-th] (cit. on p. 7).

[73] V. Somà, C. Barbieri, T. Duguet, and P. Navrátil, "Moving away from singly-magic nuclei with Gorkov Green's function theory", Eur. Phys. J. A **57**, 135 (2021), arXiv:2009.01829 [nucl-th] (cit. on p. 7).

[74] M. Frosini, T. Duguet, J.-P. Ebran, B. Bally, H. Hergert, T. R. Rodríguez, R. Roth, J. Yao, and V. Soma, "Multi-reference many-body perturbation theory for nuclei: III. Ab initio calculations at second order in PGCM-PT", Eur. Phys. J. A **58**, 64 (2022), arXiv:2111.01461 [nucl-th] (cit. on p. 7).

[75] H. Hergert, S. K. Bogner, T. D. Morris, A. Schwenk, and K. Tsukiyama, "The In-Medium Similarity Renormalization Group: A Novel Ab Initio Method for Nuclei", Phys. Rept. **621**, 165 (2016), arXiv:1512.06956 [nucl-th] (cit. on p. 7).

[76] F. Raimondi and C. Barbieri, "Algebraic diagrammatic construction formalism with three-body interactions", Phys. Rev. C **97**, 054308 (2018), arXiv:1709.04330 [nucl-th] (cit. on p. 8).

[77] M. Heinz, A. Tichai, J. Hoppe, K. Hebeler, and A. Schwenk, "In-medium similarity renormalization group with three-body operators", Phys. Rev. C **103**, 044318 (2021), arXiv:2102.11172 [nucl-th] (cit. on p. 8).

[78] T. Duguet, "Towards non-empirical nuclear energy functionals from low-momentum interactions", 2009, https://heberge.lp2ib.in2p3.fr/heberge/EcoleJoliotCurie/coursannee/cours/T-Duguet.pdf (cit. on pp. 8–10, 85).

[79] N. Schunck, J. D. McDonnell, J. Sarich, S. M. Wild, and D. Higdon, "Error Analysis in Nuclear Density Functional Theory", J. Phys. G **42**, 034024 (2015), arXiv:1406.4383 [nucl-th] (cit. on pp. 8, 84, 86).

[80] J.-P. Ebran, E. Khan, T. Niksic, and D. Vretenar, "Density Functional Theory studies of cluster states in nuclei", Phys. Rev. C **90**, 054329 (2014), arXiv:1406.2473 [nucl-th] (cit. on p. 8).

[81] G. Colò, "Nuclear density functional theory", Adv. Phys. X **5**, 1740061 (2020) (cit. on pp. 8, 9).

[82] F. Marino, C. Barbieri, A. Carbone, G. Colò, A. Lovato, F. Pederiva, X. Roca-Maza, and E. Vigezzi, "Nuclear energy density functionals grounded in ab initio calculations", Phys. Rev. C **104**, 024315 (2021), arXiv:2103.14480 [nucl-th] (cit. on pp. 8, 11).

[83] M. Bender, P.-H. Heenen, and P.-G. Reinhard, "Self-consistent mean-field models for nuclear structure", Rev. Mod. Phys. **75**, 121 (2003) (cit. on pp. 8, 28, 31, 76, 77, 84, 92, 105).

[84] N. Schunck, ed., *Energy Density Functional Methods for Atomic Nuclei* (IOP Publishing, Bristol, 2019) (cit. on pp. 8–10).

[85] T. Duguet, J.-P. Ebran, M. Frosini, H. Hergert, and V. Somà, "Rooting the EDF method into the ab initio framework: PGCM-PT formalism based on MR-IMSRG pre-processed Hamiltonians", Eur. Phys. J. A **59**, 13 (2023), arXiv:2209.03424 [nucl-th] (cit. on pp. 8, 11, 110, 111).

[86] P. Hohenberg and W. Kohn, "Inhomogeneous Electron Gas", Phys. Rev. **136**, B864 (1964) (cit. on p. 9).

[87] J. Engel, "Intrinsic-Density Functionals", Phys. Rev. C **75**, 014306 (2007), arXiv:nucl-th/0610043 (cit. on p. 9).

[88] N. Barnea, "Density Functional Theory for Self-Bound Systems", Phys. Rev. C **76**, 067302 (2007), arXiv:0711.0963 [nucl-th] (cit. on p. 9).

[89] B. G. Giraud, B. K. Jennings, and B. R. Barrett, "Existence of a Density Functional for an Intrinsic State", Phys. Rev. A **78**, 032507 (2008), arXiv:0707.3099 [nucl-th] (cit. on p. 9).

[90] J. Messud, M. Bender, and E. Suraud, "Density Functional Theory and Kohn-Sham Scheme for Self-Bound Systems", Phys. Rev. C **80**, 054314 (2009), arXiv:0904.0162 [nucl-th] (cit. on p. 9).

[91] W. Kohn and L. J. Sham, "Self-Consistent Equations Including Exchange and Correlation Effects", Phys. Rev. **140**, A1133 (1965) (cit. on pp. 9, 109).

[92] A. Bhattacharyya and R. J. Furnstahl, "The Kinetic energy density in Kohn-Sham density functional theory", Nucl. Phys. A **747**, 268 (2005), arXiv:nucl-th/0408014 (cit. on pp. 9, 21).

[93] J. Meng and P. Zhao, "Relativistic density functional theory in nuclear physics", AAPPS Bulletin **31**, 1 (2021) (cit. on p. 9).

[94] J. R. Stone and P.-G. Reinhard, "The Skyrme Interaction in finite nuclei and nuclear matter", Prog. Part. Nucl. Phys. **58**, 587 (2007), arXiv:nucl-th/0607002 (cit. on p. 9).

[95] L. M. Robledo, T. R. Rodríguez, and R. R. Rodríguez-Guzmán, "Mean field and beyond description of nuclear structure with the Gogny force: A review", J. Phys. G **46**, 013001 (2019), arXiv:1807.02518 [nucl-th] (cit. on pp. 9, 10).

[96] P.-G. Reinhard and W. Nazarewicz, "Toward a global description of nuclear charge radii: Exploring the Fayans energy density functional", Phys. Rev. C **95**, 064328 (2017), arXiv:1704.07430 [nucl-th] (cit. on pp. 9, 111, 112).

[97] A. Bulgac, M. M. Forbes, S. Jin, R. Navarro Perez, and N. Schunck, "Minimal nuclear energy density functional", Phys. Rev. C **97**, 044313 (2018), arXiv:1708.08771 [nucl-th] (cit. on pp. 9, 11, 112).

[98] M. Baldo, L. M. Robledo, P. Schuck, and X. Viñas, "Barcelona-Catania-Paris-Madrid functional with a realistic effective mass", Phys. Rev. C **95**, 014318 (2017), arXiv:1604.01543 [nucl-th] (cit. on pp. 9, 11).

[99] T. Niksic, D. Vretenar, and P. Ring, "Relativistic Nuclear Energy Density Functionals: Mean-Field and Beyond", Prog. Part. Nucl. Phys. **66**, 519 (2011), arXiv:1102.4193 [nucl-th] (cit. on p. 9).

[100] U. C. Perera, A. V. Afanasjev, and P. Ring, "Charge radii in covariant density functional theory: A global view", Phys. Rev. C **104**, 064313 (2021), arXiv:2108.02245 [nucl-th] (cit. on p. 9).

[101] M. Dutra, O. Lourenco, J. S. Sa Martins, A. Delfino, J. R. Stone, and P. D. Stevenson, "Skyrme Interaction and Nuclear Matter Constraints", Phys. Rev. C **85**, 035201 (2012), arXiv:1202.3902 [nucl-th] (cit. on pp. 9, 85, 91, 113).

[102] M. Kortelainen, J. McDonnell, W. Nazarewicz, P.-G. Reinhard, J. Sarich, N. Schunck, M. V. Stoitsov, and S. M. Wild, "Nuclear energy density optimization: Large deformations", Phys. Rev. C **85**, 024304 (2012), arXiv:1111.4344 [nucl-th] (cit. on pp. 9, 77, 84, 85, 98, 99, 101, 111).

[103] S. Hilaire and M. Girod, "Large-scale mean-field calculations from proton to neutron drip lines using the D1S Gogny force", Eur. Phys. J. A **33**, 237 (2007) (cit. on p. 9).

[104] J. Erler, N. Birge, M. Kortelainen, W. Nazarewicz, E. Olsen, A. M. Perhac, and M. Stoitsov, "The limits of the nuclear landscape", Nature **486**, 509 (2012) (cit. on pp. 9, 10, 104).

[105] I. V. Panov, I. Y. Korneev, T. Rauscher, G. Martínez-Pinedo, A. Kelić-Heil, N. T. Zinner, and F.-K. Thielemann, "Neutron-induced astrophysical reaction rates for translead nuclei", Astron. Astrophys. **513**, A61 (2010), arXiv:0911.2181 [astro-ph.SR] (cit. on p. 10).

[106] D. Martin, A. Arcones, W. Nazarewicz, and E. Olsen, "Impact of Nuclear Mass Uncertainties on the r Process", Phys. Rev. Lett. **116**, 121101 (2016), arXiv:1512.03158 [nucl-th] (cit. on pp. 10, 111).

[107] T. Kajino, W. Aoki, A. B. Balantekin, R. Diehl, M. A. Famiano, and G. J. Mathews, "Current status of r-process nucleosynthesis", Prog. Part. Nucl. Phys. **107**, 109 (2019), arXiv:1906.05002 [astro-ph.HE] (cit. on p. 10).

[108] Y. L. Zhu, K. Lund, J. Barnes, T. M. Sprouse, N. Vassh, G. C. McLaughlin, M. R. Mumpower, and R. Surman, "Modeling Kilonova Light Curves: Dependence on Nuclear Inputs", Astrophys. J. **906**, 94 (2021), arXiv:2010.03668 [astro-ph.HE] (cit. on pp. 10, 111).

[109] T. M. Sprouse, R. Navarro Perez, R. Surman, M. R. Mumpower, G. C. McLaughlin, and N. Schunck, "Propagation of Statistical Uncertainties of Skyrme Mass Models to Simulations of r-Process Nucleosynthesis", Phys. Rev. C **101**, 055803 (2020), arXiv:1901.10337 [nucl-th] (cit. on pp. 10, 107).

[110] S. Goriely and I. Kullmann, "R-Process Nucleosynthesis in Neutron Star Merger Ejecta and Nuclear Dependences", in *Handbook of Nuclear Physics*, edited by I. Tanihata, H. Toki, and T. Kajino (Springer, Singapore, 2023), pp. 1–26 (cit. on pp. 10, 111).

[111] M. Kortelainen, J. Dobaczewski, K. Mizuyama, and J. Toivanen, "Dependence of single-particle energies on coupling constants of the nuclear energy density functional", Phys. Rev. C **77**, 064307 (2008), arXiv:0803.2291 [nucl-th] (cit. on p. 10).

[112] M. Kortelainen, J. McDonnell, W. Nazarewicz, E. Olsen, P.-G. Reinhard, J. Sarich, N. Schunck, S. M. Wild, D. Davesne, J. Erler, and A. Pastore, "Nuclear energy density optimization: Shell structure", Phys. Rev. C **89**, 054314 (2014), arXiv:1312.1746 [nucl-th] (cit. on pp. 10, 77, 84, 85, 87–89, 92, 98, 111).

[113] J. D. McDonnell, N. Schunck, D. Higdon, J. Sarich, S. M. Wild, and W. Nazarewicz, "Uncertainty Quantification for Nuclear Density Functional Theory and Information Content of New Measurements", Phys. Rev. Lett. **114**, 122501 (2015), arXiv:1501.03572 [nucl-th] (cit. on pp. 10, 92, 106, 113, 114).

[114] J. L. Egido, "State-of-the-art of beyond mean field theories with nuclear density functionals", Phys. Scripta **91**, 073003 (2016), arXiv:1606.00407 [nucl-th] (cit. on p. 10).

[115] M. Grasso, "Effective density functionals beyond mean field", Prog. Part. Nucl. Phys. **106**, 256 (2019), arXiv:1811.01039 [nucl-th] (cit. on pp. 10, 113).

[116] T. Duguet and P. Bonche, "Density Dependence of Two-Body Interactions for Beyond Mean-Field Calculations", Phys. Rev. C **67**, 054308 (2003), arXiv:nucl-th/0210055 (cit. on pp. 10, 95).

[117] B. G. Carlsson, J. Dobaczewski, and M. Kortelainen, "Local nuclear energy density functional at next-to-next-to-next-to-leading order", Phys. Rev. C **78**, 044326 (2008), arXiv:0807.4925 [nucl-th], Erratum: Phys. Rev. C **81**, 029904(E) (2010) (cit. on pp. 10, 28, 33).

[118] F. Raimondi, K. Bennaceur, and J. Dobaczewski, "Nonlocal energy density functionals for low-energy nuclear structure", J. Phys. G **41**, 055112 (2014), arXiv:1402.1556 [nucl-th] (cit. on p. 10).

[119] X. Xiong, J. Pei, and W. Chen, "Extension and parametrization of high-order density dependence in Skyrme forces", Phys. Rev. C **93**, 024311 (2016), arXiv:1509.07633 [nucl-th] (cit. on p. 10).

[120] P. Becker, D. Davesne, J. Meyer, J. Navarro, and A. Pastore, "Solution of Hartree-Fock-Bogoliubov equations and fitting procedure using the N2LO Skyrme pseudopotential in spherical symmetry", Phys. Rev. C **96**, 044330 (2017), arXiv:1707.08622 [nucl-th] (cit. on p. 10).

[121] P. Baczyk, J. Dobaczewski, M. Konieczka, T. Nakatsukasa, K. Sato, and W. Satula, "Isospin-symmetry breaking in masses of $N \simeq Z$ nuclei", Phys. Lett. B **778**, 178 (2018), arXiv:1701.04628 [nucl-th] (cit. on p. 10).

[122] K. Bennaceur, J. Dobaczewski, T. Haverinen, and M. Kortelainen, "Properties of spherical and deformed nuclei using regularized pseudopotentials in nuclear DFT", J. Phys. G **47**, 105101 (2020), arXiv:2003.10990 [nucl-th] (cit. on pp. 10, 114).

[123] L. Batail, D. Davesne, S. Péru, P. Becker, A. Pastore, and J. Navarro, "A three-ranged Gogny interaction in touch with pion exchange: promising results to improve infinite matter properties", Eur. Phys. J. A **59**, 173 (2023), arXiv:2212.00400 [nucl-th], Erratum: Eur. Phys. J. A **59**, 219 (2023) (cit. on p. 10).

[124] J. Erler, P. Klupfel, and P.-G. Reinhard, "Misfits in Skyrme-Hartree-Fock", J. Phys. G **37**, 064001 (2010), arXiv:1002.0027 [nucl-th] (cit. on p. 10).

[125] A. Taninah, S. E. Agbemava, and A. V. Afanasjev, "Covariant density functional theory input for r-process simulations in actinides and superheavy nuclei: the ground state and fission properties", Phys. Rev. C **102**, 054330 (2020), arXiv:2011.13368 [nucl-th] (cit. on pp. 10, 107).

[126] R. J. Furnstahl, "EFT for DFT", in *Renormalization Group and Effective Field Theory Approaches to Many-Body Systems*, edited by J. Polonyi and A. Schwenk, Lecture Notes in Physics (Springer, Heidelberg, 2012), pp. 133–191, arXiv:nucl-th/0702040 (cit. on pp. 10, 109).

[127] M. Grasso, D. Lacroix, and U. van Kolck, "From effective field theories to effective density functionals in and beyond the mean field", Phys. Scripta **91**, 063005 (2016) (cit. on pp. 10, 109).

[128] C.-J. Yang, M. Grasso, and D. Lacroix, "Toward a systematic strategy for defining power counting in the construction of the energy density functional theory", Phys. Rev. C **96**, 034318 (2017), arXiv:1706.00258 [nucl-th] (cit. on pp. 10, 109).

[129] R. J. Furnstahl, "Turning the nuclear energy density functional method into a proper effective field theory: reflections", Eur. Phys. J. A **56**, 85 (2020), arXiv:1906.00833 [nucl-th] (cit. on pp. 10, 11, 109–111).

[130] K. Fraboulet and J.-P. Ebran, "Addressing energy density functionals in the language of path-integrals I: comparative study of diagrammatic techniques applied to the (0 + 0)-D O(N)-symmetric φ^4-theory", Eur. Phys. J. A **59**, 91 (2023), arXiv:2208.13044 [nucl-th] (cit. on pp. 10, 109).

[131] K. Fraboulet and J.-P. Ebran, "Addressing energy density functionals in the language of path-integrals II: Comparative study of functional renormalization group techniques applied to the (0+0)-D $O(N)$-symmetric φ^4-theory", (2022), arXiv:2210.07748 [cond-mat.str-el] (cit. on pp. 10, 109).

[132] A. Schwenk and J. Polonyi, "Towards density functional calculations from nuclear forces", 2004, arXiv:nucl-th/0403011 (cit. on p. 11).

[133] M. Baldo, P. Schuck, and X. Vinas, "Kohn-Sham density functional approach to nuclear binding", Phys. Lett. B **663**, 390 (2008), arXiv:0706.0658 [nucl-th] (cit. on p. 11).

[134] T. Lesinski, T. Duguet, K. Bennaceur, and J. Meyer, "Non-empirical pairing energy density functional. First order in the nuclear plus Coulomb two-body interaction", Eur. Phys. J. A **40**, 121 (2009), arXiv:0809.2895 [nucl-th] (cit. on pp. 11, 112).

[135] B. Gebremariam, T. Duguet, and S. K. Bogner, "Improved density matrix expansion for spin-unsaturated nuclei", Phys. Rev. C **82**, 014305 (2010), arXiv:0910.4979 [nucl-th] (cit. on pp. 11, 12, 21, 29, 32–35, 37, 50, 64, 72, 81, 82, 109).

[136] D. Gambacurta, L. Li, G. Colo, U. Lombardo, N. Van Giai, and W. Zuo, "Determination of local energy density functionals from Brueckner-Hartree-Fock calculations", Phys. Rev. C **84**, 024301 (2011) (cit. on p. 11).

[137] X. Roca-Maza, X. Vinas, M. Centelles, P. Ring, and P. Schuck, "Relativistic mean field interaction with density dependent meson-nucleon vertices based on microscopical calculations", Phys. Rev. C **84**, 054309 (2011), arXiv:1110.2311 [nucl-th], Erratum: Phys. Rev. C **93**, 069905(E) (2016) (cit. on p. 11).

[138] S. Kemler, M. Pospiech, and J. Braun, "Formation of selfbound states in a one-dimensional nuclear model—a renormalization group based density functional study", J. Phys. G **44**, 015101 (2017), arXiv:1606.04388 [nucl-th] (cit. on p. 11).

[139] C. J. Yang, M. Grasso, and D. Lacroix, "From dilute matter to the equilibrium point in the energy–density–functional theory", Phys. Rev. C **94**, 031301 (2016), arXiv:1604.06587 [nucl-th] (cit. on p. 11).

[140] R. Navarro Pérez, N. Schunck, A. Dyhdalo, R. J. Furnstahl, and S. K. Bogner, "Microscopically based energy density functionals for nuclei using the density matrix expansion. II. Full optimization and validation", Phys. Rev. C **97**, 054304 (2018), arXiv:1801.08615 [nucl-th] (cit. on pp. 11, 12, 35, 43, 61, 65, 67, 70, 73, 75–80, 82, 84–89, 101, 106, 109, 111).

[141] S. Shen, H. Liang, W. H. Long, J. Meng, and P. Ring, "Towards an *ab initio* covariant density functional theory for nuclear structure", Prog. Part. Nucl. Phys. **109**, 103713 (2019), arXiv:1904.04977 [nucl-th] (cit. on p. 11).

[142] G. Salvioni, J. Dobaczewski, C. Barbieri, G. Carlsson, A. Idini, and A. Pastore, "Model nuclear energy density functionals derived from ab initio calculations", J. Phys. G **47**, 085107 (2020), arXiv:2002.01903 [nucl-th] (cit. on p. 11).

[143] S. Burrello, J. Bonnard, and M. Grasso, "Application of an ab-initio-inspired energy density functional to nuclei: impact of the effective mass and the slope of the symmetry energy on bulk and surface properties", Phys. Rev. C **103**, 064317 (2021), arXiv:2103.05996 [nucl-th] (cit. on p. 11).

[144] Y. N. Zhang, S. K. Bogner, and R. J. Furnstahl, "Incorporating Brueckner-Hartree-Fock correlations in energy density functionals", Phys. Rev. C **98**, 064306 (2018), arXiv:1807.02916 [nucl-th] (cit. on pp. 11, 31, 113).

[145] B. Gebremariam, S. K. Bogner, and T. Duguet, "Microscopically-constrained Fock energy density functionals from chiral effective field theory. I. Two-nucleon interactions", Nucl. Phys. A **851**, 17 (2011), arXiv:1003.5210 [nucl-th] (cit. on pp. 11, 12, 28, 32, 34, 35, 37, 68, 72, 82, 109).

[146] Z. H. Sun, C. A. Bell, G. Hagen, and T. Papenbrock, "How to renormalize coupled cluster theory", Phys. Rev. C **106**, L061302 (2022), arXiv:2205.12990 [nucl-th] (cit. on p. 11).

[147] B. Gebremariam, S. K. Bogner, and T. Duguet, "Symbolic computation of the Hartree-Fock energy from a chiral EFT three-nucleon interaction at N^2LO", Comput. Phys. Commun. **181**, 1167 (2010), arXiv:0912.3086 [physics.comp-ph] (cit. on pp. 12, 109).

[148] M. Stoitsov, M. Kortelainen, S. K. Bogner, T. Duguet, R. J. Furnstahl, B. Gebremariam, and N. Schunck, "Microscopically-based energy density functionals for nuclei using the density matrix expansion: Implementation and pre-optimization", Phys. Rev. C **82**, 054307 (2010), arXiv:1009.3452 [nucl-th] (cit. on pp. 12, 85, 102, 109).

[149] A. Dyhdalo, S. K. Bogner, and R. J. Furnstahl, "Applying the Density Matrix Expansion with Coordinate-Space Chiral Interactions", Phys. Rev. C **95**, 054314 (2017), arXiv:1611.03849 [nucl-th] (cit. on pp. 12, 42, 63–65, 67, 68, 70, 78, 81, 82, 109, 111).

[150] L. Zurek, E. A. Coello Pérez, S. K. Bogner, R. J. Furnstahl, and A. Schwenk, "Comparing different density-matrix expansions for long-range pion exchange", Phys. Rev. C **103**, 014325 (2021), arXiv:2010.12518 [nucl-th] (cit. on pp. 13, 28).

[151] L. Zurek, S. K. Bogner, R. J. Furnstahl, R. Navarro Pérez, N. Schunck, and A. Schwenk, "Optimized nuclear energy density functionals including long-range pion contributions", 2023, arXiv:2307.13568 [nucl-th] (cit. on pp. 13, 75, 100, 101).

[152] A. Tichai, P. Arthuis, K. Hebeler, M. Heinz, J. Hoppe, A. Schwenk, and L. Zurek, "Least-square approach for singular value decompositions of scattering problems", Phys. Rev. C **106**, 024320 (2022), arXiv:2205.10087 [nucl-th] (cit. on p. 13).

[153] A. Tichai, P. Arthuis, K. Hebeler, M. Heinz, J. Hoppe, T. Miyagi, A. Schwenk, and L. Zurek, "Low-Rank Decompositions of Three-Nucleon Forces via Randomized Projections", 2023, arXiv:2307.15572 [nucl-th] (cit. on p. 13).

[154] P. Ring and P. Schuck, *The Nuclear Many-Body Problem* (Springer, Berlin, 2004) (cit. on pp. 16–18, 20–23, 25).

[155] J. Dobaczewski, "Interactions, symmetry breaking, and effective fields from quarks to nuclei: A Primer in nuclear theory", 2003, arXiv:nucl-th/0301069 [nucl-th] (cit. on pp. 16, 17, 31).

[156] P. A. M. Dirac, "Note on Exchange Phenomena in the Thomas Atom", Proc. Cambridge Phil. Soc. **26**, 376 (1930) (cit. on p. 17).

[157] K. Kumar, K. L. Couteur, and M. Roy, "Nuclear potential energy and the single-particle density matrix", Nucl. Phys. **60**, 634 (1964) (cit. on p. 17).

[158] A. Tichai, "Many-Body Perturbation Theory for Ab Initio Nuclear Structure", PhD thesis (Technische Universiät Darmstadt, 2017), https://tuprints.ulb.tu-darmstadt.de/6942/ (cit. on pp. 18, 24).

[159] E. Koch, "Mean-Field Theory: Hartree-Fock and BCS", in *Quantum Materials: Experiments and Theory*, edited by E. Pavarini, E. Koch, J. van den Brink, and G. Sawatzky (Forschungszentrum Jülich, Jülich, 2016), pp. 2.16–2.18 (cit. on p. 18).

[160] W. Younes, D. M. Gogny, and J.-F. Berger, *A Microscopic Theory of Fission Dynamics Based on the Generator Coordinate Method* (Springer, Cham, 2019) (cit. on pp. 20, 24).

[161] G. F. Bertsch, "Nuclear pairing: Basic phenomena revisited", in *Fifty Years of Nuclear BCS*, edited by R. Broglia and V. Zelevinsky (World Scientific, Singapore, Mar. 2012), arXiv:1203.5529 [nucl-th] (cit. on pp. 22, 23).

[162] B. S. Ishkhanov, M. E. Stepanov, and T. Y. Tretyakova, "Nucleon pairing in atomic nuclei", Moscow Univ. Phys. Bull. **69**, 1 (2014) (cit. on p. 22).

[163] M. Goeppert Mayer, "Nuclear Configurations in the Spin-Orbit Coupling Model. 2. Theoretical Considerations", Phys. Rev. **78**, 22 (1950) (cit. on p. 22).

[164] S. Frauendorf and A. O. Macchiavelli, "Overview of neutron–proton pairing", Prog. Part. Nucl. Phys. **78**, 24 (2014), arXiv:1405.1652 [nucl-th] (cit. on p. 23).

[165] M. Anguiano, A. M. Lallena, G. Co', and V. De Donno, "A study of self-consistent Hartree–Fock plus Bardeen–Cooper–Schrieffer calculations with finite-range interactions", J. Phys. G **41**, 025102 (2014), arXiv:1312.0774 [nucl-th], Corrigendum: J. Phys. G **42**, 079501 (2015) (cit. on p. 23).

[166] M. V. Stoitsov, J. Dobaczewski, W. Nazarewicz, and P. Ring, "Axially deformed solution of the Skyrme-Hartree-Fock-Bogolyubov equations using the transformed harmonic oscillator basis: The Program HFBTHO (v1.66p)", Comput. Phys. Commun. **167**, 43 (2005), arXiv:nucl-th/0406075 (cit. on pp. 24, 81, 83, 84).

[167] J. Dobaczewski, H. Flocard, and J. Treiner, "Hartree-Fock-Bogolyubov description of nuclei near the neutron-drip line", Nucl. Phys. **A422**, 103 (1984) (cit. on pp. 25, 83).

[168] J. W. Negele and D. Vautherin, "Density-Matrix Expansion for an Effective Nuclear Hamiltonian", Phys. Rev. C **5**, 1472 (1972) (cit. on pp. 27, 30, 33–35, 64, 72).

[169] J. W. Negele and D. Vautherin, "Density-matrix expansion for an effective nuclear Hamiltonian. II", Phys. Rev. C **11**, 1031 (1975) (cit. on pp. 27, 30, 34, 35, 72).

[170] B. G. Carlsson and J. Dobaczewski, "Convergence of density-matrix expansions for nuclear interactions", Phys. Rev. Lett. **105**, 122501 (2010), arXiv:1003.2543 [nucl-th] (cit. on pp. 27, 29, 32–35, 37, 42, 58, 64, 72, 93, 94).

[171] B. B. Gebremariam, "Towards a microscopic energy density functional for nuclei", PhD thesis (Michigan State University, 2010), https://groups.nscl.msu.edu/nscl_library/Thesis/Gebremariam,%20Biruk%20B.pdf (cit. on pp. 27, 72).

[172] L. Zurek, "Exploring density-matrix expansions for local chiral interactions", Master's thesis (Technische Universität Darmstadt, 2019) (cit. on p. 28).

[173] E. Perlińska, S. G. Rohoziński, J. Dobaczewski, and W. Nazarewicz, "Local density approximation for proton neutron pairing correlations: Formalism", Phys. Rev. C **69**, 014316 (2004) (cit. on pp. 29, 77, 84).

[174] J. C. Slater, "A Simplification of the Hartree-Fock Method", Phys. Rev. **81**, 385 (1951) (cit. on pp. 30, 31, 34, 77).

[175] J. Dobaczewski, B. G. Carlsson, and M. Kortelainen, "The Negele-Vautherin density matrix expansion applied to the Gogny force", J. Phys. G **37**, 075106 (2010), arXiv:1002.3646 [nucl-th] (cit. on pp. 31, 35, 37, 48, 50, 58).

[176] S. N. Maximoff and G. E. Scuseria, "Exchange energy functionals based on the full fourth-order density matrix expansion", J. Chem. Phys. **114**, 10591 (2001) (cit. on pp. 32, 33).

[177] D. W. L. Sprung, M. Vallieres, X. Campi, and C.-M. Ko, "A note on the validity of the density matrix expansion", Nucl. Phys. A **253**, 1 (1975) (cit. on p. 34).

[178] X. Campi and A. Bouyssy, "A simple approximation for the nuclear density matrix", Phys. Lett. **73B**, 263 (1978) (cit. on pp. 34, 38, 53, 54).

[179] R. K. Bhaduri and L. F. Zaifman, "The harmonic oscillator approximation to the density matrix", Can. J. Phys. **57**, 1990 (1979) (cit. on pp. 34, 35, 59).

[180] S. K. Ghosh and R. G. Parr, "Phase-space approach to the exchange-energy functional of density-functional theory", Phys. Rev. A **34**, 785 (1986) (cit. on p. 34).

[181] J. Meyer, J. Bartel, M. Brack, P. Quentin, and S. Aicher, "A simple Gaussian approximation for the one-body density matrix", Phys. Lett. B **172**, 122 (1986) (cit. on pp. 34, 36).

[182] T. Van Voorhis and G. E. Scuseria, "Exchange energy functionals based on the density matrix expansion of the Hartree-Fock exchange term", Mol. Phys. **92**, 601 (1997) (cit. on pp. 34, 37).

[183] M. Abramowitz and I. A. Stegun, in *Handbook of Mathematical Functions*, 10th printing (United States Department of Commerce, National Bureau of Standards, 1972), p. 364 (cit. on p. 35).

[184] G. J. Laming, N. C. Handy, and W. H. Miller, "Comparison of the Gaussian and Bessel Function Exchange Functionals with the Hartree-Fock Exchange for Molecules", J. Phys. Chem. **99**, 1880 (1995) (cit. on p. 35).

[185] R. M. Koehl, G. K. Odom, and G. E. Scuseria, "The use of density matrix expansions for calculating molecular exchange energies", Mol. Phys. **87**, 835 (1996) (cit. on pp. 35, 37, 41, 53, 54).

[186] J. F. Berger, M. Girod, and D. Gogny, "Time-dependent quantum collective dynamics applied to nuclear fission", Comput. Phys. Commun. **63**, 365 (1991) (cit. on pp. 35, 58, 93).

[187] R. G. Parr, K. Rupnik, and S. K. Ghosh, "Phase-Space Approach to the Density-Functional Calculation of Compton Profiles of Atoms and Molecules", Phys. Rev. Lett. **56**, 1555 (1986) (cit. on p. 35).

[188] M. Berkowitz, "Exponential approximation for the density matrix and the Wigner's distribution", Chem. Phys. Lett. **129**, 486 (1986) (cit. on p. 36).

[189] C. Lee and R. G. Parr, "Gaussian and other approximations to the first-order density matrix of electronic systems, and the derivation of various local-density-functional theories", Phys. Rev. A **35**, 2377 (1987) (cit. on pp. 36, 37).

[190] R. K. Bhaduri and D. W. L. Sprung, "Density matrix expansion in a solvable model", Nucl. Phys. A **297**, 365 (1978) (cit. on p. 37).

[191] K. Davies, S. Krieger, and M. Baranger, "A study of the Hartree-Fock approximation as applied to finite nuclei", Nuclear Physics **84**, 545 (1966) (cit. on p. 37).

[192] J. Dobaczewski and J. Dudek, "Time-odd components in the mean field of rotating superdeformed nuclei", Phys. Rev. C **52**, 1827 (1995), arXiv:nucl-th/9502030 [nucl-th], Erratum: Phys. Rev. C **55**, 3177 (1997) (cit. on p. 37).

[193] D. Davesne, P. Becker, A. Pastore, and J. Navarro, "Infinite matter properties and zero-range limit of non-relativistic finite-range interactions", Annals Phys. **375**, 288 (2016), arXiv:1607.00835 [nucl-th] (cit. on p. 37).

[194] Y. M. Engel, D. M. Brink, K. Goeke, S. J. Krieger, and D. Vautherin, "Time-dependent hartree-fock theory with Skyrme's interaction", Nucl. Phys. A **249**, 215 (1975) (cit. on p. 37).

[195] E. Chabanat, P. Bonche, P. Haensel, J. Meyer, and R. Schaeffer, "A Skyrme parametrization from subnuclear to neutron star densities. 2. Nuclei far from stablities", Nucl. Phys. A **635**, 231 (1998), Erratum: Nucl. Phys. A **643**, 441 (1998) (cit. on pp. 38, 42, 68, 79, 89, 94).

[196] K. Bennaceur and J. Dobaczewski, "Coordinate-space solution of the Skyrme-Hartree-Fock-Bogolyubov equations within spherical symmetry. The Program HFBRAD (v1.00)", Comput. Phys. Commun. **168**, 96 (2005), arXiv:nucl-th/0501002 [nucl-th] (cit. on pp. 42, 77, 83).

[197] B. G. Carlsson, J. Dobaczewski, J. Toivanen, and P. Veselý, "Solution of self-consistent equations for the N3LO nuclear energy density functional in spherical symmetry. The program HOSPHE (v1.02)", Comput. Phys. Commun. **181**, 1641 (2010), arXiv:0912.3230 [nucl-th] (cit. on pp. 42, 68, 79, 94).

[198] N. Schunck, J. Dobaczewski, W. Satuła, P. Bączyk, J. Dudek, Y. Gao, M. Konieczka, K. Sato, Y. Shi, X. B. Wang, and T. R. Werner, "Solution of the Skyrme-Hartree–Fock–Bogolyubov equations in the Cartesian deformed harmonic-oscillator basis. (VIII) HFODD (v2.73y): A new version of the program", Comput. Phys. Commun. **216**, 145 (2017), arXiv:1612.05314 [nucl-th] (cit. on p. 42).

[199] N. Kaiser, S. Fritsch, and W. Weise, "Nuclear energy density functional from chiral pion-nucleon dynamics", Nucl. Phys. A **724**, 47 (2003), arXiv:nucl-th/0212049 [nucl-th] (cit. on p. 42).

[200] N. Kaiser and W. Weise, "Nuclear energy density functional from chiral pion-nucleon dynamics revisited", Nucl. Phys. A **836**, 256 (2010), arXiv:0912.3207 [nucl-th] (cit. on p. 42).

[201] K. Hebeler, S. K. Bogner, R. J. Furnstahl, A. Nogga, and A. Schwenk, "Improved nuclear matter calculations from chiral low-momentum interactions", Phys. Rev. C **83**, 031301(R) (2011), arXiv:1012.3381 [nucl-th] (cit. on pp. 43, 51, 104).

[202] S. K. Bogner, R. J. Furnstahl, and L. Platter, "Density matrix expansion for low-momentum interactions", Eur. Phys. J. A **39**, 219 (2009), arXiv:0811.4198 [nucl-th] (cit. on pp. 43, 61, 63, 64).

[203] J. W. Holt, N. Kaiser, and W. Weise, "Nuclear energy density functional from chiral two- and three-nucleon interactions", Eur. Phys. J. A **47**, 128 (2011), arXiv:1107.5966 [nucl-th] (cit. on p. 43).

[204] A. Gezerlis, I. Tews, E. Epelbaum, M. Freunek, S. Gandolfi, K. Hebeler, A. Nogga, and A. Schwenk, "Local chiral effective field theory interactions and quantum Monte Carlo applications", Phys. Rev. C **90**, 054323 (2014), arXiv:1406.0454 [nucl-th] (cit. on pp. 44, 110).

[205] A. Gezerlis, I. Tews, E. Epelbaum, S. Gandolfi, K. Hebeler, A. Nogga, and A. Schwenk, "Quantum Monte Carlo Calculations with Chiral Effective Field Theory Interactions", Phys. Rev. Lett. **111**, 032501 (2013), arXiv:1303.6243 [nucl-th] (cit. on pp. 44, 110).

[206] V. Durant, P. Capel, L. Huth, A. Balantekin, and A. Schwenk, "Double-folding potentials from chiral effective field theory", Phys. Lett. B **782**, 668 (2018), arXiv:1708.02527 [nucl-th] (cit. on pp. 44, 110).

[207] I. Tews, S. Gandolfi, A. Gezerlis, and A. Schwenk, "Quantum Monte Carlo calculations of neutron matter with chiral three-body forces", Phys. Rev. C **93**, 024305 (2016), arXiv:1507.05561 [nucl-th] (cit. on pp. 44, 105, 111).

[208] V. I. Fabrikant, "Elementary exact evaluation of infinite integrals of the product of several spherical Bessel functions, power and exponential", Quart. Appl. Math. **71**, 573 (2013) (cit. on pp. 53, 57).

[209] B. Gebremariam, T. Duguet, and S. K. Bogner, "Symbolic integration of a product of two spherical Bessel functions with an additional exponential and polynomial factor", Comput. Phys. Commun. **181**, 1136 (2010), arXiv:0910.4993 [physics.comp-ph] (cit. on p. 58).

[210] J. E. Lynn, I. Tews, J. Carlson, S. Gandolfi, A. Gezerlis, K. E. Schmidt, and A. Schwenk, "Quantum Monte Carlo calculations of light nuclei with local chiral two- and three-nucleon interactions", Phys. Rev. C **96**, 054007 (2017), arXiv:1706.07668 [nucl-th] (cit. on p. 64).

[211] H. Krebs, E. Epelbaum, and U.-G. Meißner, "Nuclear forces with Δ-excitations up to next-to-next-to-leading order. I. Peripheral nucleon-nucleon waves", Eur. Phys. J. A **32**, 127 (2007), arXiv:nucl-th/0703087 (cit. on pp. 65, 76, 78, 104).

[212] J. E. Lynn, I. Tews, J. Carlson, S. Gandolfi, A. Gezerlis, K. E. Schmidt, and A. Schwenk, "Chiral Three-Nucleon Interactions in Light Nuclei, Neutron-α Scattering, and Neutron Matter", Phys. Rev. Lett. **116**, 062501 (2016), arXiv:1509.03470 [nucl-th] (cit. on p. 65).

[213] T. Lesinski, M. Bender, K. Bennaceur, T. Duguet, and J. Meyer, "The Tensor part of the Skyrme energy density functional. I. Spherical nuclei", Phys. Rev. C **76**, 014312 (2007), arXiv:0704.0731 [nucl-th] (cit. on pp. 76, 77).

[214] J. Dobaczewski, W. Nazarewicz, and M. V. Stoitsov, "Nuclear ground state properties from mean field calculations", Eur. Phys. J. A **15**, 21 (2002), arXiv:nucl-th/0203060 (cit. on p. 77).

[215] T. Kortelainen M. Lesinski, J. Moré, W. Nazarewicz, J. Sarich, N. Schunck, M. V. Stoitsov, and S. Wild, "Nuclear energy density optimization", Phys. Rev. C **82**, 024313 (2010), arXiv:1005.5145 [nucl-th] (cit. on pp. 77, 85, 88, 91, 92).

[216] M. Girod and B. Grammaticos, "Triaxial Hartree-Fock-Bogolyubov calculations with D-1 effective interaction", Phys. Rev. C **27**, 2317 (1983) (cit. on pp. 77, 101).

[217] M. V. Stoitsov, N. Schunck, M. Kortelainen, N. Michel, H. Nam, E. Olsen, J. Sarich, and S. Wild, "Axially deformed solution of the Skyrme-Hartree-Fock-Bogolyubov equations using the transformed harmonic oscillator basis (II) HFBTHO v2.00c: a new version of the program", Comput. Phys. Commun. **184**, 1592 (2013), arXiv:1210.1825 [nucl-th] (cit. on pp. 77, 84).

[218] P. Marevic, N. Schunck, E. M. Ney, R. Navarro Pérez, M. Verriere, and J. O'Neal, "Axially-deformed solution of the Skyrme-Hartree-Fock-Bogoliubov equations using the transformed harmonic oscillator basis (IV) HFBTHO (v4.0): A new version of the program", Comput. Phys. Commun. **276**, 108367 (2022), arXiv:2110.06424 [nucl-th] (cit. on pp. 77, 84, 112).

[219] W. Younes, "Gaussian matrix elements in a cylindrical harmonic oscillator basis", Comput. Phys. Commun. **180**, 1013 (2009), arXiv:0910.1855 [nucl-th] (cit. on p. 78).

[220] R. Navarro Perez, N. Schunck, R.-D. Lasseri, C. Zhang, and J. Sarich, "Axially deformed solution of the Skyrme–Hartree–Fock–Bogolyubov equations using the transformed harmonic oscillator basis (III) HFBTHO (v3.00): A new version of the program", Comput. Phys. Commun. **220**, 363 (2017), arXiv:1704.03945 [nucl-th] (cit. on pp. 78, 79, 84).

[221] J. Dobaczewski et al., "Solution of the Skyrme-Hartree-Fock-Bogolyubov equations in the Cartesian deformed harmonic-oscillator basis. (VI) HFODD (v2.40h): A new version of the program", Comput. Phys. Commun. **180**, 2361 (2009), arXiv:0903.1020 [nucl-th] (cit. on p. 78).

[222] R. Navarro Pérez and N. Schunck, "Microscopically based energy density functionals for nuclei using the density matrix expansion", J. Phys. Conf. Ser. **1308**, 012014 (2019), arXiv:1903.08537 [nucl-th] (cit. on pp. 79, 80).

[223] M. Bender, K. Bennaceur, T. Duguet, P.-H. Heenen, T. Lesinski, and J. Meyer, "Tensor part of the Skyrme energy density functional. II: Deformation properties of magic and semi-magic nuclei", Phys. Rev. C **80**, 064302 (2009), arXiv:0909.3782 [nucl-th] (cit. on p. 81).

[224] P. D. Stevenson and M. C. Barton, "Low-Energy Heavy-Ion Reactions and the Skyrme Effective Interaction", Prog. Part. Nucl. Phys. **104**, 142 (2019), arXiv:1809.05801 [nucl-th] (cit. on p. 84).

[225] M. Bender, K. Rutz, P. G. Reinhard, and J. A. Maruhn, "Consequences of the center-of-mass correction in nuclear mean field models", Eur. Phys. J. A **7**, 467 (2000), arXiv:nucl-th/9910025 (cit. on p. 84).

[226] M. V. Stoitsov, J. Dobaczewski, W. Nazarewicz, S. Pittel, and D. J. Dean, "Systematic study of deformed nuclei at the drip lines and beyond", Phys. Rev. C **68**, 054312 (2003), arXiv:nucl-th/0307049 (cit. on p. 84).

[227] M. V. Stoitsov, J. Dobaczewski, R. Kirchner, W. Nazarewicz, and J. Terasaki, "Variation after Particle-Number Projection for the HFB Method with the Skyrme Energy Density Functional", Phys. Rev. C **76**, 014308 (2007), arXiv:nucl-th/0610061 (cit. on p. 84).

[228] G. F. Bertsch, C. A. Bertulani, W. Nazarewicz, N. Schunck, and M. V. Stoitsov, "Odd-even mass differences from self-consistent mean-field theory", Phys. Rev. C **79**, 034306 (2009), arXiv:0812.0747 [nucl-th] (cit. on pp. 84, 88, 92).

[229] R. Sellahewa and A. Rios, "Isovector properties of the Gogny interaction", Phys. Rev. C **90**, 054327 (2014), arXiv:1407.8138 [nucl-th] (cit. on pp. 85, 92).

[230] C. Drischler, K. Hebeler, and A. Schwenk, "Asymmetric nuclear matter based on chiral two- and three-nucleon interactions", Phys. Rev. C **93**, 054314 (2016), arXiv:1510.06728 [nucl-th] (cit. on p. 85).

[231] C. Drischler, R. J. Furnstahl, J. A. Melendez, and D. R. Phillips, "How Well Do We Know the Neutron-Matter Equation of State at the Densities Inside Neutron Stars? A Bayesian Approach with Correlated Uncertainties", Phys. Rev. Lett. **125**, 202702 (2020), arXiv:2004.07232 [nucl-th] (cit. on pp. 86, 91, 92).

[232] S. Huth, C. Wellenhofer, and A. Schwenk, "New equations of state constrained by nuclear physics, observations, and QCD calculations of high-density nuclear matter", Phys. Rev. C **103**, 025803 (2021), arXiv:2009.08885 [nucl-th] (cit. on pp. 86, 91).

[233] J. Dobaczewski, W. Nazarewicz, and P.-G. Reinhard, "Error Estimates of Theoretical Models: a Guide", J. Phys. G: Nucl. Part. Phys. **41**, 074001 (2014), arXiv:1402.4657 [nucl-th] (cit. on p. 86).

[234] N. Schunck, J. O'Neal, M. Grosskopf, E. Lawrence, and S. M. Wild, "Calibration of energy density functionals with deformed nuclei", J. Phys. G **47**, 074001 (2020), arXiv:2003.12207 [nucl-th] (cit. on pp. 86, 88, 113, 114).

[235] M. Wang, W. J. Huang, F. G. Kondev, G. Audi, and S. Naimi, "The AME 2020 atomic mass evaluation (II). Tables, graphs and references", Chin. Phys. C **45**, 030003 (2021) (cit. on pp. 87, 95, 103).

[236] I. Angeli and K. Marinova, "Table of experimental nuclear ground state charge radii: An update", Atom. Data Nucl. Data Tabl. **99**, 69 (2013) (cit. on pp. 88, 97).

[237] F. Sommer et al., "Charge Radii of ^{55,56}Ni Reveal a Surprisingly Similar Behavior at $N = 28$ in Ca and Ni Isotopes", Phys. Rev. Lett. **129**, 132501 (2022), arXiv:2210.01924 [nucl-ex] (cit. on p. 88).

[238] E. Tiesinga, P. J. Mohr, D. B. Newell, and B. N. Taylor, "CODATA recommended values of the fundamental physical constants: 2018", Rev. Mod. Phys. **93**, 025010 (2021) (cit. on p. 88).

[239] R. L. Workman et al. (Particle Data Group), "Review of Particle Physics", Prog. Theor. Exp. Phys. **2022**, 083C01 (2022) (cit. on p. 88).

[240] B. Singh, R. Zywina, and R. B. Firestone, "Table of Superdeformed Nuclear Bands and Fission Isomers: Third Edition (October 2002)", Nucl. Data Sheets **97**, 241 (2002) (cit. on pp. 88, 101).

[241] J. Dobaczewski, W. Nazarewicz, and T. R. Werner, "Closed shells at drip-line nuclei", Phys. Scripta **56**, 15 (1995), arXiv:nucl-th/9411003 (cit. on p. 88).

[242] N. Schunck, J. Dobaczewski, J. McDonnell, J. More, W. Nazarewicz, J. Sarich, and M. V. Stoitsov, "One-quasiparticle States in the Nuclear Energy Density Functional Theory", Phys. Rev. C **81**, 024316 (2010), arXiv:0910.2164 [nucl-th] (cit. on pp. 88, 98).

[243] S. M. Wild, J. Sarich, and N. Schunck, "Derivative-free optimization for parameter estimation in computational nuclear physics", J. Phys. G **42**, 034031 (2015), arXiv:1406.5464 [physics.comp-ph] (cit. on pp. 88, 89).

[244] S. M. Wild, "POUNDERS in TAO: Solving Derivative-Free Nonlinear Least-Squares Problems with POUNDERS", in *Advances and Trends in Optimization with Engineering Applications*, edited by T. Terlaky, M. F. Anjos, and S. Ahmed (SIAM, Philadelphia, 2017), pp. 529–539 (cit. on p. 88).

[245] J. Bartel, P. Quentin, M. Brack, C. Guet, and H.-B. Håkansson, "Towards a better parametrisation of Skyrme-like effective forces: A Critical study of the SkM force", Nucl. Phys. A **386**, 79 (1982) (cit. on p. 89).

[246] A. W. Steiner, M. Prakash, J. M. Lattimer, and P. J. Ellis, "Isospin asymmetry in nuclei and neutron stars", Phys. Rept. **411**, 325 (2005), arXiv:nucl-th/0410066 (cit. on p. 89).

[247] D. R. Entem, R. Machleidt, and Y. Nosyk, "High-quality two-nucleon potentials up to fifth order of the chiral expansion", Phys. Rev. C **96**, 024004 (2017), arXiv:1703.05454 [nucl-th] (cit. on p. 92).

[248] S. Goriely, M. Samyn, and J. M. Pearson, "Further explorations of Skyrme–Hartree–Fock–Bogoliubov mass formulas; VI: Weakened pairing", Nucl. Phys. A **773**, 279 (2006) (cit. on p. 92).

[249] Y. Gao, J. Dobaczewski, M. Kortelainen, J. Toivanen, and D. Tarpanov, "Propagation of uncertainties in the Skyrme energy-density-functional model", Phys. Rev. C **87**, 034324 (2013), arXiv:1301.6151 [nucl-th] (cit. on p. 92).

[250] S. Crowder, C. Delker, E. Forrest, and N. Martin, *Introduction to Statistics in Metrology* (Springer, Cham, 2020) (cit. on p. 96).

[251] B. Zhou and Z. Ren, "Nonlocalized clustering in nuclei", Advances in Physics: X **2**, 359 (2017) (cit. on p. 96).

[252] T. Duguet and G. Hagen, "Ab Initio Approach to Effective Single-Particle Energies in Doubly Closed Shell Nuclei", Phys. Rev. C **85**, 034330 (2012), arXiv:1110.2468 [nucl-th] (cit. on p. 99).

[253] T. Duguet, H. Hergert, J. D. Holt, and V. Somà, "Nonobservable Nature of the Nuclear Shell Structure: Meaning, Illustrations, and Consequences", Phys. Rev. C **92**, 034313 (2015), arXiv:1411.1237 [nucl-th] (cit. on p. 99).

[254] N. Schwierz, I. Wiedenhover, and A. Volya, "Parameterization of the Woods-Saxon Potential for Shell-Model Calculations", 2007, arXiv:0709.3525 [nucl-th] (cit. on p. 99).

[255] G. Colò, H. Sagawa, and P. F. Bortignon, "Effect of Particle-Vibration Coupling on Single-Particle States: A Consistent Study within the Skyrme Framework", Phys. Rev. C **82**, 064307 (2010) (cit. on p. 99).

[256] L.-G. Cao, G. Colò, H. Sagawa, and P. F. Bortignon, "Properties of Single-Particle States in a Fully Self-Consistent Particle-Vibration Coupling Approach", Phys. Rev. C **89**, 044314 (2014), arXiv:1401.1983 [nucl-th] (cit. on p. 99).

[257] D. Tarpanov, J. Toivanen, J. Dobaczewski, and B. G. Carlsson, "Polarization Corrections to Single-Particle Energies Studied within the Energy-Density-Functional and Quasiparticle Random-Phase Approximation Approaches", Phys. Rev. C **89**, 014307 (2014), arXiv:1310.0435 [nucl-th] (cit. on p. 99).

[258] D. Tarpanov, J. Dobaczewski, J. Toivanen, and B. G. Carlsson, "Spectroscopic Properties of Nuclear Skyrme Energy Density Functionals", Phys. Rev. Lett. **113**, 252501 (2014), arXiv:1405.4823 [nucl-th] (cit. on p. 99).

[259] N. Schunck, D. Duke, H. Carr, and A. Knoll, "Description of Induced Nuclear Fission with Skyrme Energy Functionals: Static Potential Energy Surfaces and Fission Fragment Properties", Phys. Rev. C **90**, 054305 (2014), arXiv:1311.2616 [nucl-th] (cit. on pp. 100, 101).

[260] R. Capote, M. Herman, P. Obložinský, P. Young, S. Goriely, T. Belgya, A. Ignatyuk, A. Koning, S. Hilaire, V. Plujko, et al., "RIPL – Reference Input Parameter Library for Calculation of Nuclear Reactions and Nuclear Data Evaluations", Nucl. Data Sheets **110**, 3107 (2009) (cit. on p. 101).

[261] M. Hunyadi, D. Gassmann, A. Krasznahorkay, D. Habs, P. Thirolf, M. Csatlós, Y. Eisermann, T. Faestermann, G. Graw, J. Gulyás, et al., "Excited superdeformed $K^\pi = 0^+$ rotational bands in β-vibrational fission resonances of ^{240}Pu", Phys. Lett. B **505**, 27 (2001) (cit. on p. 101).

[262] N. Nikolov, N. Schunck, W. Nazarewicz, M. Bender, and J. Pei, "Surface Symmetry Energy of Nuclear Energy Density Functionals", Phys. Rev. C **83**, 034305 (2011), arXiv:1012.5829 [nucl-th] (cit. on p. 102).

[263] R. Jodon, M. Bender, K. Bennaceur, and J. Meyer, "Constraining the Surface Properties of Effective Skyrme Interactions", Phys. Rev. C **94**, 024335 (2016), arXiv:1606.01410 [nucl-th] (cit. on p. 102).

[264] G. Gelmini and B. Ritzi, "Chiral effective Lagrangian description of bulk nuclear matter", Phys. Lett. B **357**, 431 (1995), arXiv:hep-ph/9503480 (cit. on p. 102).

[265] M. Piarulli and I. Tews, "Local Nucleon-Nucleon and Three-Nucleon Interactions Within Chiral Effective Field Theory", Front. in Phys. **7**, 245 (2020), arXiv:2002.00032 [nucl-th] (cit. on p. 104).

[266] K. Hebeler, J. D. Holt, J. Menéndez, and A. Schwenk, "Nuclear forces and their impact on neutron-rich nuclei and neutron-rich matter", Ann. Rev. Nucl. Part. Sci. **65**, 457 (2015), arXiv:1508.06893 [nucl-th] (cit. on pp. 104, 105).

[267] T. Otsuka, T. Suzuki, J. D. Holt, A. Schwenk, and Y. Akaishi, "Three-Body Forces and the Limit of Oxygen Isotopes", Phys. Rev. Lett. **105**, 032501 (2010), arXiv:0908.2607 [nucl-th] (cit. on pp. 104, 105).

[268] H. Hergert, S. Binder, A. Calci, J. Langhammer, and R. Roth, "Ab Initio Calculations of Even Oxygen Isotopes with Chiral Two-Plus-Three-Nucleon Interactions", Phys. Rev. Lett. **110**, 242501 (2013), arXiv:1302.7294 [nucl-th] (cit. on p. 104).

[269] A. Cipollone, C. Barbieri, and P. Navrátil, "Isotopic chains around oxygen from evolved chiral two- and three-nucleon interactions", Phys. Rev. Lett. **111**, 062501 (2013), arXiv:1303.4900 [nucl-th] (cit. on p. 104).

[270] G. R. Jansen, J. Engel, G. Hagen, P. Navrátil, and A. Signoracci, "Ab-initio coupled-cluster effective interactions for the shell model: Application to neutron-rich oxygen and carbon isotopes", Phys. Rev. Lett. **113**, 142502 (2014), arXiv:1402.2563 [nucl-th] (cit. on p. 104).

[271] S. K. Bogner, A. Schwenk, R. J. Furnstahl, and A. Nogga, "Is nuclear matter perturbative with low-momentum interactions?", Nucl. Phys. A **763**, 59 (2005), arXiv:nucl-th/0504043 (cit. on p. 104).

[272] D. Vautherin and D. M. Brink, "Hartree-Fock calculations with Skyrme's interaction. I. Spherical nuclei", Phys. Rev. C **5**, 626 (1972) (cit. on pp. 105, 110).

[273] B. Friman and A. Schwenk, "Three-body interactions in Fermi systems", in *From Nuclei to Stars: Festschrift in Honor of Gerald E Brown*, edited by S. Lee (World Scientific, Singapore, 2011), pp. 141–156, arXiv:1101.4858 [nucl-th] (cit. on p. 105).

[274] P. Walker, Y. A. Litvinov, and H. Geissel, "The ILIMA project at FAIR", International Journal of Mass Spectrometry **349-350**, 247 (2013) (cit. on p. 105).

[275] E. F. Zhou, J. M. Yao, Z. P. Li, J. Meng, and P. Ring, "Anatomy of Molecular Structures in ^{20}Ne", Phys. Lett. B **753**, 227 (2016), arXiv:1510.05232 [nucl-th] (cit. on p. 105).

[276] P. Marević, J.-P. Ebran, E. Khan, T. Nikšić, and D. Vretenar, "Cluster Structures in ^{12}C from Global Energy Density Functionals", Phys. Rev. C **99**, 034317 (2019), arXiv:1810.02632 [nucl-th] (cit. on p. 105).

[277] W. Nazarewicz, P.-G. Reinhard, W. Satula, and D. Vretenar, "Symmetry energy in nuclear density functional theory", Eur. Phys. J. A **50**, 20 (2014), arXiv:1307.5782 [nucl-th] (cit. on pp. 106, 111).

[278] S. Goriely, N. Chamel, and J. M. Pearson, "Further explorations of Skyrme-Hartree-Fock-Bogoliubov mass formulas. XII: Stiffness and stability of neutron-star matter", Phys. Rev. C **82**, 035804 (2010), arXiv:1009.3840 [nucl-th] (cit. on p. 107).

[279] J. Erler, C. J. Horowitz, W. Nazarewicz, M. Rafalski, and P.-G. Reinhard, "Energy density functional for nuclei and neutron stars", Phys. Rev. C **87**, 044320 (2013), arXiv:1211.6292 [nucl-th] (cit. on p. 107).

[280] T. F. Motta, A. M. Kalaitzis, S. Antić, P. A. M. Guichon, J. R. Stone, and A. W. Thomas, "Isovector Effects in Neutron Stars, Radii and the GW170817 Constraint", Astrophys. J. **878**, 159 (2019), arXiv:1904.03794 [nucl-th], Erratum: Astrophys. J. **917**, 111 (2022) (cit. on p. 107).

[281] P.-G. Reinhard and W. Nazarewicz, "Information content of a new observable: The case of the nuclear neutron skin", Phys. Rev. C **81**, 051303(R) (2010), arXiv:1002.4140 [nucl-th] (cit. on p. 111).

[282] J. Piekarewicz, B. K. Agrawal, G. Colò, W. Nazarewicz, N. Paar, P.-G. Reinhard, X. Roca-Maza, and D. Vretenar, "Electric dipole polarizability and the neutron skin", Phys. Rev. C **85**, 041302 (2012), arXiv:1201.3807 [nucl-th] (cit. on p. 111).

[283] P.-G. Reinhard and W. Nazarewicz, "Information content of the differences in the charge radii of mirror nuclei", Phys. Rev. C **105**, L021301 (2022), arXiv:2201.02238 [nucl-th] (cit. on p. 111).

[284] S. K. Bogner, R. J. Furnstahl, H. Hergert, M. Kortelainen, P. Maris, M. Stoitsov, and J. P. Vary, "Testing the density matrix expansion against ab initio calculations of trapped neutron drops", Phys. Rev. C **84**, 044306 (2011), arXiv:1106.3557 [nucl-th] (cit. on p. 111).

[285] H. D. Potter, S. Fischer, P. Maris, J. P. Vary, S. Binder, A. Calci, J. Langhammer, and R. Roth, "Ab Initio study of neutron drops with chiral Hamiltonians", Phys. Lett. B **739**, 445 (2014), arXiv:1406.1160 [nucl-th] (cit. on p. 111).

[286] J. Bonnard, M. Grasso, and D. Lacroix, "Energy-density functionals inspired by effective-field theories: Applications to neutron drops", Phys. Rev. C **98**, 034319 (2018), arXiv:1806.01084 [nucl-th], Erratum: Phys. Rev.C **103**, 039901 (2021) (cit. on p. 111).

[287] B. S. Pudliner, A. Smerzi, J. Carlson, V. R. Pandharipande, S. C. Pieper, and D. G. Ravenhall, "Neutron drops and Skyrme energy density functionals", Phys. Rev. Lett. **76**, 2416 (1996), arXiv:nucl-th/9510022 (cit. on p. 111).

[288] F. Marino, G. Colò, X. Roca-Maza, and E. Vigezzi, "Perturbed nuclear matter studied within density functional theory with a finite number of particles", Phys. Rev. C **107**, 044311 (2023), arXiv:2211.07986 [nucl-th] (cit. on p. 111).

[289] P. Bączyk, W. Satuła, J. Dobaczewski, and M. Konieczka, "Isobaric Multiplet Mass Equation within nuclear Density Functional Theory", J. Phys. G **46**, 03LT01 (2019), arXiv:1801.02506 [nucl-th] (cit. on p. 112).

[290] R. J. Furnstahl and J. C. Hackworth, "Skyrme energy functional and naturalness", Phys. Rev. C **56**, 2875 (1997), arXiv:nucl-th/9708018 (cit. on p. 112).

[291] M. Kortelainen, R. J. Furnstahl, W. Nazarewicz, and M. V. Stoitsov, "Natural Units For Nuclear Energy Density Functional Theory", Phys. Rev. C **82**, 011304 (2010), arXiv:1005.2552 [nucl-th] (cit. on p. 112).

[292] T. Naito, X. Roca-Maza, G. Colò, and H. Liang, "Effects of finite nucleon size, vacuum polarization, and electromagnetic spin-orbit interaction on nuclear binding energies and radii in spherical nuclei", Phys. Rev. C **101**, 064311 (2020), arXiv:2003.03177 [nucl-th] (cit. on p. 112).

[293] T. Naito, "Relativistic correction of the Coulomb interaction in the local density approximation for energies and radii in doubly-magic nuclei", PTEP **2022**, 093D04 (2022), arXiv:2106.14270 [nucl-th] (cit. on p. 112).

[294] M. Kortelainen, Z. Sun, G. Hagen, W. Nazarewicz, T. Papenbrock, and P.-G. Reinhard, "Universal trend of charge radii of even-even Ca–Zn nuclei", Phys. Rev. C **105**, L021303 (2022), arXiv:2111.12464 [nucl-th] (cit. on p. 112).

[295] T. Naito, T. Oishi, H. Sagawa, and Z. Wang, "Comparative study on charge radii and their kinks at magic numbers", Phys. Rev. C **107**, 054307 (2023), arXiv:2209.02857 [nucl-th] (cit. on p. 112).

[296] J. Dobaczewski, W. Nazarewicz, T. R. Werner, J. F. Berger, C. R. Chinn, and J. Decharge, "Mean field description of ground state properties of dripline nuclei: Pairing and continuum effects", Phys. Rev. C **53**, 2809 (1996), arXiv:nucl-th/9512008 (cit. on p. 112).

[297] T. Lesinski, K. Hebeler, T. Duguet, and A. Schwenk, "Chiral three-nucleon forces and pairing in nuclei", J. Phys. G: Nucl. Part. Phys. **39**, 015108 (2012), arXiv:1104.2955 [nucl-th] (cit. on p. 112).

[298] M. Bender, T. Duguet, and D. Lacroix, "Particle-Number Restoration within the Energy Density Functional Formalism", Phys. Rev. C **79**, 044319 (2009), arXiv:0809.2045 [nucl-th] (cit. on p. 112).

[299] T. Duguet, M. Bender, K. Bennaceur, D. Lacroix, and T. Lesinski, "Particle-number restoration within the energy density functional formalism: Nonviability of terms depending on noninteger powers of the density matrices", Phys. Rev. C **79**, 044320 (2009), arXiv:0809.2049 [nucl-th] (cit. on p. 113).

[300] J. Erler, P. Klüpfel, and P.-G. Reinhard, "Exploration of a modified density dependence in the Skyrme functional", Phys. Rev. C **82**, 044307 (2010), arXiv:1009.0624 [nucl-th] (cit. on p. 113).

[301] D. Lacroix and K. Bennaceur, "Semicontact three-body interaction for nuclear density functional theory", Phys. Rev. C **91**, 011302 (2015), arXiv:1411.0360 [nucl-th] (cit. on p. 113).

[302] P. Giuliani, K. Godbey, E. Bonilla, F. Viens, and J. Piekarewicz, "Bayes goes fast: Uncertainty quantification for a covariant energy density functional emulated by the reduced basis method", Frontiers in Physics **10**, 1212 (2023), arXiv:2209.13039 [nucl-th] (cit. on pp. 113, 114).

[303] A. Arzhanov, T. R. Rodríguez, and G. Martínez-Pinedo, "Systematic study of infrared energy corrections in truncated oscillator spaces with Gogny energy density functionals", Phys. Rev. C **94**, 054319 (2016), arXiv:1606.00074 [nucl-th] (cit. on p. 114).

[304] M. Knöll, T. Wolfgruber, M. L. Agel, C. Wenz, and R. Roth, "Machine learning for the prediction of converged energies from ab initio nuclear structure calculations", Phys. Lett. B **839**, 137781 (2023), arXiv:2207.03828 [nucl-th] (cit. on p. 114).

[305] T. Wolfgruber, M. Knöll, and R. Roth, "Precise neural network predictions of energies and radii from the no-core shell model", 2023, arXiv:2310.05256 [nucl-th] (cit. on p. 114).

[306] M. A. Petroff, "Accessible Color Sequences for Data Visualization", 2021, arXiv:2107.02270 [cs.GR] (cit. on p. 151).

[307] D. Nichols, *Coloring for Colorblindness*, https://davidmathlogic.com/colorblind (cit. on p. 151).

[308] J. L. Hoppe, "The in-medium similarity renormalization group for ab initio nuclear structure: method advances and new applications", PhD thesis (Technische Universität Darmstadt, 2022), https://tuprints.ulb.tu-darmstadt.de/21576/ (cit. on p. 152).

Acknowledgments

I would like to thank my supervisor Achim Schwenk without whom this thesis certainly would not exist. Thank you for allowing me to spend essentially my whole academic career so far – from writing my Bachelor's thesis to now – as a member of the STRONGINT group. I really appreciate not only the scientific guidance and fruitful discussions but also the very welcoming and friendly work environment. Thanks for giving honest feedback and encouragement. I am grateful that I was given the opportunity to travel to many places and to participate in several summer schools, conferences, and workshops, which were not only of great scientific value but also led to many hopefully long-lasting memories.

Also I want to thank Stephanie Müller for all the important administrative support as well as Arianna Carbone and Toño Coello Pérez for co-advising me at the beginning of my scientific journey.

The work I have conducted over the years would not have been possible without my collaborators. I would like to thank them for many valuable discussions and all the work and thoughts they put into the different projects. In particular thanks to Scott Bogner, Toño Coello Pérez, Dick Furnstahl, Rodrigo Navarro Pérez, Nicolas Schunck, and Achim Schwenk for working together on the topics discussed in this thesis.

I want to thank Dick Furnstahl, Thomas Aumann, and Michael Vogel for accepting to examine this work.

Moreover, I am thankful to Pierre Arthuis, Matthias Heinz, and Achim Schwenk for valuable comments I received during writing of this thesis and to Jan Hoppe for providing the 1.8/2.0 (EM) HF orbitals used as part of the DME study in this work. I thank Jan Hoppe, Sabrina Huth, and Jonas Keller for organizational tips regarding this thesis and its defense. I am also indebted to Alex Dyhdalo, Rodrigo Navarro Pérez, and Nicolas Schunck for their DME and EDF computer codes and helping me with using them. I want to acknowledge the colorblind friendly color scheme developed in Ref. [306] and an online colorblindness simulation tool [307], which I used for creating some of the figures shown in this thesis, as well different free software that has been very helpful. This includes the MaTeX and SciDraw packages for Mathematica and IguanaTex and PPspliT for creating presentations.

My work was supported by the Deutsche Forschungsgemeinschaft (DFG, German Research Foundation) – Project-ID 279384907 – SFB 1245 and by the BMBF Contract Nos. 05P18RDFN1 and 05P21RDFNB. Calculations for this research were in part conducted on the Lichtenberg high performance computer of the TU Darmstadt and on the local cluster of the STRONGINT group. I thank Kai Hebeler for the computing support.

I would like to thank numerous people for helpful discussions. This includes, but is not limited to, Pierre Arthuis, Jacek Dobaczewski, Thomas Duguet, Matthias Heinz, Sebastian König, Thomas Papenbrock, Alex Tichai, and Stefan Wild.

Of course, I would like to thank my colleagues in Darmstadt. Thanks to all STRONGINT group members and in particular to my office mates for the very pleasant atmosphere at work and the many useful physics discussions. I thank Pierre Arthuis, Margarida Companys,

Hannah Göttling, Kai Hebeler, Matthias Heinz, Jan Hoppe, Marco Knöll, and Rodric Seutin for all the discussions about topics beyond physics and for the great times travelling with you. And I thank Jan Hoppe for investigating together the use of EDF orbitals in ab initio approaches, see also Ref. [308], and Matthias Heinz for organizing our group's journal club.

I would like to thank my friends, including colleagues in Darmstadt and around the world that became friends (hi, Garda group), for being.

Thanks a lot, Caro, for helping me hang on during the stressful last weeks of writing my thesis and preparing the defense. You are awesome!

Last but most definitely not least I would like to thank my family, especially my mum, dad, and sister for all the support, for always having my back, and simply for always being there when I need them.

Erklärungen laut Promotionsordnung

§8 Abs. 1 lit. c PromO

Ich versichere hiermit, dass die elektronische Version meiner Dissertation mit der schriftlichen Version übereinstimmt.

§8 Abs. 1 lit. d PromO

Ich versichere hiermit, dass zu einem vorherigen Zeitpunkt noch keine Promotion versucht wurde. In diesem Fall sind nähere Angaben über Zeitpunkt, Hochschule, Dissertationsthema und Ergebnis dieses Versuchs mitzuteilen.

§9 Abs. 1 PromO

Ich versichere hiermit, dass die vorliegende Dissertation selbstständig und nur unter Verwendung der angegebenen Quellen verfasst wurde.

§9 Abs. 2 PromO

Die Arbeit hat bisher noch nicht zu Prüfungszwecken gedient.

Darmstadt, den 17. Oktober 2023

Lars Zurek